

## Characterising Angular Accelerometers using a Two-Axis Motion Simulator

Jatiningrum, Dyah

**DOI**

[10.4233/uuid:7be51192-65f2-47c4-a1ca-9f15bab12dbc](https://doi.org/10.4233/uuid:7be51192-65f2-47c4-a1ca-9f15bab12dbc)

**Publication date**

2018

**Document Version**

Final published version

**Citation (APA)**

Jatiningrum, D. (2018). *Characterising Angular Accelerometers using a Two-Axis Motion Simulator*. [Dissertation (TU Delft), Delft University of Technology]. <https://doi.org/10.4233/uuid:7be51192-65f2-47c4-a1ca-9f15bab12dbc>

**Important note**

To cite this publication, please use the final published version (if applicable). Please check the document version above.

**Copyright**

Other than for strictly personal use, it is not permitted to download, forward or distribute the text or part of it, without the consent of the author(s) and/or copyright holder(s), unless the work is under an open content license such as Creative Commons.

**Takedown policy**

Please contact us and provide details if you believe this document breaches copyrights. We will remove access to the work immediately and investigate your claim.

# **CHARACTERISING ANGULAR ACCELEROMETERS USING A TWO-AXIS MOTION SIMULATOR**



# **CHARACTERISING ANGULAR ACCELEROMETERS USING A TWO-AXIS MOTION SIMULATOR**

## **Dissertation**

for the purpose of obtaining the degree of doctor  
at Delft University of Technology  
by the authority of the Rector Magnificus, prof. dr. ir. T.H.J.J. van der Hagen,  
chair of the Board for Doctorates  
to be defended publicly on  
Tuesday, 30 October 2018 at 15:00 o'clock

by

**Dyah JATININGRUM**

Master of Engineering in Aeronautics and Astronautics  
Bandung Institute of Technology, Indonesia  
born in Madiun, Indonesia

This dissertation has been approved by the promotor:  
prof. dr. ir. M. Mulder

Copromotor:  
dr. ir. C. C. de Visser

Composition of the doctoral committee:

Rector Magnificus,	chairperson
prof. dr. ir. M. Mulder,	Delft University of Technology, promotor
dr. ir. C. C. de Visser,	Delft University of Technology, copromotor

*Independent members:*

prof. dr. H. Muhammad,	Institute of Technology Bandung
dr. ir. S. K. Advani,	International Development of Technology
prof. dr. ir. D. A. Abbink,	Delft University of Technology
prof. dr. ir. L. L. M. Veldhuis,	Delft University of Technology
dr. ir. Q. P. Chu,	Delft University of Technology



Dr. ir. M. M. van Paassen of Delft University of Technology has contributed greatly to the preparation of this dissertation.

*Keywords:* angular accelerometer, calibration, novel inertial sensor, modelling, motion simulator, frequency response, axis alignment

*Printed by:* Ipskamp Printing

*Front & Back:* Designed by D. Jatiningrum, I. Wibisana & A. I. Ranakitri  
(Graphics from [www.wallpaperscraft.com](http://www.wallpaperscraft.com) and [www.pngtree.com](http://www.pngtree.com))

Copyright © 2018 by D. Jatiningrum

ISBN 978-94-6186-968-5

An electronic version of this dissertation is available at  
<http://repository.tudelft.nl/>.

*“The most dangerous world-view  
is the world-view of those who have not viewed the world.”*

Alexander von Humboldt



# SUMMARY

Fault-Tolerant Flight Control (FTFC) systems reconfigure aircraft flight control laws to help restore a controlled flight and preserve acceptable performance under system faults. A typical approach to achieve fault tolerance is using inertial sensor measurements which can provide robustness to abrupt changes in the aircraft dynamics. This method does not rely on an accurate and full aerodynamic model, but only requires an estimate of the control effectiveness and an additional reconfiguration mechanism to the control laws such as switching, model following, matching, and adaptive compensation. With the inertial sensor being at the very heart of the control laws, to have proven and well-understood sensors is essential to increase the operational performance of a post-failure aircraft.

Recent developments lead to FTFC systems that require *angular acceleration* feedback, which with the current conventional Inertial Measurement Unit (IMU) is obtained by taking the first derivative of the angular rates measured by gyroscopes. Because differentiation commonly intensifies noise and incurs a delay, a direct measurement of angular acceleration is anticipated to enhance the quality of the feedback signal. However, angular accelerometers are currently not part of the commercial aircraft system, which prompts the need to understand their characteristics. This thesis aims to investigate how an angular accelerometer can be evaluated and calibrated in a systematic fashion.

The standard of inertial sensors evaluation is, at the moment, the turntable or motion simulator system. Unfortunately, the highly accurate angular rate provided by current motion simulators does not necessarily mean that it also provides a precise angular acceleration. This capability is due to the design of the motion simulator which typically aims for superior performance in providing *static operation*, i.e., a constant rotation rate without rotational acceleration. Moreover, rigorous examination procedures for this new type of sensor are not yet well-established. This shortcoming mainly concerns isolating the possible test equipment's issues from sensor inaccuracies. With the *dynamic angular operation* and method limitation in mind, this dissertation therefore focuses on how to characterise angular accelerometers using a 2-axis motion simulator effectively.

The goal is achieved by first performing a series of preliminary checks on the available motion simulator system and measurement set-up, and subsequently identify all relevant issues. One of our first findings include the considerable electrical noise produced by the motion simulator slip ring, which transmits the sensor signal to the Data Acquisition Systems (DAS), and the problems associated with the use of different clocks by the turntable and DAS computer. Based on these findings, a customised measurement set-up was established. It utilises two auxiliary signals generated by a custom-built Sensor Data Acquisition System (SDAS) computer to aid the post-measurement processing in synchronising angular accelerometer and motion simulator data. The SDAS and synchronisation

procedures ensure that high-quality data can be acquired from the measurement. A general measurement framework that describes internal and external disturbances, and the relation between all subsystems in the measurement set-up as required to perform angular accelerometers experiments is also proposed.

After the customised set-up to obtain synchronised measurement data is prepared, a scale factor calibration of the angular accelerometer output to a known standard was the second objective. The scale factor is crucial to map the sensor output in volts to the corresponding unit of degree per second square. For this purpose, an investigation of three input excitations was performed: (i) a pendulum method, (ii) a combination of two axes rotational rate input, and (iii) angular acceleration in the form of a sinusoidal profile. A sinusoidal angular acceleration amplitude profile is then preferred as the appropriate input, over an ingenious solution offered by the coordinated two axes sequence that can only cover a small frequency range with the current turntable, and over the pendulum method which would require additional equipment that is complicated to implement.

As the standard estimated angular acceleration of the turntable turned out to be insufficient, another accurate angular acceleration reference was needed. The requirement lead to an advanced observer method that utilises Sliding-Mode Differentiation (SMD) which yields a refined approximate of angular acceleration norm for the reference. Two polynomial structure scale factor calibration models for the angular accelerometer data were identified, based on least-squares. Utilising Residual Mean Squared Error (RMSE) and the Akaike Information Criterion (AIC) principle, the model's order is evaluated. The examination led to a first order polynomial model when using the available angular acceleration reference, and a third order model for the SMD-approximated angular acceleration reference. The third order model can also capture the nonlinearity at the peak of the sine profile. These models are nevertheless limited since they rely on the accelerometer response as the only variable. To accurately model the sensor output, future calibration should take more variables into account, for instance, to include effects of temperature changes and jerk.

Before the angular accelerometer implementation in the aircraft system, the sensor dynamic model must be included within the flight control system design. The third objective of this thesis was to obtain a frequency response measurement, to model the angular acceleration feedback information accurately. Experiment conditions are designated within the motion simulator operational limit, and the angular accelerometer technical specifications. The analysis is performed based on the fundamental frequency component, which means that the motion setting is maintained to produce full sine periods of angular acceleration, chosen such that the frequency resolution minimises leakage of the signal spectra. Due to the set-up limitations, this assessment could only cover a frequency bandwidth of 0.4–10 Hz.

The Frequency Response Function (FRF) of the motion simulator and angular accelerometer systems, for different angular acceleration amplitude, is then identified from the discrete Fourier transform of selected input and output pairs. Afterwards, transfer function models, proposed with and without a separate delay term, are estimated using the time-domain data and then validated by the FRF. From the theoretical Bode plot responses, proposed models with a separate delay term show higher systems bandwidth

but substantial phase lag at higher frequencies, which indicates the rapid progress of phase shift and leads to loss of information. Therefore, a fifth-order transfer function model without a separate delay term was chosen as the best representation of the system.

The fourth and last objective addressed in this thesis is the inspection of the angular accelerometer input axis misalignment. It is carried out for an arrangement with three angular accelerometers mounted on a 3-axis mounting block, to form a complete 3-axis Angular Accelerometer Measurement Unit (AAMU). Since the angular accelerometer is only labelled for its sensitive axis orientation, it is necessary to define each sensor's non-sensitive axes to quantify the alignment in each of AAMU's axis. This axis definition agreement, together with the consideration of AAMU installation adjustment, is then rendered in the test scheme. Subsequently, the data analysis is conducted in the frequency domain, which allows an accurate inspection of the response and phase by concentrating on the primary excitation frequency.

Results show that the input motion is detected in both non-sensitive axes, indicating the presence of misalignments. The cross-axis sensitivity, calculated from the ratio of the non-sensitive axis response towards the sensitive axis response, was found to be within the specified one percent value. For this type of arrangement, i.e., an array of sensors installed on a custom-built mounting block, re-mounting could affect both the direction and magnitude of the sensitive axis alignment, as demonstrated in the outcome of repeated measurements. Correction to the voltage response signal of the angular accelerometer is performed using the misalignment angle of the sensitive axis, which can be calculated from the equivalent misalignment angle in the original and pivoted position. Most of the results comply with the maximum half degree input axis misalignment specification.

In this research, it has been demonstrated that the commercially available angular-position based turntable can indeed be utilised to perform an in-depth evaluation of angular accelerometers. The acquired knowledge contributes towards a general method of characterising such sensor, which encompasses not only accurate calibration and modelling, but also modified procedures in dealing with specific angular acceleration motion. Complementary pieces of information are included at the end of this thesis to provide a brief look upon the related tests that support the research work, as well as to highlight valuable elements that for the moment, could not be performed due to current equipment's limitations.

Interest on angular accelerometers nowadays is on the rise compared to the time when this project was started. Nevertheless, this topic still leaves many possibilities to explore. This prospect is mainly in connection with developing a common ground in angular accelerometer calibration by examining different sensors using various motion simulators. In relation with fault-tolerant flight control, the application of the sensor model obtained in this thesis in the control system design could provide validation on model performance. Incorporating effects of temperature in dynamic calibration is also crucial to consider in the future, which calls for the integrated environmental chamber on the turntable. Finally, the development of a state-of-the-art motion simulator that is built specifically to test angular accelerometer is worth an investigation as well.



# SAMENVATTING

Fouttolerante vliegtuigbesturingssystemen (FTVBS) reconfigureren de regelwetten waarmee een vliegtuig bestuurd wordt, om daarmee de controle over de vlucht te herstellen en zo acceptabele prestaties in de aanwezigheid van systeemfouten te handhaven. Een typische mogelijkheid om fouttolerantie te bereiken maakt gebruik van metingen van traagheidsensoren, deze kan robuust zijn voor abrupte veranderingen in de vliegtuigdynamica. Deze methode heeft geen accuraat of compleet aerodynamisch model nodig, maar slechts een schatting van de effectiviteit van de stuurvlakken en een mechanisme om deze vlakken opnieuw te configureren. Omdat de traagheidsensoren de basis vormen voor deze regelwetten, is betrouwbaarheid en een gedegen kennis van deze sensoren van groot belang, zodat de operatie van vliegtuigen na een falen verbeterd wordt.

Recente ontwikkelingen hebben geleid tot FTVBS die gebruik maken van de terugkoppeling van de *hoekversnelling*, die met conventionele traagheidsnavigatiesystemen verkregen moet worden door de afgeleiden van de door gyroscopen gemeten hoeksnelheden te berekenen. Omdat het berekenen van de afgeleiden gewoonlijk ruis verergert, en tot een vertraging van het signaal leidt, is de verwachting dat directe meting van de hoekversnelling de kwaliteit van het terugkoppelingsignaal ten goede kan komen. Echter, hoekversnellingsmeters zijn tot nu toe niet standaard in de systemen aan boord van commerciële vliegtuigen, vandaar dat er een behoefte is om hun eigenschappen nader te bestuderen. Dit proefschrift heeft als doel om te onderzoeken hoe een hoekversnellingsmeter op een systematische manier kan worden geëvalueerd en gecalibreerd.

Het standaardgereedschap voor de evaluatie van traagheidsensoren is de draaitafel ofwel bewegingssimulator. De huidige draaitafels bieden nauwkeurige constante hoeksnelheden, maar dat geeft nog geen garantie dat deze apparaten een nauwkeurige hoekversnelling kunnen aanbieden. Dit is een gevolg van het ontwerp van de bewegingssimulators, dat gericht is op optimale prestatie in statische omstandigheden, dus bij een constante rotatiesnelheid. Ook zijn ijkprocedures voor dit nieuwe type sensor nog geen gemeengoed. Een belangrijke zorg hierbij is het onderscheiden van onnauwkeurigheden in de testapparatuur van die in de gemeten sensor. Gebruikmakend van *dynamische hoekaansturing* en methodische beperkingen in het oog houden, concentreert deze dissertatie zich op het effectief karakteriseren van hoekversnellingsmeters met een tweedimensionale bewegingssimulator.

Om dit doel te bereiken wordt gestart met een inventarisatie van het beschikbare bewegingssimulatorsysteem en de meetopstelling, en een aansluitende identificatie van relevante eigenschappen. Een van de eerste bevindingen betreft de aanzienlijke elektrische verstoring geïntroduceerd door de sleepringen tussen de sensor en het data-acquisitiesysteem (DAS), en de problemen door het gebruik van verschillende klokken in de draaitafel en het DAS. Met deze resultaten is een aangepaste opstelling verwezenlijkt.

Die gebruikt twee hulpsignalen, gegenereerd door een op maat gemaakte sensor data acquisitie systeem (SDAS) computer, om de latere dataverwerking en het synchroniseren van hoekversnellingsmeter- en bewegingssimulatorendata mogelijk te maken. Het SDAS en de synchronisatieprocedures maken het verkrijgen van kwalitatief goede data mogelijk. Daarbij wordt een algemeen raamwerk voor de metingen voorgesteld, dat de interne en externe storingsbronnen beschrijft, alsmede de relatie tussen alle subsystemen in de meetopstelling voor de hoekversnellingsmeters.

Het volgende doel, na het voltooiën van de maatwerkopstelling voor gesynchroniseerde meetdata, was een calibratie van het hoekversnellingsmetersignaal naar een bekende standaard. Een schaalfactor is essentieel om de sensor uitgang in Volt om te zetten naar een fysische eenheid in graden per seconde in het kwadraat. Hiertoe is een onderzoek naar drie ingangssignalen uitgevoerd: (i) een slingermethode, (ii) een combinatie van rotaties in twee assen, (iii) een sinusvormig hoekversnellingsprofiel. Het sinusvormige hoekversnellingsprofiel had de voorkeur, boven het ingenieuze twee-assige rotatiesignaal, dat met de gebruikte draaitafel slechts een klein frequentiebereik kan bestrijken, en boven de slingermethode, die additionele apparatuur zou vereisen.

Omdat de standaard schatting van de hoekversnelling van de draaitafel niet bleek te voldoen, was er een andere nauwkeurige referentie van de hoekversnelling nodig. Deze vereiste leidde tot een geavanceerde schattingsmethode die glijdende modus differentiatie gebruikt, en die resulteert in een verfijnde schatting van de hoekversnellingsreferentie. Gebruikmakend van de kleinste-kwadraten methode zijn er twee polynoomvormige calibratiemodellen voor de schaalfactor opgesteld. Aan de hand van het residu van de gemiddelde kwadratische fout en het Akaike Informatie Criterium, is de modelorde bepaald. Dit leidde tot een eerste orde polynoom voor het gebruik van de al beschikbare hoekversnellingsreferentie, en een derde orde polynoom bij het gebruik van de hoekversnellingsreferentie verkregen door glijdende modus differentiatie. Het derde orde model beschrijft ook een niet-lineariteit bij de piek van het sinusprofiel. Deze modellen zijn niettemin beperkt, voor een meer accuraat model van het sensor uitgangssignaal zal toekomstige calibratie meer variabelen moeten meenemen, zoals temperatuurvariaties en de versnellingsafgeleide.

Om hoekversnellingsmeting in het vliegtuigmeetsysteem te kunnen toepassen zal er een dynamisch model van de sensor voor het ontwerp van het vliegtuigbesturingssysteem nodig zijn. Het derde doel van dit proefschrift was een meting van de frequentieresponsie, om daarmee de hoekversnellingsmeting nauwkeurig te modelleren. Hiervoor zijn experimentele condities binnen de operationele limieten van de bewegingssimulator en van de hoekversnellingsmeter gekozen. De analyse is uitgevoerd op de basisfrequentie van de ingangssinus, en hiertoe is de meting zo geconfigureerd dat lekkage in het frequentiespectrum is voorkomen. Binnen de beperkingen door de opstelling, konden deze metingen uitgevoerd worden met frequenties van 0.4 tot 10 Hz.

De frequentieresponsie functie van de bewegingssimulator en de hoekversnellingsmeetsystemen, bij verschillende grootten van de hoekversnelling, is daarna bepaald op basis van de Fourier getransformeerde van de gekozen ingangs- en uitgangssignalen. Naderhand zijn overdrachtsfunctiemodellen, met en zonder gescheiden vertragungsterm, geschat met behulp van de data in het tijdsdomein en geverifieerd met behulp van de

frequentieresponsie functie. Uit de Bode plots blijkt dat de voorgestelde modellen met gescheiden vertragingsterm een hogere systeem bandbreedte, maar ook en substantiële fasedraaiing bij hogere frequenties vertonen, wat aangeeft de snelle vooruitgang van faseverschuiving en leidt tot verlies van informatie. Omdat dit minder gewenst is, is een vijfde orde overdrachtsfunctie zonder gescheiden vertragingsterm gekozen als meest geschikte model.

Het vierde en laatste doel van dit proefschrift is het onderzoek van de uitlijning van de hoekversnellingsmeter assen. Dit is uitgevoerd voor een opstelling met drie hoekversnellingsmeters op een drie-assig montageblok, waarmee een complete drie-assige hoekversnellingsmeeteenheid gevormd wordt. Omdat alleen de richting van de gevoelige as op de hoekversnellingsmeters is aangegeven, was het nodig om de niet-gevoelige assen apart te definiëren. Met een meetprogramma is deze samenstelling van de asdefinitie-overeenkomst onderzocht, waarbij ook de effecten van het montageproces beschouwd zijn. De data analyse hiervoor is uitgevoerd in het frequentiedomein, wat een nauwkeurige inspectie van de amplitude- en faseresponsie op de primaire excitatiefrequentie mogelijk maakt.

Uit de resultaten blijkt dat het testsignaal tot een responsie in de niet-gevoelige assen leidt, wat aangeeft dat er uitlijnfouten zijn. De gevoeligheid van de niet-gevoelige assen, uitgedrukt als proportie van de responsie in de hoofdas, bleek binnen de specificatie van één procent te vallen. Bij deze opstelling, een set sensoren in een montageblok, is het montageproces van invloed op de richting en grootte van de afwijkingen van de uitlijning, zoals bleek uit herhaalde metingen in het meetprogramma. Een correctie is toegevoegd aan het spanningssignaal van de hoekversnellingsmeters, gebruikmakend van de uitlijnfout van de gevoelige as, die berekend werd uit de uitlijnfouten in de verschillende (originele en verdraaide) montageposities. De meeste resultaten voldoen aan de specificatie van een maximale uitlijnfout van een halve graad.

Dit onderzoek toont aan dat een commercieel verkrijgbare draaitafel met metingen van de hoekpositie inderdaad gebruikt kan worden voor een grondige evaluatie van hoekversnellingsmeters. De kennis opgedaan in dit onderzoek draagt bij aan een algemene methode voor het karakteriseren van dergelijke sensoren, niet alleen op het gebied van calibratie en modellering, maar ook voor wat betreft gewijzigde procedures om met de hoekversnellingsbeweging om te gaan. Additionele informatie wordt gegeven aan het eind van dit proefschrift, in de vorm van een beknopt overzicht van de betreffende experimenten die het onderzoek ondersteunen, alsook een overzicht van tests die niet uitgevoerd konden worden door beperkingen in de huidige apparatuur.

Het is gebleken dat gedurende de loop van dit project de interesse voor hoekversnellingsmeters verder is toegenomen. Ook na dit proefschrift zijn er nog vele mogelijkheden op dit terrein te onderzoeken. Het is nodig om meer – verschillende – hoekversnellings-sensoren te onderzoeken op verschillende testfaciliteiten. Op het gebied van fouttolerante vliegtuigbesturing kan de toepassing van het sensormodel uit dit proefschrift in het ontwerp van het regelsysteem een verdere validatie verschaffen. Het meenemen van temperatuureffecten is ook van belang. Dit vraagt om een geïntegreerde klimaatkamer op de draaitafel. Tenslotte is het ook aan te bevelen om een bewegingssimulator te ontwikkelen die van nature geschikt is om hoekversnellingsmeters te ijken.



# CONTENTS

<b>Summary</b>	<b>vii</b>
<b>Samenvatting</b>	<b>xi</b>
<b>Contents</b>	<b>xiv</b>
<b>Nomenclature</b>	<b>xxiii</b>
<b>1 Introduction</b>	<b>1</b>
1.1 Background	2
1.2 On Angular Acceleration Detection	4
1.2.1 The Indirect Methods	4
1.2.2 The Direct Method	6
1.3 Characterisation of Angular Accelerometers	8
1.3.1 Sensor Calibration	8
1.3.2 Sensor Modelling	9
1.3.3 Motion Simulator Use	10
1.3.4 Challenges in Angular Accelerometer Characterisation	10
1.4 Devices and Initial Findings	12
1.4.1 Acutronic High-Precision, Two-Axis Position-Based Motion Simulator	12
1.4.2 Columbia Angular Accelerometer Type SR-207RFR	13
1.5 Research Scheme	14
1.5.1 Problem Definition	14
1.5.2 Problem Definition	15
1.5.3 Research Scope and Limitations	16
1.6 Dissertation Outline	17
<b>2 Measurement Framework</b>	<b>21</b>
2.1 Introduction	22
2.2 Evaluating the Measurement Set-Up	23
2.2.1 The Motion Simulator	24
2.2.2 The Angular Accelerometer	25
2.2.3 The Data Acquisition System	26
2.2.4 Motion simulator system block diagram	26
2.3 Measured Angular Position Signal	26
2.3.1 Static Measurement Test	27
2.3.2 Constant Rate Measurement	30

2.4	Angular Accelerometer Customised Measurement Set-up . . . . .	33
2.4.1	Customised Measurement Set-up . . . . .	34
2.4.2	Synchronisation Procedure using Freeze Pulse Marker . . . . .	35
2.4.3	Test Set-up with an External Signal. . . . .	38
2.4.4	Test Results . . . . .	39
2.5	General Angular Accelerometer Measurement Framework . . . . .	42
2.6	Concluding Remarks . . . . .	45
<b>3</b>	<b>Scale Factor Calibration</b> . . . . .	<b>47</b>
3.1	Introduction to Angular Accelerometer Scale Factor Calibration . . . . .	48
3.2	Simulated Angular Acceleration Input using Turntable Motion . . . . .	49
3.2.1	Pendulum Method . . . . .	49
3.2.2	Combined Two Axes Constant Angular Rate Application . . . . .	51
3.2.3	Sinusoidal Profile from a Limited Angular Acceleration Motion . . . . .	56
3.3	Calibration Approach . . . . .	57
3.3.1	Measurement Set-Up . . . . .	57
3.3.2	Calibration Parameter Estimation . . . . .	57
3.3.3	Improving Reference Data using Advanced Observer . . . . .	59
3.3.4	Model Evaluation . . . . .	60
3.4	Scale Factor Calibration Model . . . . .	62
3.4.1	Table Estimated Angular Acceleration as the Reference . . . . .	62
3.4.2	Improved Reference Signal. . . . .	67
3.4.3	Discussion . . . . .	70
3.5	Concluding Remarks . . . . .	72
<b>4</b>	<b>Frequency Response Model</b> . . . . .	<b>73</b>
4.1	Introduction . . . . .	74
4.2	Modelling the Angular Accelerometer. . . . .	75
4.2.1	System Description . . . . .	76
4.2.2	Frequency Response Function and Transfer Function Representation . . . . .	77
4.3	Test Envelope and Method . . . . .	79
4.3.1	Test Envelope Specification . . . . .	80
4.3.2	Test Method . . . . .	82
4.3.3	Test Matrix Development . . . . .	83
4.4	Frequency Response Measurement Analysis . . . . .	86
4.4.1	Angular Accelerometer Voltage Response . . . . .	86
4.4.2	Signal-to-Noise and Harmonics Ratio . . . . .	86
4.4.3	Frequency Response Function . . . . .	89
4.5	Angular Accelerometer Model Estimation using Time-Domain Data . . . . .	92
4.6	Conclusion . . . . .	96
<b>5</b>	<b>Measurement Unit Misalignment</b> . . . . .	<b>97</b>
5.1	Introduction . . . . .	98
5.2	Misalignment in the Angular Accelerometer Measurement Unit . . . . .	99
5.2.1	Angular Accelerometer Measurement Unit Axis Definition and Orientation . . . . .	100

5.2.2	AAMU Adjustment on the Table Top . . . . .	103
5.3	Misalignment Measurement Method . . . . .	103
5.3.1	Test Plan . . . . .	104
5.3.2	Quantifying Misalignment . . . . .	106
5.4	Angular Accelerometer Measurement Unit Misalignment Check . . . . .	108
5.4.1	Non-sensitive Axes Sensor Response . . . . .	109
5.4.2	Non-sensitive to Sensitive Axis Ratio . . . . .	114
5.4.3	Phase of the Spectral Response Data . . . . .	116
5.4.4	Input Axis Misalignment . . . . .	118
5.5	Conclusion . . . . .	119
<b>6</b>	<b>Conclusions</b>	<b>121</b>
6.1	Angular Accelerometer Characterisation . . . . .	122
6.1.1	Using the Position-Based Motion Simulator System . . . . .	122
6.1.2	Angular Accelerometer Characterisation . . . . .	124
6.1.3	Axis Alignment in the Angular Accelerometer Measurement Unit (AAMU) . . . . .	125
6.2	Recommendations for Future Angular Accelerometer Characterisation . . . . .	126
6.2.1	Validating the Approach with Different Apparatus . . . . .	126
6.2.2	Implementation of the Angular Accelerometer Model . . . . .	127
6.2.3	Exploring New Motion Simulator Concepts . . . . .	127
<b>A</b>	<b>Specification Data</b>	<b>131</b>
A.1	Columbia Model SR-207RFR Angular Accelerometer . . . . .	131
A.2	ACUTROL Two-Axis Motion Simulator . . . . .	132
A.2.1	2-Axis Turntable Model AC2266L . . . . .	132
A.2.2	ACUTROL®3000 Digital Motion Controller . . . . .	133
<b>B</b>	<b>Static Tests</b>	<b>135</b>
B.1	Repeated Static Measurement . . . . .	135
B.2	Temperature Measurement . . . . .	139
B.2.1	Static Temperature Check on the Turntable . . . . .	139
B.2.2	Static Temperature Check in an Environmental Chamber . . . . .	147
B.2.3	Additional Static Temperature Check in an Environmental Chamber . . . . .	156
<b>C</b>	<b>Dynamic Tests</b>	<b>167</b>
C.1	Cross-axis Sensitivity and Misalignment . . . . .	167
	<b>References</b>	<b>169</b>
	<b>Acknowledgements</b>	<b>181</b>
	<b>Curriculum Vitæ</b>	<b>185</b>
	<b>List of Publications</b>	<b>187</b>



# NOMENCLATURE

## Acronyms

AAMU	Angular Accelerometer Measurement Unit
AIC	Akaike Information Criterion
ARMAX	AutoRegressive Moving Average with eXogenous variable
ARX	AutoRegressive eXogenous
CR	Centre of Rotation
DAS	Data Acquisition System
DFT	Discrete Fourier Transform
DUT	Device Under Test
FFT	Fast Fourier Transform
FP	Freeze Pulse
FPE	Akaike's Final Prediction Error
FRF	Frequency Response Function
FTFC	Fault Tolerant Flight Control
GF-IMU	Gyroscope Free Inertial Measurement Unit
GOF	Goodness-of-Fit
HR	Harmonics Ratio
HWIL	Hardware-in-the-Loop
IEEE	Institute of Electrical and Electronics Engineers
IMU	Inertial Measurement Unit
INCA	Incremental Nonlinear Control Allocation
INDI	Incremental Nonlinear Dynamic Inversion
INS	Inertial Navigation System
JEDEC	Joint Electron Device Engineering Council
LS	Least-Squares
LTI	Linear and Time-Invariant
MEMS	Micro-Electro-Mechanical Systems
MFCAA	Microfluidic Channel Angular Accelerometer
MS	Motion Simulator
MSE	Mean Squared Error
nAIC	Normalised Akaike Information Criterion
NDI	Nonlinear Dynamic Inversion
NPEKF	Newton Predictor Enhanced Kalman Filter
NRMSE	Normalised Root-Mean-Squared Error
PDF	Probability Density Function
PSD	Power Spectral Density
RLSN	Recursive Linear Smoothed Newton

RMS	Root-Mean-Squared
RMSE	Root-Mean-Squared Error
SBB	Sensor-Based Backstepping
SDAS	Sensor Data Acquisition System
SISO	Single-Input/ Single-Output
SMD	Sliding Mode Differentiation
SNR	Signal-to-Noise Ratio
SSE	Sum of Squares due to Error
SSR	Sum of Squares of the Regression
SST	Total Sum of Squares
TDAS	Turntable Data Acquisition System
THD	Total Harmonics Distortion

## Arrays

<b>A</b>	Regression matrix
<b>C</b>	Covariance Matrix
<b>K</b>	Correlation Matrix
<b>Y</b>	Output matrix

## Block Diagram Labels

<b><math>a_1</math></b>	Generated angular acceleration
<b><math>a_2</math></b>	Angular acceleration motion
<b><math>a_3</math></b>	Angular accelerometer raw data
<b><math>d_n</math></b>	Load disturbance
<b><math>m_n</math></b>	Motor related noise
<b><math>n_n</math></b>	Measurement noise
<b><math>p_1</math></b>	Position estimate
<b><math>p_f</math></b>	Position feedback
<b><math>p_{f,raw}</math></b>	Raw position feedback
<b><math>s_n</math></b>	Sensor noise
<b><math>t_n</math></b>	External/ environmental disturbance
<b><i>A</i></b>	Angular Accelerometer block
<b><i>a</i></b>	Angular acceleration motion
<b><i>C</i></b>	Control Centre block
<b><i>D</i></b>	SDAS block
<b><i>e</i></b>	Error
<b><i>p, p<sub>2</sub></i></b>	Position command
<b><i>R</i></b>	Position Transducer block
<b><i>r</i></b>	User input or position demand
<b><i>T</i></b>	Turntable block
<b><i>u</i></b>	Angular accelerometer measured raw data
<b><i>y</i></b>	Sampled angular accelerometer data

## Greek Symbols

$\alpha$	Angular acceleration, $^{\circ}/s^2$ , V
$\Delta\tau$	Measurement time duration
$\Delta$	Total sensor misalignment angle
$\delta$	Total sensitive axis misalignment
$\delta_x$	Misalignment component about the sensor x-axis
$\delta_y$	Misalignment component about the sensor y-axis
$\delta_z$	Deviation from the ideal z-axis
$\delta_{z_e}$	Equivalent misalignment angle
$\dot{\omega}$	Angular velocity or angular rate first derivative, $^{\circ}/s^2$
$\epsilon$	Residuals, difference between reference data and model
$\lambda, \beta$	Tuning parameter
$\Omega$	Total angular velocity, $^{\circ}/s$
$\omega$	Angular velocity or angular rate, $^{\circ}/s$
$\phi(f_{\text{mod}})$	Phase response
$\psi$	Inner-axis rotation angle, $^{\circ}$
$\sigma$	Standard deviation
$\sigma_n$	Standard deviation of the collected sample
$\Theta$	Estimated parameter vector
$\theta$	Angular position, $^{\circ}$

## Latin Symbols

$\bar{n}^2$	Noise power calculated from the level of non harmonics elements
$\bar{s}^2$	Signal power based on the fundamental frequency component
$\Delta t$	Time step, s
$\bar{y}(k)$	Mean of the measured data
$\text{Res}_f$	Frequency resolution, Hz
TF	Transfer function model
$A$	Sine amplitude, amplitude of the input signal
$A(k)$	Estimated polynomial
$a(z)$	System characteristic polynomial
$a_i$	Polynomial parameter
$a_{t_1}, a_{t_2}$	Tangential accelerations
$B$	Amplitude of the output signal
$b(z)$	System polynomial
$C$	Lipschitz's constant of the $n - 1^{\text{th}}$ derivative
$c$	Integer number of cycle
$c$	Parameter
$D$	Sample delay
$d_c$	Central Method derivative
$d_l$	5-Point Lagrange Method derivative
$D_M$	Set of possible parameter vectors
$f$	Frequency, Hz
$f(k)$	Non-linear function

$f_{\text{mod}}$	Modified frequency, Hz
$f_c$	Nyquist ceiling
$F_s$	Sampling frequency rate
$f_t$	Test frequency, Hz
$f_{\text{terminal}}$	Terminal frequency, Hz, rad
$f_{FP}$	Regular step pulse frequency
$g(k)$	Ideal straight line function
$G(z)$	Discrete linear system polynomial
$H$	Dynamic system
$h$	Data point interval, or sample spacing
$h_f$	Fundamental frequency, dB
$J, V$	Loss function
$K$	Angular accelerometer scale factor
$k$	The calculated point index
$L$	(Non)linearity
$LSFit$	Polynomial model with Least-Squares regression
$M$	Gain, dB
$N$	Data sample size
$n$	Total number of sinusoids in one measurement range, cycles
$n_p$	Number of free parameters in the model
$P$	Angular accelerometer response spectral component magnitude at 1 Hz frequency
$p$	Polynomial degree or order
$P(f_{\text{mod}})$	Phase delay
$R(f)$	Ratio of the non-sensitive axis response towards the sensitive axis response
$R^2$	Square of the correlation between the response values and the predicted response values
$r_1, r_2$	Distances from the centre of rotation
$S$	Sensor/ angular accelerometer
$S_e$	Sinusoidal signal from an external generator
$S_I$	Simulated ideal sinusoidal signal
$S_{das}$	Measured sinusoidal signal in the sensor DAS
$S_{tab}$	Measured sinusoidal signal in the calibration table control center
$S_{X_z}$	Sensor $S_X$ sensitive axis, coincides with the $P$ -axis
$S_{Y_z}$	Sensor $S_Y$ sensitive axis, coincides with the $O$ -axis
$S_{Z_z}$	Sensor $S_Z$ sensitive axis, coincides with the $I$ -axis
$T$	Period of the sinusoid, s
$t$	Time, s
$t_k$	Time at the end of the next Servo Frame interval
$t_m$	Measurement time
$T_s$	Sampling period
$t_{k-1}$	Time in the interval between the freeze pulse and the start of the next Servo Frame
$t_{start}$	Table data time correction towards the freeze pulse

$u(k)$	Input
$v_1$	Intermediate state of the differentiator
$X$	Complex representation of the input signal
$x$	Axis perpendicular to angular accelerometer sensitive axis
$Y$	Complex representation of the output signal
$y$	Axis perpendicular to angular accelerometer sensitive axis
$y(k)$	Output
$y_{\text{tf}}(k)$	Simulated or predicted response of the transfer function model
$z$	Angular accelerometer Sensitive axis

## Reference Frames

$\mathbf{i}, \mathbf{j}, \mathbf{k}$	Unit vector in DUT Reference Frame
$X, Y, Z$	AAMU axes orientation
$x, y, z$	Angular accelerometer axes orientation
$POI$	Turntable Reference Frame coincide with angular accelerometers' sensitive axes in the AAMU
$SXYZ$	Turntable Reference Frame
$xyz$	DUT Reference Frame

## Subscripts

$1, 2$	Index
$\phi$	Phase of the complex component
$H$	Harmonic amplitudes
$i$	Inner-axis
$L$	lower domain bound
$m$	Magnitude of the complex component
$o$	Outer-axis
$p$	Pivoted position
$s$	Scaled value of the complex component
$U$	Upper domain bound
$est$	Estimated variables
$AA$	Angular Accelerometer
$ID$	Identification
$t$	Turntable
$VAL$	Validation

## Superscripts

$\dots$	2 <sup>nd</sup> derivative
$\cdot$	1 <sup>st</sup> derivative
$\hat{\phantom{x}}$	Estimated function
$d$	Order of the differentiation or number of time derivatives



# 1

## INTRODUCTION

*My soul is in the sky.*

William Shakespeare, A Midsummer Night's Dream, Act V. Scene I.

## 1.1 BACKGROUND

**F**LYING has become an integrated part of modern life. It was only a century ago that man successfully became airborne in the first powered flight<sup>1</sup>, which marked one of the milestones in mobilisation. In the early days, aircraft were developed mostly for military purposes, but commercial flights quickly followed, and aviation has become a primary mode of transportation ever since. These flights not only connect different parts of the world but are also considered to be one of the critical factors in economic growth.

Undeniably, flying is not natural to the human being; nevertheless, a safe flight is possible with the aid of flight control systems. In flight, an aircraft will rotate about its centre of gravity, a point which is the average location of the aircraft's mass. A three-dimensional coordinate system is defined by the centre of gravity with each axis perpendicular to the other two axes. The flight control system controls the aircraft rotational motion in these principal axes, and thus maintains the aircraft attitude and orientation within the operational boundaries.

The current state of flight control systems is the result of decades of improvement and continuous effort in the advancement of the technology. To further improve the level of integrity, new aircraft configurations have a degree of redundancy regarding controls, sensors, and computing. The combination of these features provides the opportunity to maintain high performance even with impairments to the actuators, sensors or control surfaces, thus increasing the survivability of the aircraft. An approach which aims at making the system stable and retains acceptable performance under system faults is known as Fault-Tolerant Flight Control (FTFC) [1].

With FTFC systems, a controlled flight is achievable even in the case of failures [2–4]; however, it is necessary to modify the commands to the actuators and reconfigure the control laws [5]. Reconfiguring flight control laws can loosely be classified into two categories: model-based and sensor-based control laws. In model-based control laws, the reconfiguration is performed using a real-time aerodynamic model, which accurately captures the changes in the behaviour of the flight performance.

The reconfigurable controller in sensor-based control laws, on the other hand, only requires an estimate of the control effectiveness and an additional reconfiguration mechanism such as switching or matching logic [6, 7]. Here, the inertial sensor forms the very heart of the control law. When used as feedback, the sensor measurement provides robustness to sudden structural changes of the aircraft, since it does not rely on an, inevitably limited, aerodynamic model. Having proven and well-understood sensors is essential to increase the operational performance of the post-failure aircraft.

In recent years, researchers have started to concentrate on developing FTFC systems that require angular acceleration feedback. For example, the Incremental Nonlinear Dynamic Inversion (INDI) technique can be used to create a state-of-the-art FTFC that is robust to onboard aerodynamic model mismatches. It significantly increases the performance of the system compared to conventional nonlinear dynamic inversion [8]. Other studies discuss a Sensor-based Backstepping (SBB) approach implementation to create fault-tolerant flight control systems [9, 10]. Current studies present a hybrid Nonlinear Dynamic Inversion (NDI)/SBB which requires less online model information [11], an

<sup>1</sup><https://airandspace.si.edu/exhibitions/wright-brothers/online/fly/1903/>

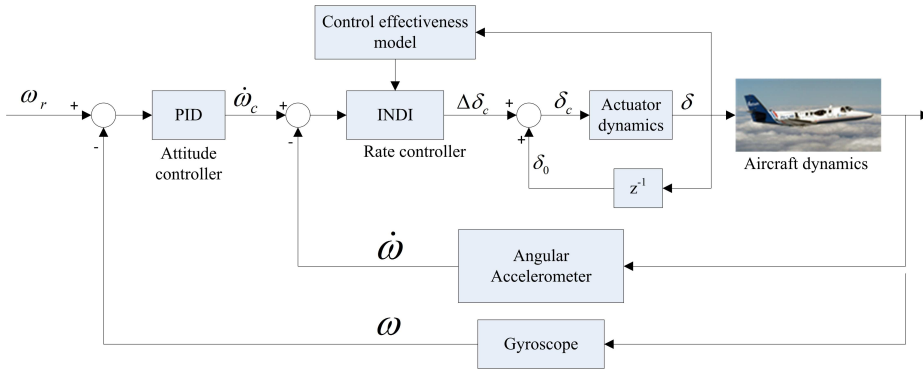


Figure 1.1: An example of an FTFC systems.

adaptive INDI that overcomes measurement and actuator delays [12], an investigation of the effects of using angular accelerometers in INDI control [13], and elaborate on an Incremental Nonlinear Control Allocation (INCA) approach that relies on angular acceleration measurements to reduce model dependency [14].

At the moment, the angular accelerometer feedback,  $\dot{\omega}$  for these control laws is obtained by calculating it from the angular rates,  $\omega$ . These rates are measured by gyroscopes in the conventional Inertial Measurement Unit (IMU). Although the feedback of angular accelerations obtained from gyroscope measurements eliminates the sensitivity to model mismatches, it has been shown that the derived angular acceleration feedback is sensitive to sensor measurement time delays [8] and misalignments. Also, differentiating the rate gyro signals amplifies the inherent noise. A set of filters could be implemented to eliminate the noise but at the cost of substantial lags. Another likely approach would be to use a pair of linear accelerometers to provide an angular acceleration estimate along with translational accelerations [15, 16]. It can be stated at this point that the performance of all NDI, INDI and INCA control approaches is excellent but expected to be significantly improved when using angular accelerometers instead of differentiated gyro signals. An example of an FTFC systems using the INDI approach is illustrated in Figure 1.1.

Recently, it has become possible to measure angular accelerations first-hand by utilising the angular acceleration sensor. It directly measures angular accelerations, in contrast to the traditional approach which requires calculating the angular accelerations by differentiating the angular rates from rate gyroscopes. These are, however, not readily available in current commercial aircraft Inertial Navigation Systems (INS). This type of sensor was initially used in the 1950s for the dynamic compensation of AC servomechanisms [17]. Other applications are in diverse fields such as missile control, pointing camera platforms, gun sights, and laser mounts.<sup>2</sup> Modal analysis is another example of its usage, patented Kistler's 8838 and 8840 quartz rotational accelerometers are used to investigate shaker performances regarding shaker head rotation [18]. Considering that angular acceleration is a crucial property in the fault-tolerant flight control system approach, and the fact that the angular accelerometer may become the central element in

<sup>2</sup>A Guide to Accelerometer Selection. <http://www.cfxtech.com/rhow.htm>

future INS systems, a comprehensive evaluation of the sensor's characteristics becomes critical. The characterisation of the angular accelerometers is the subject of this thesis.

## 1.2 ON ANGULAR ACCELERATION DETECTION

MEASUREMENTS of angular accelerations can be carried out indirectly or directly. The indirect method stems from two approaches: (i) calculation from linear accelerometers measurements, and (ii) estimation from the angular rate or angular position data. The direct method utilises a specific sensor device that can quantify angular acceleration about an input axis and produce a reaction that is usually converted into a proportional electrical signal [19]. The progress of angular acceleration measurement technology in the early 21<sup>st</sup> century, is expected to focus on developing indirect techniques for broader bandwidth and high signal-to-error ratio, as well as to establish cost-effective yet accurate angular accelerometers [20].

### 1.2.1 THE INDIRECT METHODS

Obtaining the angular acceleration with the indirect methods requires measurement data from other sensing devices in the form of linear acceleration, angular position or angular rate. This subsection outlines some of the approaches. It is probable, nevertheless, that more techniques exist or will be developed in the future.

#### AN ARRAY OF LINEAR ACCELEROMETERS

Measurement from an array of linear accelerometers with a known separation can be used to calculate the angular acceleration. Figure 1.2 exemplifies the use of two linear accelerometers at distances  $r_1$  and  $r_2$  from the centre of rotation, CR. The tangential acceleration,  $a_{t1}(t)$  measured along the circular path for the first accelerometer is equal to:

$$a_{t1}(t) = \alpha(t)r_1$$

we obtain the instantaneous angular acceleration:

$$\alpha(t) = \frac{a_{t1}(t) - a_{t2}(t)}{r_1 + r_2}$$

where  $\alpha$  is the angular acceleration, and  $t$  represents time. For the second accelerometer:

$$a_{t2}(t) = -\alpha(t)r_2$$

with the negative sign since the distance is in the opposite direction related to CR. Taking the difference:

$$\begin{aligned} a_{t1}(t) - a_{t2}(t) &= \alpha(t)(r_1 - (-r_2)) \\ &= \alpha(t)(r_1 + r_2) , \end{aligned}$$

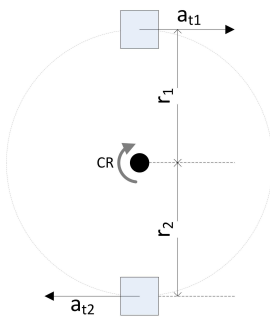


Figure 1.2: Measurement scheme of angular motion with a pair of linear accelerometers.

All elements of the rigid body rotate at the same angular acceleration, but the elements located farther from the axis of rotation move at a different tangential acceleration

than parts closer to the axis of rotation. Therefore, this method dictates that the distance between the accelerometers is exactly known at all times.

Various accelerometer configurations are possible to determine both the angular motion and the linear motion of a vehicle [21]. Alternatively, a fast, algebraic solution without any integration or estimation steps has also been investigated [22].

#### DERIVATION FROM ANGULAR POSITION OR ANGULAR RATE DATA

For the rotation of a solid body about one axis, the angular displacement,  $\theta(t)$  is the angular position of the rotation at a given time. Then, the angular velocity,  $\omega(t)$  of the body is the change of angle with respect to time and defined as:

$$\omega(t) = \frac{d\theta(t)}{dt}$$

When  $\omega(t)$  is available, the instantaneous angular acceleration,  $\alpha(t)$  can be obtained from the differential change in angular rate divided by the differential change in time:

$$\alpha(t) = \frac{d\omega(t)}{dt}$$

Alternatively, if only  $\theta(t)$  is accessible,  $\alpha(t)$  is acquired from the second derivative:

$$\alpha(t) = \frac{d^2\theta(t)}{dt^2}$$

Although the numerical differentiation is simple and straightforward, it is well-known to amplify noise, especially for real-life measurement data [23]. The derivative's gain is proportional with the frequency  $\frac{d^d}{dt^d}$  with  $d$  the number of time derivatives, leading to a significant amplification at high frequencies where the Signal-to-Noise Ratio (SNR) is often of poor quality. Additionally, numerical differentiation suffers from truncation error and is sensitive to round-off error [24]. Filtering before the differentiation process is often used to limit inaccuracies, but comes at the cost of signal delays [25]. In the case of noisy signals, different approaches have also been studied [26–28].

#### ESTIMATION BY ANALOG OR DIGITAL POST PROCESSING

Analog or digital post-processing of the available angular position or angular velocity signals could be used to obtain an accurate angular acceleration signal. The approach provides advanced estimation methods to address issues arising in the mathematical derivation. Two essential requirements applicable to the differentiation algorithm are adequate noise attenuation and appropriate delay characteristics, which can be achieved using predictive filtering and state observing approaches [20].

Predictive filters use a mathematical model of the system dynamics to reproduce the state's values and uncertainties, then integrate it with the chosen observation estimate [29]. This way, the error resulting from direct encoding of the actual sample can be reduced. This reliance is under the assumption that past values of regular signals can accurately forecast the actual value. Several applications on the angular acceleration prediction are based on the Kalman filter [30], artificial neural networks [31, 32], recursive linear

smoothed Newton (RLSN) predictors [33], and Newton Predictor Enhanced Kalman Filter (NPEKF) [34].

Instead of straightforward differentiation and post-filtering, state observers are used but typically limited to the deterministic case. For the stochastic case, an optimised Kalman filter-based state observer can be used for estimating angular accelerations [30]. This concept works by reformulating indirect angular acceleration measurements as system-state identification with real-time constraints.

### 1.2.2 THE DIRECT METHOD

The evolution of sensing elements that are capable of measuring the angular accelerations can be traced back as far as the year 1940. The first is a fluid type inertia device receptive to the rate of change of rotational speed, with an application in a brake apparatus associated with the rotating element [35]. An angular classifying accelerometer with specific utility to aircraft was developed in 1943 [36]. More recently, the newest concept of a 3-axis angular accelerometer has just been unveiled in 2017 [37]. Other technological approaches include the liquid mass displacement by Statham [38–43] between the years 1949–1970, the fluid rotor by Morris et al. [44] in 1970, and the balanced inertia mass by Zarabadi et al. in the early 2000s [45–47].

In the last three decades, there is undoubtedly a rising interest in the development of angular acceleration detection devices. Two related topics are the measurement of rotational quantities using experimental devices [48, 49], and using a PVDF and a Piezo-Composite [50]. Various studies have been conducted on the type of mechanism, such as the cantilevered beam with piezoresistor [51], optical disc [52–54], amorphous wire [55], superconducting proof mass on a torsional spring [56, 57], silicon bulk micromachined angular acceleration sensor [58], proof mass with dual anchor support [59], pendulum micromechanical angular accelerometer with force feedback [60, 61], bio-inspired circular fluid channel [62–65], unidirectional fiber optic [66], electromagnetic induction principle [67–69], proof masses supported by a rotary suspension [70], digitally operated Micro Electro Mechanical Systems (MEMS) [71], and electromagnetic processes in the angular accelerometer with a hollow non-magnetic rotor [72].

Only a handful of angular accelerometer concepts come into the market, perhaps due to its yet limited application. Figure 1.3 lists the established commercially available sensors to date. Endevco<sup>®</sup> Model 7302BM5 shown in Figure 1.3(a) utilises a temperature-compensated piezoresistive sensing device. Figures 1.3(b)–1.3(d) feature Jewell Instruments' ASM, ASB and ASXC angular accelerometer Series. ASM Series is the smallest, designed to minimise thermal errors in the outdoor application, while the ASB Series is intended for general-purpose industrial, commercial and sensing requirements. Both ASM and ASB Series are capable of detecting higher input ranges of  $\pm 200$ – $1000 \text{ rad/s}^2$ . The ASXC Series, on the other hand, is entirely distinct because its sensing mechanism uses of a fluid-filled ring chamber to measure angular acceleration. Moreover, the ASXC Series concentrates on the detection of low angular accelerations in the order of  $\pm 2$ – $100 \text{ rad/s}^2$ . Kistler disclosed a uniquely configured shear-quartz sensing element in Figure 1.3(e). The K-Shear<sup>®</sup> model 8838 responds to oscillations occurring about the unit's mounting axis when installed in a non-rotating test application, whereas model 8840 accurately measures the acceleration magnitude of oscillations laterally induced to its mounting



Figure 1.3: Commercially available angular accelerometers from Endevco<sup>3</sup> (a), Jewell Instruments<sup>4</sup> (b-d), Kistler<sup>5</sup> (e), and Columbia Research Laboratories Inc.<sup>6</sup> (f-j).

base.

For the most part, the key problem with angular accelerometers is their inability to detect inputs that are approximately steady, i.e., lower-frequency signals [73]. Columbia Research Laboratories Inc. aim to address this issue in the form of the SR-100FR and SR-200RFR Models in Figure 1.3(f), which incorporate the fluid rotor concept to provide extremely high sensitivity and full scale ranges as low as  $\pm 0.01 \text{ rad/s}^2$ . Columbia's precision force balance Models SR-107RFR and SR-207RFR maintain excellent bias stability and rejection of linear acceleration inputs, shown in Figure 1.3(g). Figure 1.3(h) shows Model SR-107VFR with selectable range. Models SR-220RNP in Figure 1.3(i) and Models SR-220RNC shown in Figure 1.3(j) differ only in their electrical interface. They work similarly with Models SR-107RFR and SR-207RFR but are electrically damped instead of depending on fluid regulation, thus hold excellent high-frequency characteristics. The main subject of this thesis is Columbia's Model SR-207RFR.

<sup>3</sup>[www.endevco.com](http://www.endevco.com)

<sup>4</sup>[www.jewellinstruments.com](http://www.jewellinstruments.com)

<sup>5</sup>[www.kistler.com/en/](http://www.kistler.com/en/)

<sup>6</sup>[www.crlsensors.com](http://www.crlsensors.com)

### 1.3 CHARACTERISATION OF ANGULAR ACCELEROMETERS

SENSOR characterisation seeks to validate the sensing results by looking into one or a combination of parameters. In characterising the angular accelerometer, this study considers two approaches: calibration and modelling. The calibration essentially aims to relate a measured response to a known standard, a process represented by Figure 1.4. Modelling the sensor means formulating a mathematical representation of the response due to external excitation, as illustrated in Figure 1.5.



Figure 1.4: Sensor calibration



Figure 1.5: Sensor modelling

#### 1.3.1 SENSOR CALIBRATION

Despite the fact that angular accelerometers are modern and robust sensors, they are still physical systems that are prone to construction inaccuracies that could affect their outputs. However small, the errors associated with them will inhibit the devices' precision. Therefore, it is crucial to accurately calibrate the sensors before their operational installation onboard aircraft or spacecraft.

The fundamental principle of sensor calibration is to compensate for all errors that may affect sensor measurement accuracy. In general, there are two categories of errors. First, the *systematic* errors, also known as *bias* errors, are consistent and repeatable in a measurement set. This classification includes the fixed measurement bias, cross-coupling and scale factor error coefficients, which can be measured and corrections can be applied to offset the repeatable components of these errors. The error contributed by the vibro-pendulous effect in the presence of slowly-varying accelerations may also be compensated to a large extent. Second, the *random* errors, also known as *precision* errors, are inconsistent and unrepeatable errors in measurements that commonly result in scattering of the data [74]. When the calibration is done correctly, then all remaining errors are random and vibration-dependent errors which can be corrected for through filtering; these cannot be modelled nor compensated accurately [75].

To evaluate inertial sensor performance, a notion of the real motion is crucial. This 'standard' or 'reference' must be a precisely known and well-defined input value that is applied to the complete sensor system, usually a combination of the basic sensor and basic data acquisition electronics, after which its output is measured. A mathematical model that can account for all disturbance effects is then constructed to model the sensor system in such a way that, ideally, the model residual is white noise. Besides exciting the sensors, the input motion should possess the required quality as a reference in a calibration. Turntable systems, referred to in this thesis as Motion Simulator (MS), are widely

used to produce the appropriate input motion sequence. Its mounting platform's bearings can be single-axis or two to three-axis degrees-of-freedom.

Ref. [76] provides quality assurance-related test procedures for non-gyroscopic inertial angular sensors. It applies to analogue and digital sensors which measure angular jerk, acceleration, rate or displacement with individual tests' guideline that are intended as a tool to verify whether the manufacturer's requirements have indeed been met. Conformance of the products to the non-operating mechanical and electrical requirements is confirmed in the non-operating tests. The operating tests are designed to establish the sensor performance characteristics such as scale factor, bias and composite error values, which require the use of an MS.

Even though much examination has been carried out on the calibration of linear accelerometers<sup>7</sup>, only a few studies have discussed the properties and possible calibration of angular accelerometers. A small number of reports and articles mention the measurement of angular acceleration and angular accelerometer calibration for a particular application. For example, in-flight steady-state and dynamic calibration for open-loop and closed-loop accelerometers [77] and a calibration technique for angular measurement devices when standards are unavailable [78]. An angular shaker has been utilised to excite a single-axis angular accelerometer with piezoresistive pressure transducer sensing element [79]. A report investigates three performance characteristics of a newly developed Endevco model 7302 S/N 102 angular accelerometer: sensitivity factor, amplitude linearity, and response to linear (non-angular) input accelerations [80]. Furthermore, the Endevco sensor is subject to evaluation by some oscillatory stimulus measured by an optical scanner equipped with a position transducer that provides a means to monitor angular deflection [81]. Ref. [82] uses free-free beam<sup>8</sup> driven by an electro-dynamic exciter as the test structure, with an open loop chirp, a closed loop random, and a closed loop swept sine test arrangement to evaluate Kistler Model 8836M01 angular accelerometer.

### 1.3.2 SENSOR MODELLING

The conceptualisation of a system, such as a sensor, to describe its properties is the main focus of modelling. A model attempts to capture essential aspects of the system behaviour, describing physical properties with a (typically) mathematical formulation. Approaches can be classified in one of three ways: *white-box*, *black-box* and *grey-box* modelling. *White-box* modelling examines the physical laws involved in the sensing process, thus require a priori knowledge of the system. The *black-box* modelling approach is purely data-driven in the sense that no physical knowledge of the underlying system is assumed. Instead, generic model structures such as Auto-Regressive eXogenous (ARX), Auto-Regressive Moving Average with eXogenous variable (ARMAX), Box-Jenkins, or Artificial Neural Networks are used to relate measured outputs to inputs. In the case some of the internal laws are known, the *grey-box* modelling is employed.

System identification is the process that takes system inputs and outputs to derive a validated black, white, or grey-box model. A properly designed experiment is required to obtain data with the highest possible information content. Next, the formulation of the input-output relationship or the model structure needs to be specified. The choice of

<sup>7</sup>In the absence of angular accelerometers, these have been commonly referred to as accelerometers.

<sup>8</sup>Both ends of a free-free beam are not fixed; it is supported at one or more nodes.

model structure differs in each case and depends on its eventual application. Lastly, the model parameters are estimated based on the measured data using a parameter estimation approach.

Various studies develop the *white-box* models of angular accelerometers. Ref. [62] was one of the first to develop an analytic model of the Microfluidic Channel Angular Accelerometer (MFCAA) concept. In the recent light, a cluster of research explores the characteristics of a liquid-circular angular accelerometer prototype. The state space model was obtained using a subspace identification method [83–85] with model order selection based on Akaike Information Criterion [86]. On the theoretical grounds, analysis backed with experiments are used to acquire the transfer function that fulfils Darcy's Law [87], frequency response based on the fluid transient theory [88], and dynamic fluid model [89] of the fluidic system. Permeability modelling of a porous transducer that measures the streaming potential of the liquid-circular angular accelerometer [90], as well as its electrokinetic property [91] was also investigated. Additionally, Ref. [92] predicts the porous transducer's permeability and streaming potential coupling coefficient using a capillary bundle model.

1

### 1.3.3 MOTION SIMULATOR USE

Generating precise input motions is crucial in inertial sensor calibration and system identification. Motion simulators are widely used to produce motion inputs that are essential for testing and calibrating such sensors. A motion simulator is a high-precision device which, through a multi-axis rotation system can simulate any rotational position, velocity, or acceleration input. Different motion simulators commonly incorporate a turntable and a control system, and are available in various specifications serving many purposes related to inertial sensor performance evaluation. Turntables are currently available in single, two, three and five axes of rotation, equipped with direct drive brushless torque motor as the axis actuator.

Examples of motion simulator systems for testing gyros, accelerometers, IMUs and optical devices under lab conditions are presented in Figure 1.6. iMAR GmbH manufactures high-precision single axis and two-axis turntables system. Their iTES-PDT07 in Figure 1.6(a) is a small size, single axis precision turntable with 0.7Nm torque. An extensive collection of single, two, three and five axes motion simulators are available from Wuhan Huazhiyang Technology Co., Ltd in the brand HEOS. Figure 1.6(b) shows an example of its two-axis variant. A 3-axis multi-function turntable displayed in Figure 1.6(c) is constructed by Shenzhen RION Technology, a company that specialised in such type of motion simulator. The last, well-known supplier is ACUTRONIC, which builds variants of all motion simulator types. One of its 5-axis models is displayed in Figure 1.6(d), which belongs to a series that is designed to address the challenging needs of Hardware-in-the-Loop (HWIL) simulation. A controlled temperature chamber is an optional feature of the motion simulator. When included, it supports an integrated test on the inertial sensors by manipulating the temperature condition inside of the compartment.

### 1.3.4 CHALLENGES IN ANGULAR ACCELEROMETER CHARACTERISATION

Comprehension of the underlying physics and measurement techniques is essential in characterising not only the angular accelerometer but also other types of inertial sensors.



Figure 1.6: Motion simulator systems from iMAR GmbH<sup>9</sup> (a), Wuhan Huazhiyang Technology Co., Ltd<sup>10</sup> (b), Shenzhen RION Technology<sup>11</sup> (c), and ACUTRONIC<sup>12</sup> (d).

Understanding how the sensing mechanism works, requires familiarity with the physical laws that govern the function of the system. For commercial sensors, this part is predominantly carried out by the manufacturer in the development process. On the other hand, how the measurements are conducted to gather the sensor response data involves an established process and often, tailored procedure. The turntable nowadays exercises the role of a standard for the inertial sensor.

Unfortunately, the rate and position turntables available to test inertial sensors are primarily designed to carry out *static calibration*, a type of testing which measures the angular rate down to zero frequency. This sort of test involves a constant rotation rate without rotational acceleration. Angular accelerometers should also be tested, however, in a *dynamic* setting, where the angular acceleration varies between its maximum and minimum sensitivity ranges. The National Bureau of Standards places the dividing line between static and dynamic measurements at 0.001 Hz [76]. The dynamic calibration introduces some challenges, and the dynamic *angular* calibration adds several unique issues as well.

To date, solutions for an in-depth assessment of angular accelerometers do not yet exist partly due to the present emphasis on gyroscopic sensors, in which static accuracy is the primary factor. Turntables can be highly accurate in providing the constant angular rate that is appropriate for calibrating gyroscopes, which are there designed to provide rate information. When turntables are used to produce angular acceleration, they are imprecise. The available test equipment consequently follows this pattern. Usually, the equipment does have a dynamic capability, but it is much less accurate than when it performs static operations. Furthermore, the motion platform of the turntable itself may

<sup>9</sup><http://www.imar-navigation.de>

<sup>10</sup><http://www.eoselectroopticalsystems.com>

<sup>11</sup><http://en.rion-tech.net>

<sup>12</sup><http://www.acutronic.com>

bring undesired dynamics, nonlinearities, transport delays, and so forth, which could make it challenging to separate sensor inaccuracies from issues with the test equipment itself [93, 94]. Additionally, a recent study highlights the influence of mounting errors between an inertial measurement unit and a turntable in dual-axis rotational INS [95].

A shortcoming in generating a viable angular acceleration reference is one of the main current motion simulator limitations. The calibration table is designed to generate a stable position reference. While the angular velocity reference is still acceptable, there are compelling ‘real’ discontinuities in the angular acceleration reference which significantly affect the calibration procedure. A particular effect is apparent in the angular accelerometer signal, where an additional frequency component is present at twice the original fundamental frequency, in constant angular velocity input motion [96]. Considering that the required input for angular accelerometers is a relatively rapid variation of angular velocity, the additional component will accumulate throughout the frequency spectrum.

To conclude, providing a sufficiently accurate angular acceleration reference is not trivial and has become one of the main concerns in dynamic angular acceleration sensor calibration. Although using a turntable is a well-known and widely employed calibration method for gyroscopes and linear accelerometers, it has limitations in dynamic angular accelerometer calibration. Additionally, there is no rigorous calibration procedure at present concerning angular accelerometers.

## 1.4 DEVICES AND INITIAL FINDINGS

TWO types of apparatus are of interest to this study. The first is the motion simulator system yielding high-precision position measurements. The second is the one-axis angular accelerometer sensor. This section summarises both devices and the preliminary assessment concerning sensor characterisation approach and measurement set-up.

### 1.4.1 ACUTRONIC HIGH-PRECISION, TWO-AXIS POSITION-BASED MOTION SIMULATOR

The motion simulator system allows testing of a wide variety of inertial navigation packages, sensors and other components requiring precision motion as a test input. The measurement calibration using a turntable has been applied to different types of inertial sensors. Such Device Under Test (DUT) are accelerometers [97, 98] and gyroscopes [99, 100] as well as a set of sensors in for instance the Inertial Measurement Unit (IMU) [101–103]. In our case, the device of interest is a two-axis, position-based turntable suitable for simultaneous testing of several medium-sized IMU as well as Micro-Electro-Mechanical Systems (MEMS) sensors.

A customised two-axis motion simulator operated by the section Control and Simulation of the Faculty of Aerospace Engineering at the Delft University of Technology produces the reference motion input for this study. It comprises two components as shown in Figure 1.7(a). The first part is the control unit, from which measurement parameters such as motion mode, sampling frequency, recording options, and motion control can be regulated. The second part is the motion unit in the form of a two-axis position table that

<sup>13</sup><http://cs.lr.tudelft.nl/facilities/calibration-lab/>

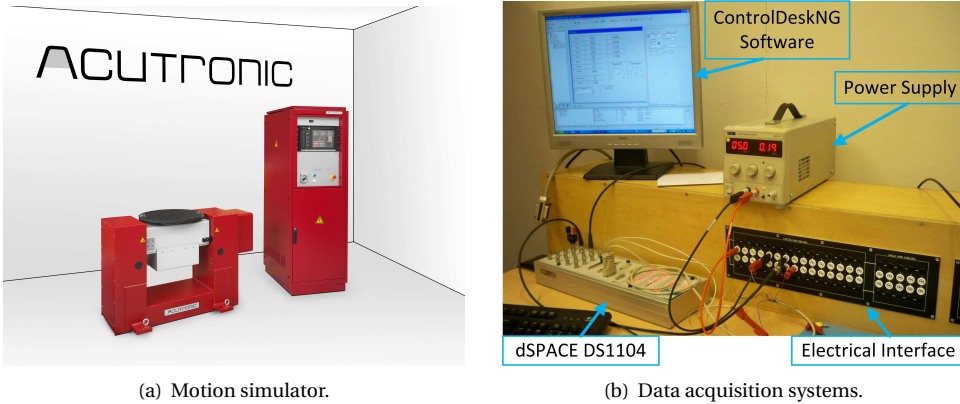


Figure 1.7: ACUTRONIC two-axis motion simulator systems<sup>13</sup> (a), dSPACE DAS and electrical interface (b)

provides accurate angular position measurements and has unlimited angular freedom. In the function of a position table, the device has a position transducer to measure the angular position, whereas angular rate and angular acceleration are estimated based on the measured angular position. The table's inner-axis carries the rotating plate, on which the DUT is mounted and secured. However, the sensor needs a separate Data Acquisition System (DAS) instrument to log the data and send these data to the laboratory DAS computer.

Figure 1.7(b) shows the DAS instruments and power supply for the DUT. The electrical interface facilitates power relays to the DUT through the slip ring access on the table top and sensor measurement signal transport to the DAS. A slip ring is an electromechanical interface that allows the transmission of power and electrical signals between a stationary to a rotating structure. The dSPACE DS1104 board gathers DUT data and other related signals to be processed in the ControlDeskNG software. Online synchronism between the motion simulator and DUT data is achieved by bypassing the dSPACE clock with motion simulators', in doing so results in one, uniform time vector. Due to the slip ring noise addition to the angular accelerometers' signals, this available DAS is not applicable in our case. A modified DAS set-up is used in this project instead, elaborated in Chapter 2.

### 1.4.2 COLUMBIA ANGULAR ACCELEROMETER TYPE SR-207RFR

The DUT in this study is a single axis, precision servo force balance angular accelerometer, SR-207RFR, in Figure 1.8. This design is a pendulous type, makes use of the fluid rotor concept of sensing angular acceleration in conjunction with the Columbia Research Laboratory Inc.<sup>14</sup> patented hydro-pneumatic suspension system. It provides excellent bias stability and rejection of linear acceleration inputs. The unit provides a high-level low impedance output and requires no additional signal conditioning. The full specification data are described in Appendix A.

A detailed sensing mechanism of the SR-207RFR angular accelerometer is not avail-

<sup>14</sup>[www.crlsensors.com](http://www.crlsensors.com)

able. It can be, however, recognised from the force balance [104] and fluid rotor concepts [40, 41]. The following description is meant to be an illustration and does not confirm to be the actual working instrument of said sensor. A force balance sensor consists of a position detector, an amplifier and an electro-mechanical system that converts a mechanical force into a proportional current which is, in turn, converted back into an equal opposing mechanical force. The mechanical system, in this case, is the fluid rotor, where liquid mass is employed to sense the motion instead of a solid mass suspended on springs. The liquid is housed in a toroid-shaped tube with a movable member or paddle, on a hinge, immersed in the fluid at one node. When subjected to an angular acceleration motion, the paddle is displaced in the direction of the fluid flow as a result of a pressure difference on both of its sides. The displacement relative to the container is measured to determine the magnitude of the current and becomes the output of the sensor. This externally induced change in mass position then results in a combination position detector, amplifier output such as that the force generator drives the paddle back to its original position.

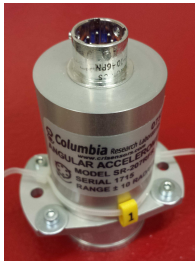


Figure 1.8: Angular accelerometer type SR-207RFR.

In our initial experiments for this particular type of angular accelerometer, however, it appeared that the electrical noise produced when the sensor's signals were transmitted over the slip ring of the measurement table exceeded the sensor's 3 mV specifications. Adding an analogue pre-sample filter in this basic set-up did not lower the noise down to the required level, as compared to the direct connection of angular accelerometer and DAS. Digital post-filtering is not preferable since the appropriate cut-off frequency is very low. Thus it might exclude useful information in the data. Therefore, a new, customised set-up and synchronisation method needed to be developed to tackle the issue. This will be discussed in this thesis.

## 1.5 RESEARCH SCHEME

At this point in time, there are some issues which prevent the efficient utilisation of the turntable to aid the angular accelerometer characterisation practice. This section formulates the open problem and approaches to solve them.

### 1.5.1 PROBLEM DEFINITION

The primary research question of this thesis is stated as follows.

#### Main Research Question

**How to accurately model and calibrate angular accelerometers using a commercially available position-based, high rate-accuracy, two-axis turntable, motion simulator system?**

This research project aims to develop a procedure for an in-depth evaluation of angular accelerometers, which can be implemented in the currently available position-based, high rate-accuracy motion simulator systems. Characterisation of the analogue, fluid-inertia angular accelerometer furthermore contributes to the development of the FTFC

systems by ascertaining that a high-quality measurement, and with that, accurate feedback is provided. The first step to meet the thesis objective is an investigation of the measurement set-up to establish the measurement adaptation schemes and validates the time-synchronisation. The framework then allows a synchronised angular accelerometer and motion simulator data to be obtained from the measurement performed on the motion simulator. After the development of optimal input sequences, the study focuses on developing a scale factor calibration model for the angular accelerometer. Then, a test envelope covering the angular accelerometer and motion simulator operating region is specified. Subsequently, the transfer function model of the sensor is inferred from the frequency response measurement data. Lastly, investigation of the axis misalignment is conducted based on the spectral component magnitude.

### 1.5.2 PROBLEM DEFINITION

The main research question is answered through addressing the following four subquestions.

As described in [Section 1.4](#), a new DAS is required to acquire a qualified angular accelerometer signal. The customised instrumentation is preferably in direct connection with the DUT to achieve the desired noise level. The most critical challenge of this problem is that no online time-synchronisation is possible between the motion simulator and the DUT. This circumstance leads to the first research question:

#### Research Subquestion 1

How to effectively collect the measurements of angular accelerometers on the motion simulator system?

The scale factor is one of the substantial operational criteria for calibration. It relates the output of a sensing device to a magnitude of a known standard. Currently, there exists no rigorous procedure for performing angular accelerometer calibration using the motion simulator. At this point, it is not apparent which sequence input for a two-axis, position-based motion simulator is optimal for angular accelerometer calibration. This indistinction is in particular due to the current state of the equipment, as explained in [Section 1.3.3](#). The types of function approximation and optimal model structures that provide the best results regarding model accuracy, efficiency, and quality guarantees were also part of the equation. Concerns over the form of such procedures and its implementation in real life are translated into the following research question:

#### Research Subquestion 2

What is the procedure to perform angular accelerometer scale factor calibration using the available position-based motion simulator?

Frequency domain methods are essential for simulation and control system design as the results often give helpful insights into the properties of the data and stability of a system, such as order, gain, phase delays, bandwidth, and resonant frequencies. Apart from being quintessential when it comes to the design and tuning of control systems,

such information is relevant for decisions on type and complexity of models to be used for further analysis of the data. In many cases, however, accuracy requirements possibly drive the use of time domain models and corresponding identification procedures. A well-defined test condition is necessary to extract those essential pieces of information for the angular accelerometer, which is unfolded in the third research question:

#### Research Subquestion 3

How to obtain an angular accelerometer model using frequency response measurements with the available position-based motion simulator?

The sensitive axis misalignment contributes to the system accuracy, especially when the sensor output is involved in the feedback loop of a high-performance flight control system. In the angular accelerometer, the misalignment represents the angular discrepancy between each sensor's axis of rotation with a defined frame of reference. Additionally, the misalignment also induces cross-axis effects on the non-sensitive axis of the sensor. Moreover, since existing angular accelerometers are single axis, three of them are needed to form an Angular Accelerometer Measurement Unit (AAMU) which can measure in all three-axis of orientation. This configuration adds the possibility of packaging misalignment. Therefore, it is essential to examine the misalignment, and the fourth research question is formulated as:

#### Research Subquestion 4

How to inspect an Angular Accelerometer Measurement Unit (AAMU) sensitive axes misalignment by means of the position-based motion simulator?

### 1.5.3 RESEARCH SCOPE AND LIMITATIONS

The issues defined above limit the exploration of the angular accelerometer characterisation topic, whether it is due to the unavailability of equipment as well as the lack of sensor variants. The experiments in this thesis consequently also run under different assumptions to facilitate the restrictions. This sub-section lists the scope and limitations of the current work.

The studies on angular accelerometers mentioned earlier mainly concern the calibration or modelling of specific sensors and mostly, for sensors in the developmental stage. This type of work uses vast a priori knowledge of the sensor mechanism or working principles. In the real world, however, users have only selected information provided by the manufacturer. These facts are often not sufficient to analyse the devices in detail. In this regard, this thesis focuses on the ***non-destructive characterisation of the off-the-shelf angular accelerometer***. The specific motion simulator and angular accelerometer are used as the *prying tools to investigate the problem*, but it is anticipated that the outcome of this research is applicable for various other types of apparatus.

This study concentrates on the input and output information of the systems. Thus, *disregarding the internal mechanical and electrical details* in the angular accelerometer and motion simulator. Consequently, systems are *viewed as black-boxes* that are de-

scribed by their frequency response characteristics. Analysis of the disturbance sources is conducted by examining the data for their relation to specific controlled settings.

Not all of the standard test for inertial sensors is performed within the capacity of this thesis; *non-operating tests*, which aims to guarantee sensor compliance with the non-operating mechanical and electrical requirements, *are especially excluded*. The static tests play an important role in examining the bias and linear acceleration sensitivity. Nevertheless, this test is not discussed in the main chapters; the results are given in Appendix B. Appendix C exhibits report on the dynamic test, particularly those that have not been included in the main thesis chapters.

One of the most crucial environmental factors is temperature. It has been found that temperature and temperature gradient are significant variables, especially in MEMS [105–111], and can have a non-linear influence on inertial sensor output [75], such as temperature-hysteresis. The present motion simulator, unfortunately, does not have an integrated environmental chamber, which makes it impractical to evaluate the temperature effect. Consequently, the *temperature impact on the angular accelerometer* will only be assessed using the existing, *independent environmental chamber in the static setting*. The result of this check will be presented as a part of Appendix B. Meanwhile, all the experiments in the chapters are conducted at a room temperature of around 22 °C.

## 1.6 DISSERTATION OUTLINE

Figure 1.9 illustrates the relation between the six chapters of this thesis. Each chapter, except for Chapter 1 and Chapter 6, addresses a specific challenge in the angular accelerometer characterisation experiment and is based on various scientific publications. Hence, they can be read independently. That being said, there are coherent links between chapters such that the results can ultimately be seen as a whole.

The first challenge in utilising the high-precision, position-based motion simulator for the angular accelerometer characterisation experiment is the contamination in the data relayed through the slip-ring. A customised measurement set-up is therefore built and reported in Chapter 2, which enables a direct recording of the sensor. Two auxiliary signals are generated by the Sensor Data Acquisition System (SDAS) computer to aid the post-measurement processing in synchronising angular accelerometer and motion simulator data. The first signal is a regular pulse of 100Hz, which is suitable to align the data. The second signal is a step function which acts as a data log trigger for the motion simulator, as well as a marker of the record starting point. Subsequently, through a careful analysis of the mechanical and electronic disturbance sources, as well as the dynamic properties of the motion controller, a framework is established. This chapter lays the foundation to acquire the synchronised angular accelerometer and motion simulator data for further use in the characterisation process.

Chapter 3 discusses the limitations of the available, two-axis motion simulator in generating a sufficiently accurate angular acceleration, and investigates a suitable method to calibrate the angular accelerometer using the generated motion from the motion simulator as the reference. Although the turntable is regularly utilised for generating precise angular position and angular rate, it has limited ability to sustain angular acceleration. By assessing one-axis and two-axes input motion, alternative outcomes for this purpose can

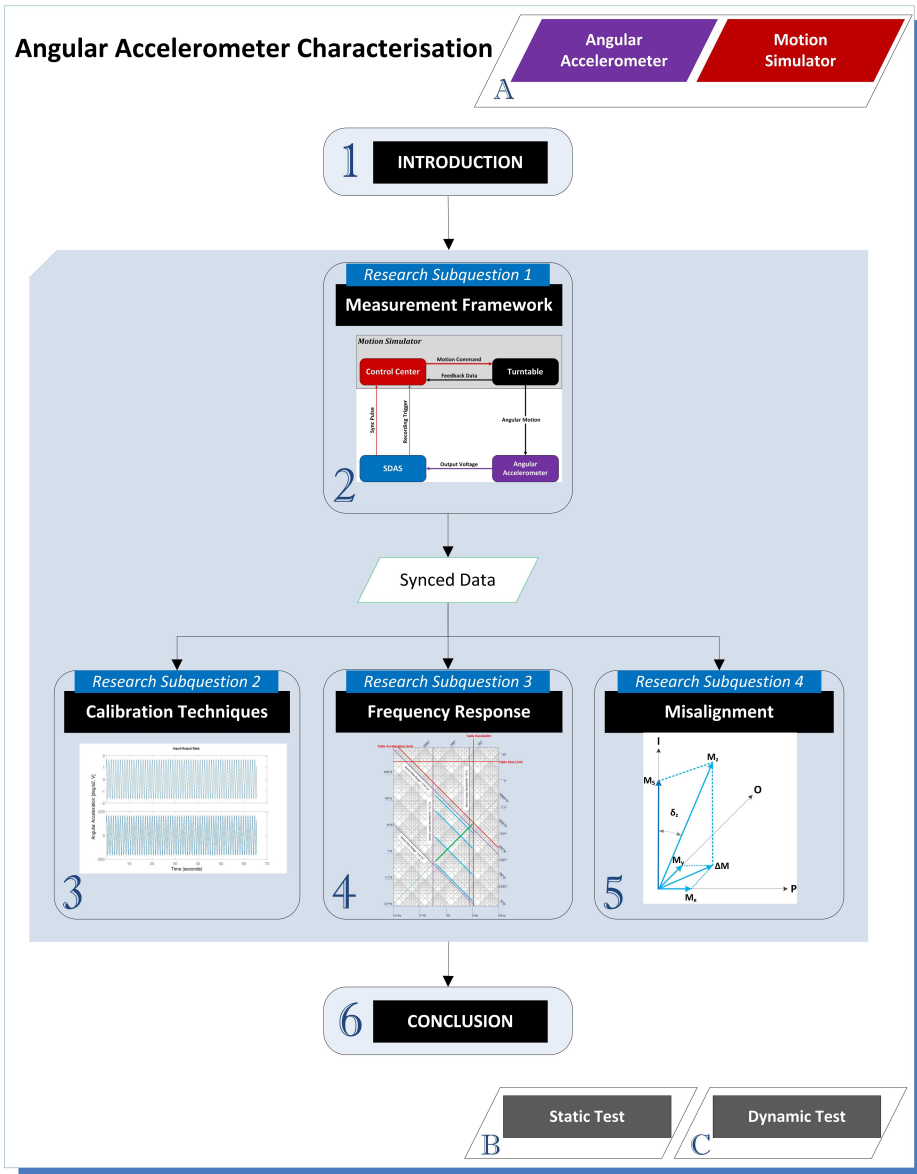


Figure 1.9: Thesis outline

be produced. Rotating both axes simultaneously, each at a constant rate can generate an input motion profile that is independent of the motion simulator's angular acceleration variation; however, it is evident that only a short range of frequencies is covered. Therefore, a sinusoidal motion is chosen instead to create a repeated cycle of angular acceleration. This chapter then implements the least squares method to acquire a scale factor calibration model from a single-axis, single frequency measurement.

The relationship between the mechanical properties of the sensor and its performance characteristics is identified in [Chapter 4](#). Noise, bandwidth, resolution, and accuracy are closely related to its role in the control system. Therefore, a characterisation of the angular accelerometer is performed before its implementation in the physical system. The sensor model is constructed using the analysis of frequency response measurement data in single-axis input, for a range of frequencies. The Frequency Response Function (FRF) is extracted from the discrete Fourier transform of selected input and output pairs. This chapter performs model validation with the time domain data and then obtains the transfer function. Another approach where the model was independently parametrised to express the disturbance in the measurement system apart from the system's dynamics is an estimation using the Box-Jenkins method [112], but this method is not included in this thesis.

Real world implementation requires angular acceleration measurement in all three aircraft primary angular motion axes. The angular accelerometers in a 3-axis orientation mounting block form the Angular Accelerometer Measurement Unit (AAMU) for this purpose. [Chapter 5](#) investigates the method to quantify the axis misalignment of the three sensors in the mentioned setting. It leads to the frequency domain data approach with a well-defined excitation, which enables the isolation of the associated input motion without the high-frequency noise implication. Mounting block installation evidently plays a part in the misalignment magnitude as shown by the repeated measurement. The presence of the non-sensitive axis response can also be revealed from the experiment result. This chapter yields the composite misalignment angle of angular accelerometers in an AAMU, to be able to compensate for the deviation between the sensor's sensitive axis and a reference frame.

Finally, [Chapter 6](#) provides the final conclusion, together with a discussion of the main findings and contributions of this study. Recommendations for future research are discussed at the end of the chapter.

Additional information regarding the angular accelerometer and motion simulator specifications is provided in [Appendix A](#). Then, a modified multi-position static test for angular accelerometers are presented. The results from the static test measurement are used to estimate constant bias and gravity-sensitive drifts detailed in [Appendix B](#). This appendix also includes the method and outcome of temperature effect examination. [Appendix C](#) presents the dynamic test results, complementing the discussion in [Chapter 5](#).



# 2

## MEASUREMENT FRAMEWORK

*He who would learn to fly one day must first learn to stand and walk and run and climb and dance; one cannot fly into flying.*

Friedrich Nietzsche

*A systematic approach to the characterisation of an angular accelerometer requires the acquisition of valid sensor responses to a known excitation input. In this regard, this chapter presents the measurement framework used to analyse the SR-207RFR angular accelerometer. First, it examines both the motion simulator and sensor performance characteristics, through a careful analysis of the mechanical and electronic disturbance sources, as well as of the dynamic aspects of the motion controller. Subsequent parts discuss the measurement set-up with a customised Sensor-Data Acquisition System. The tailored set-up enables a commercially available, angular position-based motion simulator to serve as the reference for angular accelerometer calibration experiments.*

---

This chapter is based on the following publications:

- Jatiningrum, D., de Visser, C. C., van Paassen, M. M., and Mulder, M. “A Framework for Calibrating Angular Accelerometers using a Motion Simulator”, *AIAA Modelling and Simulation Technologies Conference*, 2015 [96].
- Jatiningrum, D., Muis, A., de Visser, C. C., van Paassen, M. M., and Mulder, M. “A High-Precision Position Turn Table as the Reference for Angular Accelerometer Calibration Experiment”, *5<sup>th</sup> CEAS Air and Space Conference*, 2015 [113].

## 2.1 INTRODUCTION

SENSOR calibration is the process of minimising the difference between the output of a sensor and a known reference input which is called a calibration standard. Test and calibration of inertial sensors (e.g., gyroscopes and accelerometers), Inertial Navigation Systems, stabilised Optronic Systems, Electronic Stability Control Systems and other components require precision motion sequences as test inputs such as those generated by motion simulators. In the case of linear accelerometers, the angular-velocity-sensitive and angular-acceleration-sensitive coefficients in the performance model can be calibrated using high-rate rotations on commercially available rate tables [114].

For *angular accelerometers*, however, the calibration procedure is not as straightforward. The main reason for this is that current calibration equipment cannot directly provide an accurate angular acceleration reference. Instead of implementing a direct measurement, motion tables use indirect acceleration measuring techniques based on analogue or digital post-processing of available position signal and afterwards, band-limited differentiators to construct the acceleration signal.

In the case of angular accelerometers, providing a sufficiently accurate angular acceleration reference is not trivial and has become one of the principal concerns in dynamic angular sensor calibration, where a variable input signal is required to generate the proper excitation. Part of it is due to the fact that turntables were constructed with calibration of gyroscopic sensors in mind, in which static accuracy is the primary factor [76]. The available test equipment consequently follows this pattern. Motion simulators are usually more accurate during static (i.e., position) operations than during dynamic movements. Moreover, the motion simulator basis itself brings unwanted dynamics, non-linearity, transport delays, etc., making it difficult to separate sensor issues from test equipment problems [93, 94].

The motion simulator operated by the Control and Simulation Section of the Faculty of Aerospace Engineering at the TU Delft is the calibration standard in this study. It is capable of simulating or accurately reproduce roll, pitch and yaw motion in the laboratory environment for inertial sensors calibration. Furthermore, it can excite the Device Under Test (DUT) with simultaneous movements around two axes. It is designed primarily as a position-based motion simulator to perform exact absolute positioning, yielding highly accurate angular position data, as well as a high rate accuracy with no drift, and excellent rate stability in both axes. The angular *acceleration* reference provided by the motion simulator, however, has shown a lower accuracy than its position and rate references, as will be discussed in [Section 2.3](#).

In experiments with motion simulators, the applied inertial motion must be recorded. In the case where angular acceleration measurement data are not available, one of the approaches in determining this signal is by differentiating the measured angular displacement. However, it is well-known that numerical differentiation of these signals amplifies the measurement noise [20]. Another notable effect is that a higher sampling rate yields a significantly degraded result when differentiating the signal [30]. This outcome is of course as expected, with direct numerical differentiation noise gets amplified with a factor of  $\frac{1}{\Delta t^d}$  with  $d$  the order of the differentiation, and with  $\Delta t$  the time step in seconds.

A high-level overview of a typical measurement set-up using this apparatus is shown in [Figure 2.1](#). The motion simulator system consists of two subsystems: the control centre

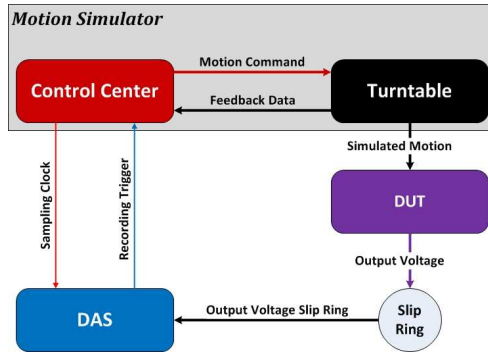


Figure 2.1: Basic diagram of calibration experiment in a typical set-up.

and the turntable, whereas the DUT system includes three subsystems: the sensor, the slip ring and Data Acquisition System (DAS).

A slip ring is an electromechanical device integrated on the turntable which facilitates the transmission of electrical power and signals from a stationary to a rotating structure, which is a standard feature in today’s motion tables. However, the measured angular accelerometer signal becomes very noisy when relayed through the slip ring, even with the addition of a pre-sample filter to eliminate high-frequency noise. In this particular case, therefore, a modified set-up needs to be arranged by bypassing the slip ring to ensure a high quality of obtained angular accelerometers data.

This chapter presents a solution on how to carry out the angular accelerometers calibration experiment by utilising a position-based motion simulator. A series of tests and checks were performed to investigate the essential motion simulator-related measurement effects on the recorded data. Correspondingly, a new measurement set-up with a special Sensor Data Acquisition System (SDAS) is developed to address the slip ring noise concern. The chapter outline is presented in [Figure 2.2](#).

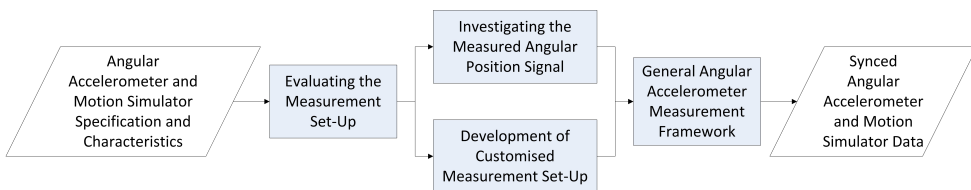


Figure 2.2: Outline of Chapter 2. The boxes represent the process, whereas the parallelograms represent the data.

## 2.2 EVALUATING THE MEASUREMENT SET-UP

**T**WO types of calibrations are static calibration and dynamic calibration. Static calibration is performed when the time is not relevant to the measurement. It relates to the properties of the system after all transient effects have settled to their final or steady state. On the other hand, dynamic calibration is required when the time is relevant to the

measurement. This type of calibration attends to the properties of the system transient response to an input.

For aircraft inertial sensors, the calibration approach as mentioned earlier also applies. Nevertheless, testing and calibration methods need to reflect the type of application, since the required performance varies widely in each. One of the purposes of testing an inertial sensor is to evaluate and validate the mathematical representation of sensor behaviour so that the description of a sensor can be predicted for particular circumstances to enhance its accuracy eventually.

Using a motion simulator that includes a turntable as the calibration standards for inertial sensors is a well-known and widely employed calibration method. The 3-axis variant is uniquely capable of simulating the three degrees-of-freedom motion of an aircraft. Others with two or one axis are also common, and 5-axis being the most complex alternative. The turntable-generated motion has been used to produce not only excitation for different types of inertial sensors such as linear accelerometers [97, 98] and gyroscopes [99, 100], but also for groups of sensors in for instance Inertial Measurement Units (IMU) [101–103].

The motion simulator operates in a closed-loop, where the measured output response, here the table angular position data, is fed back to the control centre [115]. The motion simulator and angular accelerometer system set-up consist of various subsystems and processes, assembled to obtain the desired output with desired performance, given a particular input. The analysis mechanism starts with understanding all of the components related to the angular accelerometer signal chain. Modelling the entire system architecture will help us to characterise, reduce and even eliminate non-linear behaviour of simulator motions [116]. The following subsection introduces the subsystems.

## 2

### 2.2.1 THE MOTION SIMULATOR

The first two subsystems, the control centre and the turntable, are closely interacting and together form the motion simulator. The first block in the review is the motion simulator's control centre with its two primary roles: an observer and a controller. As an observer, it incorporates a state estimator that provides estimates for the turntable angular rate and acceleration signals. The control loop then uses these estimates to calculate the motion control command to steer the turntable movement accurately.

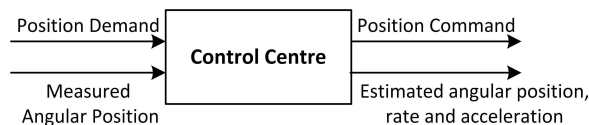


Figure 2.3: Simplified relationship diagram of the control centre.

In this study, the control centre is considered as a 'black box'. Its inputs are the position demand (i.e., the desired turntable angular position as defined by the user) and the measured, raw angular position feedback signal that comes from the turntable. The control centre output signals that are relevant to this study are the position command signal sent to the turntable, the estimated angular position, the estimated angular rate, and the estimated angular acceleration. These signals are collected in the data acquisition part of

the control centre, herewith declared as the Turntable Data Acquisition System (TDAS), to differentiate it from other DAS.

The second block in the motion simulator system is a 2-axis, high-precision, position-based turntable, which has unlimited angular freedom. It is equipped with an angular position transducer that provides an extremely accurate angular position measurement. The angular rate and angular acceleration are then estimated based on the measured angular position; more on this topic is explored in [Section 2.3](#). For the payload, the table's inner-axis carries the rotating plate, on which the DUT can be mounted and secured.

Different motion profiles can be specified from the user interface in the control centre. The device allows the definition of multiple inputs, which can either be defined regarding absolute displacements in angular position or concerning angular rate. Each of the inputs can be determined independently. These can be translated into several input motion laws on the turntable, such as a constant rate rotation, or a sinusoidal position profile.

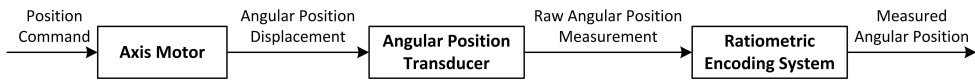


Figure 2.4: Simplified relationship diagram of the turn table components.

The angular position transducer is part of the turntable shown in [Figure 2.4](#), it measures the angular position displacement resulting from the motion input in each axis. The sensor consists of two non-contacting elements: a rotor and a stator, which gives raw measurement data in the form of angular position fine-sine, and fine-cosine variables with a high angular accuracy of  $\pm 1''$  standard <sup>1</sup>. These raw position measurements are sent to the control centre as a feedback signal, see [Figure 2.3](#). Subsequently, a ratiometric encoding system converts and scales the raw data into a comprehensible angular position measurement.

### 2.2.2 THE ANGULAR ACCELEROMETER

The DUT we study is a precision servo force balance angular accelerometer. The design is of a pendulous type, which uses the *fluid rotor concept*. It provides excellent bias stability and rejection of linear acceleration inputs <sup>2</sup>. The force balance sensor consists of a position detector which has an unbalanced pivoting mass with angular displacement, an amplifier and an electromechanical system. This combination performs the function of converting a mechanical force into a proportional current which is, in turn, transformed back into an equal opposing mechanical force <sup>3</sup>.

The angular accelerometer can be mounted and secured on the turntable top. It senses angular acceleration of the simulator motion. The detected motion is converted into a voltage output, proportional to the original mechanical input. The output signal is transmitted to the DAS through electrical connectors. The complete specification of the DUT can be found in [Appendix A](#).

<sup>1</sup>Farrand Controls Brochure, [www.ruhle.com](http://www.ruhle.com)

<sup>2</sup>Angular Accelerometer SR-107RFR, SR-207RFR, Specification Sheet, [www.crlsensors.com](http://www.crlsensors.com)

<sup>3</sup>Force Balance Sensor Technology, Technical Paper, [www.crlsensors.com](http://www.crlsensors.com)



Figure 2.5: Simplified input-output relationship diagram of the angular accelerometer.

### 2.2.3 THE DATA ACQUISITION SYSTEM

The motion simulator system provides power for the DUT and data channels connected to the DAS instrumentation via the slip ring access on the table top. The DAS receives the analogue signal of the angular accelerometer measurement, thenceforth digitise and record it for further analysis. With the message being transported through cable connectors, a delay might be present. This process is illustrated in Figure 2.6.

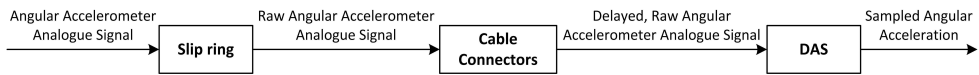


Figure 2.6: Simplified relationship diagram of the DAS.

### 2.2.4 MOTION SIMULATOR SYSTEM BLOCK DIAGRAM

Figure 2.7 shows a first system block diagram that can be assembled based on the subsystems relationships introduced above. It starts with the control centre block,  $C$  processes the angular position error,  $e$  into an angular position command signal,  $p$  which drives the turntable,  $T$ . The measured turntable output, which is the raw angular position feedback,  $p_f$  is sent back to the control centre and compared with the specified demand input signal,  $r$ . The error,  $e$  is minimised to track the desired input signal as accurately as possible. Meanwhile, the turntable output motion, in our context the angular acceleration motion,  $a$  is being sensed by the angular accelerometer  $A$ . The angular accelerometer measured raw data,  $u$  is then processed through the sensor's data acquisition system,  $D$ , resulting in sampled angular accelerometer data,  $y$ . In the following sections, we will study whether this block diagram suffices, or needs to be extended to represent actual reality better.

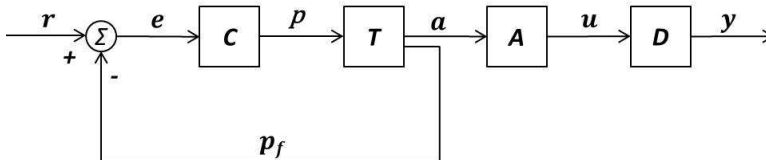


Figure 2.7: Simplified block diagram of the system.

## 2.3 MEASURED ANGULAR POSITION SIGNAL

THE calibration table is a rate and position table type, which means that it is designed to provide extremely accurate angular position and angular rate data. The turntable

only measures the angular position and from that calculates a sufficiently precise angular rate. Angular acceleration is also calculated from the angular position through double differentiation, yielding noisy data that cannot be used as a standard in the angular acceleration calibration set-up that we intend to design here.

An investigation on how the control centre processes the measured data has been performed. There are four variables of interest recorded in the control centre, which is related to the dynamic angular calibration:

1. Angular position feedback, the measured raw data from the angular position transducer;
2. Angular position estimate, calculated by the control centre based on some processing of the raw measurement (item number 1 above);
3. Angular rate estimate, calculated by the control centre from the available angular position data, and
4. Angular acceleration estimate, calculated by the control centre from the available angular position data.

Note that at this point it is unclear whether the control centre computes items 3 and 4 above from the raw angular position measurements (item 1), or from the processed angular position estimate (item 2).

To understand the characteristics of these four variables, two basic checks on noise and inaccuracy sources were performed. The first one is a *static* measurement, where all signals were recorded while the turn table stands still. The second one is a *constant rate* measurement, where the turn table rotates at several, different, constant rates. Then, calculating the signals' Fourier Transform is an efficient way to analyse the signal characteristics in the frequency domain [117]. The following subsections describe both tests and their results.

### 2.3.1 STATIC MEASUREMENT TEST

A static measurement test was conducted to determine the turntable's noise frequency baseline. The static condition for the turntable comprises two motor states: ON and OFF. The motor has a mechanical grip feature that keeps both the 'internal' and 'external' turntable axes in a specified position. During normal operation, it should be turned ON to control the turntable axis and to generate the motion input. However, the two motor states could have a different effect on the position transducer measurement through their vibration that holds the axis. Therefore, measuring both states is vital to determine the baseline noise level.

The sampling frequency,  $F_s$  and measurement time,  $t_m$  are set at 2 kHz and 100 s, respectively. Although recording at a lower sampling rate in the control centre is possible, the highest possible sampling frequency was chosen to avoid any issues that may come with aliasing. The rather long measurement time yields a sufficient frequency resolution in the Discrete Fourier Transform (DFT) (0.01 Hz).

#### THE MOTOR CONTROLLER EFFECT

First of all, when the turntable motor is OFF, the table starts drifting from its perfect zero position. Although the deviation is relatively small and not visible to the naked eye, the trend should be removed to make a valid comparison with the motor ON state. After-

wards, the signal power at each frequency component was calculated.

Figure 2.8 shows the calculated Power Spectral Density (PSD) of all four variables of interest. Being the discrete-time signal, when analysed using a frequency-domain approach, the Nyquist frequency terms of the DFT require a frequency scaling by a factor of  $\frac{1}{2}$  [118]. The motor ON state variables, plotted in the first row, show power between 30Hz and 40Hz. In the second row, the motor OFF state variables do not contain this power. Hence, these signal power components must be caused by the turn table motor, and it means that when the motor is ON all measured and estimated variables will carry the motor signal effects.

Observation of the angular position, rate and acceleration estimate data PSD shows the characteristics of the motion simulator. Angular position and rate estimate signals are clean, without any high-frequency noise components. The angular acceleration calculated data, however, contain significant high-frequency noise, and the signal in its current form is unsuitable to act as a reference in angular accelerometer calibration.

### DERIVING ANGULAR ACCELERATION FROM ANGULAR POSITION DATA

The angular position estimate from the table is known to be calculated based on a measured variable, namely the angular position feedback. The table then estimates the angular rate and acceleration from either of the available (measured and estimated) angular position data. At this moment, the angular rate and acceleration estimation approach is not yet clear. To investigate, we applied two elementary numerical differentiation methods, namely the *central difference method* and the one-dimension *five-point stencil* [119].

We used both the measured (raw) angular position data, as well as the processed (estimated) angular position data, provided by the control centre. Applying the two numerical differentiation methods on both sets of data, we obtained our own estimates of the angular rate and angular acceleration signals which we could then compare with the estimates provided by the control centre (items 3 and 4 above).

The numerical differentiation was performed using the subsequent formulas:

1. Calculate the 1<sup>st</sup> derivative:

- *central difference method*:

$$\dot{d}_c \approx \frac{f(k+h) - f(k-h)}{2h} \quad (2.1)$$

- *five-point stencil*:

$$\dot{d}_l \approx \frac{-f(k+2h) + 8f(k+h) - 8f(k-h) + f(k-2h)}{12h} \quad (2.2)$$

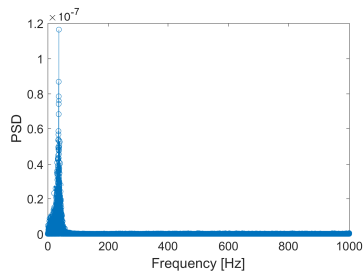
2. Calculate the 2<sup>nd</sup> derivative:

- *central difference method*:

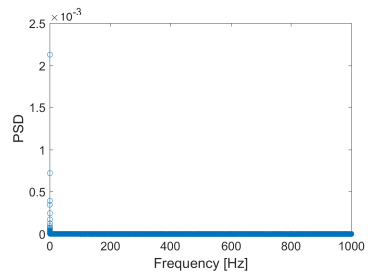
$$\ddot{d}_c \approx \frac{f(k+h) - 2f(k) + f(k-h)}{h^2} \quad (2.3)$$

- *five-point stencil*:

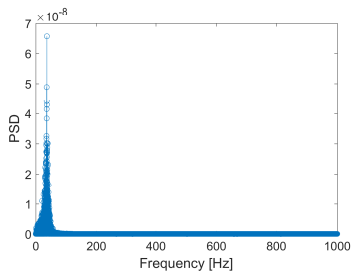
$$\ddot{d}_l \approx \frac{-f(k+2h) + 16f(k+h) - 30f(k) + 16f(k-h) - f(k-2h)}{12h^2} \quad (2.4)$$



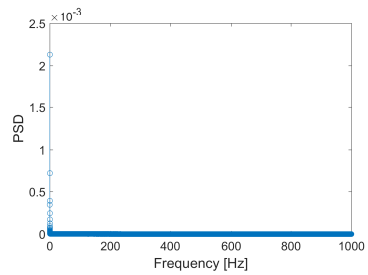
(a) POSN FBK, Motor ON



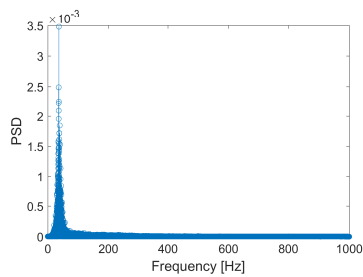
(b) POSN FBK, Motor OFF



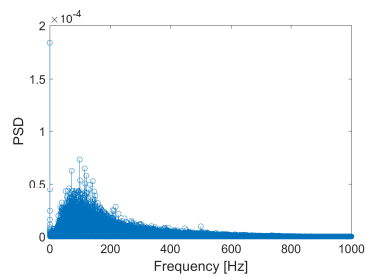
(c) POSN EST, Motor ON



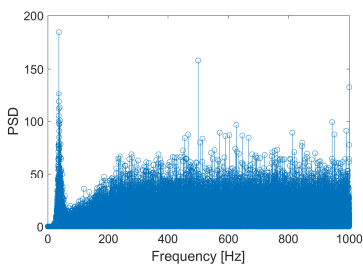
(d) POSN EST, Motor OFF



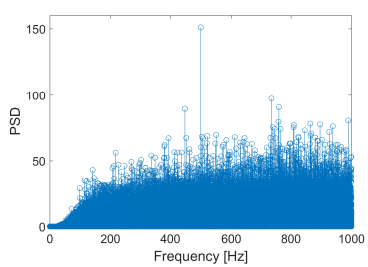
(e) RATE EST, Motor ON



(f) RATE EST, Motor OFF



(g) ACCEL EST, Motor ON



(h) ACCEL EST, Motor OFF

Figure 2.8: PSD of the motion simulator angular state variables; static measurement.

where  $k$  is the calculated point index, and  $h$  is the sample spacing.

Figure 2.9 presents the comparison of the angular rate estimates obtained with the two numerical differentiation methods, and with either the raw angular position measurement (POSN FBK) or the processed angular position estimate (POSN EST) as its inputs. The data were taken without any motion input, i.e. in static condition, thus in this case, we expect a  $0^\circ/\text{s}$  rate. Nonetheless, the acquired rate signal shows a sine-like pattern oscillation.

Using either the *central difference method*, Figure 2.9(a), or the *five-point stencil*, Figure 2.9(b), the figure clearly illustrates that angular rate obtained by numerical differentiation of the angular position estimate (POSN EST) matches the angular rate estimate provided by the control centre extremely well. The PSDs of the angular rate estimate obtained with the estimated position signal contains very little energy at high frequencies, where the approximation achieved with the raw position measurements is heavily contaminated with measurement noise and inaccuracies between 100 and 900Hz.

Hence, we can safely conclude that the control centre uses its estimate of the angular position to calculate the angular rate estimate internally; in fact, it is likely that the same state estimator computes them. Note that our simple numerical differentiation methods both yield very acceptable results as well.

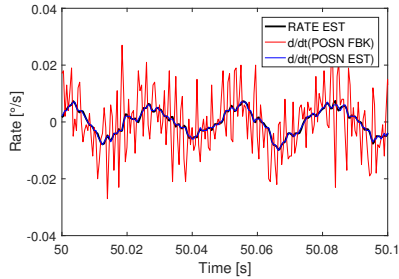
A similar result was obtained when studying the estimate of the angular acceleration, illustrated in Figure 2.10. As previous, we expect a  $0^\circ/\text{s}^2$  acceleration since the measurement was in static condition. The plot, however, shows a steady oscillation around 35 Hz. Again, we can safely conclude that the control centre receives an estimate of the angular acceleration using the derived value of the table angular position. The fact that our elementary ‘double differentiation’ methods applied to the estimated position (POSN EST) yield the same plot as the control centre calculations, tentatively leads us to conclude that the control centre applies a calculation analogous to simple double differentiation itself as well.

It is evident, however, that these direct differentiation methods may result in inaccurate and sometimes perhaps even meaningless acceleration estimates. The PSDs in Figure 2.10 show that, although the noise levels are much smaller when using the estimated angular position signal (POSN EST) instead of the raw position measurement (POSN FBK), the noise levels are still relatively high, especially at the higher frequencies. To address this, we need to consider applying pre-filtering techniques, perhaps to first improve the angular velocity signal estimate and also using that to obtain a more accurate angular acceleration estimation [31].

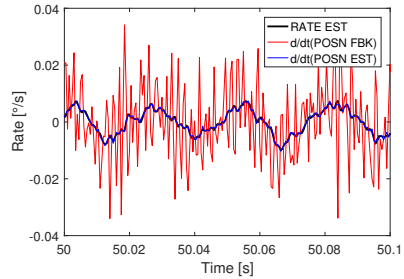
### 2.3.2 CONSTANT RATE MEASUREMENT

In the previous subsection, it was observed how the motor ‘state’ (ON or OFF) of the table affects the measurement, through introducing noticeable low-frequency mechanical noise when the motor is ON. In this subsection, we will investigate the table noise when the table is driven by a constant angular rate signal. The constant rate measurement check was conducted using the same sampling frequency and recording time as the static part, namely 2kHz and 100s. The constant rate input motion was set to  $10^\circ/\text{s}$ ,  $30^\circ/\text{s}$  and  $50^\circ/\text{s}$ .

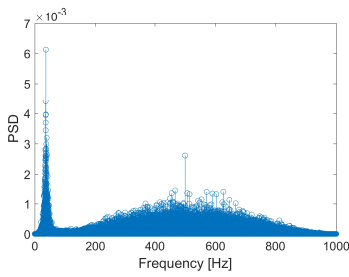
All data were pre-processed before the analysis to determine possible deviations in



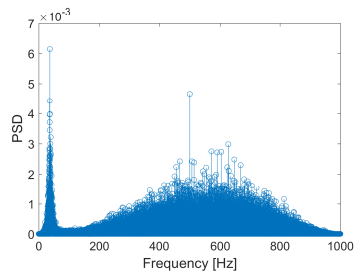
(a) Rate Comparison, *central difference method* (zoom)



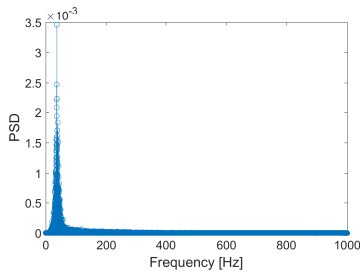
(b) Rate Comparison, *five-point stencil method* (zoom)



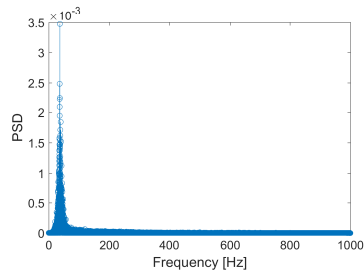
(c) Rate from POSN FBK, *central difference method*



(d) Rate from POSN FBK, *five-point stencil method*

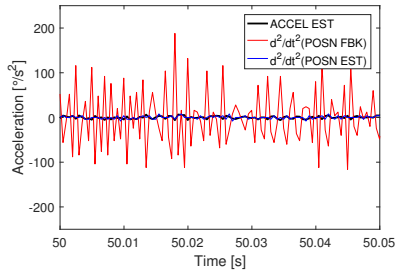


(e) Rate from POSN EST, *central difference method*

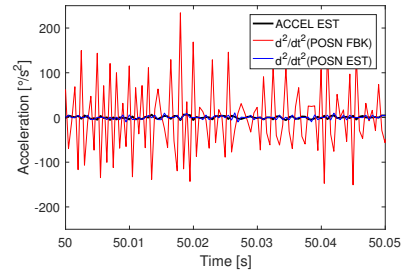


(f) Rate from POSN EST, *five-point stencil method*

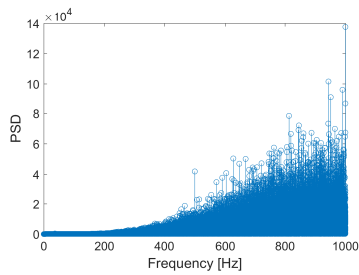
Figure 2.9: Comparison of the rate estimates with the angular rate derived from angular position feedback (top), and their PSD (bottom) (static measurements).



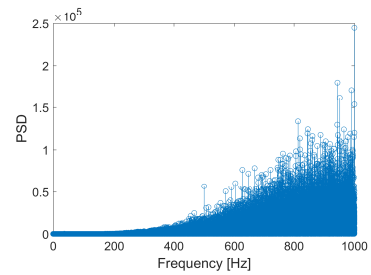
(a) Acceleration Comparison, *central difference method* (zoom)



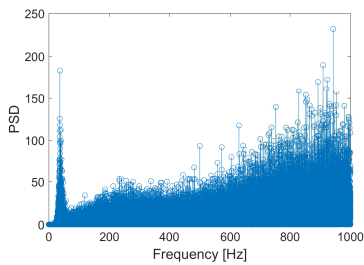
(b) Acceleration Comparison, *five-point stencil* (zoom)



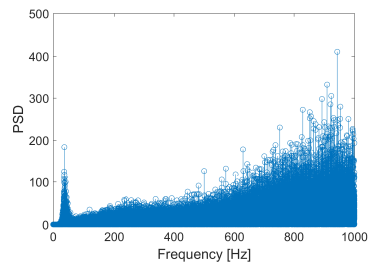
(c) Acceleration from POSN FBK, *central difference method*



(d) Acceleration from POSN FBK, *five-point stencil*



(e) Acceleration from POSN EST, *central difference method*



(f) Acceleration from POSN EST, *five-point stencil*

Figure 2.10: Comparison of the acceleration estimates with the angular acceleration derived from angular position feedback (top), and their PSD (bottom) (static measurements).

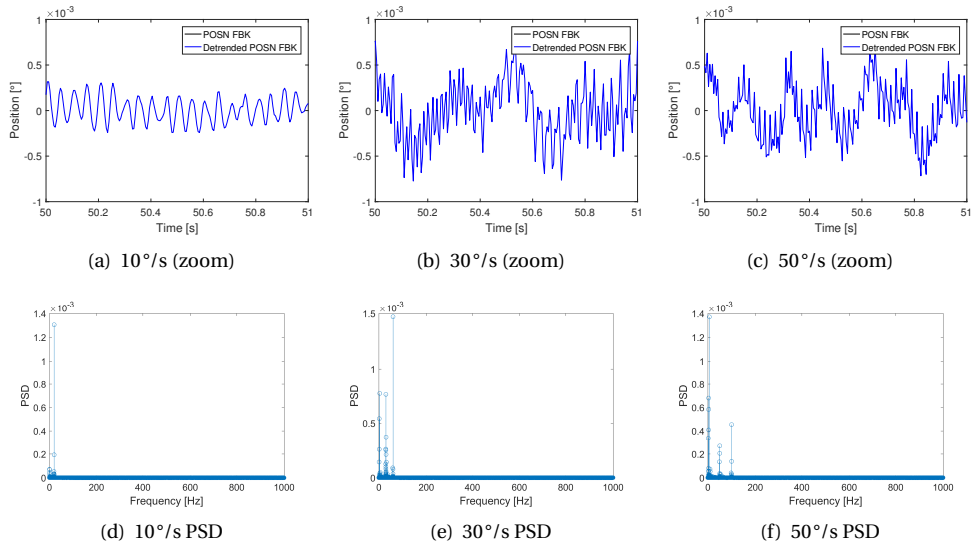


Figure 2.11: PSD of the motion simulator position feedback and estimated variable signals in constant rate input.

the ideal constant rate input signal. The angular position feedback signal in the time domain has a ‘saw tooth’ shape, as the table limits the raw angular position signal to  $360^\circ$ ; first, this signal was adjusted to obtain a continuously increasing line (because of the continuous rotation of the table). Afterwards, the signal was de-trended so that we could further inspect the data and compare these with the static measurements.

Figure 2.11 shows the de-trended angular position data for each constant rate input, together with their power spectra. The zoomed de-trended data reveal that the signal is not entirely linear, which means that the turntable has additional oscillations on top of its constant rate motion.

These oscillations could be caused by either a slight flexibility in the table inner and outer axes coupling or natural shaft resonances; both are likely to remain a problem in our investigation as these are tough to repair or mitigate [120]. The PSD plot shows that the oscillation appears at a frequency twice the angular rate input frequency. For the  $30^\circ/\text{s}$  motion input, the peaks appear at 30 Hz and 60 Hz, whereas for the  $50^\circ/\text{s}$  motion input the peaks occur at 50 Hz and 100 Hz. The lowest  $10^\circ/\text{s}$  motion input has a different characteristic, and only one peak occurs at exactly 20 Hz.

## 2.4 ANGULAR ACCELEROMETER CUSTOMISED MEASUREMENT SET-UP

THE following subsections are describing the measurement set-up, the data synchronisation and the experiment procedure for the case of an angular accelerometer. However, since passing the sensor signals through the slip ring introduces too much noise,

the sensor needs its own, separate data instrumentation. This apparatus is named SDAS, to distinguish it with the standard DAS. Additionally, two direct connections between the control centre and SDAS computer are established. One to coordinate the data sampling for both the calibration table and angular accelerometer, and another to trigger the start of the recording process, such that the initial data point and duration are perfectly synchronised.

### 2.4.1 CUSTOMISED MEASUREMENT SET-UP

In the static measurement evaluation using the set-up in [Figure 2.1](#), it was found that the measured angular accelerometer is perturbed by a noise signal that exceeds the 3 mV Root-Mean-Squared (RMS) specifications<sup>4</sup>. The angular accelerometer was then observed in a series of static measurement evaluations to identify the source of the disturbance. The configurations tested in this regard involved some power setting and locking mechanism of the turntable, as it was suspected that they might have some influence in the measurement.

The following items are the settings for the evaluation measurements to examine the noise source.

1. Normal measurement configuration;
2. Axis motor lock off;
3. Calibration table power off and axis motor lock off; and
4. Sensor power off, calibration table power off, and axis motor lock off.

Even with both the equipment and sensor off as in item number 4, the noise level in the angular accelerometer data channel reached 14 mV. With the assumption that the angular accelerometer has a 3 mV, which is its noise output ceiling, the slip ring contributes an additional of at least 11 mV noise into the sensor measurement and in this case, resulted in a much higher angular accelerometer noise.

Another test was conducted, with a direct connection between the angular accelerometer and the standard DAS unit on a stable surface to confirm the hypothesis that the slip ring be mainly responsible for the excess noise. The measurement returns a 0.992 mV noise level of the angular accelerometer. Accordingly, it can be safely assumed that to obtain meaningful angular accelerometer data the measurement should not be performed through the slip ring. This assumption means that modifying the typical measurement set-up is necessary.

The challenge of the modification is how to record angular accelerometer data directly without the use of slip ring, as depicted in [Figure 2.12\(a\)](#). A direct cable connection from the sensor to the typical DAS would be ideal; nevertheless, it is a potential hazard in dynamic excitation and inevitably limits the motion simulator to only one axis of rotation.

A viable solution is achieved by placing a compact, customised SDAS on top of the turntable plate together with the sensor, as seen in [Figure 2.12\(b\)](#). The slip ring provides power to both the sensor and SDAS, but the angular accelerometer data channels connect straight to the SDAS computer. The first noticeable effect is the high-frequency noise component as illustrated in [Figure 2.10](#), which can be eliminated using a pre-sample filter

<sup>4</sup>[www.crlsensors.com](http://www.crlsensors.com)

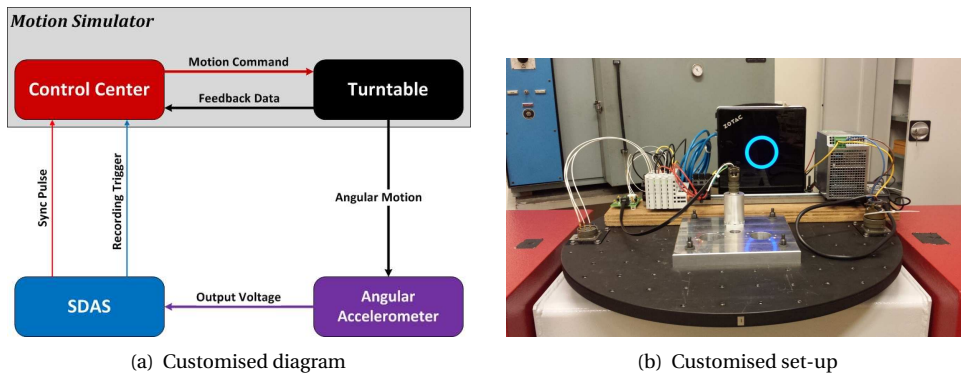


Figure 2.12: Customised diagram and customised set-up of the measurement system.

for each sensor that are added before the SDAS. Its cut-off frequency depends on the frequency content of the motion input, to ensure that the reference signal power is not lost. Here, the pre-sample filter is designed with a cut-off frequency of 100 Hz. The mounted SDAS computer can be accessed via a wireless connection from a nearby desktop.

This customised set-up is unable to accommodate the regular clock connection from the calibration table control centre, which leads to a potential timing error in the acquisition. Further data post-processing is needed to match angular accelerometer and motion table data such that the comparison can be justified. Before being able to do so, first we need to resolve how the synchronisation will be performed.

The key to our synchronisation is to have an equivalent marker that can be used to align the two simultaneous occurrences of data sets from different sources. This can be implemented with the aid of a regular pulse, utilising the rising edge of the regular pulse as the orientation. Since the SDAS starts to record once the acquisition application has commenced, but the calibration table control centre is not, a step signal is generated as a trigger for the calibration table and to mark the beginning of the recording. The synchronisation procedure and a basic test using an external stable signal are described in the following subsections.

### 2.4.2 SYNCHRONISATION PROCEDURE USING FREEZE PULSE MARKER

Each processor has a circuit for keeping track of time which is usually referred to as *clock*, typically in the form of a precisely tuned quartz crystal. In an ideal situation, the clock or timer oscillates at a distinct frequency. Although the regularity runs are usually relatively stable, it is impossible to guarantee that the crystals in different computers all operate at the same frequency. When a system has  $n$  computers, all  $n$  crystal clocks will run at slightly different rates, causing them to gradually get out of sync and give different values when being read out.

Clock synchronisation is possible and need not be absolute [121]. What this means is not that all processes match on exactly what time it is, but rather, that they concur on the order in which events occur, or their relative times. This statement applies to this chapter, which is not a *real-time* situation and therefore will attempt to just employ a logical clock

synchronisation rather than a perfect clock.

For this study, the Freeze Pulse (FP) of the motion simulator is used to mark the start of recording on the SDAS computer and control centre clocks, and furthermore to align the data. This feature is originally used to generate a set of motion variables that are accurate in time to an external reference signal. The raw data are sampled at the simulator frame time, and the estimated motion state values are retained until the next FP. The 'frozen' function shapes any variable fed here into step signal.

Figure 2.13 illustrates the schematic of the measurement set-up. First of all, the turntable and angular accelerometer are powered up, the data flow begins but is not yet recorded. Meanwhile, the standard marker or sync pulse is generated in the form of a regular pulse in the SDAS computer, with a frequency  $f_{FP}$  of 100Hz and an increment level value of 1. Simultaneously, a step signal to activate the recording function is produced in the SDAS computer with the logic of 0 before recording and 1 for the start of the log active and thereafter. Both signals are sent to the calibration table control centre through a digital input-output interface to initiate and mark the record. The received sync pulse signal is recognised as an FP by the control centre. The sampling frequency  $F_s$  for both control centre and SDAS is 2kHz.

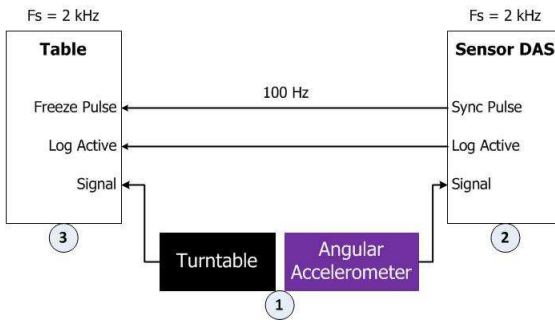


Figure 2.13: Measurement set-up with sync pulse.

The key to understanding the operation is to know when the various events involved indeed happen. The sync pulse generated and recorded in the SDAS follows the ongoing time, however, the motion simulator handles the FP features with a different approach. The motion simulator's observer, which is a predictive estimator, approximates the output variable that is valid at the end of the pulse cycle where the computations take place. The data logger then collects information at the end of the one sampling period,  $T_s = 1/F_s = 1/2\text{kHz} = 0.5\text{ms}$ . The FP received during a period is time-stamped immediately, but it is processed only until the next cycle, as shown in Figure 2.14, the timing diagram.

As a consequence of how the control centre manages the FP, its activation is registered after the actual time happened. Therefore, the motion table data needs to be time skew corrected for  $t_{start}$  to match the actual FP occurrence:

$$t_{start} = t_{k-1} + t_k, \quad (2.5)$$

where  $t_{k-1}$  is the time in the interval between the FP and the start of the next sampling, and  $t_k$  is the time at the end of the next sampling interval. For this purpose, the following variables of interest are recorded in the control centre to aid the synchronisation:

<sup>5</sup>Freeze Pulse Feature on the ACUTROL® 3000, White Paper

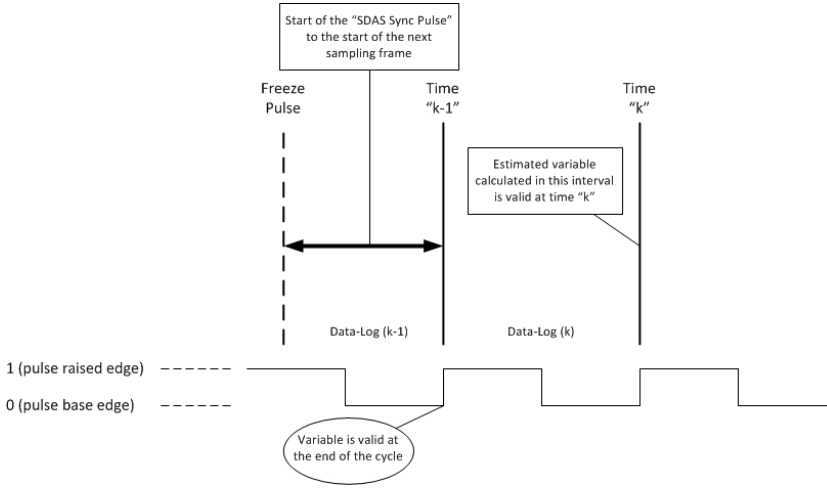


Figure 2.14: Freeze Pulse Timing Diagram<sup>5</sup>.

- Sync pulse from SDAS computer, a 100 Hz pulse;
- Trigger signal from SDAS computer, marking the beginning of the recording;
- Freeze pulse;
- Freeze pulse time in counts; and
- Freeze pulse time in seconds.

The first FP in the record is found using FP active level (1), and non-active level (0) status. A new logic variable is constructed where FP is equal to 1 and log active also equal to 1. The data record capture showing the transition of a FP occurrence is shown in [Table 2.1](#). The highlighted parts are the first FP where logging is active and the FP Latch Time is corresponding to this.

Table 2.1: Creating FP Logic from FP.

FP	FP Time	FP Logic	FP Logic*	Table Time	Remarks
0	0.00024	False	False	246.0853	Time (k-2): Data logger takes a snapshot right before the time "k-2" as shown on the diagram in <a href="#">Fig. 2.14</a> .
0	0.00024	False	True	246.0858	Time (k-1): Pulse took place between (k-2) and (k-1). Time between the sync pulse and "k-1" sample is measured, but the real-time software is unaware of this event at this time.
1	0.00023	True	False	246.0863	Time (k): real-time software is now aware of the pulse
1	0.00023	True	False	246.0868	
1	0.00023	True	False	246.0873	

Table 2.1 provides an application example of the synchronisation procedure to the measurement data. The necessary first step is to create a logic vector from FP Logic, where the data are shifted one sample backward<sup>6</sup> and TRUE only at the start of the pulse. The vector, in turn, correlates to the actual starting time of the first recorded pulse. The Table FP Time itself is the difference between Table Time and FP Latch Time. Since the FP Latch Time is the same in one pulse period<sup>7</sup>, it can be simplified by extracting FP Latch Time using FP Logic\*. Consequently, the Table Time needs to be adjusted, this can also be done using FP Logic\*. Therefore, the Table FP rate is 20 times less than the data sampling rate.

Finding the Freeze Pulse on the SDAS time is performed using a similar method. However, even though both data sets are now aligned at the start of the FP after the recording trigger was activated, they are of different length. The discrepancy exists in the absence of the shared stop recording trigger, which resulting in the SDAS FP Time longer than FP Time because its record starts earlier and stops later. TDAS has an option to log the measurement data for a specified time length, thus, allow an automatic stop. Recording in SDAS, on the other hand, should be stopped manually. Equating the data set can be performed by merely trimming the longer data set, which in this case is the sensor data from SDAS. Therefore, measurement time refers to TDAS time, which can be regulated to determine the data size for analysis.

The final step in the synchronisation procedure is to compensate for the slight difference in time interval due to the different clock rates. To match the data, first, both sequences are modified into a time series format, where each data set is paired up with their respective clock time. Then using the MATLAB<sup>®</sup> synchronize function, the two time-series are re-sampled using a normal time vector and a specified method. In this case, the Uniform method is chosen because the fixed interval can be specified. The sampling period is stated as the fixed interval, accordingly, to ensure a comparable interval.

### 2.4.3 TEST SET-UP WITH AN EXTERNAL SIGNAL

The purpose of this particular test set-up is to compare the TDAS and SDAS behaviour in sampling the same signal. Timing evaluation and signal quality in both acquisition systems will determine not only the measured signal characteristics but also the synchronisation validity. Figure 2.15 shows the test set-up diagram, which instead of measuring the angular accelerometer and the calibration table output, measures the same signal. The input signal is generated by an external signal generator to ensure a test's stability. The SDAS sent the sync pulse continuously to the Table's controller, since the begin-

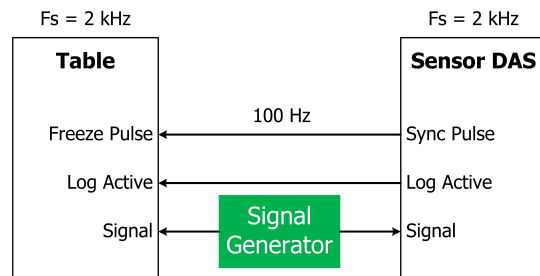


Figure 2.15: Test set-up with sync pulse and external signal.

<sup>6</sup>According to the documentation, the first recorded pulse took place at point  $k - 1$

<sup>7</sup>One pulse period,  $T_{FP}$  consist of 20 samples: 10 True and 10 False.  $T_{FP} = F_s / f_{FP}$

ning of the measurement. The log-active trigger was sent from the SDAS computer to the Table's controller, to start logging or recording the data.

Besides static measurements, the test also incorporates a configuration that can simulate the possible dynamic measurements' influence. The test set-up configuration test plan is summarised in [Table 2.2](#). Two motion profiles are applied to the turntable: a 30°/s constant rate and a 1 Hz sine, while TDAS and SDAS measure the externally generated signal. Also, the sync pulse is varied at a 100Hz and 500Hz rate, to examine whether a higher rate pulse can improve the synchronisation accuracy.

Table 2.2: Test set-up measurement plan.

FP Rate [Hz]	Motion Profile	Signal
100	Static	8 V continuous sinusoidal at 1 Hz
	Constant Rate 30°/s	
	Sinusoid	
500	Static	
	Constant Rate 30°/s	
	Sinusoid	

## 2.4.4 TEST RESULTS

In the experiment, the generated external signal  $S_e$  is measured in the calibration table as  $S_{tab}$ , and in the SDAS as  $S_{das}$ . Afterwards, the recorded data sets are subjected to the synchronisation procedures. Subsequently, timing evaluation is performed based on three criteria: signal delay, clock stability, and clock relation in synchronisation.

### RECORDED SIGNAL

The analogue signals recorded in the TDAS and SDAS, before the synchronisation, are shown in the first row of [Figure 2.16](#) for a one-second period. Based on their PSD in the second row, they represent clear signals at low frequency of 1 Hz as specified in the measurement plan. As seen,  $S_{tab}$  has a slightly higher power than  $S_{das}$  with a 0.258 difference.

### COMPARISON WITH AN IDEAL SIGNAL

The adjusted signals are compared with an ideal signal,  $S_I$  of the same amplitude, frequency and sampling time with the objective to inspect the synchrony.  $S_I$  is simulated at an arbitrary time which makes it has a different phase with the synchronised signals. Their plot in a common time vector is illustrated in [Figure 2.17](#). The difference between our measured and simulated signals expresses the relative bearings in time. Assessed individually, the discrepancies are:

$$\Delta S_{tab} = S_I - S_{tab} = 158 \text{ samples}$$

$$\Delta S_{das} = S_I - S_{das} = 158 \text{ samples}$$

The identical delays  $\Delta S_{tab}$  and  $\Delta S_{das}$  of 158 indicates that both  $S_{tab}$  and  $S_{das}$  have an equivalent orientation towards  $S_I$ . Hence, it can be said that the proper synchronisation procedure has indeed been applied to align the signals.

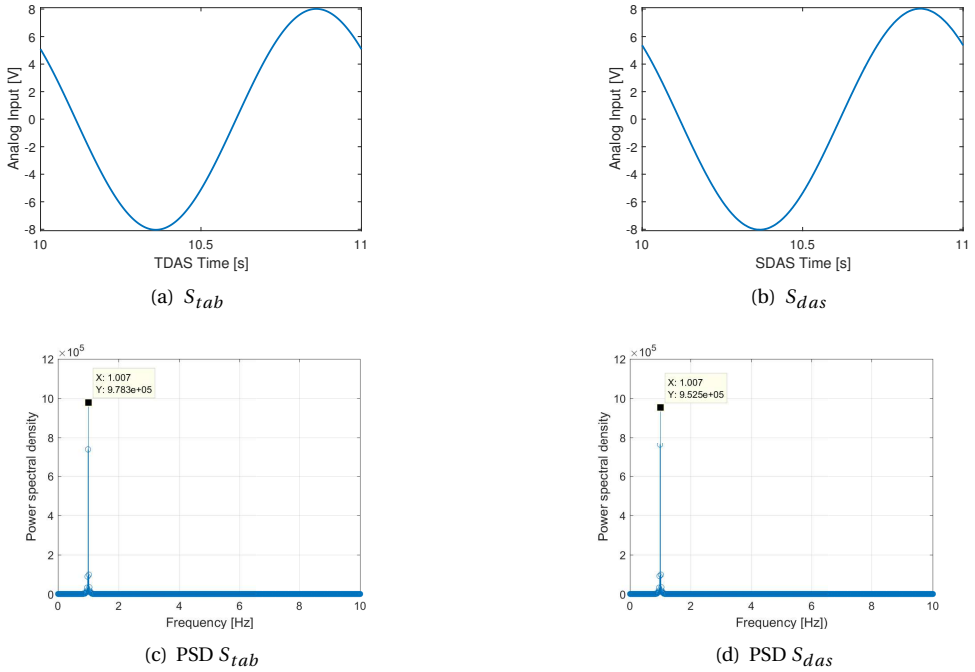


Figure 2.16: Measured signals (first row), and PSDs (second row) of the motion simulator (left column) and sensor DAS (right column).

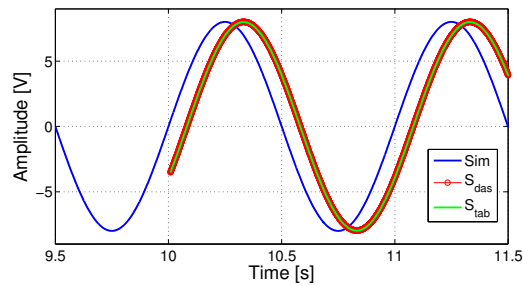


Figure 2.17: Comparison of measured and simulated sinusoidal signal.

### TIMING EVALUATION

Jitter is the timing variation of a set of signal edges from their ideal values, which in clock signals are usually caused by noise or other disturbances in the system. It causes an error when the signal fluctuates *horizontally* across the sampling point or in other words, is sampled inconsistently. In this test set-up, a comparison can be made between two clocks that both log the same waveform. Three conditions are compared: recorded time stamp, FP time, and synchronised time.

Considering that all known signals contain some jitter that has a random component, statistical criteria are sufficient to characterise the jitter correctly. Table 2.3 presents some of the commonly used measures. Mean of the jitter,  $\bar{x}$  should resemble  $T_s$  of 0.5 ms to demonstrate a constant clock interval. The before and after synchronisation clock data fulfill this requirement, as confirmed by the RMS values. Meanwhile, standard deviation,  $\sigma$  are in femto second scale, which exceeds the pico second level standard. The FP Time, which data are in columns 4 and 5, has a 20 times lower resolution. As a result, translated to  $\bar{x}$  and RMS that are one level higher, and  $\sigma$  in  $\mu$ s level.

Table 2.3: Jitter statistical measures.

Measures	Recorded Time Stamp		FP Time		Synchronised Time
	TDAS	SDAS	TDAS	SDAS	Common Time Vector
Mean [s]	$5.00000 \times 10^{-4}$	$4.99999 \times 10^{-4}$	$9.99875 \times 10^{-3}$	$1.00000 \times 10^{-2}$	$5.00000 \times 10^{-4}$
Standard Deviation, $\sigma$ [s]	$3.77841 \times 10^{-15}$	$6.34314 \times 10^{-6}$	$8.50118 \times 10^{-6}$	$7.13368 \times 10^{-6}$	$4.13280 \times 10^{-15}$
RMS [s]	$4.99999 \times 10^{-4}$	$5.00039 \times 10^{-4}$	$9.99875 \times 10^{-3}$	$7.13334 \times 10^{-6}$	$4.99999 \times 10^{-4}$

### CLOCK AND SIGNAL RELATION IN SYNCHRONISATION

TDAS and SDAS FP time relation are subject to a linear approximation to map their association; the result is presented in Figure 2.18, along with the residual in time and histogram graph. The estimates yield a linear relation which indicates the expected agreement between the two measured signals. Residuals of this synchronised clock relation yield a  $\sigma = 2.43497 \mu$ s and  $RMS = 2.43485 \mu$ s.

Figure 2.19 gives the plot of the synchronised motion table and angular accelerometer data that is perfectly aligned. Their difference contains oscillations which is shown by an element at 1 Hz and three other notable frequency components around 50 Hz, 100 Hz and 150 Hz in Figure 2.19(c). Even smaller fluctuations are visible up to 700 Hz.

The error in the RMS value,  $\epsilon_{RMS}$  can be calculated using the following equation:

$$\epsilon_{RMS} = \frac{\sigma_n}{\sqrt{2N}}, \quad (2.6)$$

where  $\sigma_n$  is the standard deviation of the collected sample, and  $N$  is the sample size.

In this case, the sample size is  $2^{17}$  or 131,072. Accordingly,  $\epsilon_{RMS}$  is  $0.00195\sigma_n$  or  $6.7977 \times 10^{-9}$  s for the clock relation. The Gaussian Probability Density Function (PDF) for this number of samples as specified by the Joint Electron Device Engineering Council (JEDEC) standard<sup>8</sup> is  $\pm 5.672$ . Therefore,  $\epsilon_{RMS}$  falls below the mentioned limit.

<sup>8</sup>www.jedec.org

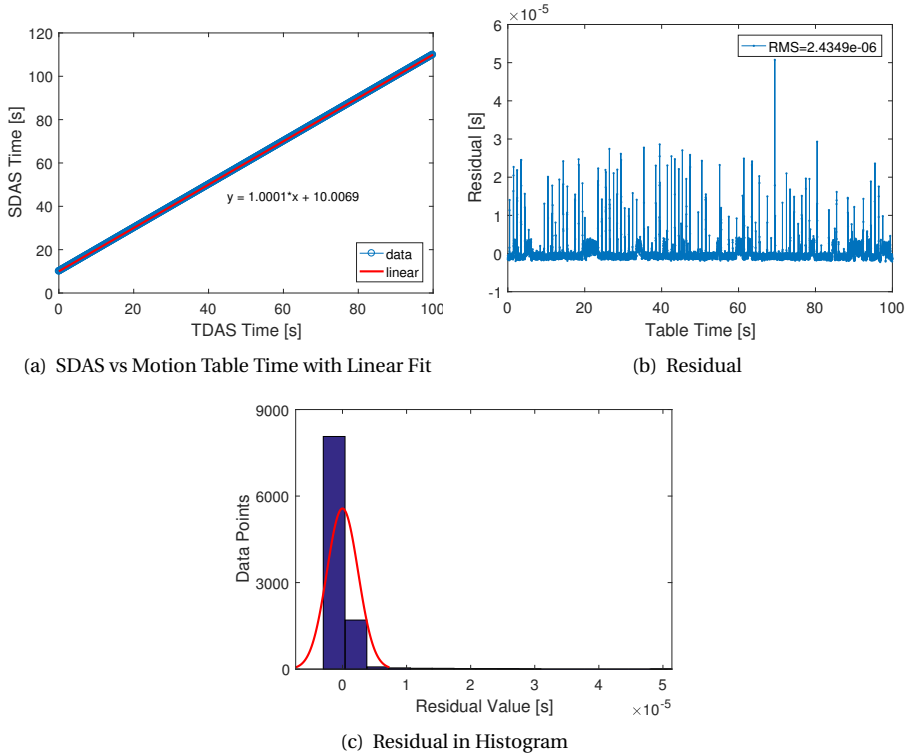


Figure 2.18: SDAS vs motion table time with linear fit and residual value at static measurement.

The previous, provided example originated from the static measurement of a 100 Hz FP. Table 2.4 presents the summary of clock relation error RMS, synchronised signals error RMS, and synchronised signals delay, from all three, applied profiles and two different FP frequencies. We can see that either FP combination with the motion input return insignificant remains in  $\mu\text{s}$  and mV level, also, no delay in the synced signals. Having considered the properties as mentioned earlier, it is reasonable to consider that the proposed synchronisation procedure is acceptable for the customised set-up.

## 2.5 GENERAL ANGULAR ACCELEROMETER MEASUREMENT FRAMEWORK

IN Section 2.2, a first system block diagram was introduced to represent the calibration measurement system, as well as the process of calibrating an angular accelerometer. Note that in this study only a part of the motion simulator, namely the measured angular position, rate and acceleration states are discussed.

Based on the investigations discussed, five main challenges can be identified in the calibration of angular accelerometers using the motion simulator:

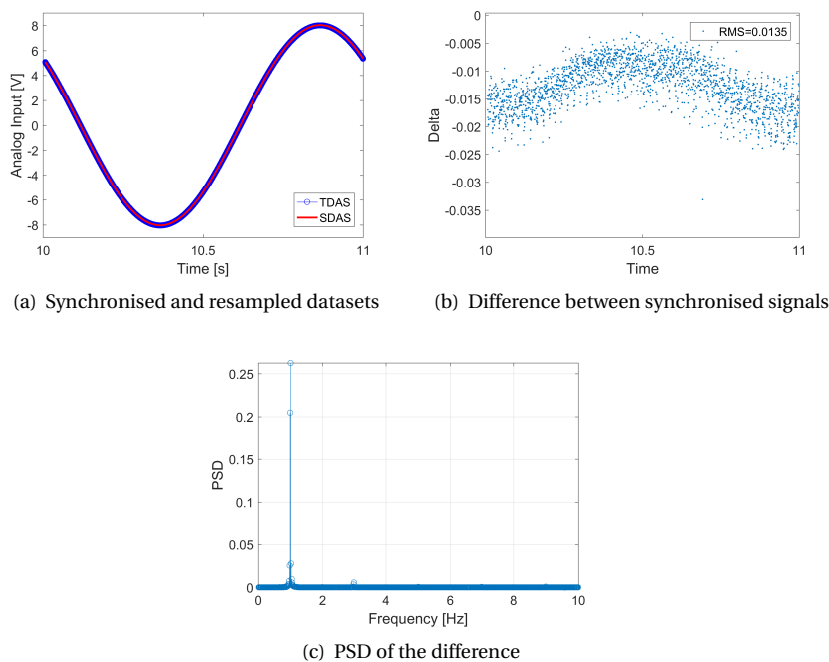


Figure 2.19: Synchronised and re-sampled datasets at Static, with residual and its PSD.

Table 2.4: Comparison of the synchronisation error properties.

Input Description		Clock relation error RMS [ $\mu$ s]	Sync-ed signals error RMS [mV]	Sync-ed signals delay (sample)
100 Hz	Static	3.486	13.787	0
	Constant Rate	2.861	12.76	0
	Sine	3.086	12.412	0
500 Hz	Static	3.079	12.505	0
	Constant Rate	3.546	12.474	0
	Sine	3.058	12.495	0

### 1. Dynamic capability of the motion simulator

Since the motion simulator is of the position and rate type, it was not built to accommodate angular acceleration experiments.

### 2. Estimated motion simulator angular acceleration data

The motion simulator control centre does provide an estimate of the angular acceleration data. However, the noise levels render this estimate unsuitable to be used as a reference for sensor calibration purposes.

### 3. Oscillation during constant rate motion

The turntable slightly oscillates during its constant rate motion, which manifests itself in the additional peaks in the PSD analysis. These peaks are potentially complicating the dynamic test measurement, as here the input may cover a range of frequencies.

### 4. Higher angular accelerometer noise level via slip ring

Angular accelerometer's noise levels exceed the specification when the data are transferred using the basic slip-rings set-up.

### 5. Synchronisation of the motion simulator and angular accelerometer data in the customised set-up

It is not possible to establish a direct clock connection between the motion simulator and SDAS in the customised measurement set-up. Consequently, additional signals are employed to assist in the off-line synchronisation process.

From the investigations and measurements in [Section 2.3](#) and [Section 2.4](#), the first system block diagram in [Figure 2.7](#) is extended, resulting in [Figure 2.20](#). In particular, all noise and disturbance signals that we found in our first set of measurements have been inserted, to obtain an overarching and general block diagram for the angular acceleration calibration framework.

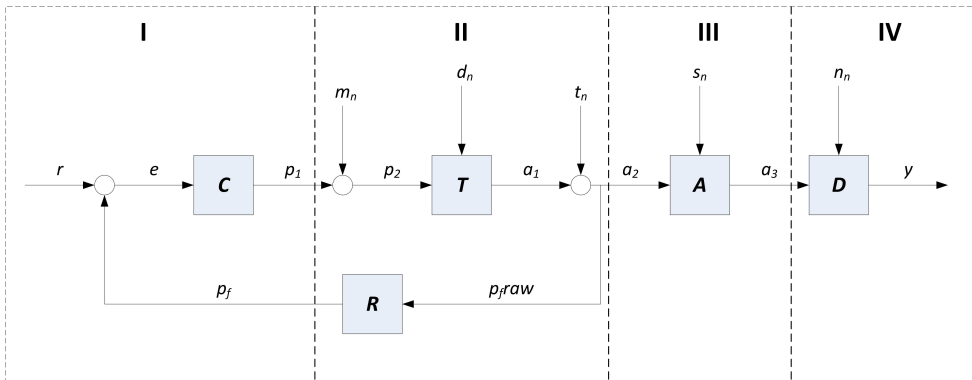


Figure 2.20: Block diagram of the system for the angular accelerometer calibration framework.

The framework is divided into four subsystems, similar to the description in [Section 2.2.4](#), but with addition of the related noise and disturbances.

**Block I** is the input command subsystem with the control centre block  $C$ . Position demand input  $r$  together with position feedback  $p_f$  gives the error signal  $e$ , which is then processed to obtain position estimate  $p_1$ .

**Block II** is the input generator, where the position command  $p_2$  is the combination of  $p_1$  and motor related noise  $m_n$ . The turntable block  $T$  generates the angular acceleration input  $a_1$  which is influenced by load disturbance  $d_n$ . Therefore, the measured data contain components other than the real motion. External or environmental disturbance manifested in  $t_n$ , which in this case is negligible, since the measurement is managed in a stable laboratory environment. The resulted angular acceleration motion  $a_2$  is observed by the position transducer block  $R$  in the form of a raw position feedback  $p_{f_{\text{raw}}}$  and furthermore translated into  $p_f$ . In case of an experiment using the temperature chamber only for the sensor,  $f_r$  will observe  $a_1$  (as here,  $t_n = 0$ ).

**Block III** is the sensor subsystem. Here the angular accelerometer block  $A$  detects  $a_2$ , but also contains sensor noise  $s_n$ , resulting in the angular accelerometer raw data  $a_3$ .

**Block IV** is the SDAS subsystem, where the sampled angular accelerometer data  $y$  contains  $a_3$  with the inclusion of measurement noise  $n_n$ .

The full list of blocks, variables and disturbances is presented in [Table 2.5](#).

Table 2.5: List of blocks, variables and disturbances of the system block diagram.

Blocks		Variables	Disturbances
$C$	control center	$r$ user input or position demand	$m_n$ motor related noise
$T$	turntable	$e$ error	$d_n$ load disturbance
$R$	position transducer	$p_1$ position estimate	$s_n$ sensor noise
$A$	angular accelerometer	$p_2$ position command	$t_n$ external/ environmental disturbance
$D$	sensor data acquisition system	$a_1$ generated angular acceleration	$n_n$ measurement noise
		$a_2$ angular acceleration motion	
		$a_3$ angular accelerometer raw data	
		$y$ sampled angular accelerometer data	
		$f_r$ raw position feedback	
		$p_f$ position feedback	

## 2.6 CONCLUDING REMARKS

THE primary objective of this chapter was to highlight the necessity of an accurate angular acceleration reference in angular accelerometer dynamic calibration, and to present a general framework for dealing with all the system dynamics. In this case, the demand applies to the commercially-available motion simulator, comprised of a turntable to accurately reproduce the input motion. Such a calibration procedure has been proven acceptable for calibrating gyroscopes. However, the equipment performance is not sufficiently accurate and accessible in the case of calibrating an angular accelerometer.

Several tests have been conducted to resolve the main challenges. This investigation results in a general measurement framework, which includes all internal and external

effects, and is classified into four segments, where each part is to be analysed as a separate subsystem. With the proposed structure, users can utilise the currently available position-based motion simulator to perform static and dynamic angular accelerometer calibration experiments.

Explicitly, the possible solution on how to carry out the angular accelerometers calibration test has been presented. It comprises establishing a new, customised set-up for angular acceleration calibration. In the set-up, SDAS connects directly to the angular accelerometer data channels, resulting in a much lower noise level which remains within the sensor specification. A test set-up measuring a standard signal generated by a stable pulse generator is used to check the set-up noise.

This chapter has not addressed the detail of the angular accelerometer calibration itself. Work on the input sequence design and calibration method will be further discussed in [Chapter 3](#).

# 3

## SCALE FACTOR CALIBRATION

*Getting over painful experience is much like crossing monkey bars. You have to let go at some point in order to move forward.*

CS Lewis

*A feasible solution to perform angular accelerometer calibration is proposed in [Chapter 2](#), comprising a measurement framework with a customised set-up. In this chapter, we address the scale factor calibration of the angular accelerometer by the principle of controlled test with a known acceleration reference. Due to physical constraints, turntables cannot sustain constant angular accelerations for an extended period. In light of this, we discuss three alternative procedures: a pendulum method, a combination of two axes rotational rate input, and angular acceleration in the form of a sinusoidal profile, to comply with the turntable limitations. Although the coordinated two axes sequence provides an elegant solution for producing an angular acceleration effect, the motion simulator limits confine the excitation at the low-frequency input. For that reason, a sinusoidal angular acceleration amplitude profile is preferred as the appropriate input.*

*The quality of the angular acceleration data, however, render it inadequate as a reference. Besides employing the standard estimated angular acceleration, a Sliding Mode Differentiation method in a non-linear extended state observer was developed to approximate a refined angular acceleration norm for the reference. A scale factor calibration model for the angular accelerometer data with a polynomial structure was then identified based on a least-squares approach, utilising Residual Mean Squared Error and the Akaike Information Criterion principle to evaluate the model order.*

---

This chapter is based on the following two publications:

- Jatiningrum, D., de Visser, C. C., van Paassen, M. M., and Mulder, M. “Motion Simulator 2-axis Input Design for Angular Accelerometer Calibration”, *AIAA Modelling and Simulation Technologies Conference*, 2016 [122].
- Jatiningrum, D., Lu, P., de Visser, C. C., Chu, Q. P., and Mulder, M., “Development of a New Method for Calibrating an Angular Accelerometer Using a Calibration Table”, *AIAA Guidance, Navigation and Control Conference*, 2015 [123].

### 3.1 INTRODUCTION TO ANGULAR ACCELEROMETER SCALE FACTOR CALIBRATION

**P**ROPORTIONALITY between the incremental change in output response to the input excitation is the result of a scale factor. Exact quantification of this norm is a significant aspect of sensor calibration. In various cases, reflecting the actual output characteristics prompt the need to provide an accurate calibration model.

Although angular accelerometers are precise and robust sensors, they are still *physical* measuring devices, and their imperfections introduce errors in the measurements. For our research on advancing fault-tolerant flight control systems, it is crucial to investigate how to calibrate a high-grade angular accelerometer. However, the specified calibration is a non-trivial problem as it is challenging to provide a sufficiently accurate, *dynamic* angular acceleration reference.

The literature on the study of comparable angular accelerometer devices calibration is scarce, particularly in comparison to the literature on other well-established inertial sensors. The scarcity may be a direct result of the novelty of this sensor type. Perhaps the most comprehensive relevant work is a report investigating the performance characteristics of a newly developed angular accelerometer with input produced by electrical means and a dual spin-axis rate-table [80]. Another report offers some oscillatory stimulus measured by an optical scanner equipped with a position transducer that provides a means to monitor angular deflection [81]. Several studies include calibration approaches for different angular accelerometer devices. One discusses a bio-inspired, circular channels Micro-Electro-Mechanical Sensor (MEMS) in which the external angular acceleration is measured using thermal transduction principles [124]. An automated test system is presented in [125], which aims to assist the angular accelerometer manufacturing and acceptance process. A combined translational-angular micro capacitive accelerometer is calibrated using a semi-empirical nonlinear relation in [126].

It would seem that the primary challenge lies in providing an established angular acceleration reference using specialised test equipment, or, the lack thereof. The absence of substantial guidelines compounds the matter. Consequently, assessment using different apparatus leads to divergent approaches, especially the design of proper excitation input sequences to obtain a global model. The Institute of Electrical and Electronics Engineers (IEEE) Standard 671-1985 did include a test procedure for angular accelerometers in one of its Annexes, which is formulated similarly to the procedure for rate sensors without response at zero frequency [76]. Nevertheless, this is merely an informative type procedure and is preceded by a notable mention on the problematic nature of the dynamic angular acceleration test.

This complexity raises the question of how to calibrate the angular accelerometer using the available turntable device: in this case, a two-axis, position-based motion simulator with the specification data presented in Appendix A. The test table features excellent instantaneous rate stability and precise, stable absolute positioning, as it is designed for calibrating gyroscopes and linear accelerometers. Its utilisation of the angular accelerometer has not yet been ascertained, however. The first step to approach the problem is by developing a calibration measurement framework described in Chapter 2.

This chapter develops a systematic comparison [127] for the calibration procedure

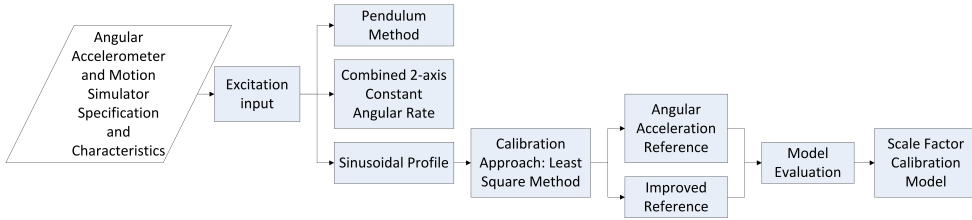


Figure 3.1: Outline of Chapter 3

and model for a force-balance angular accelerometer. It encompasses an offline calibration method using a high-precision turntable output as the standard quantity applied to the Device Under Test (DUT). The approach implies the use of a mechanically generated motion as the proportionate stimulus.

The chapter overall outline is presented in Figure 3.1. In carrying out the study, first, we explore the optimal design of an input sequence in connection with the motion simulator characteristics. As a result, a sinusoidal profile based on an angular acceleration value as the sine amplitude was considered an appropriate input excitation. Subsequently, a polynomial model structure is used to construct a relevant scale factor calibration model. The method of Least-Squares (LS) fits a polynomial to input-output data obtained by varying cyclical excitation over the input range [19]. Next, an advanced observer technique, based on Sliding-Mode Differentiation (SMD), which is a robust, delay-free differentiation method, is used to provide an improved reference. The SMD features optimal asymptotic behaviour on input noise [128]. Criteria based on Root-Mean-Square-Error (RMSE) level and the Akaike Information Criterion (AIC) are applied to evaluate the regression analysis to determine the most suitable model structure.

## 3.2 SIMULATED ANGULAR ACCELERATION INPUT USING TURNTABLE MOTION

SINCE the output response represents a physical variable as a function of time, the correct excitation input must be specified following the temporal range. For testing of a gyroscope, usually, a constant rate of rotation is applied, with low or even zero acceleration [129]. However, this is not suitable for an angular accelerometer which requires varying angular velocity input for a non-zero response. The standard practice to continuously accelerate the angular accelerometer on the turntable is unattainable, or viable only under limited circumstances. Therefore, the motion input should refer to an alternate method in generating angular acceleration. This section examines three possible alternatives to simulate angular acceleration using a turntable motion.

### 3.2.1 PENDULUM METHOD

A possibility to acquire angular acceleration excitation is to employ the pendulum method, which harnesses the potential energy of a swinging rod which is pivoted at one fixed end. In general, this approach is implemented for Inertial Measurement Units

(IMU), typically for the combination of gyroscopes and accelerometers. The following are three application examples from different studies.

1. The first example discusses the calibration of an IMU that consists of three MEMS gyroscopes and three MEMS accelerometers using pendulum motion [130]. The following equation of motion governs the one-dimensional pendulum motion:

$$\ddot{\theta}(t) + c_1 \dot{\theta}(t) + c_2 \sin\theta(t) = 0$$

Here, the second term represents damping, and the third component is associated with gravity.

The pendulum calibration device is manufactured in-house, with the IMU to be calibrated located at the tip of the rod. The swing angles are measured using a resolver mounted at the rotation hinge, and the data acquisition system is located next to the resolver. Angle determinations using a resolver or an encoder are regularly employed for obtaining the initial pendulum angle  $\theta_0$ , the oscillation decay rate and the oscillation period. These three values were then entered into a neural network as inputs, and the neural network estimates of  $c_1$ ,  $c_2$ ,  $\theta$  and  $\dot{\theta}$  were then calculated using the pendulum equation of motion [130].

2. Another study investigates the accuracy of IMUs in estimating 3D orientation during simple pendulum motion [131]. The IMU consists of accelerometers, magnetometers and gyroscopes, with data fusion integration. The device used is a wooden pendulum which rotated about a high-quality cylindrical bearing. The device length was 90 cm with a 50 cm transverse arm oriented along the axis of rotation. Two IMUs were attached to the pendulum at 35 cm and 70 cm from the centre of rotation with the local IMU X-axis oriented along the pendulum shaft. The motion of the pendulum was obtained using two Sony DRV-940E camcorders shuttered at 1/500 s.

The authors state that no single fusion algorithm was capable of accurate measurements in all situations and future research should concentrate on developing such an algorithm. Also, vendors of IMUs should provide more exact specifications about the errors to be expected in different measurement conditions, not just the errors in a best-case scenario. If real-time results are required, a particle filter may be better than either a Kalman filter solution or a variation of the fusion algorithm presented in [131].

3. The third research project discusses two calibration procedures for a gyroscope-free IMU (GF-IMU) using an *ad hoc* double-pendulum apparatus [132]. The instrumented double pendulum is capable of generating known translational and rotational accelerations to the accelerometer cluster in repetitive trials. The rotation along the fixed axis given by an electrical motor coupled to a harmonic steel plate; an extension spring imposes the second rotation along a mobile axis.

The two procedures involved are static trial and dynamic trial. The static test consists of placing an instrumented test subject on the double-pendulum with different attitudes in the gravity field, so the only force acting on the accelerometers was gravity. The dynamic trial consisted of fixing the appliance on the double pendulum and imposing established rotational time sequence on the accelerometer cluster along the two perpendicular axes. It is concluded that the first procedure can determine the calibration parameters of the accelerometers array with higher accuracy than the second procedure [132].

The above methods require a particular pendulum apparatus, and in most cases, one that is customised for a particular type of IMU or sensor. It is possible to apply the pendulum technique to the turntable by tilting the outer-axis 90° and unlocking the inner-axis shaft. Additionally, the angular accelerometer sensitive axis needs to be parallel with the turntable inner-axis. The initial drive to the turntable disk then provided manually, as such that resulted in a swinging pendulum motion. Compatible inertia and payload balance will be needed to create and maintain the motion, which is likely to become an issue since the set-up on the turntable top consists of the sensor and Sensor Data Acquisition System (SDAS) apparatus as described in [Chapter 2](#). Furthermore, managing the input would be complicated, particularly to define a complex excitation.

Similar to the pendulum method is the turning platform method [133], which consists of turning the tested instrument's axis of sensitivity through a precisely known angle about the vertical. Then the acceleration along this axis is determined by the turning angle and the acceleration due to gravity. Various precise turning devices (for instance, optical dividing heads) are widely used as a means for producing acceleration. The measurement of acceleration is based on the measurement of the angle and the knowledge of gravitational acceleration at a specific point on the Earth's surface. Nevertheless, this method is particularly applicable for linear accelerometers and small accelerations typically below 1G.

Another known alternative is the centripetal method, which serves to produce accelerations higher than those caused by gravity. The centrifugal acceleration is determined by the platform's angular velocity and the distance from the rotation axis to the applied acceleration point. For providing considerable acceleration amplitudes in the range of 0.01–30 Hz, a preferable method is by using a dual centrifuge. The installation consists of two rotating platforms with parallel axes of rotation and one of the platforms mounted on the other. The amplitude of the produced acceleration is then determined by the angular velocity of one platform and the distance between the platform axes, whereas the angular velocity of the second platform determines the frequency. From the applicability point of view, however, the centrifugal method is unsuitable for our 2-axis turntable due to its perpendicular axes.

Considering our ultimate goal to calibrate the angular accelerometer by taking advantage of the available motion table advanced features, the reviewed methods are all unsuitable. The appropriate procedure should be developed ideally without any excessive addition to the set-up. Hence, the next sub-section discusses the combined two axes constant rate motion technique to generate the angular acceleration.

### 3.2.2 COMBINED TWO AXES CONSTANT ANGULAR RATE APPLICATION

It is possible to use a system consisting of two platforms which rotate at a constant velocity about mutually-perpendicular axes to obtain sufficient amplitudes of low-frequency angular accelerations. Some work on this concept includes the biaxial test installation [134] and a testbed for calibrating angular-acceleration transducers [135]. This subsection will discuss the 2-axis platform frame of reference and the equation of motion for constant angular velocity application.

[Figure 3.2](#) shows the 2-axis motion simulator frame of reference system in Cartesian coordinates. The  $S_i X_i Y_i Z_i$  coordinate system represents the inner-axis which carries the

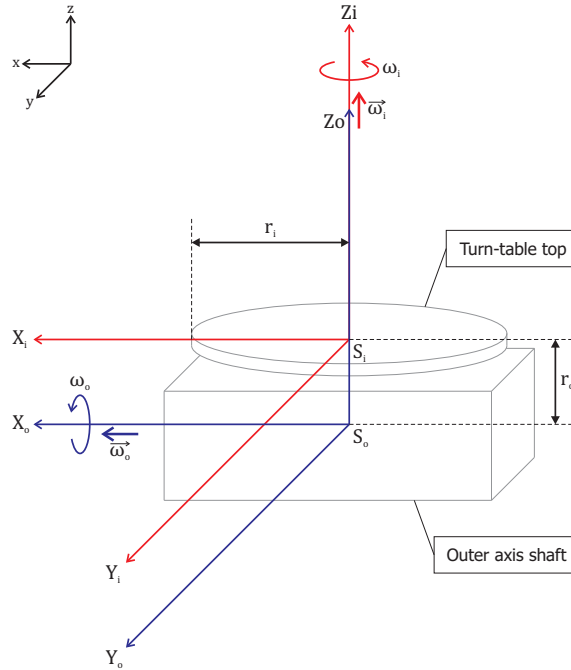


Figure 3.2: The 2-axis motion simulator reference frame.

motion simulator top, where the sensor is mounted and rotates around its  $Z$  axis. The  $S_o X_o Y_o Z_o$  coordinate system serves as the outer-axis. Thus, its axis of rotation  $X_o$  is parallel to the angular accelerometer sensitive axis. The two systems are within distance  $r_o$  from each other's coordinate origin. Nevertheless, the rotational motion quantities are independent of the length  $r_o$  between the table top and the axis of rotation for  $\omega_o$ .

The outer-axis is rigidly mounted on the table support, perpendicular to the inner-axis. Both axes meet at the centre of a rotating basis; the inner-axis is rotating without slipping and undergoes two simultaneous rotations. The table top is spinning about its axis with an angular speed  $\omega_i$  and associated angular velocity  $\vec{\omega}_i$ . On the other hand, the outer-axis shaft is rotating about its axis with angular velocity  $\omega_o$  and associated angular velocity  $\vec{\omega}_o$ . Since the outer-axis is fixed, the rotation  $\omega_i$  does not affect its motion. Therefore its angular acceleration is due solely to  $\dot{\omega}_o$ . Meanwhile, for the inner-axis, the angular velocity vector will change with time both due to  $\dot{\omega}_i$  and  $\omega_o \times \omega_i$ .

The approach is to rotate both axes simultaneously, each with a constant angular velocity. The coupling of inner and outer-axis rotation generates the required angular acceleration. This way, the generated input motion is independent of simulator's angular acceleration function. The analysis of the turntable 2-axis kinematics is using the principle of constrained motion, and for simplicity at this stage, the motion analysis is limited to the 2-axis turntable. Mechanical friction and aerodynamic effects are neglected.

Consider three sets of axes shown in the [Figure 3.2](#). Examine the problem by first defining the fixed coordinate system,  $x y z$ . Axes  $X_o Y_o Z_o$  rotate with angular velocity  $\omega_o \mathbf{i}_o$

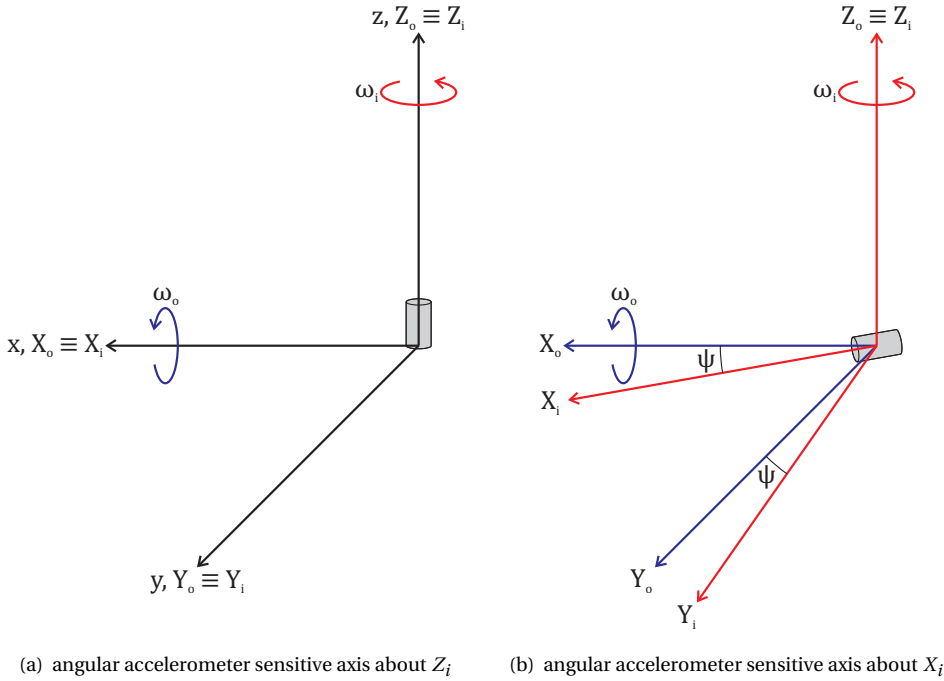


Figure 3.4: Motion diagram of angular accelerometer sensitive axis orientations, about  $Z_i$  and about  $X_i$ .

with respect to  $xyz$ . Axes  $X_i Y_i Z_i$  rotate with angular velocity  $\omega_i \mathbf{k}_i$  with respect to  $X_o Y_o Z_o$ . The total angular velocity with respect of the fixed axes is then:

$$\Omega = \omega_o \mathbf{i}_o + \omega_i \mathbf{k}_i, \tag{3.1}$$

where  $\mathbf{i}_o$  is the unit vector of axis  $X_o$  and  $\mathbf{k}_i$  is the unit vector of axis  $Z_i$ . Figure 3.3 illustrates the total angular velocity vector  $\Omega$ .

The measured angular acceleration, however, depends on the orientation of the angular accelerometer sensitive axis. In the typical 1-axis set-up, the angular accelerometer is mounted on the table top with its sensitive axis parallel to the inner-axis rotation, as the motion diagram in Figure 3.4(a). Another possible set-up is by positioning the angular accelerometer on its side, such that its sensitive axis is parallel to the table top or perpendicular to the inner-axis rotation, with the motion diagram shown in Figure 3.4(b). These two set-ups will be discussed in the following subsections.

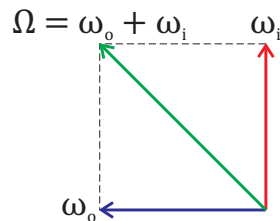


Figure 3.3: Total angular velocity vector.

### ANGULAR ACCELEROMETER SENSITIVE AXIS ABOUT THE MOTION SIMULATOR INNER-AXIS

In this first set-up, the angular accelerometer installed at the centre of the  $S_i X_i Y_i Z_i$  coordinate system, with its sensitive axis along the  $Z_i$  axis. Hence, it immediately detects  $\omega_i$  and any other rotation that affects the inner-axis. To calculate angular acceleration of the angular accelerometer about the fixed axes  $xyz$ , consider the derivative of Equation (3.1):

$$\begin{aligned} \left( \frac{d\Omega}{dt} \right)_{xyz} &= \left( \frac{d}{dt} (\omega_o \mathbf{i}_o + \omega_i \mathbf{k}_i) \right)_{xyz} \\ &= \left( \frac{d}{dt} (\omega_i \mathbf{k}_i) \right)_{xyz} + \dot{\omega}_o \mathbf{i}, \end{aligned} \quad (3.2)$$

at the instant,  $\mathbf{i}_o = \mathbf{i}$ . Here,  $\mathbf{i}$  does not change with respect to the axes  $xyz$  and therefore only the magnitude of  $\omega_o$  changes.

Next, we apply the Coriolis Theorem to calculate the time derivative of  $\omega_i \mathbf{k}_i$  about the fixed frame. Take  $\omega_i$  constant in magnitude, but not direction, and  $\omega_o$  as a constant. The rotation  $\omega_o$  will rotate the vector  $\omega_i$ , changing its direction:

$$\left( \frac{d}{dt} (\omega_i \mathbf{k}_i) \right)_{xyz} = \left( \frac{d}{dt} (\omega_i \mathbf{k}_i) \right)_{X_o Y_o Z_o} + \omega_o \mathbf{i} \times \omega_i \mathbf{k}_i, \quad (3.3)$$

with  $\mathbf{k}_i = \mathbf{k}_o$ . In the  $X_o Y_o Z_o$  frame,  $\mathbf{k}_o$  does not change direction, then:

$$\left( \frac{d}{dt} (\omega_i \mathbf{k}_i) \right)_{xyz} = \dot{\omega}_i \mathbf{k}_o + \omega_o \mathbf{i} \times \omega_i \mathbf{k}_o. \quad (3.4)$$

The combination of Equation (3.2) and Equation (3.4) gives:

$$\begin{aligned} \left( \frac{d\Omega}{dt} \right)_{xyz} &= \dot{\omega}_i \mathbf{k}_o + \omega_o \mathbf{i} \times \omega_i \mathbf{k}_o + \dot{\omega}_o \mathbf{i} \\ &= \dot{\omega}_o \mathbf{i} - \omega_o \omega_i \mathbf{j}_o + \dot{\omega}_i \mathbf{k}_o. \end{aligned} \quad (3.5)$$

Since  $\omega_o$  and  $\omega_i$  are constant, then  $\dot{\omega}_o = 0$  and  $\dot{\omega}_i = 0$ . Equation (3.5) becomes:

$$\left( \frac{d\Omega}{dt} \right)_{xyz} = -\omega_o \omega_i \mathbf{j}_o. \quad (3.6)$$

The generated angular acceleration vector shown in Figure 3.5 has a direction along  $-\mathbf{j}_o$ . This vector is perpendicular to the angular accelerometer sensitive axis about  $k_o$  and consequently, does not affect the measured angular acceleration by the angular accelerometer.  $\omega_o$  that is perpendicular to the angular accelerometer sensitive axis will serve as the angular frequency, but furthermore, this set-up will not produce the expected angular acceleration range for the angular accelerometer.

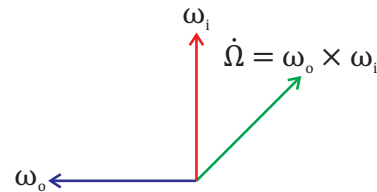


Figure 3.5: Angular acceleration as the cross product of the outer-axis and inner-axis angular velocity vector.

### ANGULAR ACCELEROMETER SENSITIVE AXIS PERPENDICULAR TO THE MOTION SIMULATOR INNER-AXIS

In the second set-up as shown in Figure 3.4(b), the angular accelerometer is installed at the centre of the  $S_i X_i Y_i Z_i$  coordinate system, with its sensitive axis along the  $X_i$  axis which is parallel with the inner-axis of rotation,  $X_o$ . With a fixed inner-axis, only rotation  $\omega_o$  is affecting measurements in this direction. However, from the angular accelerometer point-of-view, its sensitive axis will follow axis  $X_i$  which rotates with angular velocity  $\omega_i$  and rotational angle  $\psi$  towards axis  $X_o$ . This relation means that the angular velocity which influences the angular accelerometer sensitive axis is equal to the projection of  $\omega_o$  on the  $X_i$  axis. Moreover, the angular accelerometer will measure a time-varying term due to its change of orientation.

The angular velocity sensed by the angular accelerometer then can be defined as:

$$\omega_{AA} = \omega_o \cos(\psi) \mathbf{i}_i, \quad (3.7)$$

with  $\psi = \psi_0 + \omega_i t$ . Assuming the initial inner-axis rotational angle  $\psi_0 = 0$ , gives:

$$\omega_{AA} = \omega_o \cos(\omega_i t) \mathbf{i}_i. \quad (3.8)$$

In order to calculate angular acceleration of the angular accelerometer with respect to the fixed axes  $xyz$ , consider the derivative of Equation (3.8),

$$\begin{aligned} \alpha_{AA} &= \frac{d\omega_{AA}}{dt} = \frac{d}{dt} \left( \omega_o \cos(\omega_i t) \mathbf{i}_i \right) \\ &= -\omega_i \omega_o \sin(\omega_i t) \mathbf{i}_i \end{aligned} \quad (3.9)$$

The above expression shows that the combined two axes, constant angular velocity motions produce an alternating angular acceleration response for the angular accelerometer. The angular acceleration vector is in the direction of the unit vector  $\mathbf{i}_i$  of axis  $X_i$ , i.e., similar to the angular accelerometer sensitive axis. The response profile is in the form of a periodic sinusoidal output with an amplitude of  $\omega_i \omega_o$  and an angular frequency of  $\omega_i$ .

Two important aspects arise based on the system's limitations related to Equation (3.9). The first implication is that to achieve an angular frequency of 1 Hz,  $\omega_i$  should be set to  $360^\circ/\text{s}$ . With an angular velocity limit of  $1200^\circ/\text{s}$ , the inner-axis can only accommodate an angular frequency up to 3.3 Hz. The second effect concerns the relation of  $\omega_i \omega_o$ , which defines the amplitude of the sine and represent the angular acceleration magnitude. To yield an angular accelerometer maximum range of  $\alpha = 10 \text{ rad/s}^2 = 572.958^\circ/\text{s}^2$  at the frequency  $f_i = 1 \text{ Hz}$ , for example, gives

$$\alpha = \omega_i \omega_o \quad \Rightarrow \quad \omega_o = \frac{\alpha}{\omega_i} = \frac{572.958}{360} = 0.416^\circ/\text{s},$$

where  $f_i$  is translated into a radial frequency of  $\omega_i = 2\pi f_i$ .

Table 3.1 demonstrates the calculated  $\omega_i$  and  $\omega_o$  input pair for three angular acceleration values and four frequency points. Note that the 4 Hz frequency is included as a comparison only since it is exceeding the  $1200^\circ/\text{s}$  angular velocity limit and therefore, cannot be accomplished. The three angular acceleration marks are selected for  $300^\circ/\text{s}^2$  (52%),  $450^\circ/\text{s}^2$  (78%) and  $572.958^\circ/\text{s}^2$  (100%).

Table 3.1: Calculated  $\omega_i$  and  $\omega_o$  input pair at a particular frequency point.

Frequency [Hz]	$\omega_i^1$ [°/s]	$\omega_o$ [°/s]		
		$\alpha = 300^\circ/\text{s}^2$	$\alpha = 450^\circ/\text{s}^2$	$\alpha = 572.958^\circ/\text{s}^2$
1	360	0.972	1.250	1.59988
2	720	0.486	0.625	0.79994
3	1020	0.324	0.417	0.53329
4	1440	0.243	0.313	0.39997

<sup>1</sup>  $\omega_i$  as the angular frequency

Although the proposed method successfully generates the angular acceleration output motion for the angular accelerometer, a prominent constraint emerges regarding frequency bandwidth. The inner-axis, which drives the angular frequency, has a mechanical limit in generating the angular velocity. Additionally, the customised payload set-up might attribute to the axis balance when running to the maximum. With an objective to identify the full angular accelerometer dynamics, unfortunately, the combined two axes constant rate motion is not an ideal solution for this variety of motion simulator.

## 3

### 3.2.3 SINUSOIDAL PROFILE FROM A LIMITED ANGULAR ACCELERATION MOTION

When an object is in motion, and its velocity changes then it is declared in an acceleration state. That acceleration is the variation in velocity of a moving object in time. When an object moves along a circular trajectory, then its velocity is proportional to the angular velocity. The angular velocity is in the perpendicular orientation of the rotation plane, and it is related to the difference in the angular speed and scale with a factor of radians per second or revolutions per second.

Although turntables are incapable of maintaining a continuous angular acceleration input, it is still possible to actuate a limited angular acceleration motion. The axis is accelerated into one direction until reaching the required angular acceleration level, and then immediately rotated to the other direction until arriving at the same target. The course of this rotational acceleration data in time forms a sine curve.

For producing a sinusoidal profile in the motion simulator, first, we need to comprehend the input option. A direct angular acceleration instruction is not possible for our position and rate-based equipment. Instead, the sine wave can be created using the SYNTHESIS mode [136, 137]. This method works by relating amplitude,  $A$  in [°] and frequency input,  $f$  in [Hz], along with restriction in angular position, rate, and acceleration. The amplitude translates as the angular position at the peak of the sine, the point where the direction of motion changed. Meanwhile, the frequency describes how many complete sine cycles exist in 1 s.

In the following, the second derivation of angular position is obtained from the sinu-

soid equation to achieve the angular acceleration effect:

$$\theta = A \sin(\omega t) \quad (3.10)$$

$$\omega = \frac{d\theta}{dt} = \omega A \cos(\omega t) \quad (3.11)$$

$$\alpha = \frac{d^2\theta}{dt^2} = \frac{d\omega}{dt} = -\omega^2 A \sin(\omega t) \quad (3.12)$$

As can be seen from Equation (3.12), the angular frequency  $\omega = 2\pi f$  influences the sine amplitude as well. With chosen  $f$ , the amplitude can be resolved as:

$$A = \frac{\alpha}{\omega^2} = \frac{\alpha}{(2\pi f)^2} . \quad (3.13)$$

This way, the turntable can apply a limited angular acceleration motion to produce the proper input for the angular accelerometer test. In this chapter, we focus on a single frequency input of 1 Hz to acquire the data used for the scale factor calibration. Examination for a range of frequencies to obtain the Frequency Response Function (FRF) will be discussed in Chapter 4.

### 3.3 CALIBRATION APPROACH

THIS section defines the calibration approach including the measurement set-up, the way to estimate the calibration parameters from the measured data, and how to provide an improved reference data using an advanced observer.

#### 3.3.1 MEASUREMENT SET-UP

The experiment is performed for the devices described in Chapter 1 and specification data in Appendix A, and measurement framework developed in Chapter 2. At this stage, the test is conducted with a single sensor. Figure 3.6 shows a schematic diagram of the system where the red box represents the motion simulator controller, the black box serves as the turntable, and the blue box symbolises the SDAS. Although the DUT instantly senses the simulated motion, the two data-logging systems work independently which therefore requires a supplementary marker to align their responses. Green lines depict these additional connections: the start trigger of data recording, and the sync pulse used to assist in the post-measurement synchronisation.

In this case, the target angular acceleration is approximately 70% of the maximum sensor range, or  $400^\circ/\text{s}^2$ . The measurement specification to conduct the data collection is displayed in Table 3.2.

#### 3.3.2 CALIBRATION PARAMETER ESTIMATION

The measurement data contain the input and output pair  $\{u(k), y(k)\}_N$  for the sensor modelling. Data obtained from experiments typically contain a significant amount of random noise, leading to modelling residuals. The model for  $y(k)$  is given by:

$$y(k) = H[u(k)] + \epsilon(k) , \quad (3.14)$$

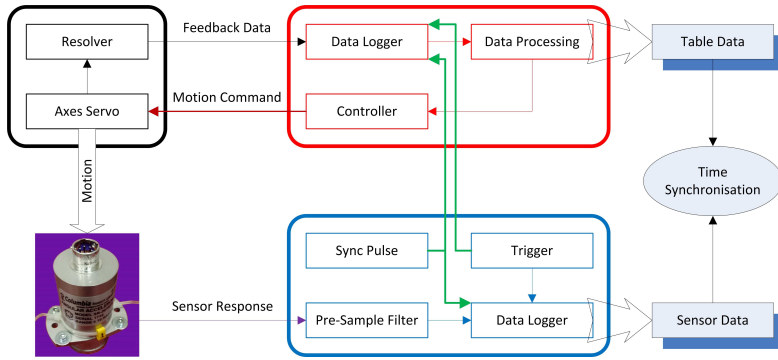


Figure 3.6: A simplified schematic diagram of the calibration measurement system

Table 3.2: Measurement specification

Parameter	Value
Angular acceleration	400 °/s <sup>2</sup> (6.981 rad/s <sup>2</sup> )
Sampling rate	2 kHz
Sampling time	70 s
Sinusoidal input:	
Amplitude	9.99°
Frequency	1 Hz

with  $H$  as the unknown system dynamics, and  $\epsilon(k)$  the residual.

Linear regression analysis postulates a mathematical relationship between dependent and independent variables [138]. This regression results in a parametric model which can be described by a model structure, and its parameters [139]. In this study, the regression model is assumed to be a polynomial of the form:

$$\hat{y}(k) = \sum_{i=0}^p a_i u(k)^i, \quad (3.15)$$

with  $p$  denoting a non-negative integer that defines the degree of the polynomial and  $i = 0$  gives the bias term. For model structure selection, the model identification process is performed for  $p = 0-15$ .

The LS approach gives a method to find the best estimate, assuming that  $\epsilon(k)$  is a Gaussian distributed white noise. It minimise the following cost function:

$$J_N(\Theta) = \frac{1}{N} \sum_{k=1}^N \epsilon^2(k|\Theta), \quad (3.16)$$

where  $\epsilon(k) = y(k) - \hat{y}(k)$ , the difference between the observed response and the estimated output  $\hat{y}(k)$ , and  $\Theta$  is the parameter vector of  $a_i$ .

Adopting the parameters composed in the parameter vector,  $\Theta$  then the optimal

model within the selected model structure is:

$$\hat{\Theta}_N = \arg \min_{\hat{\Theta} \in D_M} J_N(\hat{\Theta}), \quad (3.17)$$

where  $D_M$  is the set of possible parameter vectors for a chosen model parametrisation.

The regression model is linear in  $\hat{\Theta}$ :

$$\hat{y}(k|\hat{\Theta}) = A(k)^i \hat{\Theta} \quad (3.18)$$

Defining  $\hat{\Theta}$  in matrix form:

$$\hat{\Theta} = \begin{bmatrix} a_i \\ \vdots \\ a_p \end{bmatrix} \quad (3.19)$$

The regression matrix  $\mathbf{A}$ , and vector output  $\mathbf{Y}$ :

$$\mathbf{A} = \begin{bmatrix} u(k)^i \\ \vdots \\ u(N)^i \end{bmatrix} \quad \mathbf{Y} = \begin{bmatrix} y(k) \\ \vdots \\ y(N) \end{bmatrix} \quad (3.20)$$

The criterion function then becomes:

$$J_N(\hat{\Theta}) = \|\mathbf{Y} - \mathbf{A}\hat{\Theta}\|_2^2 \quad (3.21)$$

The normal equation is:

$$[\mathbf{A}^T \mathbf{A}] \hat{\Theta} = \mathbf{A}^T \mathbf{Y} \quad (3.22)$$

from which the least squares estimator,  $\hat{\Theta}$  is obtained via:

$$\hat{\Theta} = [\mathbf{A}^T \mathbf{A}]^{-1} \mathbf{A}^T \mathbf{Y} \quad (3.23)$$

In the model identification process of this study, we are identifying the scale factor which converts the measured response in [V] to [ $^\circ/s^2$ ]. Accordingly, the input  $u(k)$  is the angular accelerometer's acceleration,  $\alpha_{AA}$  in V, and the reference output  $y(k)$  is the turntable's angular acceleration,  $\alpha_t$  in  $^\circ/s^2$ .

### 3.3.3 IMPROVING REFERENCE DATA USING ADVANCED OBSERVER

Two conventional methods are possible to determine the perception of a mechanical motion quantity. With the first method it is measured directly, and with the second it is defined by differentiation and integration of the associated mechanical movement. For example, an *angular position* transducer measures the rotational displacement of the turntable's travelled arc. The integration or differentiation operations in this case (for the Acutronic AC2266L) are performed directly in the motion simulator computer.

The turntable angular velocity and angular acceleration are then estimated through direct differentiation techniques, which can be approximated with the Central Method or Five Point Stencil Method, as explored in [Chapter 2](#). This distinction leads to a noisy

angular acceleration signal, however, and a more advanced differentiation technique is required. Here an advanced observer method that utilises Sliding-Mode Differentiation (SMD), a robust and delay-free differentiation technique [128, 140], is used.

Consider an auxiliary equation:

$$\dot{\omega} = \alpha, \quad (3.24)$$

where  $\omega$  is the angular velocity.

The differential equations of an SMD [128] which keeps  $y - \omega = 0$  are:

$$\alpha = v_1 - \lambda|y - \omega|^{1/2} \text{sign}(y - \omega) \quad (3.25)$$

$$\dot{v}_1 = -\beta \text{sign}(y - \omega) \quad (3.26)$$

Here,  $y$  is the tracking of  $\omega$ ,  $v_1$  is an intermediate state of the differentiator,  $\alpha$  is the angular acceleration,  $\lambda$  and  $\beta$  are the tuning parameters which according to Levant [128] have to satisfy the following conditions:

$$\beta > C \quad (3.27)$$

$$\lambda^2 \geq 4C \frac{\beta + C}{\beta - C} \quad (3.28)$$

where  $C > 0$  is the Lipschitz's constant of the  $(n - 1)^{th}$  derivatives. In this paper, we use the first derivative with  $\lambda = 200$  and  $\beta = 2.2$ .

### 3.3.4 MODEL EVALUATION

Cross-validation is chosen as the evaluation scenario using identification and validation data, i.e., a data set different from the one used for estimating the model parameters is used for validation of the model. It is aimed at preventing 'over-fitting' which happens when a too large number of parameters are selected to be estimated. This validation is possible by dividing the data batch into two parts by partitioning or random selection. The following scenarios are considered here:

- 6633 [141], 66.7 % identification (parameter estimation) data and 33.3 % validation data
- 2575 [142], 25 % identification (parameter estimation) data and 75 % validation data

The second scenario is preferred in this case since more validation data will improve the significance of the model and validate its accuracy. The data points are arbitrarily selected from a measurement set using an index permutation with a 25% : 75% ratio. Subsequently, the data points are allocated into identification or validation parts. For this reason, a statistical measure took place by repeating the training process three times, referred as rand1–rand3. Furthermore, the result is compared to a fixed data cluster fix, where the first 25% are assigned to the identification and the second 75% to the validation process.

Following the LS estimation, selection of the best estimate involves an assessment of model order using two criteria: the Root-Mean-Square-Error (RMSE) and the Akaike Information Criterion (AIC). The minimum RMSE level is calculated using the following equation with a normalised residual:

$$\epsilon_{RMSE} = \sqrt{\frac{1}{N_{ID}} \sum_{k=1}^{N_{ID}} |\epsilon(k)|^2} \quad (3.29)$$

where  $N_{ID}$  is the number of samples in the identification data. Then, an additional analysis to assess the trade-offs between the model decency of fit and complexity is done using the AIC as follows [143]:

$$AIC = 2p - 2\log L, \quad (3.30)$$

where  $p$  is the number of the independently adjusted parameters in the model, and  $L$  is the maximised value of the likelihood function for the model. According to Akaike's theory, the most accurate model has the smallest AIC [144].

The following equation implements the normalised AIC:<sup>1</sup>

$$nAIC = \log V + \frac{2n_p}{N_{ID}}, \quad (3.31)$$

where  $V$  is the loss function,  $n_p$  is the number of estimated parameters, and  $N$  is the number of samples. The loss function  $V$  is defined by:

$$V = \det \left( \frac{1}{N_{ID}} \sum_{k=1}^{N_{ID}} \epsilon(k)\epsilon(k)^T \right) \quad (3.32)$$

The Goodness-of-Fit (GoF) examines the selected model using the statistics for parametric models:<sup>2</sup>

- Root mean squared error (RMSE), as explained by Equation (3.29).
- The sum of squares due to error (SSE), also called the summed square of residuals. This quantity measures the total deviation of the response values from the fit to the response values:

$$SSE = \sum_{k=1}^{N_{ID}} (y(k) - \hat{y}(k))^2 \quad (3.33)$$

- R-square is the square of the correlation between the response values and the predicted response values; it measures how strong the fit is in explaining the variation of the data. The ratio of the sum of squares of the regression (SSR) and the total sum of squares (SST) defines the R-square:

$$R^2 = \frac{SSR}{SST} = 1 - \frac{SSE}{SSR}, \quad (3.34)$$

where SSR is defined as

$$SSR = \sum_{k=1}^{N_{ID}} (\hat{y}_k - \bar{y})^2,$$

with  $\bar{y}$  is average of the data, and SST

$$SST = \sum_{k=1}^{N_{ID}} (y_k - \bar{y})^2$$

The R-square value is between 0 and 1, where a value closer to 1 indicates that the model accounts a large fraction of the observed variance.

<sup>1</sup>Akaike Information Criterion for estimated model. <https://nl.mathworks.com>

<sup>2</sup>Evaluating Goodness of Fit. <https://nl.mathworks.com>

The degree of resemblance or closeness of the calibration curve to a specified straight line describes how linear a system is. A non-linearity analysis can be performed to assess the model's accuracy compared to the factory scale factor. Emancipator and Kroll (1993) propose that non-linearity should be some measure of the average deviation of a non-linear function  $f(k)$  from an ideal linear function  $g(k)$ . An appropriate measure of nonlinearity would be the average of the absolute value of  $f(k) - g(k)$ ; that is:

$$\int_{k_L}^{k_U} \frac{|f(k) - g(k)|^2 dk}{k_U - k_L}, \quad (3.35)$$

with  $k_L$  and  $k_U$  the lower and upper bounds of the function's range  $k$ . The graphical representation of the qualitative nonlinearity is shown in [Figure 3.7](#).

Conceptually, this definition makes sense. The contributions of  $f(k) - g(k)$  along the various portions of the domain will not cancel each other. Unfortunately, this definition is mathematically intractable – the appropriate linear function  $g(k)$  can be calculated only by process of trial and error. Another way of preventing the contributions of different portions of the domain from cancelling each other out would be to average the square of  $f(k) - g(k)$ . It turns out that this quantity is mathematically tractable but has the minor problem of being measured in squared units. Preferably, the degree of nonlinearity would have the same units as the function  $f(k)$  itself. The problem is solved by taking the square root of the quantity after calculating the average [145]. Thus the (non)linearity,  $L$  can be defined as:

$$L = \sqrt{\int_{k_L}^{k_U} \frac{|f(k) - g(k)|^2 dk}{k_U - k_L}}, \quad (3.36)$$

### 3.4 SCALE FACTOR CALIBRATION MODEL

THREE excitation sequences, with the primary purpose to provide dynamic excitation for the Device Under Test (DUT) were considered in the previous section. A sinusoidal profile with a constant angular acceleration peak was considered to be the appropriate input. This section describes the experiment performed to verify the proposed calibration method and model structure described in [Section 3.3](#).

#### 3.4.1 TABLE ESTIMATED ANGULAR ACCELERATION AS THE REFERENCE

As higher order polynomial introduces complexity and is often sensitive to over-fitting, the model order should not be much higher than needed. However, a linear or first order might not be sufficient to represent the possible nonlinearity. Accordingly, the polynomial structure order is selected from 0–15 to provide a comprehensive evaluation of

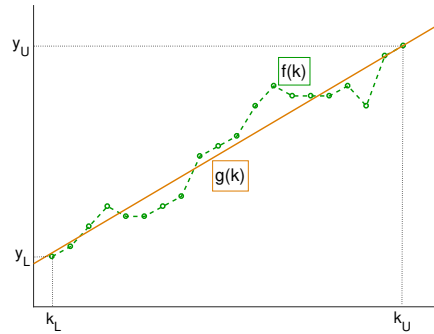


Figure 3.7: Quantitative nonlinearity definition.

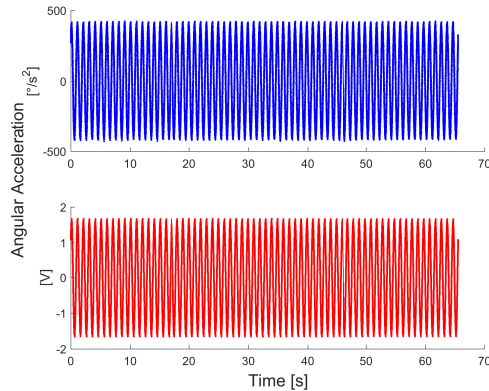


Figure 3.8: Input angular accelerometer voltage and output table angular acceleration data to be used for model identification.

model fit. In this sub-section, the table estimated angular acceleration is used as the reference.

The sensor input and output data are shown in Figure 3.8 and a closer look over a three-second sampling interval is displayed in Figure 3.9. As pointed out in Chapter 2, the motion simulator angular acceleration is approximated from the angular displacement, resulting in a harmonic oscillation shown in blue with  $[\text{°}/\text{s}^2]$  unit. The red line shows the sensor response with the mean removed in [V]. Bias calibration through the multi-position test reported in Appendix B removes the bias from the angular accelerometer data.

The predicted output from each model structure was then compared to the motion simulator angular acceleration identification data, to obtain the residual  $\epsilon$  for calculating the RMSE. The values presented in Figure 3.10(a) provide the means to examine the accuracy of the model for the polynomial model structures of order 0–15. As observed, the RMSE for each data allocation group both in identification and validation process show a considerable drop in order 0 and 1. No dramatic change is visible along the increased order afterwards, which implies that model structures of order 1–15 perform equivalently.

Looking into order 1–15 comparison in Figure 3.11(a), the validation data gives contrasting RMSE for every set: order 7 from the fix<sup>3</sup> run, order 2 from the rand1<sup>3</sup>, order 1 from the rand2<sup>3</sup>, and order 8 from the rand3<sup>3</sup>. Differences between the values, however, are negligible. In respect to the AIC values in Figure 3.11(b), the similar trend with the RMSE comes into sight. Selecting the 7<sup>th</sup> order model based on the lowest RMSE and AIC of the fix data allocation set value is arguable. Nevertheless, the insignificant discrepancy in valuation indicates no real benefit gained by using a higher order model. For that reason, the polynomial structure of the 1<sup>st</sup> order is chosen as the suitable calibration model in this case.

Coefficient values for the 1<sup>st</sup> order polynomial model with their 95% confidence bounds are listed in Table 3.3. The first order coefficient  $a_1$  contributes the most with a

<sup>3</sup>Explained in Section 3.3.4

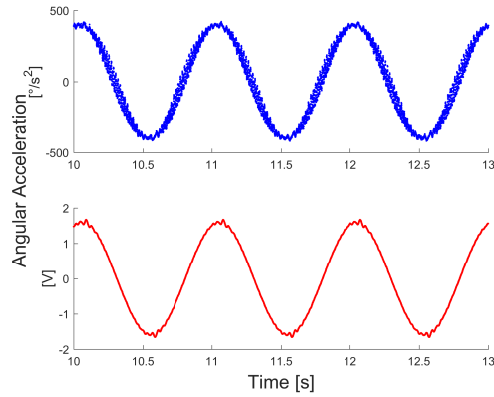


Figure 3.9: Table angular acceleration (blue) and angular accelerometer response (red) over a three-second sampling interval.

3

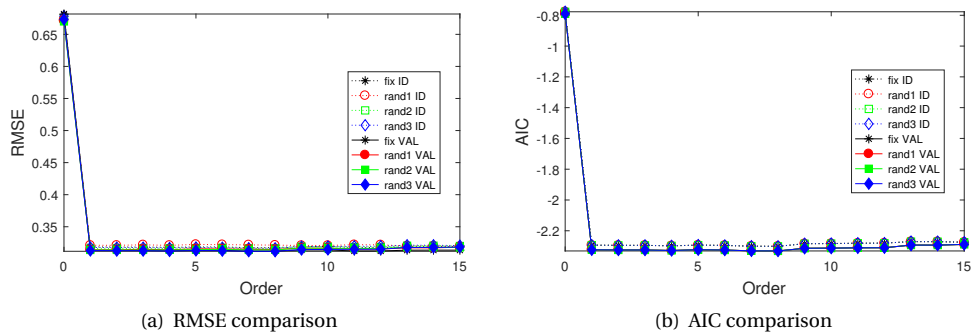
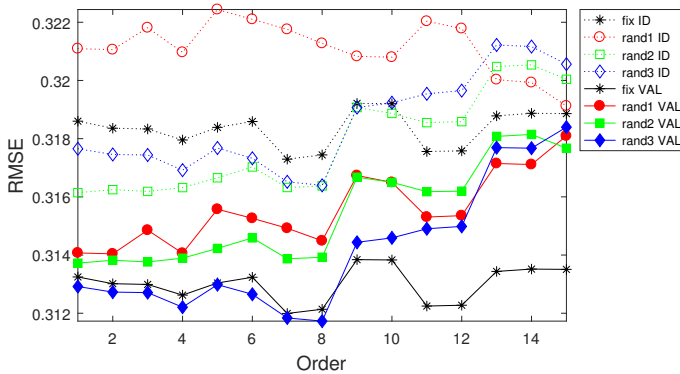
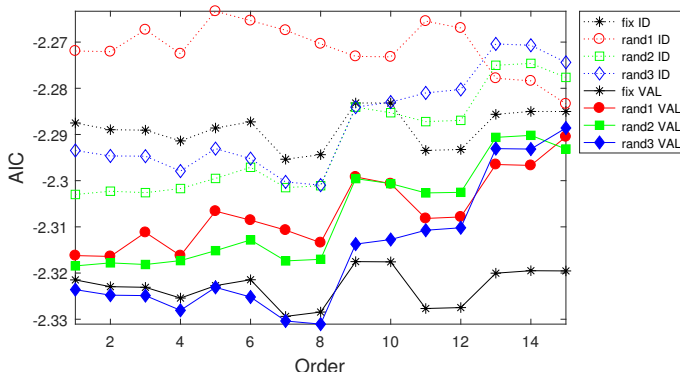


Figure 3.10: Comparison of the RMSE (left) and AIC (right) values from one run of fixed data allocation and three runs of random data allocation, for both identification (ID) and validation (VAL) process in order 0–15.



(a) RMSE comparison



(b) AIC comparison

Figure 3.11: Comparison of the RMSE (top) and AIC (bottom) values from one run of fixed data allocation and three runs of random data allocation, for both identification (ID) and validation (VAL) process in order 1–15.

Table 3.3: Polynomial model 1<sup>st</sup> order coefficients with turntable estimated angular acceleration as the reference (95% confidence bounds).

Coefficients	Values	Lower Bounds	Upper Bounds
$a_1$	250	249.7	250.3
$a_2$	-0.3192	-0.6418	0.00336
$\hat{\alpha}_{AA} [^\circ/s^2] = a_1 u + a_2$			

coefficient value of 250, compared to the zero order or constant coefficient  $a_2$  of  $-0.3192$ . The covariance matrix  $\mathbf{C}$  in Equation (3.37) shows a positive relationship between the two coefficients, a variance of  $7.9626 \times 10^{-6}$  for  $a_1$  and  $1.0175 \times 10^{-5}$  for  $a_2$ . Equation (3.38) shows the correlation matrix  $\mathbf{K}$ .

$$\mathbf{C} = \begin{bmatrix} 7.978e-06 & 4.758e-08 \\ 4.758e-08 & 1.023e-05 \end{bmatrix} \quad (3.37)$$

$$\mathbf{K} = \begin{bmatrix} 1 & 0.00527 \\ 0.00527 & 1 \end{bmatrix} \quad (3.38)$$

Figure 3.12 shows the input-output relation and the regression line with 95% confidence bounds (top), and the residual plot (bottom). The residual is much larger at low angular acceleration magnitudes, approximately between  $-0.9$ – $0.8$  V, where the data also lie outside of the confidence bounds of the fit. Furthermore, a pattern can be noticed in the residuals which indicates that the model does not fully match the data. This formation most likely is due to the LS estimation and the model structure that has to fit the noise in the reference data.

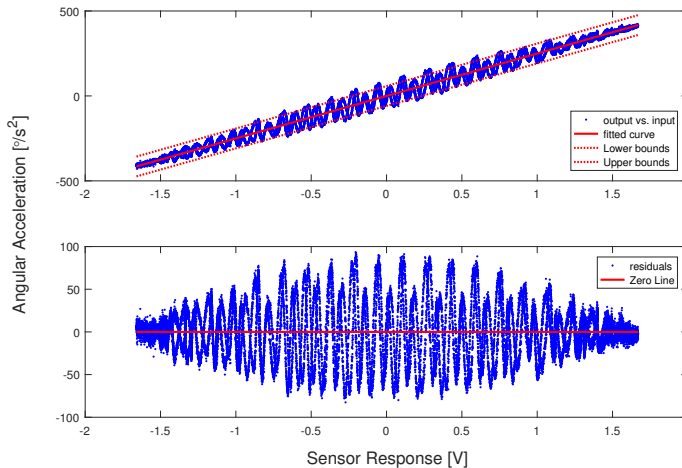


Figure 3.12: Fitted curve of polynomial model 1<sup>st</sup> order with 95% confidence bounds (top) and the residual plot (bottom).

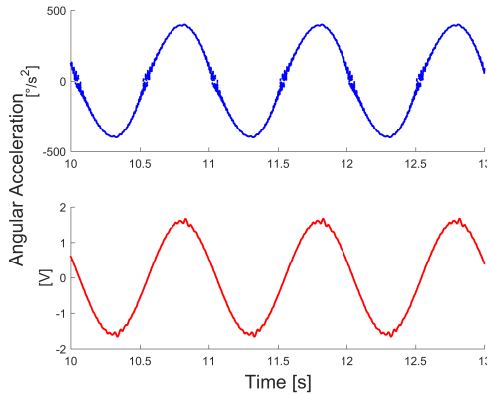


Figure 3.13: Angular acceleration derived with a first order SMD (blue) and angular accelerometer response (red) over a three second sampling interval.

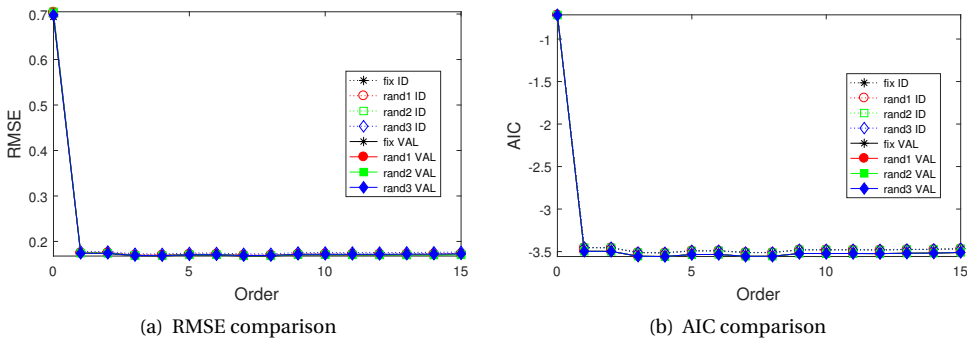


Figure 3.14: Comparison of the RMSE (left) and AIC (right) values from one run of fixed data allocation and three runs of random data allocation, for both identification (ID) and validation (VAL) process in order 0–15.

### 3.4.2 IMPROVED REFERENCE SIGNAL

In this sub-section, a Sliding-Mode Differentiation (SMD)<sup>c</sup> was employed to improve the quality of the reference signal. Preferably, the calculated angular acceleration is based on the real measurement which is obtained from the motion simulator angular position data. However, at this point, the estimated angular velocity was used with the standard SMD instead. Figure 3.13 presents the SMD-derived angular acceleration data and angular accelerometer response during a three-second sampling interval. The derived signal is smoother, which shows that the differentiation method has substantial influence. Still, it contains oscillations on the sinusoidal slopes around  $0^\circ/s^2$ .

The estimation was repeated using the new reference signal. Compared to the previous, RMSE and AIC values determine the finest approximate. Both identification and validation batches demonstrate a similar trend of the RMSE, which is a steep drop between order 0 and 1. No further decrease is visible over the polynomial order 1–15 in Figure 3.14(a). Results of the validation process of fix, rand1 and rand2 return lowest RMSE

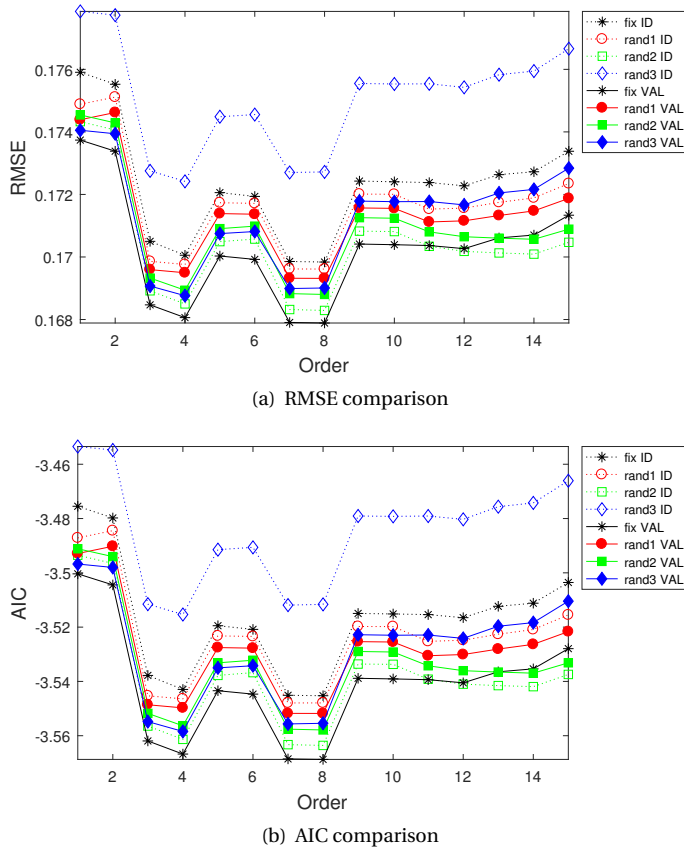


Figure 3.15: Comparison of the RMSE (top) and AIC (bottom) values from one run of fixed data allocation and three runs of random data allocation, for both identification (ID) and validation (VAL) process in order 1–15.

at order 8, while rand3 is of order 4. Examination with the AIC gives an identical result, shown in [Figure 3.14\(b\)](#).

By examining results for polynomial model order 1–15 only in [Figure 3.15](#), it is clear that each data set has comparable RMSE and AIC in the lower order, at the same level with the lowest value. fix, rand1 and rand2 all display similar value at order 3, 4 and 7, whereas rand3 is at order 3, 7 and 8. Preference for lowest order yields polynomial order 3 to be the acceptable calibration model when the reference is SMD-improved.

Coefficients values for the 3<sup>rd</sup> order polynomial model with 95% confidence bounds are listed in [Table 3.4](#). The first order coefficient,  $a_3$  with a coefficient value of 255.1 contributes the most. Also, the odd order coefficients have a greater influence on the model compared to the even order coefficients. [Equation \(3.39\)](#) shows the covariance matrix SMD of the 3<sup>rd</sup> order model terms. The variances are on the same level, with the  $a_3$ . The correlation matrix  $\mathbf{K}_{\text{SMD}}$  is presented in [Equation \(3.40\)](#).

Table 3.4: Polynomial model 3<sup>rd</sup> order coefficients with SMD-improved turntable angular acceleration as the reference (95% confidence bounds).

Coefficients	Values	Lower Bounds	Upper Bounds
$a_1$	-3.017	-3.231	-2.803
$a_2$	0.1321	-0.04089	0.3051
$a_3$	255.1	254.7	255.6
$a_4$	-0.4768	-0.7479	-0.2058

$$\alpha_{AA} [^\circ/s^2] = a_1 u^3 + a_2 u^2 + a_3 u + a_4$$

$$\mathbf{C}_{\text{SMD}} = \begin{bmatrix} \mathbf{1.906e-05} & -7.547e-08 & -3.657e-05 & 5.534e-08 \\ -7.547e-08 & \mathbf{1.245e-05} & 1.197e-07 & -1.586e-05 \\ -3.657e-05 & 1.197e-07 & \mathbf{7.820e-05} & -7.954e-08 \\ 5.534e-08 & -1.586e-05 & -7.954e-08 & \mathbf{3.042e-05} \end{bmatrix} \quad (3.39)$$

$$\mathbf{K}_{\text{SMD}} = \begin{bmatrix} \mathbf{1} & -0.004890 & -0.94727 & 0.00230 \\ -0.004890 & \mathbf{1} & 0.00384 & -0.81477 \\ -0.94727 & 0.00384 & \mathbf{1} & -0.00163 \\ 0.00230 & -0.81477 & -0.00163 & \mathbf{1} \end{bmatrix} \quad (3.40)$$

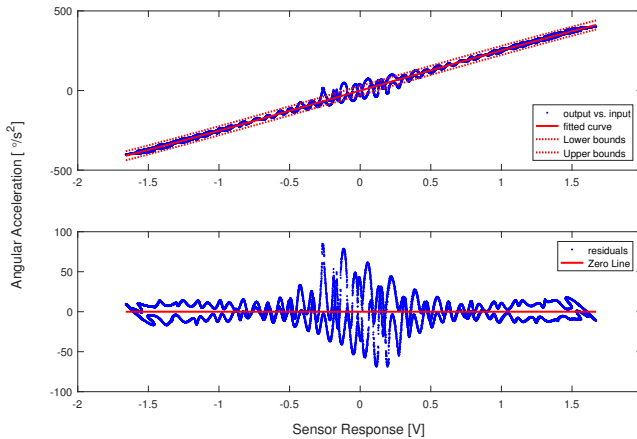


Figure 3.16: Fitted curve of polynomial model 3<sup>rd</sup> order with 95% confidence bounds (top) and the residual plot (bottom) with an SMD derived reference.

The input-output relation and the regression line with 95% confidence bounds is exhibited in Figure 3.16 (top), and the residual plot (bottom). The much larger residual is still visible at low angular acceleration but in a narrower response interval, namely between  $-0.3$ – $0.3$  V, where the data are still present outside of the confidence bounds of the

fit. There seems to be a less distinctive pattern in the residuals, however, which hints that the model does has an adequate match.

### 3.4.3 DISCUSSION

For simplicity, the selected 1<sup>st</sup> order polynomial model from Section 3.4.1 is labeled as LSFit, and the 3<sup>rd</sup> order polynomial model from Section 3.4.2 as LSFit<sub>SMD</sub>.

#### GOODNESS-OF-FIT STATISTICS

The analysis is performed to the residual between data and the estimated output to assess the identified model performance. Table 3.5 compares the Goodness-of-Fit between LSFit and LSFit<sub>SMD</sub> using the concept in Section 3.3.4. The Goodness of Validation measure is included in the last two columns. It is obvious that with a lower order, LSFit has less coefficients compared to LSFit<sub>SMD</sub>.

Table 3.5: Goodness-of-Fit statistics of LSFit and LSFit<sub>SMD</sub>.

Model	Order	Coefficient	SSE	RMSE	$R^2$	SSE <sub>VAL</sub>	RMSE <sub>VAL</sub>
LSFit	1	2	2.905e+07	29.783	0.989	8.647e+07	29.737
LSFit <sub>SMD</sub>	3	4	6.868e+06	14.48	0.997	2.057e+07	14.503

The Goodness-of-Fit statistics demonstrate a lower SSE and RMSE for the LSFit<sub>SMD</sub> model both in the identification and validation results. The  $R^2$  indicates that LSFit<sub>SMD</sub> is favoured over LSFit, where it explains 99.7% of the total variation in the data about the average compared to 98.9% of LSFit. Therefore, the 3<sup>rd</sup> order model is likely better to represent the scale factor of the sensor response from [V] to [°/s<sup>2</sup>].

#### MODEL (NON)LINEARITY

A check on the linearity of the fitted curve for both selected models is presented in Table 3.6. The lines obtained from linear regressions of the models are shown in the second column. The third column gives model (non)linearity,  $L$  from Equation (3.36). With the values of  $L$  much closer to 0% (purely linear), both models apparently are only slightly nonlinear. However, it is interesting to notice that the improved angular acceleration reference develops a model with higher  $L$  than the model with the standard reference.

Figure 3.17 and Figure 3.18 shows the calibration model and an ideal linear function as in Table 3.6 (top) as well as the divergence of the model (bottom). LSFit residual deviates the most at higher angular acceleration, but with a much smaller value, since it is a

Table 3.6: Fit (non)linearity statistics of LSFit and LSFit<sub>SMD</sub>.

Model	Ideal linear function	(non)Linearity
LSFit	$g = 250.02u - 0.31923$	$L = 0.464$
LSFit <sub>SMD</sub>	$g_{SMD} = 249.35u - 0.29956$	$L_{SMD} = 1.261$

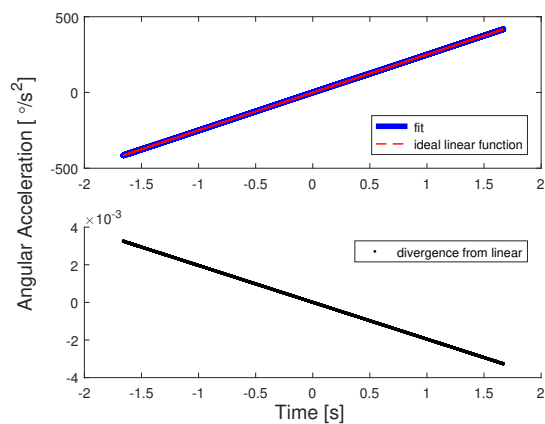


Figure 3.17: Fitted curve of polynomial model 1<sup>st</sup> order compared with an ideal linear function  $g$  (top) and the divergence plot (bottom).

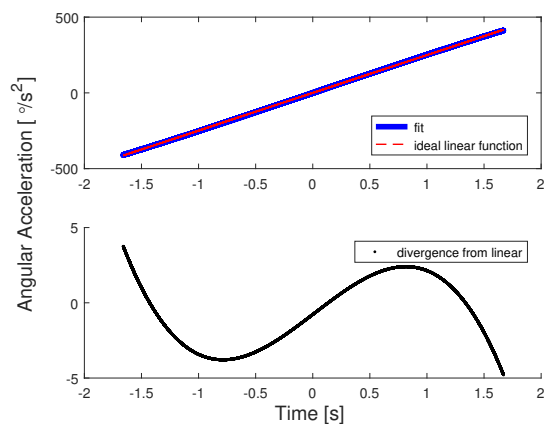


Figure 3.18: Fitted curve of polynomial model 3<sup>rd</sup> order compared with an ideal linear function  $g_{SMD}$  (top) and the divergence plot (bottom).

1<sup>st</sup> order model. Meanwhile,  $LSFit_{SMD}$  deviation eminently happens at moderate angular acceleration in addition to the maximum, which represents its higher order. Nevertheless, the model is capable of describing the nonlinearity that is observed at the extreme of the response.

### 3.5 CONCLUDING REMARKS

**T**HIS study develops a new calibration procedure for an angular accelerometer using a high-precision, position-based turntable of a motion simulator. The first part of the process determines the proper input, taking into account the characteristics and specification of both angular accelerometer and motion simulator. It provides an alternative means to generate an excitation that can be employed to calibrate angular accelerometers using calibration tools that were not primarily designed to deliver accurate angular acceleration inputs. Subsequently, two calibration models are developed with the LS approach based on the time domain data using a standard and an improved angular acceleration estimation. Since the high-precision motion simulator provides only angular position and rate precisely, SMD is employed to obtain an enhanced angular acceleration reference for the calibration.

The limited angular acceleration motion in the form of a sinusoidal profile is recognised as the suitable angular accelerometer dynamic calibration input over the pendulum method and combined 2-axis constant angular rate. The pendulum method requires a different apparatus, or if applied to the current turntable, it will be difficult to manage the input, and especially, complex excitation. On the other hand, the 2-axis, constant angular velocity motion could generate an angular acceleration effect for the angular accelerometer in the form of sinusoidal response, with an amplitude of  $\omega_i \omega_o$  and an angular frequency of  $\omega_i$ . Unfortunately, the angular acceleration obtained through this method is restricted by the mechanical limitations of the motion simulator where the resulting acceleration amplitudes are only accurate over a narrow angular frequency range and thus falls short of the sensor specification.

A scale factor calibration model structure in the form of the polynomial function is investigated. The examination returns a 1<sup>st</sup> order polynomial for  $LSFit$  and a 3<sup>rd</sup> order for  $LSFit_{SMD}$ , where the model structure is defined using the RMSE and AIC norm. Goodness-of-Fit statistics exhibit lower SSE,  $R^2$  and RMSE for  $LSFit_{SMD}$ , but higher nonlinearity, in comparison with  $LSFit$ . The current model nevertheless, relies only on the angular accelerometer response. To accurately model the sensor output, future calibration should take more variables into account, for instance, to include the effects of temperature changes and jerk.

Results indicate that the proposed method can indeed be successfully applied to calibrate an angular accelerometer. This developed practice is, however, limited to the time domain and requires additional, off-line processing to achieve more accurate angular acceleration reference data.

# 4

## FREQUENCY RESPONSE MODEL

*A wise woman wishes to be no one's enemy; a wise woman refuses to be anyone's victim.*

Maya Angelou

*This chapter presents a frequency response measurement approach using a motion simulator, to assess the angular accelerometer dynamic properties. Angular acceleration input from the motion simulator and the angular accelerometer's voltage output are then represented in a transfer function form. For its ensuing application, the angular accelerometer response can be adjusted to  $[\text{°}/\text{s}^2]$  unit using the scale factor obtained in [Chapter 3](#).*

*The measurement design considers the motion simulator limitations and angular accelerometer operational specification, as well as the customised set-up, to define a constrained test envelope. Measurements are conducted for different acceleration peak magnitudes along a varied frequency range. The specified input motion maintains full sine periods in a frequency resolution to minimise leakage of the signal spectra. In the model identification, first, a non-parametric Frequency Response Function is estimated through an analysis of the angular accelerometer input-output relation in the frequency domain. Subsequently, time domain data are used to validate the transfer function model. Besides representing the angular accelerometer dynamics, the angular accelerometer model is essential for the design of sensor-based, fault-tolerant flight control systems.*

---

This chapter is based on the following publication:

Jatiningrum, D., de Visser, C. C., van Paassen, M. M., and Mulder, M. "Modelling an Angular Accelerometer using frequency response Measurements", *AIAA Guidance, Navigation and Control Conference*, 2016 [146].

## 4.1 INTRODUCTION

WHEN developing a flight control system utilising signals from a new inertial sensor, the angular accelerometer, it is essential to understand how the sensor system behaves with the application of different inputs. Knowing this behaviour will give an approximation of the angular accelerometer's dynamic response which might have an impact on controller design. Additionally, recognising the angular accelerometer limitations and performance characteristics is essential when designing a control system. Hence, a reliable sensor model is crucial in developing the novel concept of sensor-based flight control systems.

Among three common domains to study linear system dynamic responses: the *s-plane*, the *frequency response*, and the *time response* [147], the primary method to predict and adjust performance by looking at input-output behaviour rather than analytical solutions to the equations of motion is the Frequency Response Method. The frequency response is a method where the system response to sinusoidal signals characterises its frequency-dependent behaviour. In many cases, it provides an excellent solution to the uncertainty aspect of the plant model. When the individual component values, i.e., the mathematical model is unknown, the frequency response of the system, from input to output can be obtained experimentally and used to approximate the transfer function [115].

Although angular accelerometers are expected to have significant potential in increasing the performance of several flight-control approaches [6, 8, 9], little is known regarding the relationship between sensor's characteristics and its performance. One of the studies describes the development of an automated test system for the angular accelerometer to assist the manufacturing and acceptance process [148]. It concentrates on research and development for an indirect angular acceleration sensor, which consists of a single-axis rate gyro, gear and an electromagnetic inductorium<sup>1</sup>. Assorted research examines a prototype of a liquid circular angular accelerometer and uses angular vibration table experiments data as the input to derive the transfer function [87] and model the fluid transient [88], as well as a dynamic fluid model in addition to the mathematical model [89]. These investigations concentrate on a self-developed prototype which deliberately possesses known a-priori features.

Thus far, the most direct approach for testing the frequency response of inertial sensors such as gyroscopes is with an inertial rate table, or motion table, which is capable of introducing the appropriate frequency content [150]. Motion tables are widely used to produce motion input with a single-axis, or multi degree-of-freedom two or three-axis mounting platforms. Motion tables can simulate aircraft attitude and orientation, with measurement applications not only for different types of inertial sensors, for instance, accelerometers and gyroscopes, but also for groups of sensors in for instance an IMU. Besides angular rate, this equipment typically provides an estimated angular acceleration as well. Since rate tables typically include a programmable servo motor and an optical encoder that verifies programmed rotation on the motor shaft, they can precisely drive the sine wave with specified frequency. The benefit of this test approach is that it

<sup>1</sup>The induction-coil stimulator used in the biomedical engineering field, although primitive as it was by modern standards, was very popular because it could provide single, as well as repetitive stimuli of easily controlled intensity (but not duration) [149].

applies actual inertial motion with sensor-specific excitation.

At present, however, the available motion tables are mainly intended for static operation [76]. This designation means the estimated angular acceleration accuracy is inadequate to carry out dynamic angular accelerometer experiments. The specific aspect of this subject has been discussed in Chapter 2. Furthermore, Chapter 3 introduces an offline calibration method using an improved angular acceleration reference at a single motion frequency of 1 Hz.

This chapter develops a system identification technique to acquire the angular accelerometer dynamic characteristics over a range of frequencies. The frequency response method has been extensively considered in different fields, both in theoretical and simulation studies [151–153] as well as the identification from experimental data [154–160], the approach that is also used here. The concept of using a motion table in a frequency response based test is hypothetically applicable to angular accelerometers as well. For this purpose, a turntable is used to generate the motion input for the sensor with an experiment set-up developed in Chapter 2. Also, the measurement is carried out with a frequency-extended version of the method presented in Chapter 3 to acquire the most informative data. The input-output relationship is analysed in the frequency domain as the main observation. Once the frequency response is obtained from the steady-state output in the form of sinusoid amplitude and phase angle, the data are combined in a Bode plot. Subsequently, the transfer function of the system can be estimated from the Frequency Response Function (FRF), which gives the functional relationship between physical input motion in  $[\text{°}/\text{s}^2]$  and the electrical output signal in [V]. As a final point, the transfer function model is compared with the time-domain data identification result [161].

The chapter is divided into six sections, starting with an introduction to the topic. Section 4.2 contains theoretical background knowledge regarding the frequency response method. Section 4.3 describes the test envelope specification and measurement method for the frequency response system identification. Section 4.4 discusses the frequency response measurement result, and FRF extracted from the frequency domain data. The transfer function model development using time domain data is established in Section 4.5. Finally, Section 4.6 gives the final remarks on the angular accelerometer model. The overall chapter outline is presented at Figure 4.1.

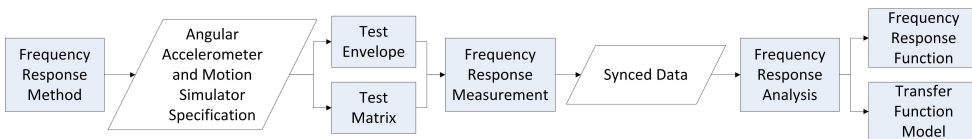


Figure 4.1: Outline of Chapter 4. The boxes represent the processes, whereas the parallelograms represent the data.

## 4.2 MODELLING THE ANGULAR ACCELEROMETER

A common approach to discover the response of a system, is to apply a test input and observe the output response. This method is particularly useful for off-the-shelf sensors, where a theoretical model is rarely available. Different test input signals are possi-

ble, but a simple and effective form is the sine wave. The steady-state output of a linear system subjected to a sinusoidal input is also a sinusoid, with the identical frequency as the input, but with different amplitude and phase. Our system is not necessarily linear, however, as of many other systems. In this regard, the advantage of the sine wave as the test signal is that well-known frequency domain analysis techniques are possible. This section outlines the approach to represents the angular accelerometer using FRF and transfer function identified from the frequency response measurement.

#### 4.2.1 SYSTEM DESCRIPTION

The system of interest here comprises the sensor subsystem in **Block III** and the SDAS subsystem in **Block IV**, depicted in the measurement framework of [Figure 2.20](#) in [Chapter 2](#). In this chapter, however, these two subsystems are lumped together and viewed as one system entity  $H$ , displayed in [Figure 4.2](#). Since angular accelerometers detect the turntable's angular acceleration, it is chosen as parameter input of the system and expressed as  $\alpha_t$  in  $[\text{°}/\text{s}^2]^2$ . Even though the ideal system output is the continuous angular accelerometer response, the measured electrical signal form has to be retrieved through the Sensor Data Acquisition System (SDAS). Therefore, the sampled angular accelerometer data,  $\alpha_{AA}$  in volt, [V], is used as the system output. This way, the scheme in the discussion is viewed as a single-input/ single-output (SISO) system, represented by two sets of data obtained from the frequency response measurement.



Figure 4.2: Merged angular accelerometer and SDAS systems block diagram.

As discussed in [Section 3.2](#), the chosen input profile excitation in this study is a sinusoidal profile. The mathematical representation of the angular acceleration input signal of the motion simulator implementation is given in [Equation \(4.1\)](#), based on [Equation \(3.12\)](#):

$$\alpha_t(t) = -\omega^2 A \sin(\omega t) \quad (4.1)$$

The minus sign in the equation was a result of the double differentiation from the angular position data. Here,  $A$  is the amplitude of the input signal,  $(\omega^2 A)$  shows the amplitude of the generated angular acceleration,  $\omega = 2\pi f$  with  $f$  is the test frequency, and  $t$  represents the time.

The steady-state response in the output variable is represented by:

$$\alpha_{AA}(t) = -\omega^2 B \sin(2\pi f t + \phi) = -\omega^2 A M \sin(2\pi f t + \phi) \quad (4.2)$$

Here,  $(\omega^2 B)$  is the amplitude of the output signal,  $B$  is the product of the (amplitude) gain,  $M$  with  $A$ , and  $\phi$  is the phase lag as a function of frequency. When the system is assumed Linear and Time-Invariant (LTI), the frequency of  $\alpha_{AA}(t)$  will be the same as of  $\alpha_t(t)$ .

Through measuring the output amplitude and phase of a system over a range of frequencies of the sine wave input, and analysing the resulting steady-state response, the

<sup>2</sup>° is the default unit of the motion simulator

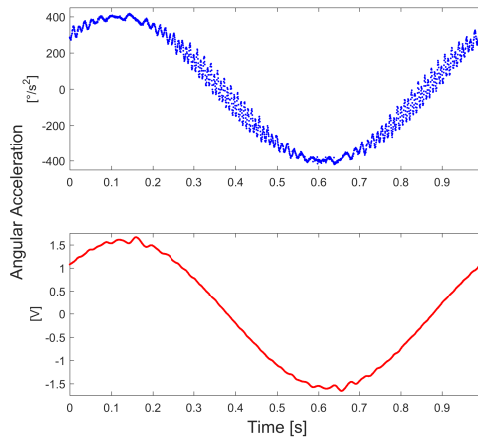


Figure 4.3: Sampled table angular acceleration (blue) and angular accelerometer response (red) of a 1 Hz sine

frequency response is obtained. The magnitude of the frequency response is usually defined as the amplitude ratio of the signal or profile. With oscillations presents in the recorded input signal, this can result in impaired peak detections. In our case, not only noise is noticeable in the measured data in Figure 4.3 but also a real oscillation at the peak of the sine, as discussed in Chapter 2. For this reason, looking into the signal equivalent in the frequency domain perhaps yields a more efficient outcome.

An overview of the angular accelerometer-motion simulator test system is presented in Figure 2.12(a) of Chapter 2. The tests performed here use this open loop customised set-up which is not subject to instability problems. Accordingly, the synchronised input and output values can be directly implemented for the frequency analysis.

#### 4.2.2 FREQUENCY RESPONSE FUNCTION AND TRANSFER FUNCTION REPRESENTATION

Fundamentally, an FRF is a frequency-based measurement function which expresses the frequency domain relationship between an input and output of an LTI system. Data collected from an experiment in general are digitised in the time domain. Therefore, the data are first transformed to the frequency domain with the help of the Fast Fourier Transform (FFT) algorithm. Our notation for the frequency domain data then become  $\alpha_t(f)$ ,  $H(f)$ , and  $\alpha_{AA}(f)$ .

This subsection does not intend to closely examine on how to perform an FFT, aside from mentioning that it delivers the result in complex notation where the use of is the key to our study. Each of these complex points represent the signal in a vector form and is composed of two terms, the real part and the imaginary part. For the input signal  $\alpha_t$ , this is expressed as  $X = \text{Re}_X + j \text{Im}_X$ . These two components define the individual FFT output magnitude,  $X_m$  and phase angles as specified in:

$$X_m(f) = |\text{Re}_X + j \text{Im}_X| = \sqrt{\text{Re}_X^2 + \text{Im}_X^2} \quad (4.3)$$

Distinctive phase angles,  $X_\phi$  are computed from the ratio of the imaginary and real part of the FFT outcomes:

$$X_\phi(f) = \tan^{-1} \left( \frac{\text{Im}_X}{\text{Re}_X} \right) \quad (4.4)$$

Similarly for the output signal,  $\alpha_{AA}$  the FFT result is  $Y = \text{Re}_Y + j \text{Im}_Y$ , and its magnitude and phase follows:

$$Y_m(f) = |\text{Re}_Y + j \text{Im}_Y| = \sqrt{\text{Re}_Y^2 + \text{Im}_Y^2}, \quad (4.5)$$

and:

$$Y_\phi(f) = \tan^{-1} \left( \frac{\text{Im}_Y}{\text{Re}_Y} \right) \quad (4.6)$$

A linear spectrum estimator is recommended for a periodic signal [162]. To make use of this valuation, first, the mean should be removed in the time domain to attain bias-free data. Second, we need to prevent spectral leakage, an FFT property that distorts the measurement. Although windowing could take place to minimise leakage, our work adopts an acquisition technique which accommodates for full sine cycles in a frequency resolution explained in Sections 4.3.2–4.3.3.

The implementation which uses a specific integer of number periods gives unique spectral lines at each input frequency; therefore, the FRF is calculated by extracting these components only. Since  $X_m$  and  $Y_m$  are the double-sided spectrum, it is first scaled with the data length,  $N$  and truncated at the Nyquist ceiling of  $f_c \leq F_s/2$  with  $F_s$  is the sampling rate. The spectrum is then multiplied by a factor of 2 to get both values from the positive and negative frequency. The following equations estimate the scaled value for the input signal,  $X_s$ :

$$X_s(f) = 2 * \frac{X_m(f)}{N}, \quad (4.7)$$

and output signal,  $Y_s$ :

$$Y_s(f) = 2 * \frac{Y_m(f)}{N} \quad (4.8)$$

A Bode plot representation of the FRF can be built from the magnitude (gain) and phase angle of each test frequency,  $f_t$ . The FRF magnitude for each measurement point is calculated in dB as:

$$|G(f_t)| = 20 * \log_{10} \frac{Y_s(f_t)}{X_s(f_t)}, \quad (4.9)$$

whereas the phase is evaluated as follows:

$$\angle G(f_t) = \Phi(f_t) = Y_\phi(f_t) - X_\phi(f_t) \quad (4.10)$$

The transfer function is a conventional method for formulating a mathematical description of a system. It is a convenient representation of an LTI dynamical system's steady-state output to its input, in the complex Z-transform domain for this case. The transfer function model estimation can be applied to both time and frequency domain data. Figure 4.4 shows the system of interest, where the input is in [ $^\circ/s^2$ ] and the output in [volt].

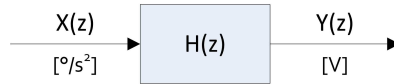


Figure 4.4: Angular accelerometer identification system block diagram.

The transfer function estimation is conducted by selecting a piece of the measurement data to be used in the estimation and the rest as the validation data. The first measure of the model quality is the normalised Akaike Information Criterion (AIC), defined as:

$$\text{nAIC} = \log \left( \det \left( \frac{1}{N_{\text{VAL}}} \sum_{k=1}^{N_{\text{VAL}}} \epsilon(k) \epsilon(k)^T \right) \right) + \frac{2n_p}{N_{\text{VAL}}}, \quad (4.11)$$

where  $N_{\text{VAL}}$  is the number of data in validation set,  $k$  is the data index, and  $n_p$  is the number of free parameters in the model.  $\epsilon(k)$  is the prediction errors or residual, whose norm is minimised for estimation and assumed to be zero-mean white noise:

$$\epsilon(k) = \|y(k) - y_{\text{tf}}(k)\|$$

with  $y(k)$  the measured data and  $y_{\text{tf}}(k)$  the simulated or predicted response of the transfer function model. As a second criterion, the Normalised Root Mean Squared Error (NRMSE) is expressed as a percentage, which is prescribed as:

$$\text{Fit} = 100 \left( 1 - \frac{\|y(k) - y_{\text{tf}}(k)\|}{\|y(k) - \bar{y}(k)\|} \right), \quad (4.12)$$

where  $\bar{y}(k)$  is the measured data mean. The last criterion to evaluate the best possible compromise between model accuracy and complexity is Akaike's Final Prediction Error (FPE):

$$\text{FPE} = \det \left( \frac{1}{N} \sum_{k=1}^{N_{\text{VAL}}} \epsilon(k) \epsilon(k)^T \right) \left( \frac{1 + \frac{n_p}{N}}{1 - \frac{n_p}{N}} \right) \quad (4.13)$$

with  $N$  the number of data points.

### 4.3 TEST ENVELOPE AND METHOD

TYPICALLY, the input in the frequency response method to characterise the dynamic frequency response of a Device Under Test (DUT) is a continuous swept-sine or broadband input [163, 164]. This type of excitation, is also known as the continuous sweep, where the sine frequency is modulated in one run. It reduces a considerable amount of measurement time but also causes a loss of accuracy when provisions are not taken care of.

When devising an optimised input in an experiment, it is necessary to consider the systems involved and the model identification approach. In this case, where the frequency domain is the focal point, we establish the preferred method to acquire a robust and explicit component in each frequency point. Besides minimising leakage, the goal is to have a closer look at the lower frequency data. Therefore, the stepped swept-sine measurement is utilised, and its measurement specification is detailed in this section.

### 4.3.1 TEST ENVELOPE SPECIFICATION

Choosing test points for the frequency response measurement should take into account the limitations of all the subsystems involved. Adhering to these constraints is for the operational safety reason of the motion simulator. The second reason is to concentrate on the corresponding angular accelerometer operational envelope concerning its application in the future aircraft flight control systems. The test envelope boundaries are defined both by the motion simulator and angular accelerometer specifications<sup>3</sup> and are illustrated in Figure 4.5.

#### MOTION SIMULATOR FACTORY SETTING AS THE MAXIMUM MOTION LIMITS

The motion limitations in this experiment are determined based on the motion simulator performance envelope of the inner-axis and sinusoidal motion input. The factory setting is employed to establish the maximum restriction. It gives an angular acceleration limit of  $1000^\circ/\text{s}^2$  represented by the sloped red line in Figure 4.5, and an angular rate limit of  $1200^\circ/\text{s}$  depicted in the horizontal red line. The minimum motion restriction is specified solely by the sensor characteristics described in the next part.

#### ANGULAR ACCELEROMETER OPERATIONAL RANGE AS THE MINIMUM CEILING AND INPUT

The angular accelerometer specification is used for completing the test envelope boundary. The angular accelerometer has a customized range of  $10\text{ rad}/\text{s}^2$  or approximately  $572.958^\circ/\text{s}^2$ . For the purpose of the test, the maximum angular acceleration limit is set to 80% of the angular accelerometer range at the most, which is  $458.366^\circ/\text{s}^2$ , or simplified to  $450^\circ/\text{s}^2$ .

Then, the test envelope should include the minimum level that can be measured by the angular accelerometer. Since the sensor lowest range is not specified in the datasheet, the noise level is used instead. The angular accelerometer output noise level should be  $\leq 3\text{ mV}$ ; therefore, the value of  $3\text{ mV}$  will serve as the minimum threshold of the input. To include the minimum threshold into the test envelope presented in Figure 4.5, the noise level should be converted from [V]. Using the factory scale factor of  $0.23\text{ V}/\text{rad}/\text{s}^2$ , results in a  $0.013\text{ rad}/\text{s}^2$  or  $0.747^\circ/\text{s}^2$  angular acceleration. To simplify, the level is rounded up to  $0.8^\circ/\text{s}^2$ .

#### MOTION SIMULATOR AND ANGULAR ACCELEROMETER SPECIFICATIONS TO DETERMINE THE BANDWIDTH

Another critical motion simulator limit is the bandwidth, a frequency range where the measurement test points are established. The specific motion simulator bandwidth can reach up to  $30\text{ Hz}$  for the inner-axis. Nevertheless, in practice, the actual terminal frequency,  $f_{\text{terminal}}$ , for the sinusoidal profile is highly dependent on the motion simulator angular acceleration limit,  $\alpha_{MS}$  and excitation amplitude,  $A$ , as expressed in:

$$f_{\text{terminal}} < \sqrt{\frac{\alpha_{MS}}{A}} \quad [\text{rad}] \quad (4.14)$$

$A$  is input related and therefore, it is determined by the motion simulator bandwidth.

<sup>3</sup>The motion simulator and angular accelerometer specifications are presented in Appendix A.

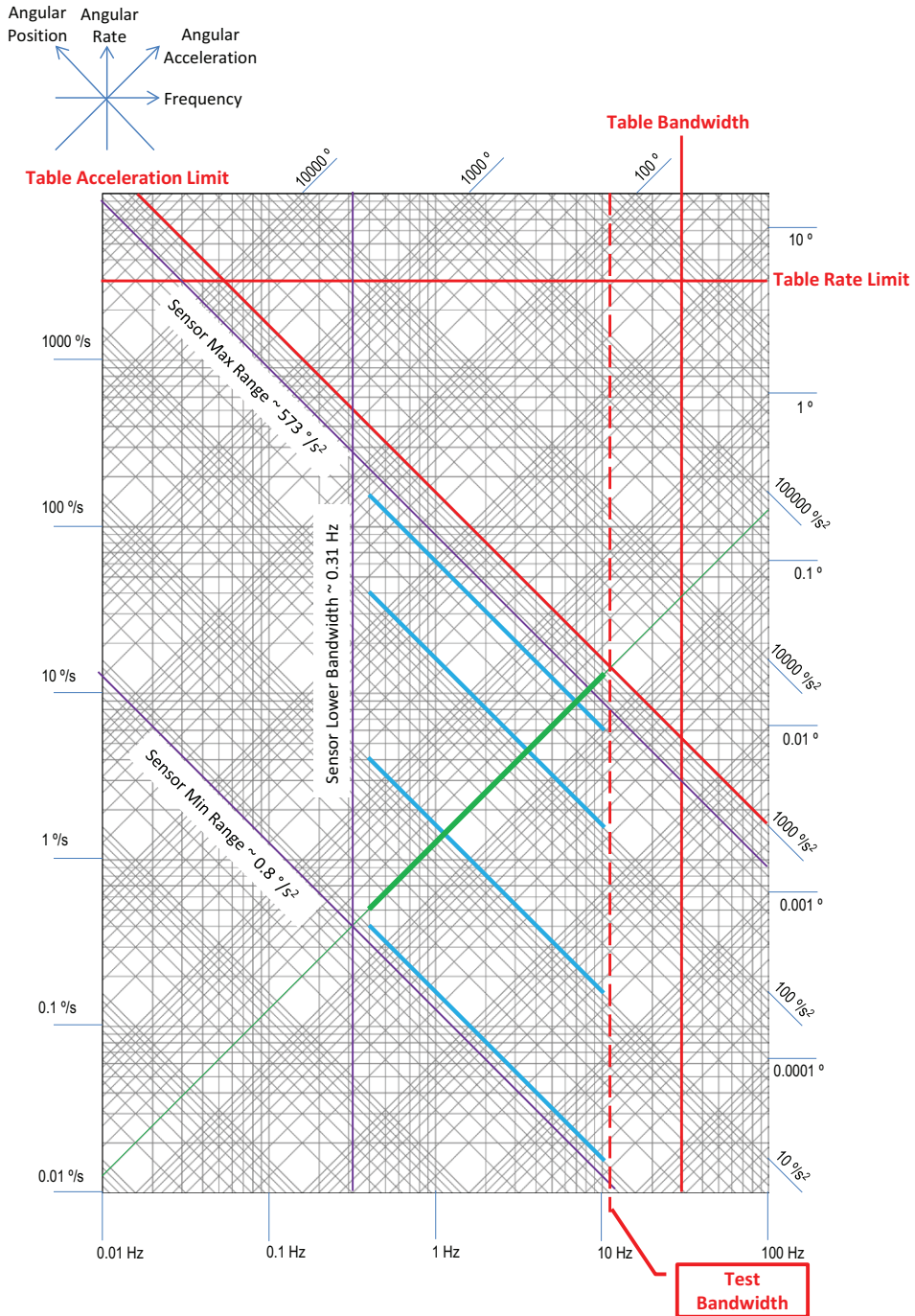


Figure 4.5: Frequency response test envelope for the test axis. Test points of the constant position measurement are represented with the green line; blue lines show the constant acceleration test point groups.

To effectively capture the test information, the DUT minimum is used to define the starting measurement bandwidth. Referring to [Figure 4.5](#), the angular accelerometer minimum range and lower bandwidth intersection cross the amplitude of approximately  $0.2^\circ$ . This amplitude is then regarded as the optimum value that covers the possible frequency range up to the angular acceleration limit. With the motion simulator inner-axis angular acceleration limit of  $1000^\circ/\text{s}^2$ ,  $f_{\text{terminal}} = 70.711$  rad.

Converting to Hz, the terminal frequency should be less than 11.254 Hz. This value applies to the systems without payload. In this case, the terminal frequency is consequently reduced to 10 Hz, considering the additional weight of the new SDAS arrangement on top of the mounting plate. The minimum input line crosses the  $0.2^\circ$  amplitude line at approximately 0.33 Hz, as shown in [Figure 4.5](#). The minimum frequency threshold is therefore set at 0.4 Hz.

### 4.3.2 TEST METHOD

The tests comprise measurements under steady-state conditions which are simpler to analyse than to measurements of transient responses. The initial conditions are such that there is no transient response, or the transient response can be assumed to have decayed to zero. This condition is achieved by initially running the turntable for some time under a particular input sequence, and then starting the recording.

The experiment consists of two groups of tests: constant-position and constant-acceleration across frequencies. The constant-position test is bounded by a constant-amplitude sinusoidal input of the angular position, but varying in frequency and angular acceleration. This group of measurements is conducted at the  $0.2^\circ$  amplitude to accommodate the entire frequency range. The constant-acceleration test on the other hand, has four sub-groups that represent different accelerations at  $1^\circ/\text{s}^2$ ,  $10^\circ/\text{s}^2$ ,  $100^\circ/\text{s}^2$  and  $400^\circ/\text{s}^2$ . Each of the four angular acceleration levels is varied in frequency and amplitude of the sinusoidal input. The green line represents the constant-position test points in [Figure 4.5](#), whereas blue lines are representing constant-acceleration tests.

The measurements to examine the system dynamics are spread within the test bandwidth. The starting point is the minimum frequency threshold at 0.4 Hz. Subsequent test points are in the increment of 20% from the previous value, up to 10 Hz. Additionally, round frequencies point of 1, 2, 3, 4, 5, 6, 7, 8 and 9 Hz are included, which then gives a total of 28 frequency points.

In addition to the five variables in [Section 2.4.2](#) required for synchronisation procedure, the following list provides all the variables of interest recorded in the experiment:

- $\theta$ , motion simulator measured angular position, [°].
- $\theta_{\text{est}}$ , motion simulator estimated angular position, [°].
- $\omega_{\text{est}}$ , motion simulator estimated angular rate, [°/s].
- $\alpha_{\text{t}}$ , motion simulator estimated angular acceleration, [°/s<sup>2</sup>].
- $\alpha_{\text{AA}}$ , angular accelerometer measured angular acceleration, [V].

The recommended measurement time duration,  $\tau$  is at least 100s. Meanwhile, the number of data points,  $N$  needed for the FFT calculation is the most efficient when it is a power of 2. Using the calibration table maximum sampling rate of 2 kHz, it will result in 200,000 data points for a 100s time span. Thus, the nearest power of 2 is  $2^{18}$  or 262,144. Unfortunately, the motion simulator computer could only accommodate up to 230,000

data points given the quantity of currently recorded variables. Lowering the sampling rate is not preferable in favour of data synchronisation. It was found in [Chapter 2](#) that the synchronisation has a 0.5 ms uncertainty for a lower sampling of 1 kHz. Therefore, the sampling rate,  $F_s$  should be 2 kHz by default. A lower, nearest power of two number,  $2^{17}$  or 131.072 data points was therefore chosen instead. The measurement time itself was then adjusted to become  $\tau = 65.536$  s.

### 4.3.3 TEST MATRIX DEVELOPMENT

In [Section 4.3.2](#), the test frequency points are defined as the 20% increment of the previous value, starting from 0.4 Hz up to 10 Hz, and including the round frequency points. Furthermore, data size and measurement time were also prescribed to form a good base for the FFT calculation. However, when the sinusoid does not fit an integer number of times in the measurement period, leakage will occur. Eliminating leakage entails the chosen frequency points to be modified as such that each accommodates full cycles of a sinusoid within the time required to obtain  $N$  data points.

Consequently, the frequency points need to be specified with a proper approach to ensure the validity of the data. The adjusted sinusoid frequency,  $f_{\text{mod}}$  is shown in the last column of [Table 4.1](#), whereas the second column presents the original frequencies. Their association,  $c$  is asserted in the third column, which modifies the frequency to be as close as possible to the original but still contains an integer number of cycles.

To achieve the expected adjustment, first the frequency resolution,  $\text{Res}_f$  is calculated as:

$$\text{Res}_f = \frac{F_s}{N} = \frac{2,000}{131,072} = 0.01526 \text{ Hz} \quad (4.15)$$

The modified frequency can then be determined from:

$$f_{\text{mod}} = c \times \text{Res}_f, \quad (4.16)$$

with  $c$  an integer number.

When used for the constant position measurement, the modified frequency points in [Table 4.1](#) will follow the green line in [Figure 4.5](#). In this measurement type, the sine input has a constant amplitude and is varied in frequency. This way, the angular acceleration increases quadratically with frequency. Also, several measurement points are exceeding the angular accelerometer maximum range at the higher frequency, which leads to clipping of the signal. Therefore, it is better to use a constant acceleration test where the measurement can be maintained within the envelope's range.

For the constant acceleration frequency response test, the blue lines in [Figure 4.5](#) illustrate the specific location. Here, the measurements are performed with fixed accelerations magnitude throughout the frequency extent. As a consequence, the input should be specified by different sine amplitudes for each angular acceleration,  $\alpha$ , in combination with frequency as presented in the test matrix in [Table 4.2](#). Refer to [Equation \(4.1\)](#), the following equation calculates the sinusoidal input amplitude,  $A_s$ :

$$A_s = \frac{\alpha}{\omega^2} = \frac{\alpha}{2\pi f_{\text{mod}}}, \quad (4.17)$$

with  $f_{\text{mod}}$  the modified frequency point obtained from [Equation \(4.16\)](#).

Table 4.1: Modified test frequency.

Test Point (#)	Original Frequency Hz	$c$ cycles	Modified Frequency Hz
1	0.4	26	0.396728516
2	0.48	31	0.473022461
3	0.576	38	0.579833984
4	0.6912	45	0.686645508
5	0.82944	54	0.823974609
6	0.995328	65	0.991821289
7	1	66	1.007080078
8	1.1943936	78	1.190185547
9	1.43327232	94	1.434326172
10	1.719926784	112	1.708984375
11	2	131	1.998901367
12	2.063912141	135	2.059936523
13	2.476694569	163	2.487182617
14	2.972033483	195	2.975463867
15	3	197	3.005981445
16	3.566440179	234	3.570556641
17	4	262	3.997802734
18	4.279728215	280	4.272460938
19	5	328	5.004882813
20	5.135673858	337	5.142211914
21	6	393	5.996704102
22	6.16280863	404	6.164550781
23	7	459	7.003784180
24	7.395370356	485	7.400512695
25	8	524	7.995605469
26	8.874444427	582	8.880615234
27	9	590	9.002685547
28	10	655	9.994506836

Table 4.2: Constant acceleration sinusoidal input amplitude in [°] for each angular acceleration (within the blue lines in Figure 4.5).

Test Point	Modified Frequency Hz	Sinusoidal Input Amplitude, °			
		$\alpha = 400^\circ/s^2$	$\alpha = 100^\circ/s^2$	$\alpha = 10^\circ/s^2$	$\alpha = 1^\circ/s^2$
1	0.396728516	64.374433330	16.093608333	1.609360833	0.160936083
2	0.473022461	45.283160252	11.320790063	1.132079006	0.113207901
3	0.579833984	30.136507666	7.534126917	0.753412692	0.075341269
4	0.686645508	21.489934316	5.372483579	0.537248358	0.053724836
5	0.823974609	14.923565519	3.730891380	0.373089138	0.037308914
6	0.991821289	10.299909354	2.574977338	0.257497734	0.025749773
7	1.007080078	9.990155423	2.497538856	0.249753886	0.024975389
8	1.190185547	7.152714827	1.788178707	0.178817871	0.017881787
9	1.434326172	4.924979290	1.231244822	0.123124482	0.012312448
10	1.708984375	3.469157925	0.867289481	0.086728948	0.008672895
11	1.998901367	2.535814756	0.633953689	0.063395369	0.006339537
12	2.059936523	2.387770482	0.596942620	0.059694262	0.005969426
13	2.487182617	1.637890663	0.409472666	0.040947267	0.004094727
14	2.975463867	1.144434373	0.286108593	0.028610859	0.002861086
15	3.005981445	1.121315082	0.280328771	0.028032877	0.002803288
16	3.570556641	0.794746092	0.198686523	0.019868652	0.001986865
17	3.997802734	0.633953689	0.158488422	0.015848842	0.001584884
18	4.272460938	0.555065268	0.138766317	0.013876632	0.001387663
19	5.004882813	0.404494321	0.101123580	0.010112358	0.001011236
20	5.142211914	0.383177778	0.095794444	0.009579444	0.000957944
21	5.996704102	0.281757195	0.070439299	0.007043930	0.000704393
22	6.164550781	0.266622862	0.066655715	0.006665572	0.000666557
23	7.003784180	0.206554540	0.051638635	0.005163863	0.000516386
24	7.400512695	0.185002092	0.046250523	0.004625052	0.000462505
25	7.995605469	0.158488422	0.039622106	0.003962211	0.000396221
26	8.880615234	0.128473675	0.032118419	0.003211842	0.000321184
27	9.002685547	0.125013263	0.031253316	0.003125332	0.000312533
28	9.994506836	0.101432590	0.025358148	0.002535815	0.000253581

## 4.4 FREQUENCY RESPONSE MEASUREMENT ANALYSIS

THIS section examines the synchronised frequency response measurement data to inspect the sensor response sensitivity, signal-to-noise ratio (SNR) and harmonics ratio (HR), and finally the FRE.

### 4.4.1 ANGULAR ACCELEROMETER VOLTAGE RESPONSE

The means,  $\mu$ , of each data set obtained from each angular acceleration input throughout the frequency range are plotted in Figure 4.7. Large deviations are observed for the high angular acceleration at low frequencies. Nevertheless, nearly all means remain within the sensor's specified  $(2.495 \pm 0.001)$  V boundary. On average, the values lie at 2.49 V or with a 0.005 V discrepancy from the norm.

Figure 4.8 presents the response amplitude across frequency, for all angular acceleration input. The amplitudes here represent the maximum reaction of the angular accelerometer for every excitation input. Low angular acceleration input seems to produce a constant sine amplitude in different frequencies. As the angular acceleration level gets higher, fluctuations are evident especially at lower frequencies.

Inspecting for linearity, we are taking the average sine amplitudes of the measurement set in varying frequencies. A plot of the angular acceleration input and the voltage output association is shown in Figure 4.9. The graph demonstrates a steady, apparently very linear relationship between the input and output signals.

### 4.4.2 SIGNAL-TO-NOISE AND HARMONICS RATIO

Due to the specific problem in this study, the frequency-domain representation of the signal is first examined. The characteristic is expressed in SNR *power* ratio, which is defined as:

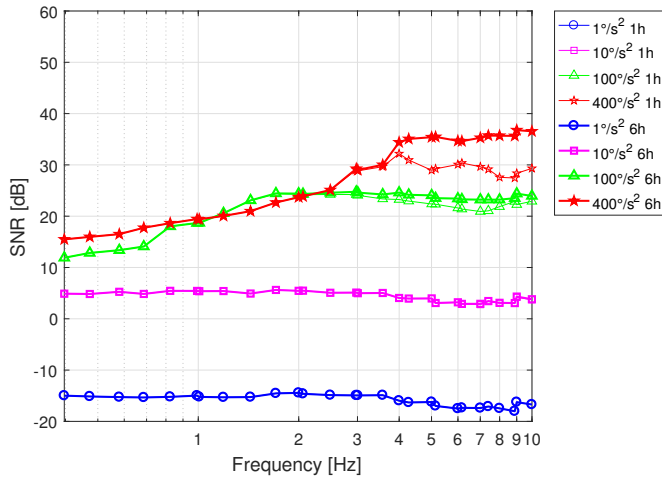
$$\text{SNR} = \frac{\bar{s}^2}{\bar{n}^2}, \quad (4.18)$$

where  $\bar{s}^2$  is the signal power based on the fundamental frequency component, and  $\bar{n}^2$  is the noise power calculated from the level of non harmonics elements. The SNR is commonly expressed in dB, thus:

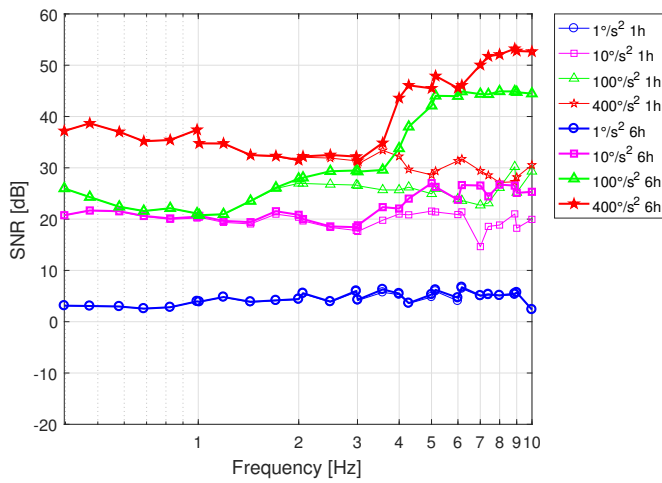
$$\text{SNR}|_{\text{dB}} = 10 \log_{10} \frac{\bar{s}^2}{\bar{n}^2} \quad (4.19)$$

The signal power is usually characterised from the first six harmonics of the signal, whereas the noise power is the level of the background noise. A comparison that takes into account the SNR of these first six harmonics, (6h) and only the fundamental frequency or the first harmonic, (1h) is presented in Figure 4.6(a) for the motion simulator signal, whereas Figure 4.6(b) shows the SNR of the angular accelerometer. The figures show the angular accelerometer and motion simulator SNR from the angular acceleration at a constant amplitude measurement, for each angular acceleration input.

Figure 4.6 gives four insights. First, the motion simulator SNR at  $1^\circ/\text{s}^2$  shows considerably more noise than useful signal, shown by a power ratio of around  $-15$  dB. Second, the SNR level for each angular acceleration input is higher in the angular accelerometer as compared to the motion simulator, suggesting that noise is much lower in the angular accelerometer's signal. Third, the SNRs tend to increase with frequency at the two



(a) Motion simulator.



(b) Angular accelerometer.

Figure 4.6: Motion simulator and angular accelerometer SNR of the constant acceleration measurement.

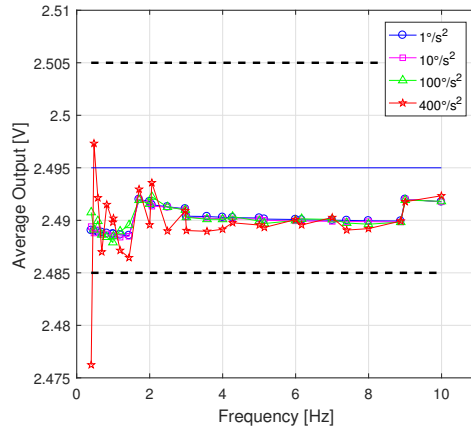


Figure 4.7: Angular accelerometer average voltage output across frequency for each angular acceleration input.

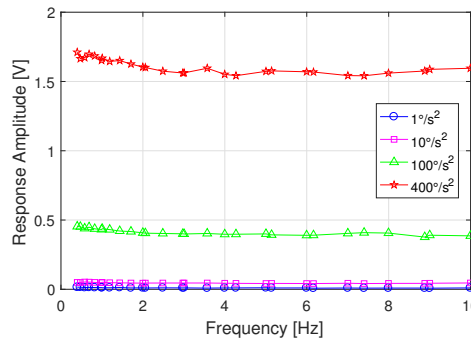


Figure 4.8: Angular accelerometer response amplitude across frequency for each angular acceleration input.

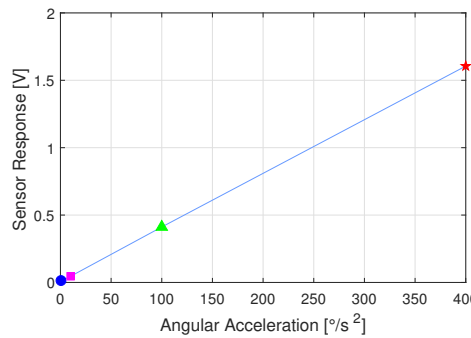


Figure 4.9: Angular accelerometer average response amplitude for each angular acceleration input.

highest angular acceleration input levels; nevertheless, this is only visible in the angular accelerometer for 6h set. The discrepancy demonstrates that the next five harmonics after the fundamental frequency in the angular accelerometer data contribute substantially

at high frequency. Fourth, distortions are observed between 1h and 6h sets at higher frequencies. The distortions are greater apparent in the angular accelerometer data, except for the  $1^\circ/\text{s}^2$  angular acceleration input where no shift is visible. Whereas in the motion simulator case, the two lowest angular acceleration inputs of  $1^\circ/\text{s}^2$  and  $10^\circ/\text{s}^2$  show no SNR distortion between the six harmonics and the fundamental harmonic calculation.

To better inspect the effects of high amplitude frequency components that are included in measurements or generations of a given signal frequency on the instrument, the following equation defines the total harmonics distortion, THD:

$$\text{THD} = \frac{\sqrt{\sum_{k=2}^6 A_H^2(k)}}{A_H(k)|_{k=1}}, \quad (4.20)$$

with  $A_H$  the harmonic amplitudes and  $k$  the index.

Taking the ratio of the sum of the powers of the first five harmonics to the power of the fundamental frequency gives [Figure 4.10\(b\)](#) and [Figure 4.10\(a\)](#). Both figures show that the additional harmonics are increasing with frequency and acceleration. In each angular acceleration input, the effect of the next five harmonics is higher, starting at around 4 Hz. The angular accelerometer responses show a similar trend, with approximate triples in comparison with the motion simulator. This THD implies that the sinusoid motion input is not entirely linear at higher frequencies. Furthermore, the sensor dynamics amplify the nonlinearities, which makes it present with a noticeably higher level in the angular accelerometer measurement.

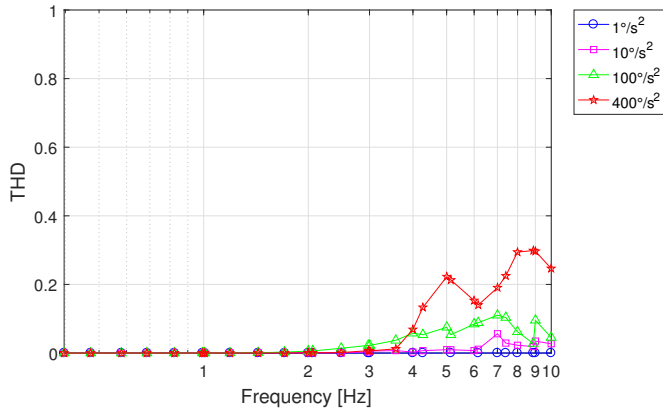
#### 4.4.3 FREQUENCY RESPONSE FUNCTION

The FRF magnitude is equal to the gain in [Equation \(4.9\)](#) and the phase relates to [Equation \(4.10\)](#). As explained in [Section 4.2.2](#), the FRF magnitude is calculated from the spectral component at the input frequency only. The FRF result shows all angular acceleration measurement sets with the measurement bandwidth of 10 Hz. The table angular acceleration is the input reference in  $[\circ/\text{s}^2]$ , while the output is the angular accelerometer response in [V].

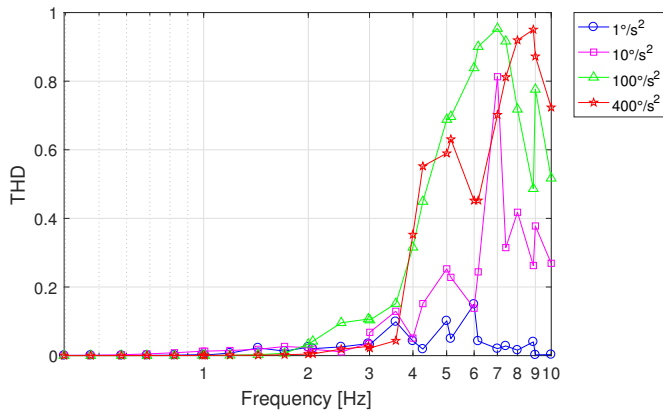
The numerical value of the input is considerably larger than the output due to the separate unit of measurement. This result in the FRF magnitude level around  $-48$  dB in [Figure 4.11](#), or attenuated output. The trend appears flat at lower frequencies for all angular accelerations, where the two highest accelerations maintain the ratio up to 4 Hz and only decline approximately 0.2 dB and 0.4 dB at the highest measured frequencies. The two lowest accelerations start to decrease at around 2 Hz, with final values of 0.5 dB and 1 dB lower than at the initial frequencies. Nevertheless, we have not yet seen a  $-3$  dB decline within the test frequency range.

The phase response of the system is given in [Figure 4.12](#). All responses are decreasing exponentially and show a substantial phase delay at high frequencies. The figure demonstrates that the phase responses are very similar, indicating that they are not influenced by different accelerations, but are only frequency-dependent.

For every frequency component, the phase response  $\phi(f_{\text{mod}})$ , gives the phase delay,



(a) Motion simulator.



(b) Angular accelerometer.

Figure 4.10: Motion simulator and angular accelerometer THD of the constant acceleration amplitude frequency response measurement.

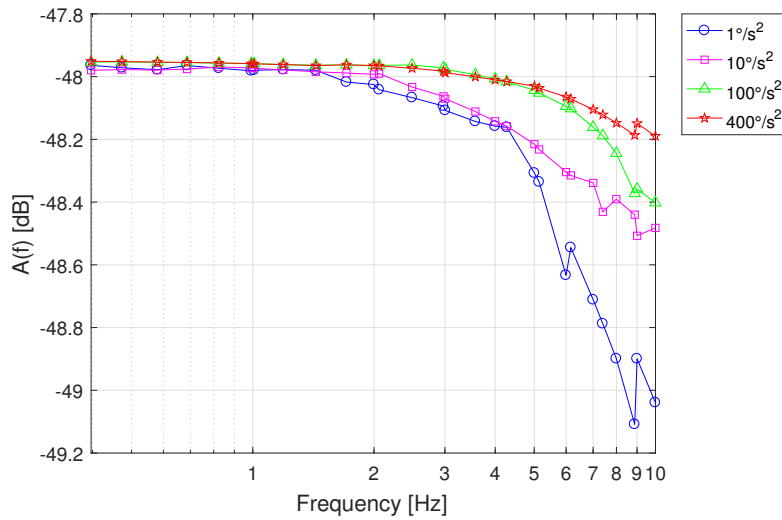


Figure 4.11: FRF Magnitude of the frequency response measurement, constant angular acceleration input series.

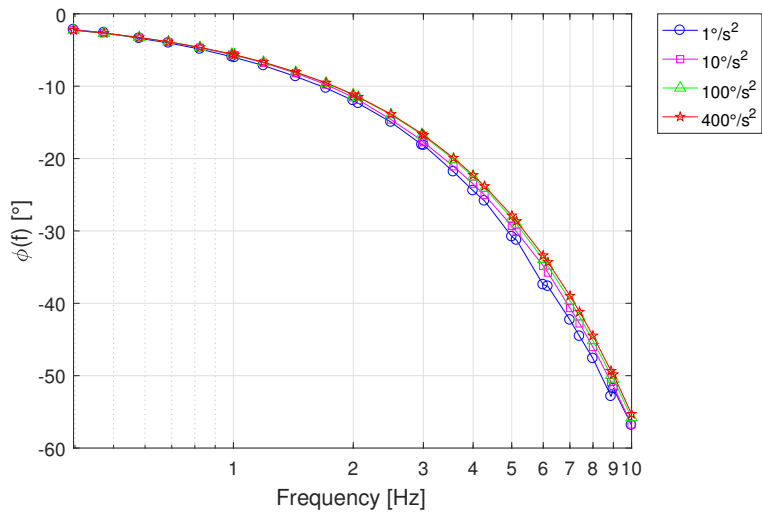


Figure 4.12: FRF phase of the frequency response measurement, constant angular acceleration input series.

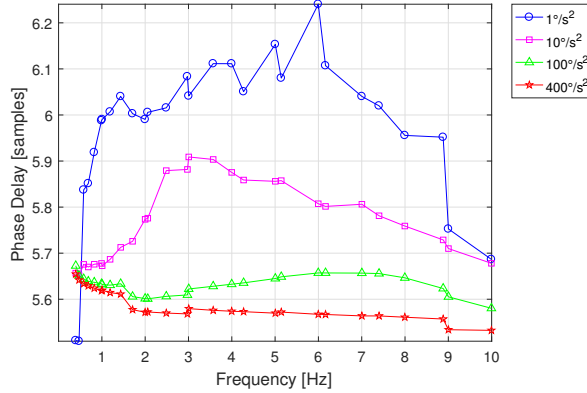


Figure 4.13: Phase delay of the constant acceleration phase response

$P(f_{\text{mod}})$  defined as:

$$P(f_{\text{mod}}) \cong -\frac{\phi(f_{\text{mod}})}{f_{\text{mod}}} \quad (4.21)$$

Figure 4.13 presents the phase delay  $P(f_{\text{mod}})$  for constant acceleration measurement, which in this case gives the time delay in samples experienced by each sinusoidal component of the input signal. At high accelerations of  $100^\circ/\text{s}^2$  and  $400^\circ/\text{s}^2$ , the phase delay resembles a transport delay, where it has the same time delay for all frequencies or phase shift that is linear with frequency. However, the low angular acceleration of  $10^\circ/\text{s}^2$  and especially  $1^\circ/\text{s}^2$  have more significant variations. This result indicates that there is probably an influence from non-linear system dynamics at very low angular accelerations.

4

## 4.5 ANGULAR ACCELEROMETER MODEL ESTIMATION USING TIME-DOMAIN DATA

CONSIDER a linear system with the rational transfer function, which can be represented by a ratio of polynomials:

$$G(z) = \frac{b(z)}{a(z)} \quad (4.22)$$

The denominator  $a(z) = \sum_{i=0}^n a_i z^n$  is the system characteristic polynomial, where its order is equal to the model order and the roots are referred to as the model poles. The numerator  $b(z) = \sum_{i=0}^m b_i z^m$  is the system polynomial and its roots are referred to as the model zeros.

Ideally, the model should yield the similar order of input and output polynomials in the transfer function when the same variables are used to build the frequency response

Table 4.3: Time-domain data model validation quality criteria, no delay.

Model	Fit[%]	nAIC	FPE
TF <sub>54</sub>	98.59	-8.5663	$1.9042 \times 10^{-4}$
TF <sub>51</sub>	98.39	-8.0956	$3.0489 \times 10^{-4}$
TF <sub>41</sub>	98.37	-8.3389	$2.3904 \times 10^{-4}$
TF <sub>40</sub>	98.36	-8.3061	$2.4700 \times 10^{-4}$
TF <sub>00</sub>	78.56	-1.0971	0.3338

representation. In this case, however, we use different units of the variables namely, angular acceleration from the motion simulator as the input and voltage response of the angular accelerometer as the output. Thus, the resulted gain does not yield a 0 dB magnitude as shown in Figure 4.11. The model orders or the number of poles,  $n$  are varied from 0 to 5, so it is with the zeros,  $m$ , to better approximate the input and output data. When estimating a proper transfer function from discrete data, i.e., measurement data, the number of zeros should be equal or less than the number of poles,  $m \leq n$ . The first iteration then results in 21 initial models labelled as TF<sub>ab</sub>, where the subscripts represent the model poles and zeros combination.

For illustration purposes, the evaluation is performed to the time domain data set of  $400^\circ/\text{s}^2$  angular acceleration input. The round frequencies data sets at 7, 11, 15, 17, 19, 21, 23, 25, 27 Hz are used as the estimation data and the sets at 1, 2, 3, 4, 5, 6, 8, 9, 10, 12, 13, 14, 16, 18, 20, 22, 24, 26, 28 Hz are used as the validation data. The estimation was performed using transfer function estimation algorithm, tfest in Matlab<sup>®</sup> with an Autoregressive eXogenous (ARX) method initialisation.

Based on the quality criteria, a 5<sup>th</sup> order system, TF<sub>54</sub> produce the best fit, nAIC and as well as the lowest predicted error. Its pole-zero plot, however, reveals that positive-valued zeros are present. A discrete-time model represents a stable system if the poles are inside the unit circle of the pole-zero plot, whereas the zeros can be inside or outside of the unit circle [115]. Nevertheless, the presence of zeros in the right-half plane causes the system to exhibit non-minimum phase behaviour, which is not desirable from the perspective of the control system design since it could result in a slow response at the start of the stimulated input.

Table 4.3 shows the best three models without zeros at the right half plane, with TF<sub>54</sub> and the 0<sup>th</sup> order included as a comparison. The Fit[%], nAIC and FPE are the quality measure of the residual  $\epsilon$ , detailed in Section 4.2.2. Overall, the performance of this selection is considerably close and demonstrates a substantial improvement from the 0<sup>th</sup> order transfer function. TF<sub>51</sub> is the best model without zeros on the right half plane; it is ranked the 5<sup>th</sup> out of the 21 models.

Non-minimum phase could be arising due to time delay in the system. Therefore, this section also discusses an additional case that applies another possible parameter of a transfer function model: a transport delays. The delay calculated using finddelay function from the time domain, input-output data varies from 24 to 31 with the frequency. The average of 28 samples is chosen to estimate the model. The rational transfer function in

Table 4.4: Time-domain data model validation quality criteria, delay 28 samples.

Model	Fit[%]	nAIC	FPE
TF <sub>43-d28</sub>	95.32	-6.8178	0.0011
TF <sub>20-d28</sub>	93.07	-6.5770	0.0014
TF <sub>30-d28</sub>	92.93	-6.6167	0.0013
TF <sub>10-d28</sub>	92.83	-6.5205	0.0015
TF <sub>00-d28</sub>	83.26	-5.1352	0.0059

Equation (4.22) then becomes:

$$H(z) = z^{-D} \frac{b(z)}{a(z)} \quad (4.23)$$

where D is the sample delay.

The best model with a separate delay term ranked by Fit[%], TF<sub>43-d28</sub>, also contains positive zeros. The three best models without zeros on the right half plane are presented in Table 4.4, together with TF<sub>43-d28</sub> and TF<sub>00-d28</sub>. In this estimation, TF<sub>20-d28</sub> is indexed the 8<sup>th</sup> best fit. Compared to the best models without separate delay terms in Table 4.3, these alternatives exhibit a lower fit by a difference of around 5–6 %.

Comparison between the FRF from Figure 4.11, which depicted in dashed red line with a pentagram marker, and the best fit models are presented in Figure 4.14. By observing the bode plot, we can see that the phase representations are almost indistinguishable. On the other hand, it is visible that not all of the candidate models yield accurate conformance to the FRF magnitude. At this point, it can be concluded that models with separate delay terms are not necessarily the proper choice regarding the frequency response.

One could mention that the frequency response measurement did not demonstrate the full sensor dynamics. At the  $f_{\text{terminal}}$  of 10Hz, the magnitude plot has not shown the -3 dB roll off per decade which indicates the system's bandwidth. Unfortunately, the measurement of higher frequencies is not possible due to limitations in our set-up. The transfer function model, of course, could *predict* the response for broader bandwidth as shown in Figure 4.15, thus demonstrate the *theoretical* approximation of the system dynamics. The red pentagram markers highlight the area of the frequency response measurement result. TF<sub>43-d28</sub> and TF<sub>20-d28</sub> forecast wider system's bandwidths, but also anticipate significant phase delay at higher frequencies compared to TF<sub>54</sub> and TF<sub>51</sub>.

The result leads to further narrowing-down preference into a model that best describes the measurement data and can be used for the control system design objective, TF<sub>51</sub>:

$$G(z) = \frac{-4.203 \times 10^{-07} z}{z^5 - 2.763z^4 + 1.554z^3 + 1.974z^2 - 2.554z + 0.7891} \quad (4.24)$$

The corresponding continuous time transfer function can be obtained by converting the discrete transfer function in Equation (4.24), resulting in the following equation:

$$G(s) = \frac{0.0003388s^5 - 2.197s^4 + 1.692e04s^3 - 6.753e07s^2 + 1.509e11s - 1.494 \times 10^{14}}{s^6 + 473.7s^5 + 3.959e07s^4 + 1.872 \times 10^{10}s^3 + 4.464 \times 10^{12}s^2 + 6.663 \times 10^{14}s + 3.555 \times 10^{16}} \quad (4.25)$$

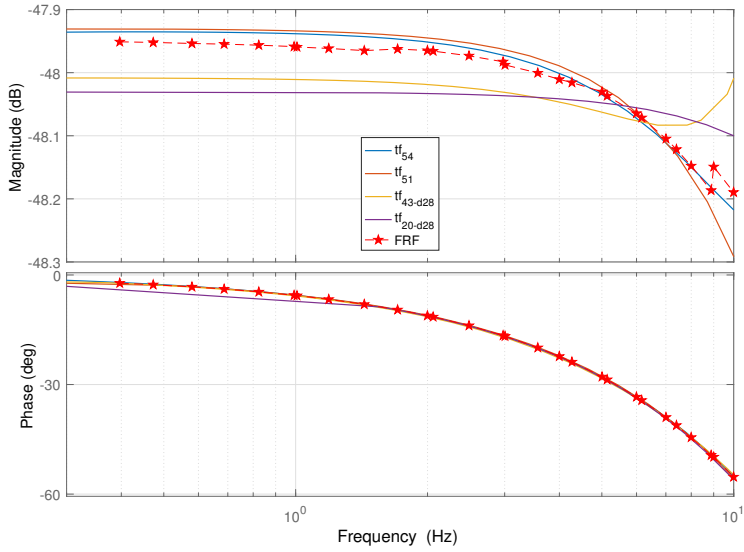


Figure 4.14: FRF and Bode plot of the four best fit transfer function models.

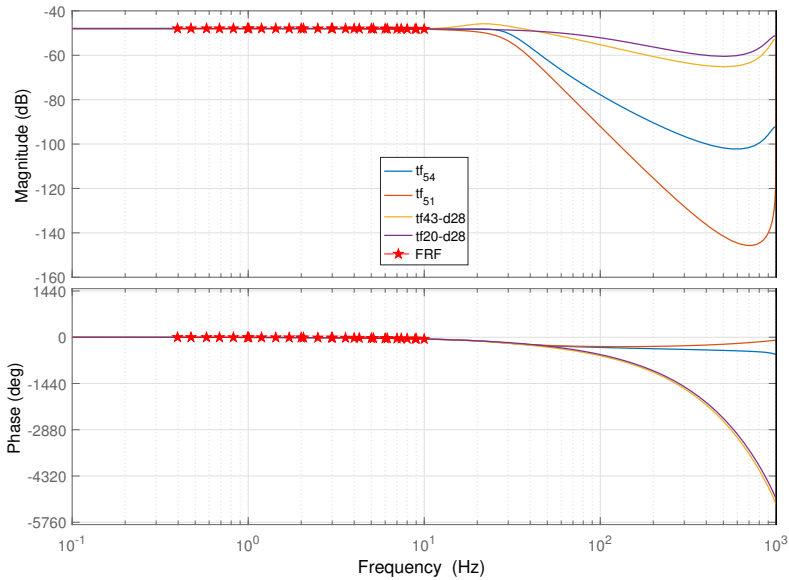


Figure 4.15: FRF and extrapolated Bode plot of the four best transfer function model. The red pentagram markers represent the test frequency range zoomed in in Figure 4.14.

Further extension of the frequency response model, but not included in this chapter, would be an estimation using the Box-Jenkins method, where the model is independently parametrised to express the noise in the measurement system apart from the system's dynamics [112]. This approach enables an equivalent selection made for the lower order candidate models, as many structures with approximately close AIC values exist at the lowest value spectrum. The choice would be beneficial, for example, in the implementation of sensor model for control systems design.

## 4.6 CONCLUSION

Angular accelerometer responses induced by a motion simulator input were measured with the goal of obtaining the frequency response of the system for the FRF and transfer function model estimation. With the analysis conducted in the frequency-domain, the test points were specified as such to reduce variance and prevent leakage around the fundamental frequency in the spectral estimate. The boundary condition of the examination was determined based on the angular accelerometer specification, and motion simulator limitations resulted in a test envelope of the experimental set-up and a test matrix for the selected frequency points.

Even though the input [ $^{\circ}/s^2$ ] and output [V] amplitudes exhibit a stable, linear relation, the THD shows that nonlinearities are present at frequencies above 4 Hz. The FRF of the system, for every acceleration value, is obtained based on the spectral component output-input ratio at the fundamental frequency. For the specified bandwidth and acceleration, the transfer function estimation is employed to approximate the relation of motion simulator angular acceleration as the input and angular accelerometer data as the output. Estimated transfer function models were generated using the time-domain form of the data and validated by the FRF

Best models selection is based on the Fit percentage and Pole-Zero map of the systems. From the *theoretical* Bode plot responses, proposed models with a separate delay term show higher systems bandwidth and considerable phase lags at higher frequencies. In the end, a fifth-order transfer function model without a separate delay term,  $TF_{51}$ , was chosen as the appropriate representation of the system. This model gives an excellent approximation of the measurement result within 0.009–0.7% accuracy. The models developed in this chapter are expected to facilitate the development of the novel fault-tolerant, flight control system, by providing an accurate model of the angular acceleration feedback information.

# 5

## MEASUREMENT UNIT MISALIGNMENT

*Do not go where the path may lead, go instead where there is no path and leave a trail.*

Ralph Waldo Emerson

*Previous chapters discussed calibration measurement utilising the motion simulator, scale factor calibration and a frequency response model of a single angular accelerometer. However, a crucial aspect in the characterisation of an inertial sensor, the quality of its sensitive axis alignment, has not yet been explored. An Angular Accelerometer Measurement Unit in this study is constructed from three single-axis angular acceleration sensors, established on a 3-axis oriented mounting block. Thus, investigating the cross-axis sensitivity and input axis misalignment characteristics is critical when considering the unit's role as a basis for an inertial reference system, or for providing inputs to a flight control system. Standard multi-position and rotation tests employed for a conventional Inertial Measurement Unit that consists of gyroscopes and linear accelerometers are not applicable to angular accelerometers; oscillatory inputs are more appropriate for this type of sensor instead. This chapter uses spectral component analysis to inspect both cross-axis sensitivity and input axis misalignment aspects. The examination covers the procedure to acquire the specified excitation, and the frequency domain data approach which enables the isolation of the associated input motion without the involvement of high frequency noise. The measurement and estimation process discussed in this paper yields the alignment data for each angular accelerometer in the measurement unit axis. Also, effects of block mounting, de-installation and re-mounting of the sensors are investigated.*

---

This chapter is based on the following publication:

Jatiningrum, D., de Visser, C. C., van Paassen, M. M., and Mulder, M. "Investigating Misalignment in a 3-Axis Angular Accelerometer Measurement Unit", *AIAA Guidance, Navigation and Control Conference*, 2017 [165].

## 5.1 INTRODUCTION

**A**N Angular Accelerometer Measurement Unit (AAMU) can provide the required angular acceleration feedback in a state-of-the-art fault-tolerant flight control system. It features three angular accelerometers installed on a mounting block, orthogonal to each other, thus measuring angular acceleration in three perpendicular axes. Since angular accelerometers directly sense angular acceleration, it will simplify the implementation of the recently developed sensor-based flight control system approaches [11, 12]. Nevertheless, an AAMU is not a standard part of the present day aircraft Inertial Measurement Unit (IMU), and calibration procedures for AAMUs are not yet well defined.

In current aerospace technology, an IMU produces the necessary data both for the Inertial Navigation System (INS) and flight control system. It typically consists of three gyroscopes and three linear accelerometers. As accurate inertial sensor alignment is crucial, in any case, to achieve aid-independent navigation fidelity over an extended period [75], misalignment compensation requires an adequate amount of attention. Hence, various studies explore different approaches to manage the effects of sensor misalignment, whether onboard or for laboratory/ on-ground misalignment calibration.

Misalignment, or non-orthogonality, could exist within and between the sensors. It describes the angular difference between each sensor's axis of rotation and the system defined *inertial reference frame*. Ideally, each of the sensor's sensitive axes is mutually orthogonal to the other axes to ensure optimal measurement. Nonetheless, manufacturing imperfection and packaging inaccuracies are known to inflict slight shifts in physical condition. Nowadays precise manufacturing, as well as factory calibration, can help decrease this error. Even so, regular inspection in the operational span should also take place to detect and adjust any irregularity.

Notably, studies discussing the alignment of standard IMU cover the application of multi-position calibration methods [166–168], or a combination with constant angular rate rotation [103]. Onboard alignment error compensation has been applied in an aircraft [169] and spinning projectile [170]. Eliminating the misalignments in IMU arrays [171, 172] likewise garnered attention. The use of a Kalman filter to represent the IMU and the error parameters is also widely considered [173–176]. Other subjects investigate the utilisation of a 6-degree-of-freedom hexapod instead of a turntable [177] and sensor axis misalignment in fibre-optic linear accelerometers [178].

An angular accelerometer is a new inertial sensor in flight control system applications, and currently only a limited number of studies have examined its characterisation. One of the few is an evaluation report which discusses a prototype angular accelerometer for the measurement of angular head motion during impact, in a biomechanics study [80]. It briefly inspects the transverse axis angular sensitivity, using motion generated by a dual spin-axis rate table, which proved to be inconclusive due to the difficulty to determine the phase shifts. The manufacturer also presents a measurement technique on angular and linear sensitivities of the sensor mentioned above [79]. Another report is the first to examine some oscillatory stimulus to resolve the unsustainable high-level angular acceleration for any extended period [81]. Subjects of these investigations are only single-axis angular accelerometer sensors.

This study investigates the angular accelerometers input axes misalignment in the AAMU package installation. Thus, the defined deviation is collective of the sensors' and

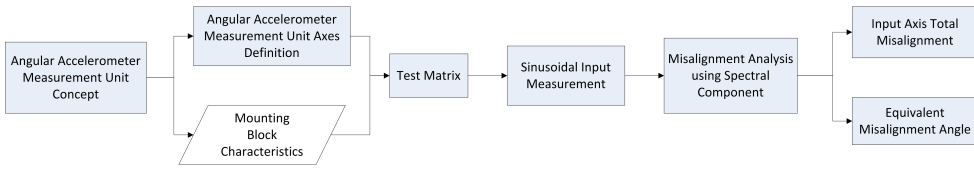


Figure 5.1: Outline of Chapter 5.

the in-house developed mounting block. A standard multi-position test [76] and a functional misalignment test are employed, in a customized measurement set-up expanded in Chapter 2. For this purpose, a multi-axis motion simulator, better known as a calibration table, is used as the motion generator to excite the AAMU, while at the same time representing the aircraft body frame. The input sequences are based on the accepted periodic motion elaborated in Chapter 3 and a 1 Hz motion specification from Chapter 4. Sensor response analysis is conducted in the frequency domain, to allow the use of spectral component magnitude instead of signal peak-to-peak amplitude. The definition of the non-sensitive axes  $x$  and  $y$  for each sensor in their particular installation is an essential part of estimating the input axis misalignment components and identifying the equivalent misalignment angle.

This chapter is divided into five sections, starting with an introduction to the topic. The general chapter outline is visualised in Figure 5.1. Section 5.2 contains an overview of the AAMU and its misalignment complication, as well as the angular accelerometers axis orientation definition. Section 5.3 presents the experiment set-up and plan. Section 5.4 discusses the misalignment check on the AAMU based on the non-sensitive axes responses. Finally, Section 5.5 gives final remarks on the AAMU misalignment measure for the use of sensor-based flight control systems.

## 5.2 MISALIGNMENT IN THE ANGULAR ACCELEROMETER MEASUREMENT UNIT

The term IMU regularly refers to a single unit in the aircraft avionics suite which collects measurements of angular velocity and linear acceleration data sent to the central system processor. It commonly generates six analogue signals describing the linear accelerations and angular rates along each of its axes, which are produced by and acting on the vehicle. This concept is similar to the AAMU, with the distinction that the AAMU measures angular acceleration along the three rotational axes of the aircraft body frame.

The typical geometry of an IMU involved in the INS is shown in Figure 5.2. Each of the sensitive axes of gyroscopes and linear accelerometers corresponds

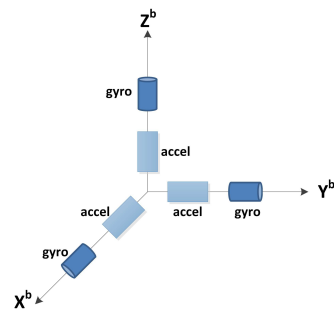


Figure 5.2: Typical gyroscopes and linear accelerometers arrangement in an IMU.

pitch, roll, and yaw axis. When no misalignment error is present, the directions of the mutually orthogonal  $X^b$ ,  $Y^b$ , and  $Z^b$  axes of the reference body-fixed coordinate system define the orientation of the input axes of the three sensors. The crucial part of the misalignment is that it could induce an accumulated error with the magnitude proportional to the angular acceleration and duration of the motions. It furthermore propagates to the attitude and position estimation inaccuracy in the INS.

The developed AAMU follows the standard IMU arrangement. This composition means the AAMU is designed to measure the angular acceleration in three axes with similar orientation as the IMU. The presence of alignment errors leads to a correlation between sensors in an arranged 3-axis oriented device. For example, assume one axis pointed up correctly, and the AAMU is level. The angular accelerometer on this axis measures the angular acceleration input directly in the sensitive axis. If the other two axes were correctly orthogonal, they would not measure any of the effects of this excitation. If there is a non-orthogonality, the other axes also measure the input, leading to a correlation in the responses. The challenges in assessing the misalignment of this configuration are explained in this section.

### 5.2.1 ANGULAR ACCELEROMETER MEASUREMENT UNIT AXIS DEFINITION AND ORIENTATION

A set-up of the motion simulator and AAMU is established for the sensor's input axis misalignment check, where the AAMU is composed of two parts: sensors and a mounting block. Three single-axis angular accelerometers of the same type, with specifications included in Appendix A, are utilised to measure the excitation input in each orientation axis. The in-house designed and manufactured mounting block holds the sensors and is compatible with the turntable top attachment. Figure 5.3 displays the three angular accelerometers installed in a 3-axis orientation mounting, with each sensitive axis mutually orthogonal. The three sensors' sensitive axes do not intersect at a single reference point due to the mounting block arrangement. Nevertheless, since these sensors measure rotational quantity, this composition does not produce any problem.



Figure 5.3: The angular accelerometers arrangement in an AAMU.

The non-orthogonality, in this case, might occur from the following three sources:

- Within the angular accelerometers themselves, due to manufacturing imperfection.
- Due to the attachment between the sensor and the enclosure, or among the angular accelerometers and the mounting.
- The imprecision in aligning the AAMU package and the table plate installation of the motion simulator.

Since these items are implemented collectively as an AAMU, the observed misalignment will be the total of all three elements.

First of all, the motion simulator reference system that acts as the local frame for the AAMU is described. Being a two-axis turntable, it has two fixed axes perpendicular to one another. The inner-axis carries the motion simulator top, where the sensor is mounted,

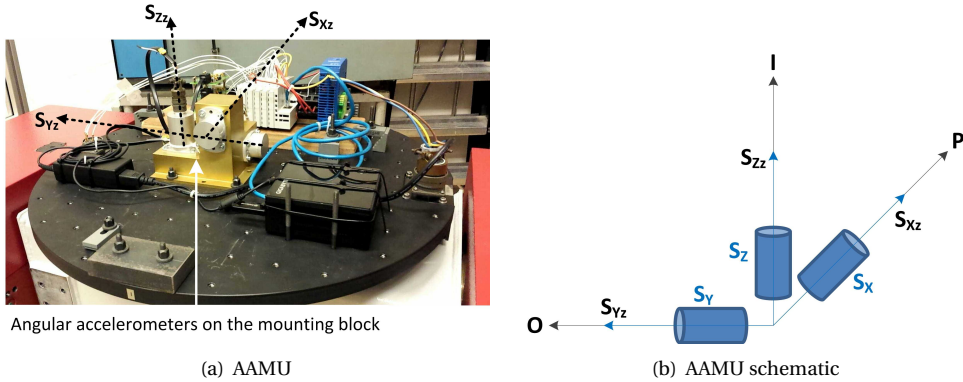


Figure 5.4: Measurement setup of the AAMU on the turntable and its sensitive axes orientation towards the turntable system axes.

as presented in [Figure 5.4\(a\)](#). It is pointing up, away from the table surface and referred to as the  $I$ -axis. The outer shaft is installed rigidly on the table support, perpendicular to the inner axis, and both axes meet at the centre of rotation. The fixed shaft of the outer axis is assigned as the  $O$ -axis, with its positive orientation to the West direction of the magnetic norm. The third axis is introduced as the perpendicular axis  $P$ , that does not exist physically since the turntable is a 2-axis type. The  $P$ -axis is mutually orthogonal with the previous axes with positive pointing to the magnetic North, following the right-hand rule.

[Figure 5.4\(a\)](#) shows the three angular accelerometers' arrangement in a mounting block to form an AAMU, and the customised Sensor Data Acquisition System (SDAS) installed on the turntable plate. In the measurement set-up, each sensor's positive, sensitive axis coincides with one of the motion simulator's axes, which also represents one of the aircraft body axes. [Figure 5.4\(b\)](#) presents the pairs as follows:

- $S_{Z_z}$ , the sensitive axis of sensor  $S_Z$  with the  $I$ -axis,
- $S_{Y_z}$ , the sensitive axis of sensor  $S_Y$  with the  $O$ -axis, and
- $S_{X_z}$ , the sensitive axis of sensor  $S_X$  with the  $P$ -axis.

As described, the angular accelerometer is only labelled for its sensitive axis orientation, here referred to as the  $z$ -axis. Consequently, it is necessary to define each sensor's  $x$  and  $y$ -axes for the misalignment identification. Per definition, as illustrated in [Figure 5.5](#), the  $x$  and  $y$ -axes are mutually orthogonal with each sensors'  $z$ -axis, using the right-hand rule. Note that all of them coincide with the reference positive axes.

[Figure 5.6](#) on the other hand, presents the sensor's axis system when they are pivoted  $180^\circ$  from the original orientation. The rotation is performed referring to the angular accelerometer  $z$ -axis and the angular accelerometers in this position are denoted as the  $S'_{Z_z}$ ,  $S'_{Y_z}$  and  $S'_{X_z}$ . As a result, their sensitive axis orientation towards the motion simulator reference system remains as before. The  $x$  and  $y$ -axes, however, now lie in the opposite directions, along with the negative axis of the  $POI$  system.

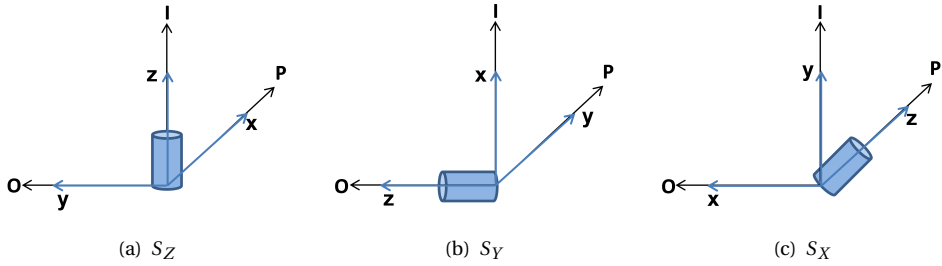


Figure 5.5: Angular accelerometer original axes definition with respect to the table axes.

5

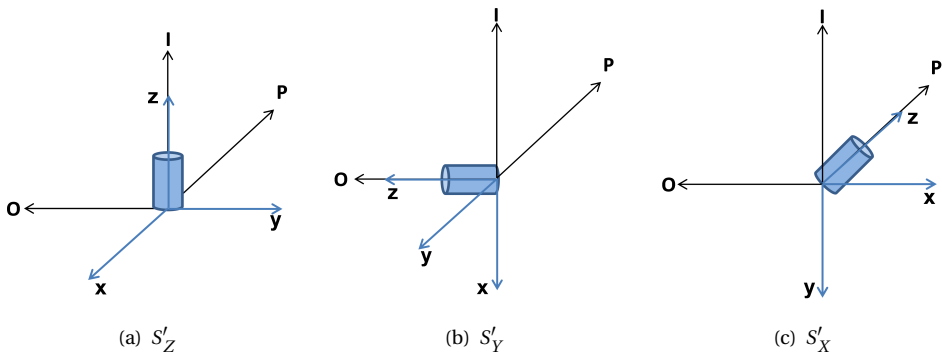
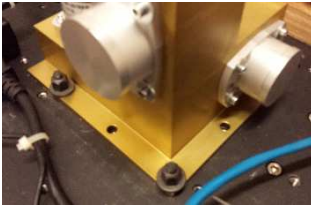


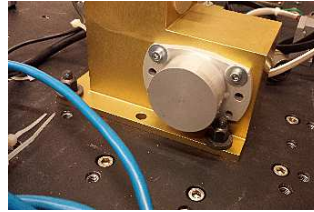
Figure 5.6: Angular accelerometer 180° pivoted axes definition with respect to the table axes.

### 5.2.2 AAMU ADJUSTMENT ON THE TABLE TOP

One prominent issue in this particular set-up is the adjustment between the AAMU and the table reference axis. The table top has threaded holes for mounting of the sensor which, ideally, automatically align a unit under test. However, a small play exists between the mounting block and the stud bolt attached to the tabletop. This slim difference will affect  $S_Y$  and  $S_X$  (as well as  $S'_Y$  and  $S'_X$ ), where their orientation towards the  $I$  and  $P$  axes might alter slightly each time the block is reinstalled.



(a) Ref mounting block holes



(b) Mounting block holes next to  $S_Y$

Figure 5.7: Mounting block attachment holes.

It is therefore needed to align the mounting block with a fixed bearing, the table outer-axis in this instance. This alignment was done by first rotating the outer axis  $90^\circ$  and the mounting block hanging on the thread-less part of the stud bolt. For this purpose, the mounting holes along the AAMU  $Y$ -axis, or  $S_{Y_z}$  axis, in [Figure 5.7\(a\)](#) are used as reference. The alignment of these holes coincides with the turntable's outer axis,  $O$ . Then, the level was checked using an inclinometer<sup>1</sup>, and the mount is subsequently secured.

However, this alignment has two consequences for the attachment of the AAMU to the table top:

1. The inner mounting holes can no longer be fastened to the table top because the stud bolt head can no longer fit into these particular holes.
2. Since securing the block was done using the mounting block's corner holes, it is not possible to attach one of the  $S_Y$ 's screws, leaving  $S_Y$  with only three fasteners as shown in [Figure 5.7\(b\)](#).

Nevertheless, the installation is acceptable since  $S_Y$  is secured in the mounting block.

## 5.3 MISALIGNMENT MEASUREMENT METHOD

**A**LIGNMENT is the process by which the reference axis system determines the orientation of an INS axes. The fundamental concept of aligning an INS is quite straightforward. However, some complications make practical alignment both a time-consuming and intricate procedure. The following test plan is designed to inspect the misalignment of the  $x$  and the  $y$  axis of each angular accelerometer in the mounting block package.

<sup>1</sup>Kell-Strom Aero Angle II DP-60

### 5.3.1 TEST PLAN

IEEE Standard 671™-1985 (R2008) [76] provides a comparable approach to develop the test plan in this chapter. The selected excitation input is a single-frequency sinusoid based on the discussion in Chapter 3, performed using either motion simulator axes. The reference suggests that the misalignment calculation of the sensor  $x$  and  $y$ -axes are performed using the oscillatory signal peak-to-peak magnitude of both the sensor response and the input motion [76]. In this study, however, the frequency domain approach is preferred as it is expected that the response contains higher frequency oscillations at the sine peak. Hence, the measurement is conditioned to obtain a certain 1 Hz spectral component and prevent leakage.

The input motion is limited to a maximum angular acceleration of  $100^\circ/\text{s}^2$ . This chosen value is due to the maximum limitation of  $200^\circ/\text{s}^2$  in the outer axis. The table angular position amplitude to achieve the  $100^\circ/\text{s}^2$  angular acceleration is set to  $2.498^\circ$ . Furthermore, the number of samples is specified to be a power of two, which in this case yields  $2^{17}$ . For synchronisation purposes, the measurement took a little longer (70 s), but the measurement time,  $t_m$  for the DFT/FFT was 65.536 s. The sampling rate is 2 kHz as conferred in Chapter 2.

In this experiment, the AAMU is excited in three different measurements along each respective angular accelerometer sensitive axis. The table inner-axis generates the input for  $S_Z$ , whereas the table outer-axis produces the input for  $S_Y$  and  $S_X$ . Table 5.1 describes the measurement conditions in detail, and also shows the angular accelerometers' axis orientation towards the *POI* system in each test.

Initially, in experiment number 1 of Table 5.1, the motion simulator  $I$  and  $O$  axes are both set to  $0^\circ$  angular position. Subsequently, the input excitation is applied to the  $I$  axis, or along  $S_{Z_z}$ . In the second observation, both motion simulator axes also start from  $0^\circ$  angular position, but with the excitation applied only to the  $O$  axis, or  $S_{Y_z}$ . Lastly, the motion simulator inner-axis is rotated  $90^\circ$  to situate  $S_{X_z}$  in the positive  $O$  axis, then employ it to excite the sensor in experiment 3. The sensor position is then pivoted  $180^\circ$  in the measurement number 4, 5, and 6, and the identical sequence follows.

An additional procedure to address the mounting variation effect on the misalignment is specified. This scheme sees experiment 1–3 to be recurrently applied in Set I, and experiment 4–6 in Set II. The first sets in the dynamic test are measured at the sensors' 'original' position, labelled as set  $(A), (C), (E), (G)$ . Whereas in the second sets for the appointed 'pivoted  $180^\circ$ ' position, all sensors are dismantled from the block, pivoted  $180^\circ$  along their  $z$ -axis, and re-mounted. These second measurements, marked as set  $(B), (D), (F), (H)$ , are included to provide a cross-examination point in the misalignment check. The repeated measurements are executed three times, each with ending the motion input and returning the table to the  $0^\circ$  position after recording the data.

The scenario comprises of four possible variations, each with two sets of measurements, which amount a total of eight items with the following definition: Scenario I, Sequential Recording

**(A) Sequential recording for original sensor position**

Three repeated measurements are performed sequentially with all sensors in their 'original' position.

**(B) Sequential recording for  $180^\circ$  pivoted position**

Table 5.1: Experiment conditions.

Exp	Setting	Orientation			Angular Position [°]		Angular Acceleration [°/s <sup>2</sup> ]		
		S <sub>Z</sub>	S <sub>Y</sub>	S <sub>X</sub>	Inner	Outer	Inner	Outer	
1	Test Configuration (Original)				0		100	0	
2								0	
3					90		0	100	
4		Test Configuration (pivoted 180°)				0		100	0
5									0
6						90		0	100



All sensors are dismantled from the block, pivoted 180° along their  $z$ -axis, and re-mounted. Afterwards, three repeated measurements are carried out sequentially.

#### Scenario 2, Re-mounting Sensors

##### (C) Sensor mounting variability, original sensor position

All sensors are dismantled from the block and re-installed in their 'original' position. The mounting block is detached and re-aligned using the available procedure. After each recording, all three sensors are removed and then fitted again in their respective holder. Every time a sensor re-mounted, it is also re-aligned to the mounting block using the alignment holes.

##### (D) Sensor mounting variability, 180° pivoted position

All sensors are dismantled from the block and re-established in their 180° pivoted position. Similar with (C), all three sensors are de-installed and then restored following the end of each recording.

#### Scenario 3, Re-mounting Mounting Block

##### (E) Mounting block variability for original sensor position

All sensors are placed in their 'original' position. The mounting block is dismantled and re-aligned, as well as after each data recording.

##### (F) Mounting block variability for 180° pivoted position

All sensors are installed in their 180° pivoted position. Likewise (E), only the mounting block that is adjusted after every recording cycle.

#### Scenario 4, Re-mounting Sensors and Mounting Block

##### (G) Mounting block and sensor mounting variability, original sensor position

All sensors are mounted in their 'original' position. Both mounting block and sensors are disassembled and refitted after each data recording.

##### (H) Mounting block and sensor mounting variability, 180° pivoted position

All sensors are fixed in their 180° pivoted position. At the end of the recorded series, the mounting block and the three sensors are dislodged and then reconditioned with the proper arrangement.

### 5.3.2 QUANTIFYING MISALIGNMENT

The IEEE standard [76] include a particular procedure for quantifying the misalignment of gyroscopes. In this process, errors due to input axis misalignment in the  $x$  and  $y$ -axis components are compared directly to the ratio of sensor response and input motion, with the small angle assumption. Furthermore, the scale factor is needed to relate the unit of response to the unit of input. Thus it evaluates the data in engineering units, not as raw voltage sensor output. The misalignment about the  $y$ -axis can be calculated using:

$$\delta_y = \frac{A_y}{K\alpha_y}, \quad (5.1)$$

where:

- $\delta_y$  = misalignment component about the sensor  $y$ -axis,
- $A_y$  = angular accelerometer's peak-to-peak amplitude of the sine profile when the  $y$ -axis aligns with the motion input axis,
- $K$  = scale factor,

- $\alpha_y$  = input motion peak-to-peak amplitude of the sine profile in the  $A_y$  measurement. The misalignment about the  $x$ -axis is then calculated as follows:

$$\delta_x = \frac{A_x}{K\alpha_x}, \tag{5.2}$$

where:

- $\delta_x$  = misalignment component about the sensor  $x$ -axis,
- $A_x$  = angular accelerometer’s peak-to-peak amplitude of the sine profile when the angular accelerometer  $x$ -axis align with the motion input axis,
- $\alpha_x$  = input motion peak-to-peak amplitude of the sine profile in the  $A_x$  measurement.

Subsequently, the total sensitive axis misalignment,  $\delta$  can be calculated as:

$$\delta = \sqrt{\delta_x^2 + \delta_y^2}, \tag{5.3}$$

In this thesis, however, we take a different approach to circumvent three concerns: the peak-to-peak sine magnitude, turntable alignment and the scale factor. The peak-to-peak value is often of interest for observing the magnitude of the non-sensitive axes sensors’ responses compared to the sensitive axis sensor response in the periodic signal. However, the results of the peak-to-peak calculation might not necessarily represent the actual peak of the sine in the noisy signal. The result is mainly on account of fluctuations around the sine peak which introduce uncertainty. Second, even though the customised set up on top of the table top is balanced as much as practically possible, a minor imbalance effect could still influence the turntable axis measurement. Lastly, to implement Equations (5.1)–(5.3), the scale factor converts the angular accelerometer response in [V] to relate it to the motion simulator input unit in [°/s<sup>2</sup>]. Omitting this modification allows retaining the factual information from the sensor response. Therefore, the subsequent analysis is preferred, where the angular accelerometer sensitive axis misalignment is determined from its non-sensitive axes response. The analysed responses are in the form of the fundamental spectral component that is acquired from the voltage output data.

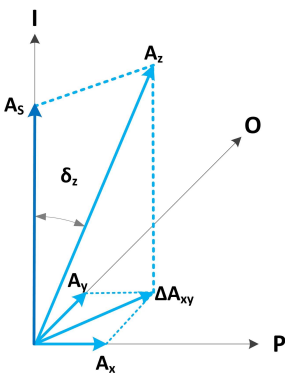


Figure 5.8: One of the AAMU axis misalignment description ( $S_Z$ ).

Misalignment errors introduce cross-axis influences on each of the non-sensitive axes. Quantifying these effects in the angular accelerometer set-up requires dividing the misalignment of the sensitive axis down into two components, which relate to the two other non-sensitive axes as presented in Figure 5.8. For an input rotation about the angular accelerometer  $z$ -axis, there will be a response  $A_z$  along the sensitive axis, as well as two non-sensitive axes components  $A_y$  in the sensor’s  $y$ -axis, and  $A_x$  in its  $x$ -axis.  $A_z$  deviates from the ideal  $z$ -axis by a value of  $\delta_z$ . We assume that  $A_x$  and  $A_y$  work perpendicular to the input axis  $I$ , thus along axes  $P$  and  $O$  respectively, since in reality, there is no physical  $x$  and  $y$ -axis in the angular accelerometer.  $A_S$  is the perfectly aligned response which coincide with the sensitive axis and acquired from the corrected  $A_z$ .

The responses needed to calculate the cross-axis sensitivity of these two defined non-sensitive axes are acquired by applying a motion profile along these axes. For example, sensor  $S_Z$  is excited along its sensitive axis in experiment 1. This sensor response about its  $x$ -axis is obtained from experiment 3, where the input excitation is about the  $P$ -axis. Similarly, the response about its  $y$ -axis is obtained from experiment 2, where the input excitation is about the  $O$ -axis. With the detailed approach in Table 5.1, the necessary data to determine the AAMU misalignment can be obtained from these three measurements.

As previously mentioned, the main spectral component of the response is used to calculate the misalignment. Hereafter,  $A_{z_f}$  is the primary spectral response of the angular accelerometer, which works along the sensor sensitive axis  $z$ , and at a  $\delta_z$  angle, or  $\delta_{z_f}$  equivalent misalignment angle to the  $i$ -axis.  $A_{y_f}$  and  $A_{x_f}$  are the angular accelerometer non-sensitive axes' responses along the  $P$  and  $O$ -axes, respectively, with  $\Delta A_{xy_f}$  as its resultant. Thus, data are transformed to the frequency domain, introducing the following equations:

$$\Delta A_{xy_f} = \sqrt{A_{x_f}^2 + A_{y_f}^2}, \quad (5.4)$$

where:

- $\Delta A_{xy_f}$  = total misalignment magnitude of the angular accelerometer  $y$ -axis,
- $A_{x_f}$  = angular accelerometer response spectral component at 1 Hz frequency, when the  $x$ -axis aligns with the motion input axis,
- $A_{y_f}$  = angular accelerometer response spectral component at 1 Hz frequency, when the  $y$ -axis aligns with the motion input axis,

With the non-sensitive axes resultant expected to be in a perfect, mutually orthogonal orientation with the input axis, the equivalent misalignment angle  $\delta_{z_e}$  can be found using the sine inverse of the ratio between the magnitude of  $\Delta A_{xy_f}$  and  $A_{z_f}$ :

$$\delta_{z_e} = \arcsin \frac{|\Delta A_{xy_f}|}{|A_{z_f}|}, \quad (5.5)$$

The sensor's input-axis misalignment is acquired from the average of two equivalent misalignment angles from the 'original' position of set  $A, C, E, G$ , and the  $180^\circ$  pivoted position of set  $B, D, F, H$ :

$$\delta_z = \frac{\delta_{z_e} - \delta_{z_e p}}{2}, \quad (5.6)$$

where  $\delta_{z_e p}$  is the equivalent misalignment angle at the  $180^\circ$  input-axis pivoted position set-up.  $\delta_z$  then adjust  $A_z$  into  $A_S$  as in the following equation:

$$A_S = A_z \cos \delta_z \quad (5.7)$$

## 5.4 ANGULAR ACCELEROMETER MEASUREMENT UNIT MISALIGNMENT CHECK

THIS section observes the magnitude of the cross-axis sensitivity and misalignment of the AAMU.

### 5.4.1 NON-SENSITIVE AXES SENSOR RESPONSE

First of all, one should inspect whether the non-sensitive axes' responses do exist in the AAMU. For illustration purposes, [Figure 5.9](#) shows all the non-sensitive axes sensors response examples from nine measurements in Set *A*, while [Figure 5.10](#) shows the result of Set *B*. On the left-hand side of every figure is the sensitive axis response, whereas the other two sensor responses in non-sensitive axes are plotted on the right-hand side. Each row represents a different input axis, i.e., [Figure 5.9\(a\)](#) to [Figure 5.9\(c\)](#) for  $I$  input or  $S_Z$  as the main sensor, [Figure 5.9\(d\)](#) to [Figure 5.9\(f\)](#) for  $O$  input or  $S_Y$  as the main sensor, and [Figure 5.9\(g\)](#), and [Figure 5.9\(i\)](#) for  $P$  input or  $S_X$  as the main sensor.  $S_Z$  responses are illustrated by the red colour,  $S_Y$  by the green colour, and  $S_X$  by the blue colour.

Observing [Figure 5.9\(a\)](#) to [Figure 5.9\(c\)](#), the non-sensitive axes' sensors responses clearly show a sinusoid-like oscillation with different phases. If the input axis is perfectly aligned, the non-sensitive axes should have zero response. Thus, these responses are the confirmation of the presence of the AAMU input axis total misalignment. In this case,  $S_Y$  is in phase with the main sensor  $S_Z$ , while  $S_X$  appears to be in antiphase ( $180^\circ$  phase difference). This result reveals a crucial property of the input axis misalignment, which is the phase difference between the non-sensitive axes response. With the  $180^\circ$  phase shift, these two responses will have the opposite sign, the in-phase response is positive, while the out-of-phase response is negative.

In the subsequent measurements, where  $S_Z$  becomes one of the non-sensitive axis sensors, and the table outer-axis generates the input motion,  $S_Z$  responses contain higher level noise which makes it difficult to see the sine pattern. Nevertheless, non-sensitive axes sensor responses also bear a resemblance with a sinusoidal oscillation. Unfortunately, their phase is not immediately apparent to identify. Moreover, a peak pattern appears in the  $S_Z$  data, on both runs. The peak is most likely due to the compensation action by the turntable controller. In this case, the table outer-axis generates the input motions, but since the set-up on the table top is not perfectly balanced, the controller needs to apply some correction to counter the payload inertia. Additionally,  $S_Z$  might pick up the table top wobble<sup>2</sup> motion due to this imbalance.

When the physical sensor position is pivoted  $180^\circ$ , the responses of the non-sensitive axes sensors are inverted. This Set *B* results allows a validation upon Set *A*. As the sensors are revolved  $180^\circ$ , their  $x$  and  $y$ -axis now lies on the negative  $P$  and  $O$  reference axes, which change both of their signs and phases to their opposites accordingly as can be seen in [Figure 5.10](#).

For a more accurate analysis, it is necessary to transform the signals to the frequency domain. The Power Spectral Density (PSD) of all sensor responses of Set *A* are presented in [Figure 5.11](#), and Set *B* in [Figure 5.12](#), focused on the low frequency components below 50 Hz. A quick observation reveals that all sensors measure the motion at a distinct 1 Hz. By examining the frequency components amplitudes, the non-sensitive axes sensors show a much lower value compared to the sensitive axes sensors, with 4 to 5 orders of magnitude.

For the table inner-axis input, the non-sensitive axes sensors detect the table vibration around 30 Hz, at an order of magnitude lower than its response. Meanwhile, for the

<sup>2</sup>Wobble is one of the geometrical inaccuracy that exist in the rotary table and happens about the two other axes perpendicular to the axis of rotation.

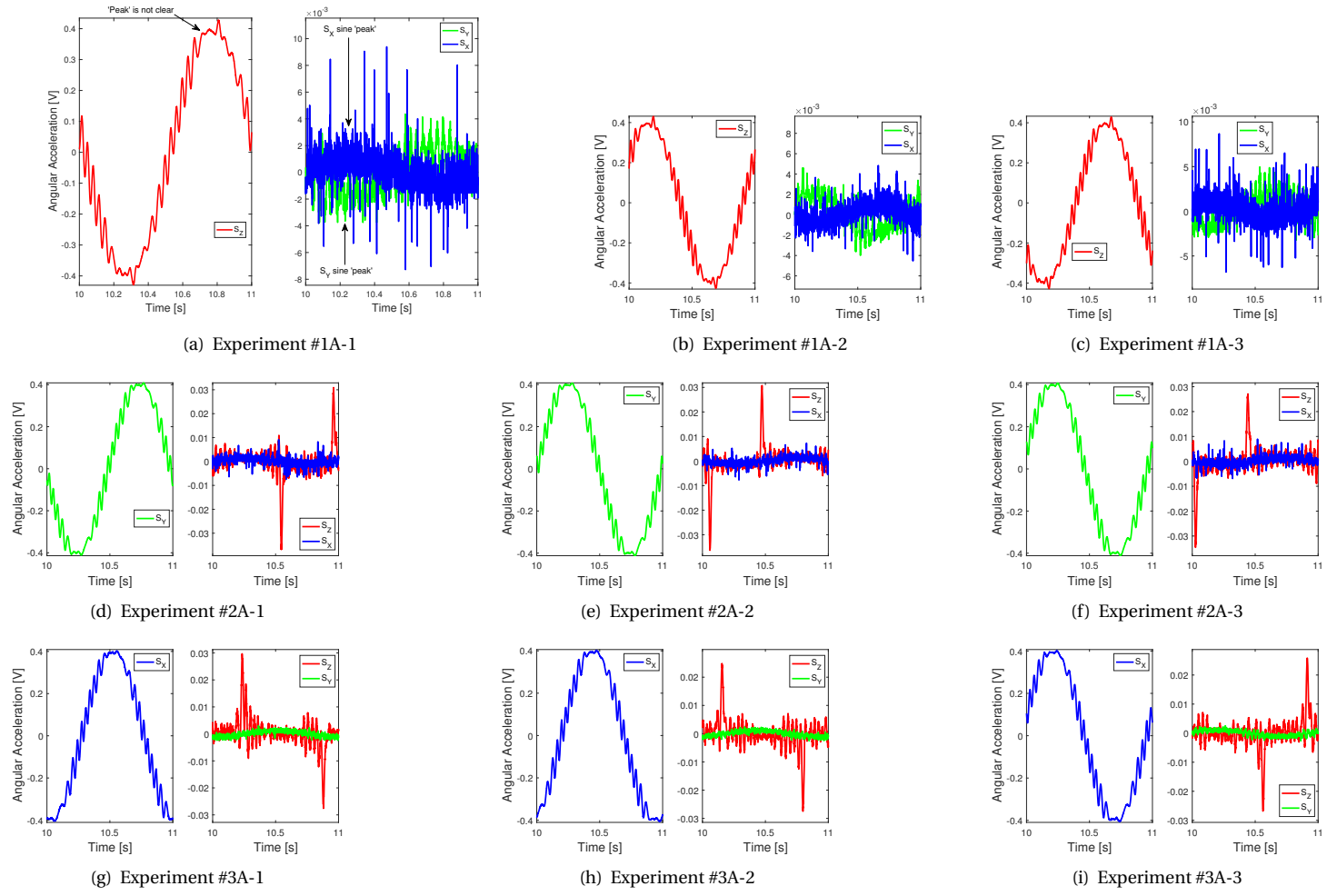


Figure 5.9: Angular accelerometers responses to a  $100^\circ/s^2$  sinusoidal input at 1 Hz in a turn-table, three repetitions, original sensor position, sequential recording (experiment 1–3, set A). Phase shifts apparent in the non-sensitive axes sensors' response, shown by the opposite or different 'peaks' direction.

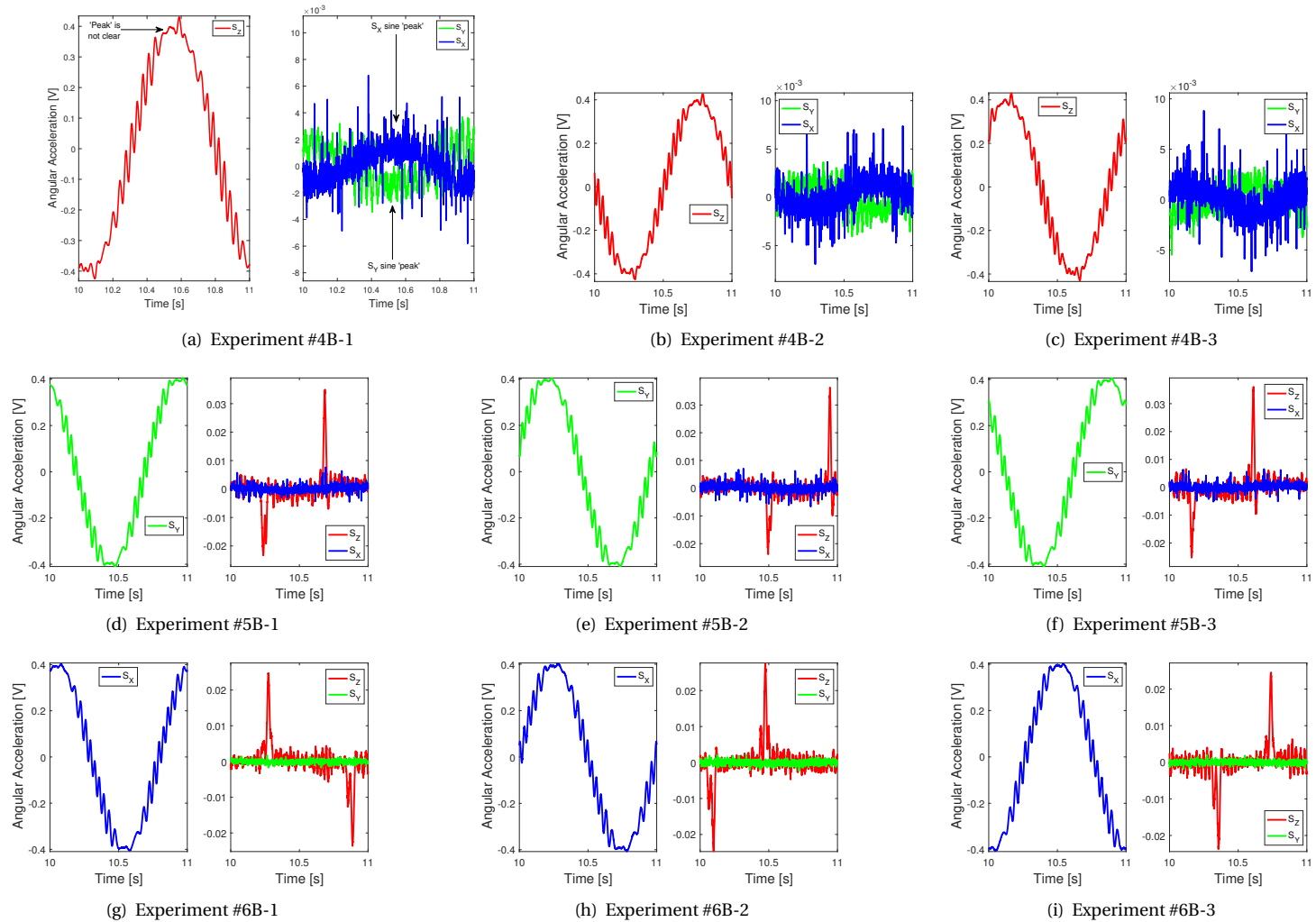
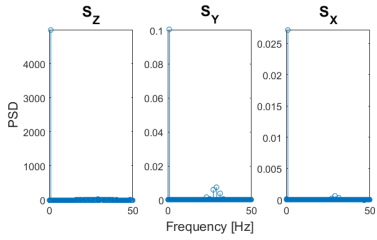
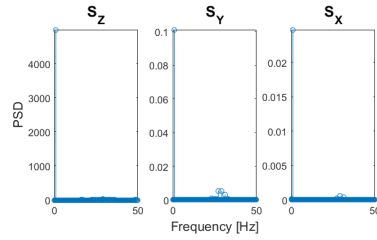


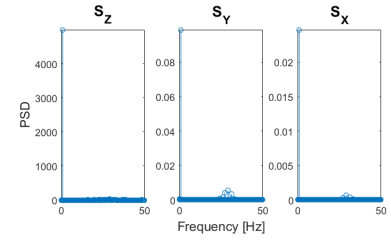
Figure 5.10: Angular accelerometers response to a  $100^\circ/\text{s}^2$  sinusoidal input at 1 Hz in a turn-table, three repetitions,  $180^\circ$  pivoted sensor position, sequential recording (experiment 4–6, set B). Phase shifts apparent in the non-sensitive axes sensors' response, shown by the opposite or different 'peaks' direction.



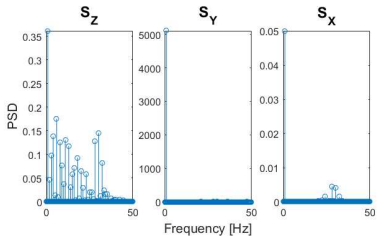
(a) Experiment #1A-1



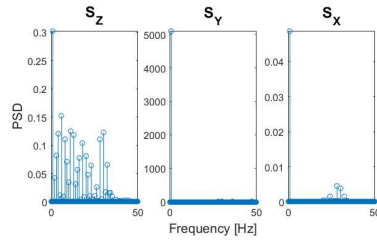
(b) Experiment #1A-2



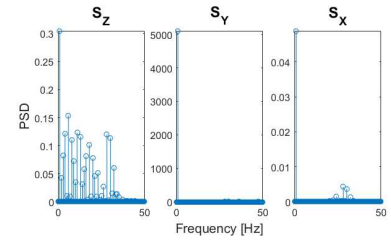
(c) Experiment #1A-3



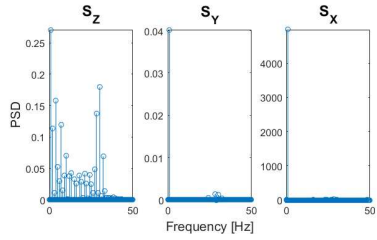
(d) Experiment #2A-1



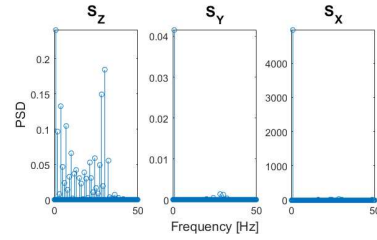
(e) Experiment #2A-2



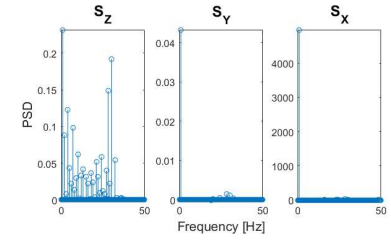
(f) Experiment #2A-3



(g) Experiment #3A-1

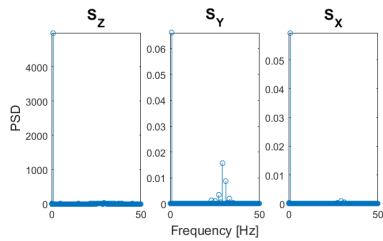


(h) Experiment #3A-2

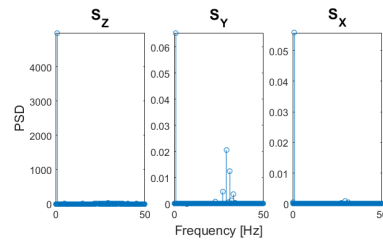


(i) Experiment #3A-3

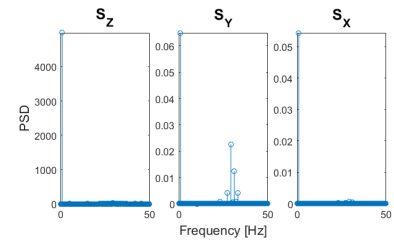
Figure 5.11: Angular accelerometers response PSD of a  $100^\circ/\text{s}^2$  sinusoidal input at 1 Hz in a turn-table, three times repetition, original sensor position, sequential recording (experiment 1–3, set A).



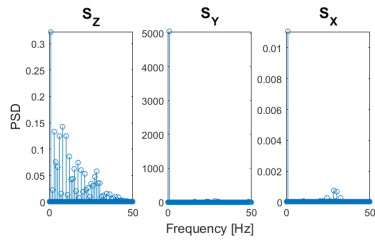
(a) Experiment #4B-1



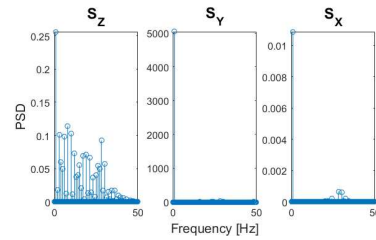
(b) Experiment #4B-2



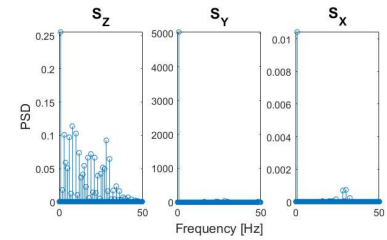
(c) Experiment #4B-3



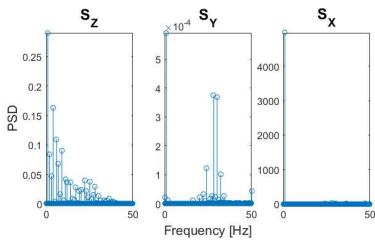
(d) Experiment #5B-1



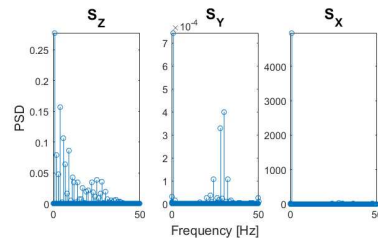
(e) Experiment #5B-2



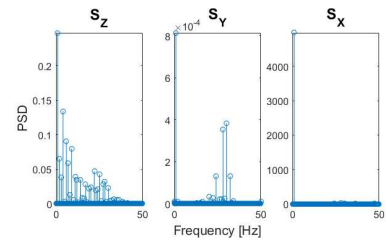
(f) Experiment #5B-3



(g) Experiment #6B-1



(h) Experiment #6B-2



(i) Experiment #6B-3

Figure 5.12: Angular accelerometers response PSD of a  $100^\circ/s^2$  sinusoidal input at 1 Hz in a turn-table, three times repetition,  $180^\circ$  pivoted sensor position, sequential recording (experiment 4–6, set B).

table outer-axis input, the PSDs in Figures 5.11(d)–5.11(i), as well as in Figures 5.12(d)–5.12(i) show the presence of spectral components up to around 35 Hz at the same level of magnitude as in the  $S_Z$  response. This reaction demonstrates that there are additional low-frequency, parasitic motion and vibration along the outer-axis rotation. The source of this effect could originate from the outer-axis shaft itself, or the load asymmetry.

#### 5.4.2 NON-SENSITIVE TO SENSITIVE AXIS RATIO

To comprehend the non-sensitive sensor axes response proportion, the spectral magnitudes at 1 Hz frequency is compared with the magnitude of the sensitive axis sensor in each measurement. The ratio of the non-sensitive axis magnitude about the sensor  $y$ -axis towards the sensitive axis magnitude based on the 1 Hz spectral component,  $R(f)_y$  is given by:

$$R(f)_y = \frac{P_y}{P_z} \quad (5.8)$$

where,  $P$  is the magnitude of the angular accelerometer responses' spectral component at 1 Hz, and the subscripts denote the respective axis. While the ratio of the non-sensitive axis magnitude about the sensor  $x$ -axis towards the sensitive axis magnitude based on the 1 Hz spectral component,  $R(f)_x$  is:

$$R(f)_x = \frac{P_x}{P_z} \quad (5.9)$$

The ratios from all the repeated measurements in all sets are depicted in Figures 5.13–5.15. Here,  $A$  and  $B$  series are the sequential recording sets (seq),  $C$  and  $D$  are the sensors mounting variation sets (sm var),  $E$  and  $F$  are the mounting block variation sets (mb var),  $G$  and  $H$  are the mounting block and sensor mounting variation sets (sm-mb var). Ratio variation of  $S_Z$  spectral magnitude at  $S_Y$  input in Figure 5.13(a) is 0.32%, and due to the  $S_X$  input in Figure 5.13(b) is 0.53%. For  $S_Y$ , the ratio variation as a result of  $S_Z$  input indicated in Figure 5.14(a) is 0.11%, and  $S_X$  input in Figure 5.14(b) is 0.49%. Lastly,  $S_X$ 's ratio variation caused by  $S_Z$  input marked in Figure 5.15(a) is 0.22%, and  $S_Y$  input in Figure 5.15(b) is 0.48%.

The highest non-sensitive axes magnitude is produced by  $S_X$  with 1.095% ratio at  $I$ -axis input, while  $S_Y$  generates the lowest ratio of 0.034% at  $P$ -axis excitation. Based on this result, in general, all of the non-sensitive axes sensors demonstrate a cross-axis sensitivity below the maximum 1% specification.<sup>3</sup> Two exceptions are observed of  $S_Z$  in Figure 5.13(a) and  $S_X$  Figure 5.15(a), where the ratios are slightly above 1%. These violations to standards show that changes in installation can easily affect the angular accelerometer response.

In regards to the data trends, the recording in sequence provides a consistent change between the sensor's original and 180° pivoted position of Scenario  $A$  and Scenario  $B$  data. Scenario  $C$  and Scenario  $D$  show a similar tendency as well, except for the last data point in Figure 5.14(a). Nevertheless, Scenario  $E$ , Scenario  $F$ , Scenario  $G$ , and Scenario  $H$  seem to have a more arbitrary inclination, which is understandable when considering the larger possible number of variations in set-up.

<sup>3</sup>SR-207RFR specification, <http://www.crlsensors.com/>

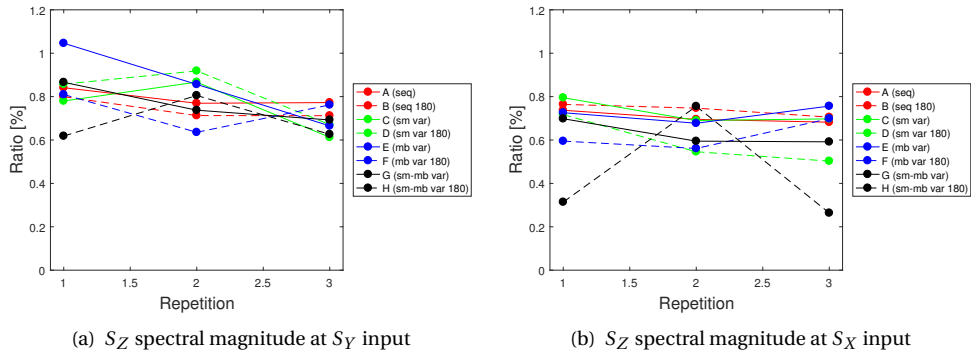


Figure 5.13: 1 Hz spectral magnitude ratio of  $S_Z$  in the repeated measurement for all sets.

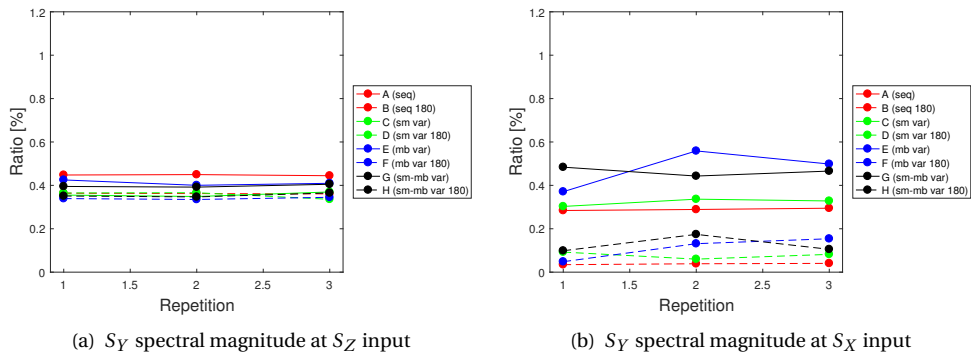


Figure 5.14: 1 Hz spectral magnitude ratio of  $S_Y$  in the repeated measurement for all sets.

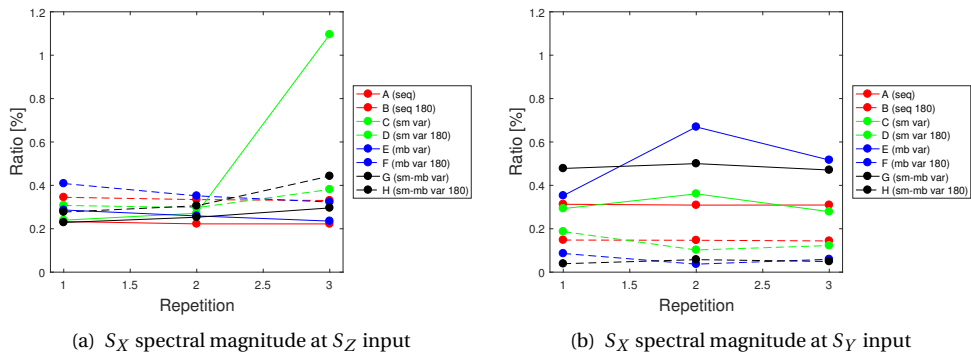
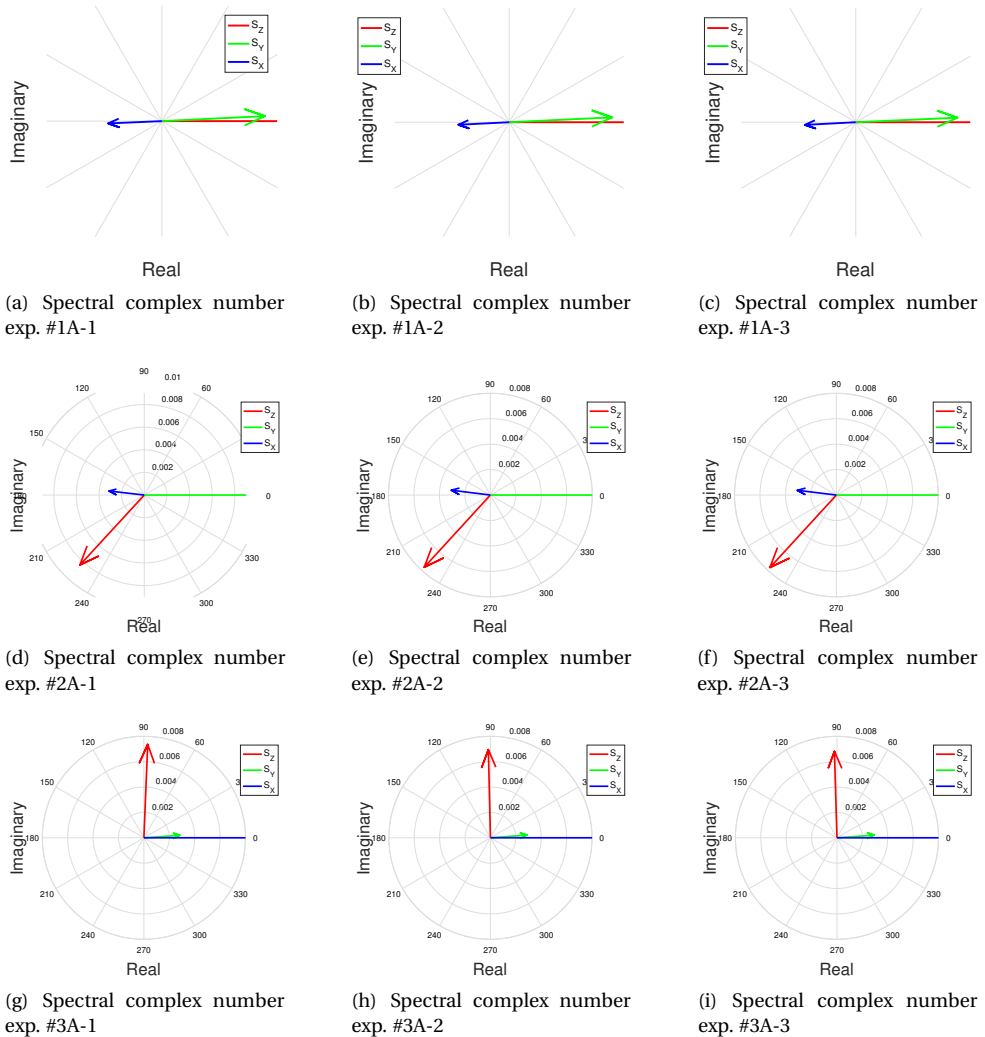


Figure 5.15: 1 Hz spectral magnitude ratio of  $S_X$  in the repeated measurement for all sets.

### 5.4.3 PHASE OF THE SPECTRAL RESPONSE DATA

Another extracted piece of information obtained from the spectral response data is the phase. Comparison between sensors in each experiment and measurement are presented in Figure 5.16 and Figure 5.17, with a close up of the non-sensitive axes spectral response. Again, the red colour illustrates  $S_Z$  responses,  $S_Y$  by the green colour, and  $S_X$  by the blue colour. Each figure displays all three spectral responses but only shows the full magnitudes of the non-sensitive axes. The sensitive axis' spectral component indicates the phase, nevertheless, not exposing the total extent due to its considerable proportion.



5

Figure 5.16: Angular accelerometers' response PSD in complex number plot, three times repetition, original sensor position, sequential recording (experiment 1-3, set A).

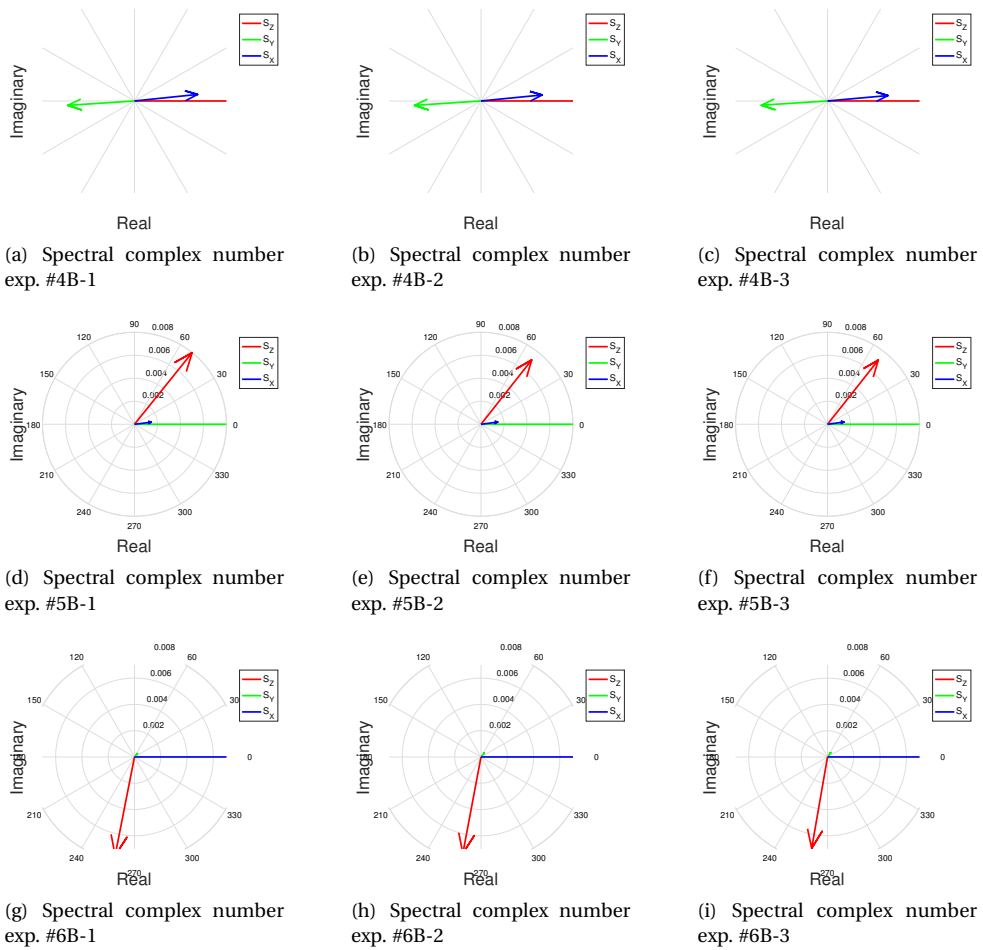


Figure 5.17: Angular accelerometers' response PSD in complex number plot, three times repetition, 180° pivoted sensor position, sequential recording (experiment 4–6, set B).

Both  $S_X$  spectral responses as non-sensitive axis in Figures 5.16(a)–5.16(f) are in anti-phase ( $180^\circ$  phase difference) with the main sensor. Meanwhile,  $S_Y$  is in-phase with the input axis sensor, as can be seen in Figures 5.16(a)–5.16(c), and Figures 5.16(g)–5.16(i). However,  $S_Z$  is neither in-phase nor anti-phase, but at a certain angle illustrated in Figures 5.16(d)–5.16(i). For the  $180^\circ$  pivoted sensor position in Figure 5.17, all the non-sensitive responses show similar behaviour, except that they are in a  $180^\circ$  phase difference with Set A.

So far, this spectral response component analysis allows a specific inspection on the angular accelerometer non-sensitive axes responses and phase out of the noisy signals, by concentrating on the primary excitation frequency. The complex number data, in particular, provide an explicit interpretation of the signal behaviour in its original and  $180^\circ$  pivoted position. One could also identify the output signal's magnitude and furthermore, apply this to ascertain the sensitive axis misalignment.

#### 5.4.4 INPUT AXIS MISALIGNMENT

In this examination, the table *POI* axis system functions as the reference system for the AAMU. Figure 5.8 in Section 5.3.2 illustrates an example of the angular accelerometer magnified input axis misalignment towards this baseline. For the reasons explained in Section 5.3.2,  $A_{x_f}$  and  $A_{y_f}$  are assumed to be mutually orthogonal with the input axis.

To investigate the input axis misalignment, first, the average sensor's spectral responses are calculated. Each sensor acquires its sensitive axis spectral response,  $A_{z_f}$ , and non-sensitive axes spectral responses,  $A_{y_f}$  and  $A_{x_f}$ , from the average of three different measurements. The numerical result is presented in Table C.1 of Appendix C, from which  $\Delta A_{xy_f}$  is determined by Equation (5.4), and the results from all sets are presented in Table C.3.

### 5

Implementing Equation (5.5) for each angular accelerometers in all sets results in Table 5.2, which shows the angular accelerometer's equivalent misalignment angle  $\delta_{z_e}$  and  $\delta_{z_e p}$ , for each sensors in the AAMU. The misalignment error for each sets based on Equation (5.6) are shown in Table 5.3. The numbers in red point out the values above the factory-specified  $0.5^\circ$  alignment.

The data in Table 5.3 demonstrate that in general,  $S_Z$  has the most significant input axis misalignment among the three angular accelerometers, especially in Set 2 and 3. Set 2 indicates the average misalignment error of sensor re-mounting. Furthermore, the result of Set 3 suggests that re-mounting the mounting block could create the most substantial typical misalignment in all sensors. This consequence is in accordance with the issue described in Section 5.2.2. Interestingly, the smallest misalignment errors average for two of the sensors,  $S_Z$  and  $S_Y$ , is obtained from Set 4, where both sensors and mounting block are re-mounted in every measurement.

With the result in Table 5.3, the adjustment for the angular misalignment can be made directly to the signal. This compensation involves  $A_z$ , which based on Figure 5.8 held a cosine association with  $A_S$  and can be calculated using Equation (5.7). For each angular

Table 5.2: Angular accelerometer equivalent misalignment angle,  $\delta_{ze}$  and  $\delta_{ze p}$  (\*) in [°] of each angular accelerometer for each measurement scenario.

Set	Scenario	$S_Z$	$S_Y$	$S_X$
1	A	0.93132	0.34674	0.10618
	B*	1.13392	0.07247	0.10225
2	C	0.82580	0.11525	0.46138
	D*	0.33622	0.27885	0.34117
3	E	1.45392	0.49926	0.15400
	F*	0.39420	0.21681	0.67644
4	G	0.36299	0.31476	0.36260
	H*	0.53356	0.13703	0.19689

Table 5.3: Angular accelerometer misalignment angle,  $\delta_z$  in [°] of each angular accelerometer for each test set.

	Set	$S_Z$	$S_Y$	$S_X$
1	Sequential recording	-0.10130	0.13714	0.00393
2	Re-mounting sensors	0.24479	-0.08180	0.06011
3	Re-mounting mounting block	<b>0.52986</b>	0.14123	-0.26122
4	Re-mounting sensors and mounting block	-0.08529	0.08887	0.08286

accelerometer in the AAMU sensitive axes, we obtain:

$$A_{S_Z} = A_{z_{S_Z}} \cos(\delta_{z_{S_Z}}) \quad (5.10)$$

$$A_{S_Y} = A_{z_{S_Y}} \cos(\delta_{z_{S_Y}}) \quad (5.11)$$

$$A_{S_X} = A_{z_{S_X}} \cos(\delta_{z_{S_X}}) \quad (5.12)$$

For further application, the scale factor identified in [Chapter 3](#) adjusts the enhanced voltage responses to [°/s<sup>2</sup>].

## 5.5 CONCLUSION

THIS chapter investigates the AAMU input axis misalignment using a functional dynamic test, in a customised measurement set-up. A motion simulator in the category of a 2-axis turntable carries out the role of the reference system and generates the acceleration excitation profile. Eight arrangements are defined that implement a well-designed input motion to measure the AAMU installation variability. The spectral response analysis then allows an accurate inspection of the angular accelerometer non-sensitive axes responses' and phase, out of the noisy signals, by concentrating on the primary excitation frequency.

The ratio of the non-sensitive axis response and the sensitive axis response provides the extent of the cross-axis sensitivity. Based on the 1 Hz spectral component, we find that this measure falls below the specified 1% maximum, for all sensors. The resultant of each sensor's  $y$ -axis component  $A_y$ , and  $x$ -axis component  $A_x$  are calculated to inspect the input axis misalignment. The relation of the non-sensitive axes resultant,  $\Delta A_{xy}$  and the sensitive or  $z$ -axis component,  $A_z$  obtains the angular misalignment. The misalignment angle  $\delta_z$ , in each sensitive axes, can be calculated from the equivalent misalignment angle in the original and pivoted 180° positions,  $\delta_{z_e}$  and  $\delta_{z_{ep}}$ .  $\delta_z$  applies the discrepancy compensation to the voltage response signal of the angular accelerometers. Most of the results comply with the maximum 0.5° input axis misalignment specification.

The disparity of the  $\delta_{z_e}$  and  $\delta_{z_{ep}}$  are higher in the measurement sets with more re-mounting variability. This attribute shows that re-fitting the sensor mounting and mounting block, or both, can affect the correct sensor orientation and eventually, its response. Therefore, the effort to compensate for the misalignment should take this significance into account.

In this study, the outcome is based on the evaluation of an AAMU, which does not automatically represent an individual angular accelerometer. Nevertheless, in the event where an AAMU is implemented as a complete package in novel sensor suites, these results contribute to establishing an applicable calibration method for this type of sensors arrangement.

# 6

## CONCLUSIONS

*It is good to have an end to journey toward; but it is the journey that matters, in the end.*

Ursula K. Le Guin, *The Left Hand of Darkness*

ANGULAR accelerometers have not yet been widely used as inertial sensors in aerospace applications. These sensors may offer significant advantages in, for instance, future adaptive flight control system designs. Having a directly measured angular acceleration signal available as input to these systems is foreseen to enhance their performance by minimising effects of delay and noise, or even effectively eliminate these entirely [8, 10, 12–14]. Currently, there is insufficient knowledge to rigorously characterise angular accelerometers, especially concerning proper test equipment and detailed test procedures. The overall research objective of this thesis therefore was:

#### Main Research Objective

*To accurately model and calibrate angular accelerometers using a commercially available position-based, high rate-accuracy, 2-axes turntable motion simulator system.*

This thesis aimed to establish a procedure to evaluate the performance of angular accelerometers in a laboratory setting. The primary objective was achieved by answering four sub-questions of Chapter 1. These research sub-questions address: (i) efficient data collection in the measurement framework; (ii) scale factor calibration method; (iii) angular accelerometer model identification based on its frequency response; and (iv) input axis misalignment in an Angular Accelerometer Measurement Unit (AAMU). This chapter first summarises the main findings and contributions of the study as discussed in Chapter 2 to Chapter 5 of this thesis. It then offers a glimpse of the potential future research.

## 6.1 ANGULAR ACCELEROMETER CHARACTERISATION

### 6.1.1 USING THE POSITION-BASED MOTION SIMULATOR SYSTEM

A motion simulator provides accurate, angular input motions and commonly consists of a turntable and a control unit. Turntables are available in one or multiple axes, providing the degrees of freedom in simulating motion in different orientations. One of the most crucial environmental effects on the sensor, the temperature change, can also be simulated by adding a temperature chamber on the turntable. Complemented by a state-of-the-art control computer which translates user input into a controlled sequence, this system has become the standard in modern-day inertial sensor calibration.

The preliminary assessment identified three challenges which hinder the efficient use of the motion simulator available for this research, for the angular accelerometer characterisation. The first is additional noise from the slip ring device. The second challenge is how to design and optimise a proper test input signal. Lastly, a proper experiment plan taking into account the limitations of all equipment and instruments needs to be formulated. Answering these questions lead to the solution in the following seven contributions.

#### MEASUREMENT FRAMEWORK

Awareness of what exactly occurs in the motion simulator operation is crucial before performing the angular accelerometer characterisation. Three states, the measured angular

position, the estimated angular rate, and the estimated angular acceleration, were studied to investigate the influence of the specific configurations to the output motion. One of the effects we found was the persistent turntable vibration at a frequency of 35 Hz, which although very small, is blended in the motion simulator data. Another finding concerns the effects of small oscillations in the turntable's constant rate motion, which could complicate the dynamic test. Also, the quality of the estimated angular acceleration provided by the motion simulator is shown to be inadequate to use as the standard for the Device Under Test (DUT). Together with the evaluation of the measurement set-up, the discovery ensues the first contribution of this thesis:

**C1**

Propose an angular accelerometer measurement framework using a 2-axis motion simulator, that includes all identified internal and external disturbances.  
(Chapter 2)

### CUSTOMISED SENSOR DATA ACQUISITION SYSTEM (SDAS)

Acquiring high-quality data is fundamental to this study. It has been found from test results that the noise level in the angular accelerometer increased by a factor of ten when signals were transferred via the slip ring. Since the ordinary method to collect the DUT data through the slip ring turned out to include high noise levels, a custom-made SDAS was devised in Chapter 2. Since clock overrides from the motion simulator showed to be unfeasible, the 'Freeze Pulse' feature was utilised instead to facilitate the data synchronisation. Fundamentally, the synchronisation employs mutual markers to align the two simultaneous records of data sets in the SDAS and motion simulator computer. Sent from the SDAS, the first signal is continuously transmitted in the form of a 100 Hz pulse, while the second is a step signal which is raised once the recording command is activated. The logical clock synchronisation is then done offline, yielding a standard time that linked the two data sets. In conclusion, the second contribution of this thesis:

**C2**

Provide a method to gather the DUT data without the slip ring, together with a synchronisation procedure aided by sync pulse and log active signal.  
(Chapter 2)

### ANGULAR ACCELERATION INPUT

Specifying the optimal angular acceleration input in a motion simulator that is designed to accurately produce angular positions and angular rates, presents a significant challenge. The motion platform cannot maintain the continuous accelerations needed to generate the required excitation; even though it is possible with a restricted condition. An alternative solution has been achieved by a combination of two-axis constant angular rate motion; a concept first explored in the 1970s [134] and 1980s [135], and a specific angular accelerometer sensitive axis orientation. An ongoing constraint for the current motion simulator, however, comes from the mechanical limitation which results in a frequency bandwidth of up to 3 Hz. It is considered not the ultimate answer since the DUTs

need to be tested for higher frequencies as well. Furthermore, it can only accommodate one DUT because the sensitive axis should be aligned with the turntable's outer axis, and thus it is not ideal for characterising the Angular Accelerometer Measurement Unit (AAMU). An applicable angular acceleration input was then explored in search for other solutions. By looking into the finite motion, a repetitive actuation can be produced in the profile of a sinusoid where its peak magnitude is the intended input value. The excitation is specified by ascribing amplitude,  $A$  in [ $^\circ$ ] and frequency input,  $f$  in [Hz], along with adjusted angular position, rate, and acceleration. This approach conveniently provided a suitable workaround even for producing different frequency inputs, which in this case were defined by the number of complete sine cycles in a time frame. These two input signal definitions form the third contribution of this thesis:

**C3**

Formulate proper excitation inputs for the angular accelerometer: a combined 2-axis constant angular rate motion and a 1-axis cyclical acceleration motion.  
(Chapter 3)

## EXPERIMENT DESIGN

Frequency response analysis is performed to characterise the transfer function of an underlying linear dynamic system. Nearly all real world systems are nonlinear, but can be linearised, supported by measurements which resemble the linearity. The most difficult non-linear forms in the dynamic analysis are related to actuation signals and the acquisition of responses, which actually may not have an association with the system dynamics. This study attempted to overcome this kind of non-linearity by modifying the measurement procedure. The specified test sequence is based on the test envelope defined according to the motion simulator and DUT specifications and limitations. It was found that, with the current set-up, tests can be performed in the range of 0.8–573  $^\circ/s^2$  angular acceleration and between 0.4–11 Hz excitation frequency. Subsequently, it is recommended that the analysis takes place in the frequency domain to exercise accurate assessment of the motion. Then, the fourth contribution of this thesis:

**C4**

Establish a test envelope by taking into account angular accelerometer and motion simulator constraints, and develop a test matrix to obtain leakage-free spectral component data.  
(Chapter 4)

6

### 6.1.2 ANGULAR ACCELEROMETER CHARACTERISATION

The DUT response usually is in the form of an electrical signal and therefore, mapping this output to the correct standard unit is one of the focal points in calibration. The translation of the angular accelerometer's response in [V] and a reference from the motion simulator in [ $^\circ/s^2$ ] is evaluated using a sine profile excitation in the time domain. Two standards, the estimated angular acceleration and the Sliding Mode Differentiation (SMD) approximated norm, are compared as the reference. The calibration is done through a

polynomial scale factor model structure, which is chosen to describe the possible non-linearity best. The examination returns a 1<sup>st</sup> order polynomial when using the estimated angular acceleration reference and a 3<sup>rd</sup> order for the SMD approximated norm. The current model nevertheless, entirely relies only on the angular accelerometer response. To accurately model the sensor output, future calibration should take more variables into account, for instance, to include the effects of temperature changes and jerk. The calibration work leads to the fifth contribution of this thesis:

**C5**

Develop a scale factor calibration method which maps the angular accelerometer output to the motion simulator standard.

(Chapter 3)

A frequency response model is useful in providing information about the dynamic response of a particular DUT. In this circumstance, the excitation is defined to cover the frequency band within the established test envelope. The spectral component output-input ratio at the fundamental frequency for every acceleration value determines the Frequency Response Function (FRF) of the system. A transfer function representation of the time domain data then formulates the input-output relation for the specified bandwidth and angular acceleration, which is visualised in a bode plot and can then be validated using the FRF. A fifth-order transfer function model without a separate delay term was found to be the best representation of the sensor, based on the Fit percentage and Pole-Zero map of the systems. This model gives an excellent approximation of the measurement result within 0.009–0.7 % accuracy. With this outcome, the sixth contribution of this thesis is to:

**C6**

Facilitate the development of novel fault-tolerant, flight control systems in the design phase by identifying an accurate angular accelerometer dynamic model.

(Chapter 4)

### 6.1.3 AXIS ALIGNMENT IN THE ANGULAR ACCELEROMETER MEASUREMENT UNIT (AAMU)

Three single-axis angular accelerometers are arranged in a 3-axis orientation to form an AAMU. Beside the DUT's respective axis misalignment, the installation includes the mounting block inaccuracies as well. Upon a specified dynamic test, the responses in the non-sensitive axes are observed, which demonstrates the existence of slight deviations in the alignment of the principal axes. The misalignment is then calculated from the fundamental spectral component and compared for different settings. Although almost all of the ratios expressed as spectral magnitude were below the specified 1 %, repetitive measurements also show that a small change in the installation affects the misalignment. The relation of the non-sensitive axes resultant,  $\Delta A_{xy}$  and the sensitive or  $z$ -axis component,  $A_z$  obtains the angular misalignment. Nearly all of the results comply with the maximum 0.5° input axis misalignment specification. The investigation yields the seventh contribution of this thesis:

**C7**

Adopt the dynamic test technique and spectral component method to identify and study the effects of AAMU input axes misalignment.

(Chapter 5)

The relation between the four research subquestions and the seven contributions is graphically presented in Figure 6.1.

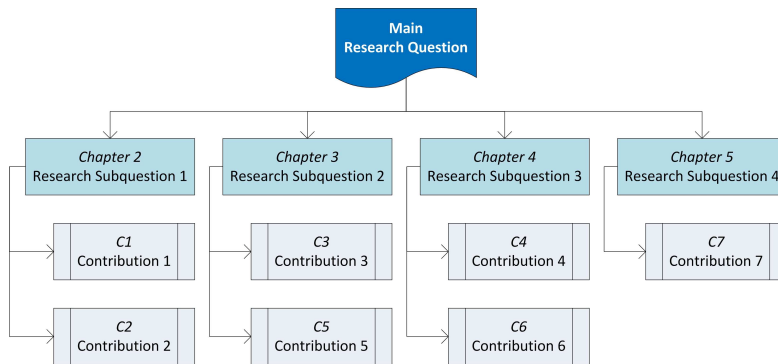


Figure 6.1: Map of the research questions and contributions.

## 6.2 RECOMMENDATIONS FOR FUTURE ANGULAR ACCELEROMETER CHARACTERISATION

Reflecting on the dissertation outcome, the current study focused on one type of angular accelerometer and used one particular motion simulator. In this section recommendations are given to extend this research and turn the presented method into a proven general methodology.

### 6.2.1 VALIDATING THE APPROACH WITH DIFFERENT APPARATUS

#### UTILISATION OF DIFFERENT MOTION SIMULATOR TYPES

Motion simulators come with different number of axes and sizes. The turntables currently available in single, two, three and five axes of rotation, are commonly equipped with direct-drive brushless torque motors as the axis actuator and incremental angular encoder. This thesis develops a characterisation approach for angular accelerometers using the 2-axis type device. For an individual sensor, the developed method could be adapted in a single-axis motion simulator. The 3-axis variant could be useful in investigating the combination of stimuli in all three rotational orientations. When the angular accelerometer is part of a larger unit, testing it in a Hardware-in-the-Loop (HWIL) system will employ the 5-axis flight motion simulator. All of these applications call for comparative studies in assessing the proper measurement set-up and input sequence since the available motion simulators are not built specifically to test angular accelerometers.

### TESTING VARIOUS CATEGORIES OF ANGULAR ACCELEROMETER

This dissertation used a precision force balance angular accelerometer with fluid rotor concept to investigate the characterisation method. Undeniably, diverse sensing mechanisms exist, and their specific responses might differ. Therefore, it is invaluable to study the particularities between analogue, digital and MEMS angular accelerometer types, for example, in terms of the accuracy of the models we can derive from their responses.

### INTEGRATING THE TEMPERATURE EFFECT

To date, no known angular accelerometer characterisation study incorporates the influence of temperature in the dynamic test. Our research merely performs this check in a static environmental chamber, apart from the turntable, as presented in Appendix B, and only measures static bias. Thermal influences vary for different sensor types and are related to parameters such as bias, sensitivity and misalignment. As identifying this type of implication can reduce error and improve the sensor's performance, future studies that take temperature effects in dynamic angular accelerometer examination into account are advised.

### IN-FLIGHT CALIBRATION STUDY

In this study, the angular accelerometer is prepared to be part of a new inertial measurement unit that provides measurements as the feedback to the state-of-the-art Fault-Tolerant Flight Control (FTFC) concept. Besides a controlled evaluation in the laboratory setting, the sensor response in real flight should also be examined, as has recently been done in a collaborative study between the Control and Simulation research group of Aerospace Engineering Faculty - TU Delft with the German Aerospace Center (DLR). In the operational stage, also periodic calibrations need to take place. Therefore, establishing an applicable flight test plan for this new unit addition should be on the list.

## 6.2.2 IMPLEMENTATION OF THE ANGULAR ACCELEROMETER MODEL

To build an angular accelerometer model is one of the primary purposes of this work. It is expected that this model could advance the design phase of FTFC by providing an accurate substitute of the real sensor. The next exploration could study the model performance in such an application, in addition to the analysis of the flight control system itself.

## 6.2.3 EXPLORING NEW MOTION SIMULATOR CONCEPTS

One of the prominent issues discussed in this dissertation is the lack of availability of test equipment that is specially made to examine the angular accelerometer. Commercial motion simulators nowadays are of high-precision, which makes them suitable for advanced calibration and Hardware-in-the-Loop (HWIL) applications of inertial sensors, such as gyroscopes and linear accelerometers. They are, however, designed for precision angular *position* measurement. Even though estimates of angular position and angular rate are made reliable, this is not the case for angular acceleration estimates. This complicates the efforts to properly characterise the angular accelerometer.

A straightforward answer would be to incorporate direct angular acceleration measurement in the motion simulator to provide a more accurate result. In connection with

further improvement in dynamic rotational drives, this could for example be achieved by using the Ferraris Principle as the angular acceleration sensor [179]. This would yield not only a variable angular acceleration but also improves the dynamic disturbance stiffness of the motion simulator [180–182]. Current motion simulators use acceleration feedback as well, but this feedback originates from linear accelerometers measurements [116].

Another possibility would be to develop an apparatus that is capable of generating continuous angular acceleration with the combination of two or three axes motion and broader frequency bandwidth. It has been described in [Chapter 2](#) that a particular 2-axis constant rate sequence, along with sensitive axis orientation, can produce angular acceleration effects to the DUT. However, it is limited to low-frequency excitation of up to around 3 Hz and the customised SDAS in our case. That being said, such effects might be feasible in three and 5-axis motion simulators as well, leading to the recommendation to investigate the feasibility of these devices for this purpose.

# APPENDICES



# A

## SPECIFICATION DATA

### A.1 COLUMBIA MODEL SR-207RFR ANGULAR ACCELEROMETER

The following tables list the Columbia Model SR-207RFR operational, environmental and physical specifications<sup>1</sup>.

Table A.1: SR-207RFR operational specifications.

Operational Specifications	Value
Range	$\pm 10 \text{ rad/s}^2$
Output Voltage	0.2–4.8 V DC into 100K Load
Excitation	24–32 V DC <25 mA
Output Impedance	$<5 \times 10^3 \Omega$
Sensitive Axis Alignment	0.5°
Scale Factor Tolerance	$\pm 1 \%$
Scale Factor Temp Coefficient	0.05 %/°C Max.
Zero Bias	(2.50 $\pm$ 0.01) V DC
Null Temp Sensitivity	$\pm 0.4 \text{ mV/}^\circ\text{C}$
Natural Frequency	10–100 Hz Dependent Upon Range
Damping	07 $\pm$ 02
Linear Acceleration Sensitivity	0.1 % F.R./G or 0.01 rad/s <sup>2</sup> /G (greater value applies)
Cross Axis Sensitivity	1 % Max.
Output Noise (DC To 400 Hz)	<3 mV RMS
Non-Linearity	$\pm 0.05 \%$ F.R.
Hysteresis & Non-Repeatability	$\pm 0.1 \%$ F.R.
Threshold & Resolution	0.005 % F.R.

<sup>1</sup><https://www.crlsensors.com/prodDocs/sr-207rfr.pdf>

Table A.2: SR-207RFR environmental specifications.

Environmental Specifications	Value
Temperature, Operating	-40–85 °C
Temperature, Storage	-40–85 °C
Vibration Survival (2–2000 Hz)	15G RMS, 0.5" Disp D.A.
Linear Acceleration Survival	100G
Shock Survival	1000G, 1 ms
Ambient Pressure	0–5 atm
Humidity	95 % R.H.

Table A.3: SR-207RFR physical specifications.

Physical Specifications	Value
Weight	10 oz (283 g)
Size	1.5 in Dia. (Excluding Mtg Flange) x 2.97 in H (3.8 cm Dia. Excluding Mtg Flange x 7.6 cm H)
Case Material	Anodized Aluminum
Sealing	Environmental
Connector	PT1H-10-6P or Equiv.
Optional Mating Connector	PT06A-10-6S or Equiv.

## A.2 ACUTROL TWO-AXIS MOTION SIMULATOR

### A.2.1 2-AXIS TURNABLE MODEL AC2266L

The ACUTROL AC2266L 2-axis turntable is a customised version of AC2246. Tables A.4–A.6 describes the dimensions and specifications of AC2246<sup>2</sup>, with items marked with asterisk (\*) are the AC2266L data.

Table A.4: AC2266L dimensions.

Dimension	Unit	Value
Height	mm	1'150
Height of outer axis	mm	750
Width across outer axis	mm	1'410
Base dimension	mm	1'250 x 750 (LxW)
Table top diameter	mm	600 (50 x M6 helicoils)*
Table top offset	mm	-166
Table top flatness	mm	0.05

<sup>2</sup>[http://www.acutronic.com/uploads/tx\\_AcutronicProducts/Datasheet-2-Axis-Rate-Table-AC2246.pdf](http://www.acutronic.com/uploads/tx_AcutronicProducts/Datasheet-2-Axis-Rate-Table-AC2246.pdf)

Table A.5: AC2266L Device Under Test (DUT).

DUT	Unit	Value
Payload weight	kg	40 (nominal)
Clearance envelope	mm	500 x 500 (ØxH)*

Table A.6: AC2266L axes specifications and performances.

	Inner Axis	Outer Axis
<b>Mechanical specifications</b>		
Orthogonality		≤ 3''*
Wobble	≤ 2''*	≤ 3''*
<b>Static and dynamic performances</b>		
Angular freedom	continuous	
Positioning accuracy	1'' RSS*	
Rate range	1200 °/s	500 °/s*
Acceleration range, no load	1000 °/s <sup>2</sup> *	200 °/s <sup>2</sup> *

### A.2.2 ACUTROL®3000 DIGITAL MOTION CONTROLLER

The following tables present the ACUTROL®3000 Digital Motion Controller interfaces, performance, measurement, servo and mechanical features<sup>3</sup>.

Table A.7: ACUTROL®3000 interfaces.

Interfaces
<ul style="list-style-type: none"> <li>• Graphical User Interface (GUI): selection of simulation modes and motion parameters, monitoring of system variables and system states</li> <li>• Computer Interfaces <ul style="list-style-type: none"> <li>– TCP/IP and GPIB (IEEE-488)</li> <li>– Real Time Interface: UDP (up to around 100 Hz , VMIC (Option), SRAMNET GT (option))</li> </ul> </li> </ul>

<sup>3</sup>[http://www.acutronic.com/uploads/tx\\_AcutronicProducts/Data\\_sheet\\_ACUTROL3000.pdf](http://www.acutronic.com/uploads/tx_AcutronicProducts/Data_sheet_ACUTROL3000.pdf)

Table A.8: ACUTROL@3000 performance features.

Performance Features	Unit	Value
Position Accuracy	"	$\leq 0.05$
Position Stability	"	$\leq 0.02$
Position Resolution	"	0.01
Position Sensitivity to Rate	"/rad/s	$\leq 0.1$

A

Table A.9: ACUTROL@3000 measurement features.

Measurement Features	Value
Number of axes	1–3 axes
Display Format	Full Scale User Units (bi-polar or uni-polar)
Data Format	FP or 32 bit binary
Analog I/O	$\pm 10$ V (= 16 Bits)
Axis Synchronization	Simultaneous sampling command & measure
Position Event Pulses	2 events, N/revolution; 32 ns resolution

Table A.10: ACUTROL@3000 servo features.

Servo Features	Value
Digital Control	State space, classical, or hybrid architecture
Sample Rate	up to 5 kHz
State Estimation	Position, rate, and acceleration
State Limits	$\pm$ position, rate, and acceleration

Table A.11: ACUTROL@3000 mechanical features.

Mechanical Features	Value
Chassis	19 in Rack mount; 10.5 in height
Display	12 in LCD with touch screen

# B

## STATIC TESTS

This Appendix present two static test results: the repeated static measurement to determine the bias, and the temperature measurement that includes static temperature check on the turntable and in the environmental chamber.

### B.1 REPEATED STATIC MEASUREMENT

The static measurement is performed when the turn-table is stationary, and the measurements were performed with the angular accelerometer input axis vertical and inverted. The static test matrix is developed based on the IEEE standard [76] and each experiment is repeated three times. The measurements were performed for two set-ups: original, as displayed in [Table B.1](#), and pivoted 180° in [Table B.2](#).

The sensor bias is derived from the sensor static response mean. The average of the mean from the repeated three measurements represents the bias in each orientation set. Then, bias for each sensor is obtained from the following equation and described in the sensor mean columns in [Table B.3](#) and [Table B.4](#).

$$K_0[V] = \frac{A_+ + A_-}{2} \quad (\text{B.1})$$

where

$A_+$  = vertical angular accelerometer sensitive axis orientation.

$A_-$  = inverted angular accelerometer sensitive axis orientation.

The sensor data sheet specifies that  $S_Z$  has a bias of  $(2.499 \pm 0.010)$  V or in the range of 2.489 to 2.509 V. While  $S_Y$  and  $S_X$ , have a bias of  $(2.495 \pm 0.010)$  V or in the range of 2.485 to 2.505 V. Results with yellow highlights are lower than the minimum range.  $S_Z$  and  $S_X$  average responses are all within the specified boundary. Two of the  $S_Y$  average responses for experiments 5 and 6 in both set-ups are 1 mV below the minimum range.

In this static measurement, however, the experiment pairs represent different main axis input sensors. The gravitational input for  $S_Z$  is applied in experiments 1, 2, 7, and 8; for  $S_Y$  in experiments 3, 4, 9, and 10; for  $S_X$  in experiments 5, 6, 11, and 12. Sensor mean values for gravitational input in each sensors main axis are highlighted in blue.

Table B.1: Static test matrix, original test configuration.

Exp	Orientation			Angular Position [°]		Recording Time [s]
	S <sub>Z</sub>	S <sub>Y</sub>	S <sub>X</sub>	Inner	Outer	
1				0	0	67.5
2				180	270	
3				270	270	
4				90	270	
5				0	180	
6				180	180	

B

Table B.2: Static test matrix, pivoted 180° test configuration.

Exp	Orientation			Angular Position [°]		Recording Time [s]
	Sz	Sy	Sx	Inner	Outer	
1				0		67.5
2				180		
3				270		
4				90		
5				270		
6				0		
6				180		

B

Table B.3: Static data mean from each measurement, vertical and inverted set, and sensor in original position setup.

Exp	Measurement	Mean each Measurement			Orientation	Mean each Set			Sensor Mean		
		$S_Z$	$S_Y$	$S_X$		$S_Z$	$S_Y$	$S_X$	$S_Z$	$S_Y$	$S_X$
1	1	2.492	2.487	2.485	A_+	2.492	2.486	2.485	2.493	2.487	2.489
	2	2.492	2.486	2.484							
	3	2.492	2.486	2.484							
2	4	2.495	2.487	2.495	A_-	2.494	2.487	2.494	2.494	2.485	2.487
	5	2.494	2.487	2.494							
	6	2.494	2.487	2.494							
3	7	2.487	2.486	2.494	A_+	2.487	2.486	2.494	2.494	2.485	2.487
	8	2.487	2.486	2.494							
	9	2.487	2.486	2.494							
4	10	2.501	2.485	2.480	A_-	2.501	2.485	2.480	2.494	2.485	2.487
	11	2.501	2.485	2.480							
	12	2.501	2.485	2.480							
5	13	2.471	2.476	2.485	A_+	2.471	2.476	2.485	2.488	2.484	2.486
	14	2.471	2.476	2.486							
	15	2.471	2.476	2.486							
6	16	2.505	2.492	2.487	A_-	2.505	2.491	2.487	2.490	2.483	2.488
	17	2.505	2.491	2.487							
	18	2.505	2.491	2.487							

Table B.4: Static data mean from each measurement, vertical and inverted set, and sensor in pivoted 180° position setup.

Exp	Measurement	Mean each Measurement			Orientation	Mean each Set			Sensor Mean		
		$S_Z$	$S_Y$	$S_X$		$S_Z$	$S_Y$	$S_X$	$S_Z$	$S_Y$	$S_X$
1	1	2.492	2.486	2.498	A_+	2.492	2.486	2.497	2.493	2.487	2.492
	2	2.492	2.486	2.497							
	3	2.492	2.485	2.496							
2	4	2.494	2.488	2.487	A_-	2.494	2.488	2.487	2.494	2.485	2.490
	5	2.494	2.488	2.487							
	6	2.494	2.488	2.486							
3	7	2.498	2.486	2.488	A_+	2.498	2.486	2.488	2.494	2.485	2.490
	8	2.498	2.486	2.488							
	9	2.498	2.486	2.488							
4	10	2.490	2.484	2.492	A_-	2.490	2.484	2.492	2.490	2.483	2.488
	11	2.490	2.484	2.492							
	12	2.490	2.484	2.492							
5	13	2.502	2.493	2.490	A_+	2.502	2.493	2.490	2.490	2.483	2.488
	14	2.502	2.493	2.490							
	15	2.502	2.493	2.490							
6	16	2.478	2.473	2.487	A_-	2.478	2.473	2.487	2.490	2.483	2.488
	17	2.478	2.473	2.487							
	18	2.478	2.473	2.487							

## B.2 TEMPERATURE MEASUREMENT

### B.2.1 STATIC TEMPERATURE CHECK ON THE TURNTABLE

The long static measurement results, comprise of an eight hours static measurement with only table mechanical lock (controller entirely off), a one-hour static measurement with the table interlock ON and mode OFF, and a one-hour static measurement with the table interlock ON and mode POSITION, are presented in this section. Temperature check was done every 30 min.

Two items to be observed in the long static measurements are the sensors response and the temperature fluctuation over an extended period of measurements. The angular accelerometer specification does not mention the sensor temperature range, only the environmental operating and storage temperature of  $-40-85^{\circ}\text{C}$ . Another specification related to temperature change is the Scale Factor Temperature Coefficient of a maximum  $0.05\%/^{\circ}\text{C}$ . The following sub-sections discuss the three experiments performed for the long static measurement.

#### 1. An Eight Hours Static Measurement with Only Table Mechanical Lock (Controller Entirely Off)

Procedure of the eight hours static measurement with only table mechanical lock (controller entirely off):

- Sensors are placed on the calibration table in the original setup. The table controller was off, only the mechanical lock of the outer axis holds the turntable in place.
- The measurement lasted eight hours.
- Sensor temperature was measured using FLUKE VT04 Visual Infrared IR Thermometer every 30 min, during the static measurement. The results are shown in [Table B.5](#) and [Figure B.1](#).

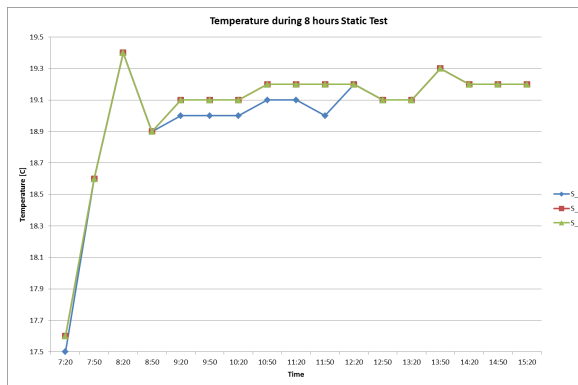


Figure B.1: Measured temperature during an 8 hours static test with mechanical lock.

The full eight hours static measurement data are presented in [Figure B.2](#). It is observed that a big spike occurs in  $S_Z$  and  $S_Y$  data, whereas a smaller one appears in  $S_X$  data. Since they took place approximately at the same time, the spikes might be caused by the external event.

Table B.5: Measured temperature during an 8 hours static test with mechanical lock.

Time	Sensor		
	S_Z	S_Y	S_X
7:20	17.5	17.6	17.6
7:50	18.6	18.6	18.6
8:20	19.4	19.4	19.4
8:50	18.9	18.9	18.9
9:20	19	19.1	19.1
9:50	19	19.1	19.1
10:20	19	19.1	19.1
10:50	19.1	19.2	19.2
11:20	19.1	19.2	19.2
11:50	19	19.2	19.2
12:20	19.2	19.2	19.2
12:50	19.1	19.1	19.1
13:20	19.1	19.1	19.1
13:50	19.3	19.3	19.3
14:20	19.2	19.2	19.2
14:50	19.2	19.2	19.2
15:20	19.2	19.2	19.2

B

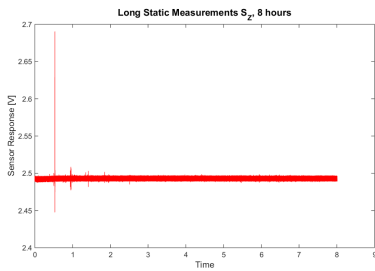
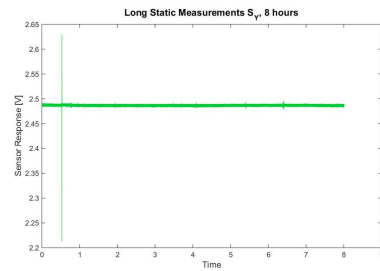
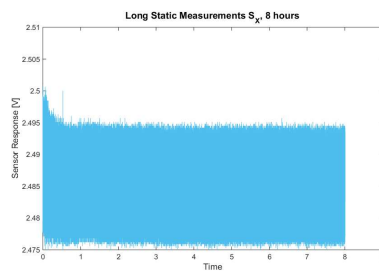
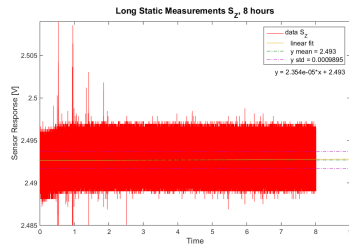
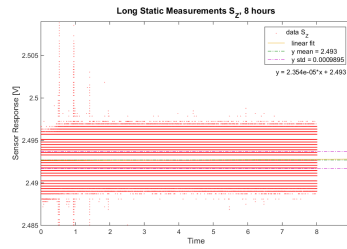
(a)  $S_Z$ (b)  $S_Y$ (c)  $S_X$ 

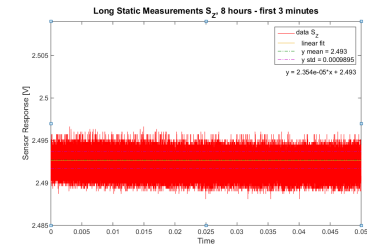
Figure B.2: Angular accelerometers 8 hours of data response in static measurement with mechanical lock, full scale.



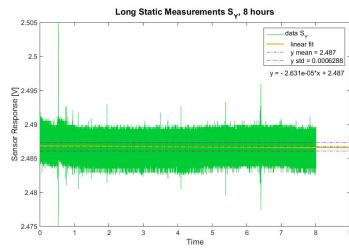
(a) Data with linear fit



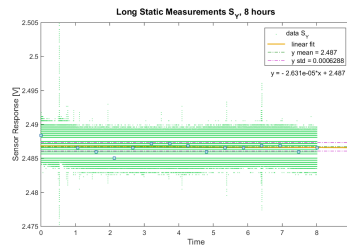
(b) Data points



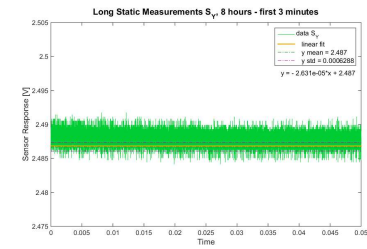
(c) First three minutes of data



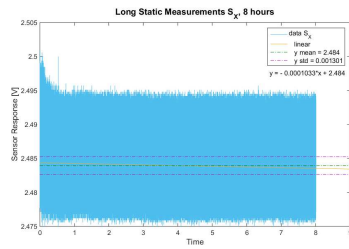
(d) Data with linear fit



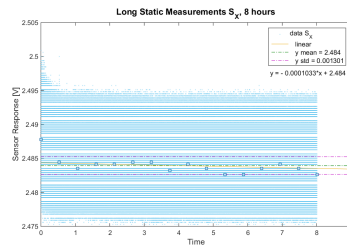
(e) Data points



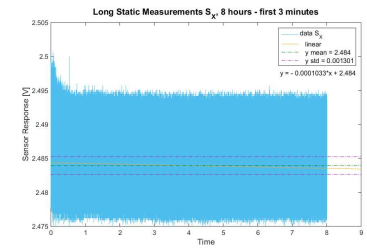
(f) First three minutes of data



(g) Data with linear fit



(h) Data points



(i) First three minutes of data

Figure B.3: Angular accelerometers 8 hours of data response in static measurement with mechanical lock, full scale.



Table B.6: Statistical properties 8 hours measurement with mechanical lock.

Stats	Sensor		
	S_Z	S_Y	S_X
Min	2.44751	2.213135	2.416077
Max	2.69043	2.629395	2.500916
Mean	2.492695	2.486718	2.483945
STD	9.90E-04	6.29E-04	0.001301
Var	9.79E-07	3.95E-07	1.69E-06
Range	0.24292	0.41626	0.084839

Close up to the sensor measurement range are provided in [Figure B.3](#), where the red colour represents  $S_Z$ , green for  $S_Y$ , and blue is  $S_X$ . Three graphs are displayed for each sensor, first is a full-time data, the second one is a data points depiction, and third is the first three minutes of the data for a quick look on a shorter measurement. A linear fit is added to the data, which indicates the data slope trend and mean throughout the measurement. Additionally, the standard deviation of the data is also supplied in the plot. Statistical properties from all sensors in the eight hours long measurement are shown in [Table B.6](#).

## 2. A one hour static measurement with the table interlock ON and mode OFF

This static measurement was performed with the table interlock ON, but mode OFF for both table axes. The duration of the measurement is one hour, and similarly, the sensor temperature is checked every 30 min. The temperature measurement results are presented in [Table B.7](#) and [Figure B.4](#). Close up to the sensor measurement range are provided in [Figure B.5](#). [Table B.8](#) give the statistical properties for the one-hour measurement, mode OFF.

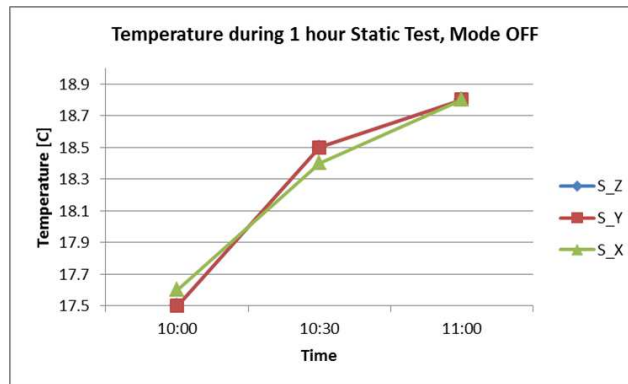
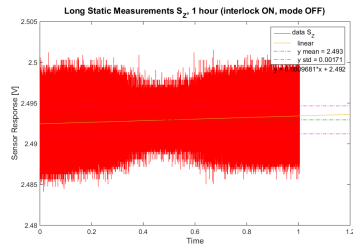
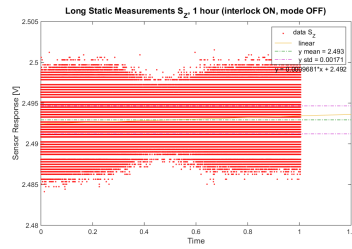


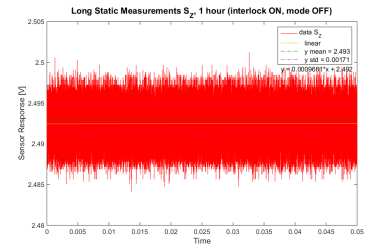
Figure B.4: Measured temperature during a 1 hour static test with interlock and mode OFF.



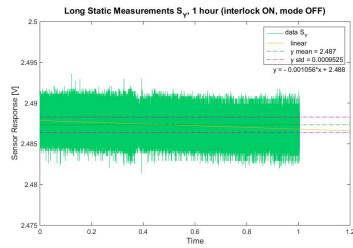
(a) Data with linear fit



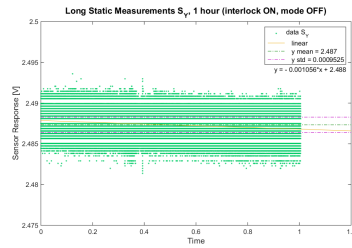
(b) Data points



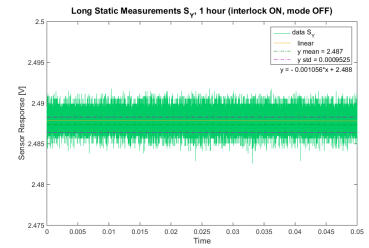
(c) First three minutes of data



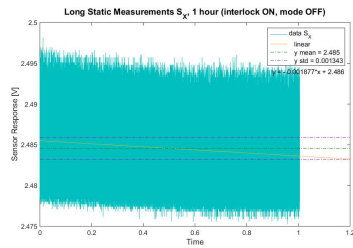
(d) Data with linear fit



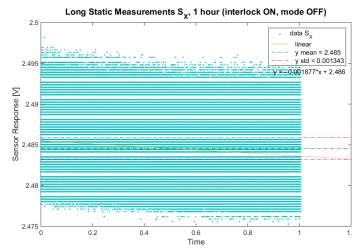
(e) Data points



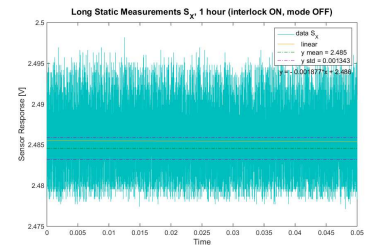
(f) First three minutes of data



(g) Data with linear fit



(h) Data points



(i) First three minutes of data

Figure B.5: Angular accelerometers 1 hours of data response in static measurement with interlock, mode OFF.

Table B.7: Measured temperature during a 1 hour static test with interlock and mode OFF.

Time	Sensor		
	S_Z	S_Y	S_X
10:00	17.5	17.5	17.6
10:30	18.5	18.5	18.4
11:00	18.8	18.8	18.8

B

Table B.8: Statistical properties 1 hour measurement with interlock ON, mode OFF.

Stats	Sensor		
	S_Z	S_Y	S_X
Min	2.484	2.481	2.475
Max	2.502	2.494	2.498
Mean	2.493	2.487	2.485
STD	1.710E-03	9.525E-04	1.343E-03
Var	2.923E-06	9.073E-07	1.805E-06
Range	0.017	0.012	0.023

3. A one hour static measurement with the table interlock ON and mode POSITION

This static measurement was performed with the table interlock ON, but mode OFF for both table axes. The duration of the measurement is one hour, and similarly, the sensor temperature is checked every 30 min. The temperature measurement results are presented in Table B.9 and Figure B.6. Close up to the sensor measurement range are provided in Figure B.7. Table B.10 give the statistical properties for the one-hour measurement, mode POSITION.

Table B.9: Measured temperature during a 1 hour static test with interlock and mode POSITION.

Time	Sensor		
	S_Z	S_Y	S_X
11:10	19	19	19
11:40	19.3	19.4	19.2
12:10	19.5	19.5	19.5

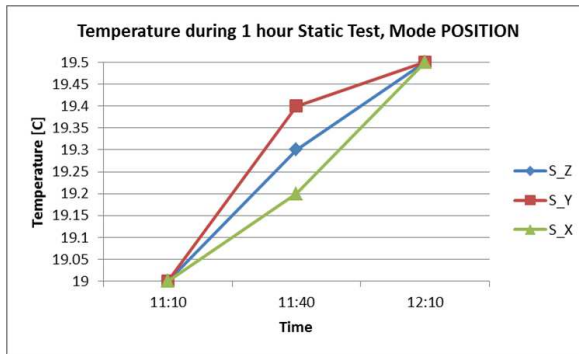
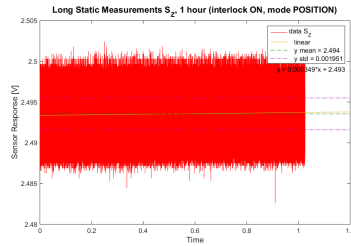


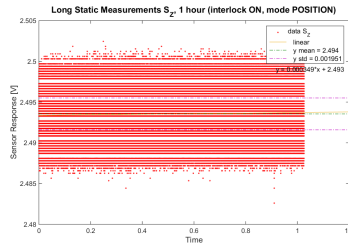
Figure B.6: Measured temperature during a 1 hour static test with interlock and mode POSITION.

Table B.10: Statistical properties 1 hour measurement with interlock ON, mode POSITION.

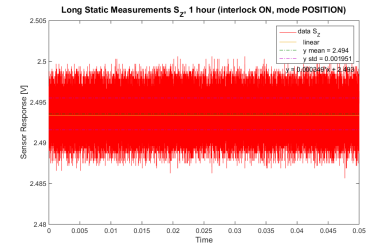
Stats	Sensor		
	S_Z	S_Y	S_X
Min	2.483	2.481	2.475
Max	2.502	2.492	2.496
Mean	2.494	2.487	2.484
STD	1.95E-03	8.10E-04	1.22E-03
Var	3.81E-06	6.56E-07	1.48E-06
Range	0.020	0.010	0.021



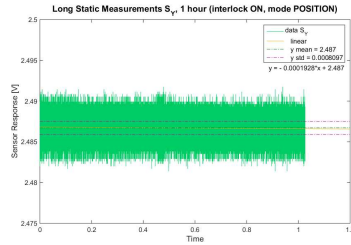
(a) Data with linear fit



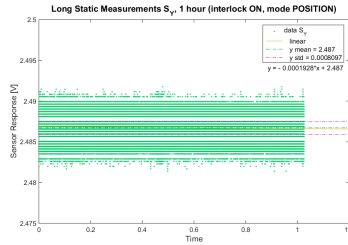
(b) Data points



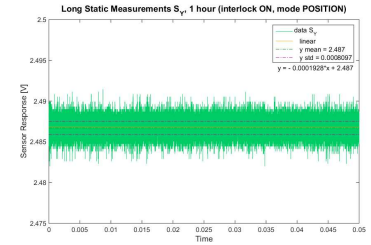
(c) First three minutes of data



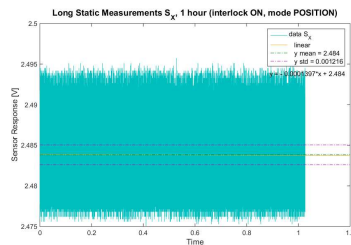
(d) Data with linear fit



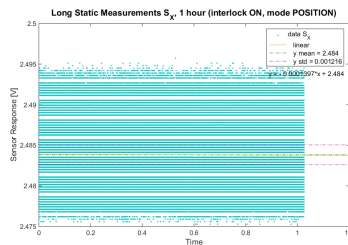
(e) Data points



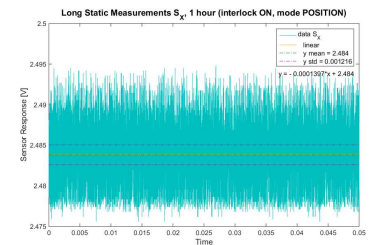
(f) First three minutes of data



(g) Data with linear fit



(h) Data points



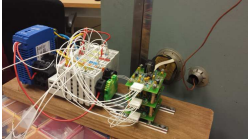
(i) First three minutes of data

Figure B.7: Angular accelerometers 1 hours of data response in static measurement with interlock, mode POSITION.

### B.2.2 STATIC TEMPERATURE CHECK IN AN ENVIRONMENTAL CHAMBER TEST SET-UP

Arrangement of the sensors and test equipments are as follow:

Table B.11: Setup of the sensors and equipment for the static temperature test

	<p>Angular accelerometers are secured on the mounting block and placed on the middle rack inside the temperature chamber. Power and data connectors are passed through an access hole with the insulator on the side of the chamber.</p>
	<p>The sensor data acquisition system is located outside the temperature chamber and next to the access hole, where it connects to the sensor's power and data cables.</p>
	<p>Temperature input is regulated from the control panel on the outside of the chamber. The first input function is a toggle to switch between heat and mechanical refrigerator. The second is a button to select temperature input in the <math>-70</math> to <math>175</math> °C range.</p>
	<p>A thermometer equips the temperature chamber. It has a probe installed in the inner part of the door as can be seen in the first figure, and a display on the outer side of the door.</p>
	<p>Since the built-in thermometer accuracy has deteriorated, the temperature will be monitored using a multimeter (Fluke 179 True RMS Multimeter). The device provides a cable probe inserted via an access hole on the side of the chamber.</p>

Four additional modification on the setup:

1. A bond-ply which is thermally conductive and electrically isolating is applied between the sensor housing and Fluke's probe. Then, paper tape wraps the other side of the probe.
2. Silica gel packages are placed in the chamber instead of a household-grade dehumidifier. Ten bags @10 gram are used throughout the measurement, during both the cooling and heating phase. On a side note, it is not known whether there is condensation forming at the coldest point or not, since the chamber is not opened for inspection

until the end of the test.

3. The target temperature is no longer based on the chamber's temperature input button but the Fluke measurement. Additionally, this goal temperature does not need to be at the specific objective; only the indicated, stabilised value.
4. The full test matrix is conducted continuously on the same day and without opening the chamber.

The following procedure is employed and resulting in 15 measurement points. The experiment condition and measured temperature from two tests are presented in [Table B.12](#).

- Initial closed chamber condition.

The first measurement took place without any cooling nor heating, but with the chamber closed and 30 min after the sensor power is turned on.

- Lower temperature condition.

For the cooling phase between the initial temperature to  $-20^{\circ}\text{C}$  (test number 2 to 5), the sensor is cooled down using the chamber's refrigeration function. The cooling was done first with an input of  $5\text{--}10^{\circ}\text{C}$  lower than the target to help to speed the process up. Once Fluke's indication reaches the target temperature, the input button is stabilised at the aimed temperature for 15 min. The fridge switch is turned off, and one minute later, the sensors' response are recorded.

In test number 6 to 9, the sensors' temperature are raised using the chamber's heater function until Fluke indicates the target. The heating involved a  $10\text{--}20^{\circ}\text{C}$  higher input. Subsequently, it is switched to refrigeration mode and stabilised for 15 min. Similar to before, the data recording is executed one minute after the fridge is turned off. An exception in test number 9, although lower than the initial temperature, it is stabilised using the heater function for 15 min.

- Higher temperature condition.

In the first part (test number 10 to 12), the sensors are heated with a  $10\text{--}20^{\circ}\text{C}$  higher input then maintained a target temperature using the chamber's heater for 15 min. Again, the data logging performed one minute after the input is shut off.

On the contrary, test number 13 to 14 employ the chamber's refrigeration function with a  $10\text{--}20^{\circ}\text{C}$  lower input. Afterwards, sustained for 15 min at the target temperature using the heater function. One minute after the heater is turned off; the data is recorded.

- In the last test, the data is taken approximately 45 min later to allow the chamber's temperature to return to the normal condition.

The sensor responses are measured at the stabilised temperature described in the 'Fluke Probe' column of [Table B.12](#) for around 70 s, which results in 140000 data points. Nevertheless, only  $2^{17}$  or 131072 data points are extracted for the analysis.

### SENSOR RESPONSES

Time history responses from all measurement points of the first test are shown in [Figure B.8](#), and the second test in [Figure B.10](#). The factory specified range are  $2.489\text{--}2.509\text{ V}$  for  $S_Z$  (red) and  $2.485\text{--}2.505\text{ V}$  for  $S_Y$  (green) and  $S_X$  (blue). Nevertheless, the sensor output is presented on the range of 2.4 to 2.6 in Volt, to include the oscillation range.

[Figure B.9](#) display the PSD of the sensor response data from the first test. Meanwhile, [Figure B.11](#) shows the second test PSD. The plot is zoomed in the level  $10^{-3}$  for  $S_Z$  (red),

Table B.12: Static temperature test condition, contact measurement

No	Temperature Input	Chamber Thermometer		Fluke Probe	
		Test 1	Test 2	Test 1	Test 2
1	-	21	21	22.2	22.7
2	20	6	5	7.5	-0.5
3	10	-4	-5	-2.1	-0.9
4	0	-15	-11	-11.3	-9.2
5	-10	-22	-23	-21.3	-18.7
6	0	-13	-15	-14.1	-11.5
7	10	-5	-5	-5.4	-1.8
8	20	3	4	4.1	6.8
9	20	20	20	20.4	20.1
10	30	30	28	29.3	28.5
11	40	37	36	38.3	38.6
12	50	45	44	47.6	47.2
13	40	35	35	38.2	38.4
14	30	27	28	29.4	29.8
15	20	20	21	22.2	21.4



also  $10^{-1}$  for  $S_Y$  (green) and  $S_X$  (blue), to show the oscillation frequency in the data. The DC component is at the level of  $10^6$ .

The following discuss observation of the test result.

- $S_Z$  seems to have much lower noise level than the other two sensors. This is confirmed by the mean and standard deviation presented in [Table B.13](#) and [Table B.14](#).
- In some of the data sets, peaks appears at certain points. The peaks are possibly due to the unisolated foundation of the temperature chamber so that any shifting loads, expansion or contraction and vibrations happen in the building can be picked up by the sensor. The effect was most profoundly visible on  $S_Y$  and  $S_X$  data, which is most likely as a result of the sensor orientation. Their sensitive axis is parallel to the floor, which makes them susceptible to any fluctuations.
- $S_Z$  sensitive axis direction that is perpendicular to the floor does not make it immune to the building impact. The data also reflects this visible effect, especially when it is big enough, such as in record number 7 of the first test and number 10 of the second test.
- The PSD zoom-in plot in [Figure B.9](#) and [Figure B.11](#) show various oscillation between 20 – 40 Hz frequency.  $S_Z$  level in average is  $10^9$  lower than the DC component, whereas  $S_Y$  and  $S_X$  are  $10^7$  lower than the DC component.
- Two of the response data sets are inspected in [Figure B.12](#). For this purpose, measurement #1 and #7 of test 1 are compared at a one-second interval (2000 samples), in the range of 2.4 to 2.6 Volt. Additionally, converted value in  $deg/s^2$  are presented to illustrate the magnitude of response. For the second test, measurement #1 is compared to #10 in [Figure B.13](#). Some oscillations are visible in these sequences, which suggest that the data did not represent a white noise as it should in the static measurement.

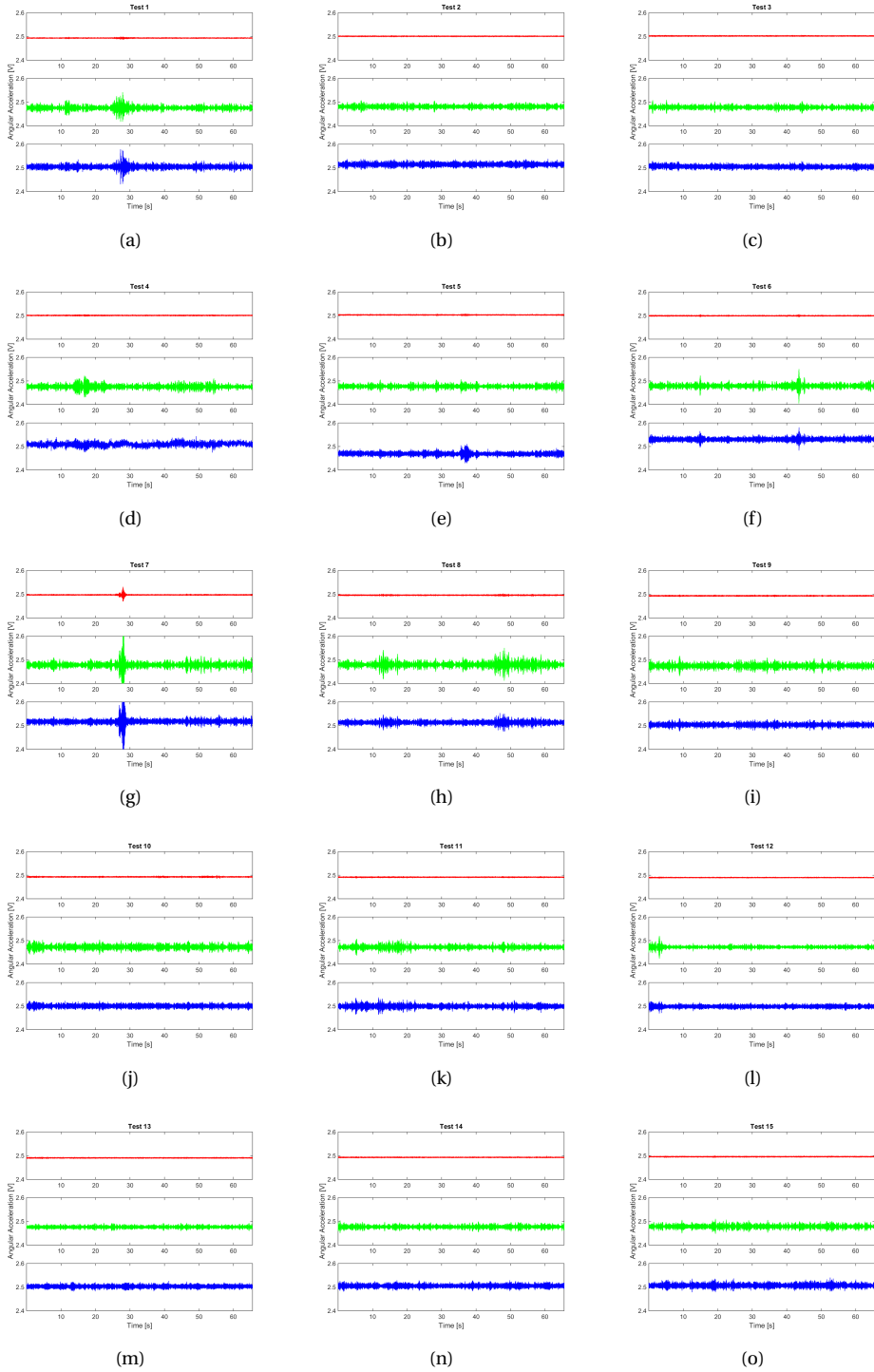
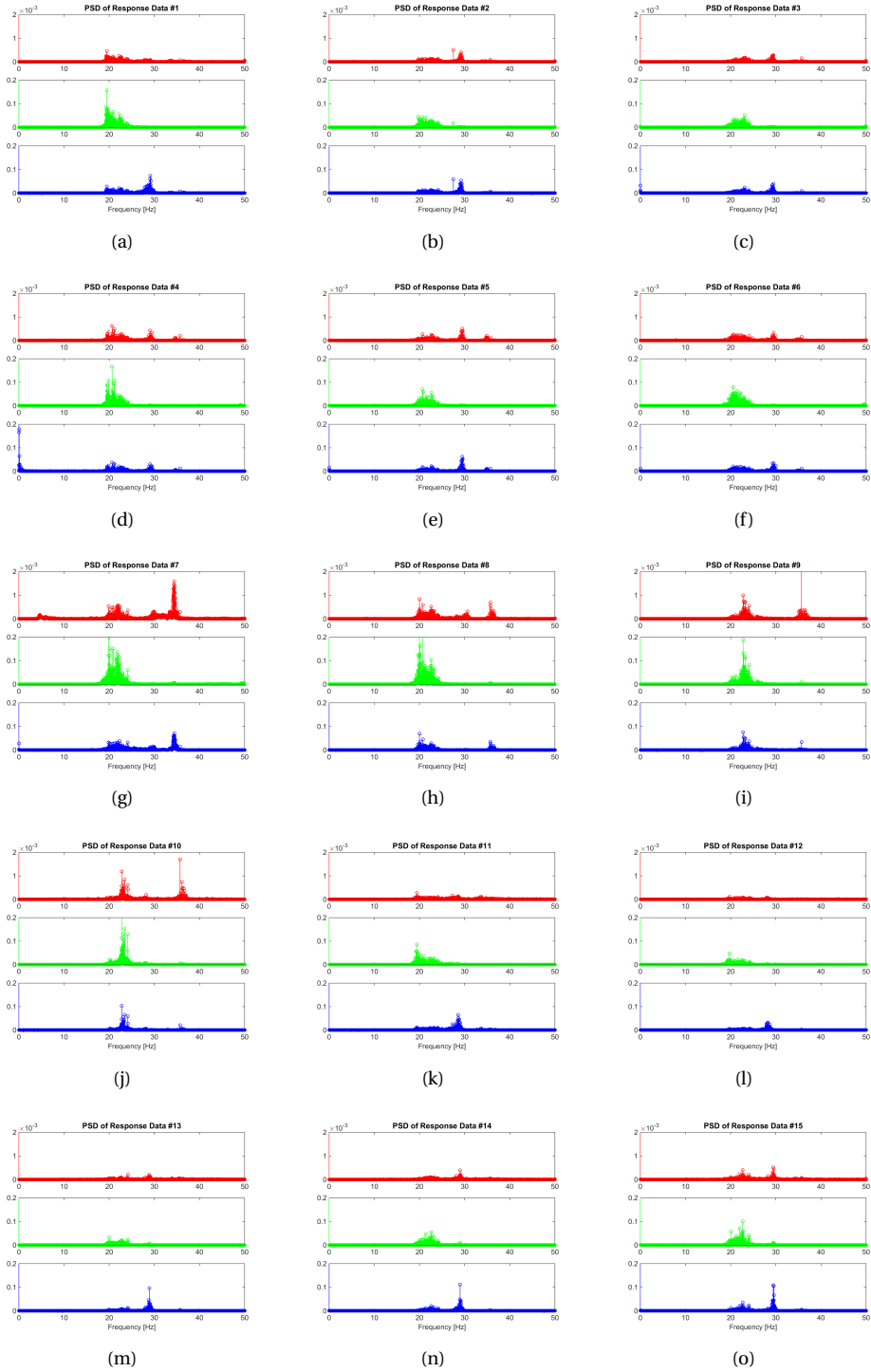


Figure B.8: First test sensor response:  $S_Z$  (red),  $S_Y$  (green),  $S_X$  (blue)



B

Figure B.9: PSD of sensor response:  $S_Z$  (red),  $S_Y$  (green),  $S_X$  (blue)

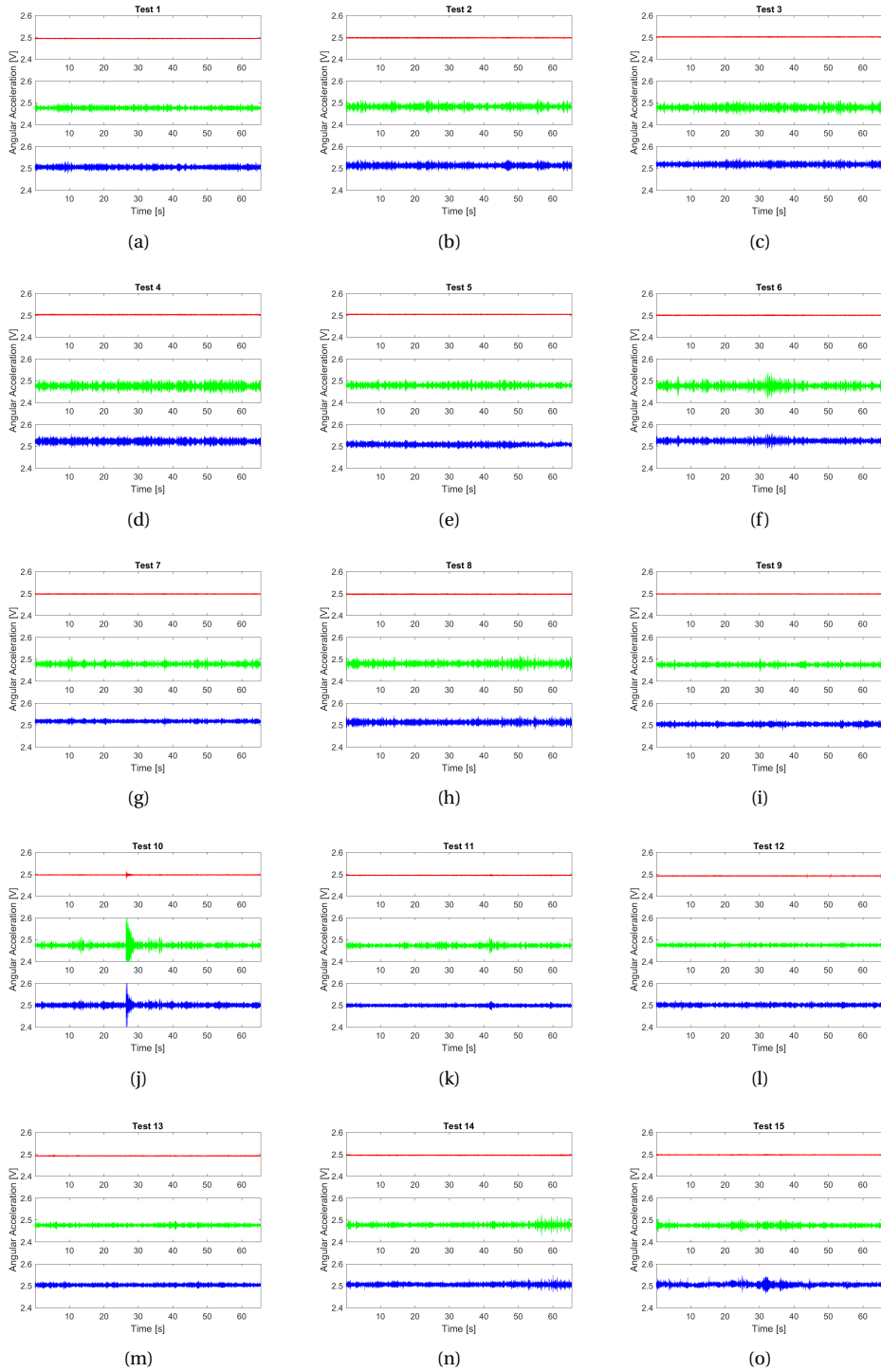


Figure B.10: Second test sensor response:  $S_Z$  (red),  $S_Y$  (green),  $S_X$  (blue)

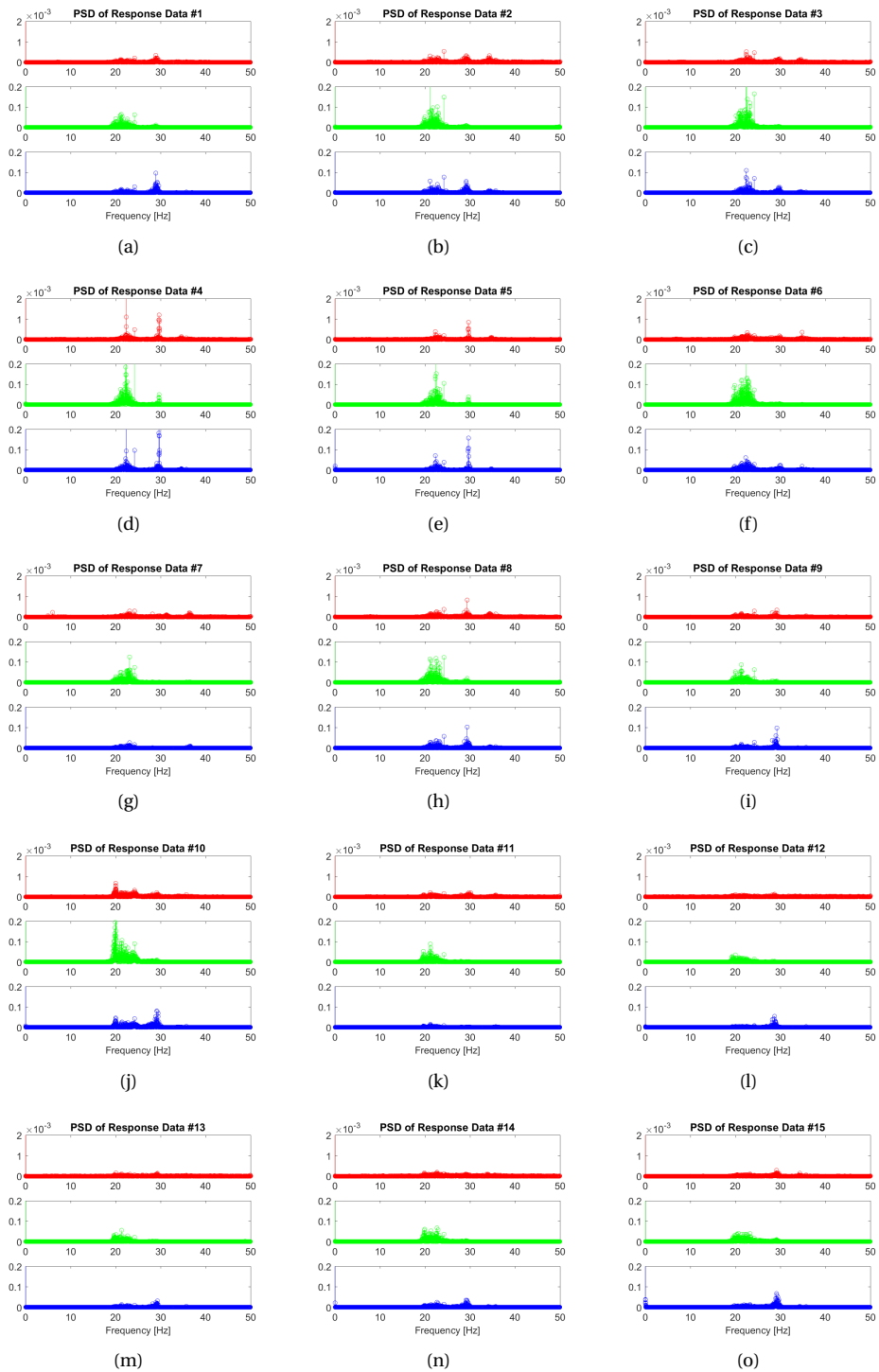
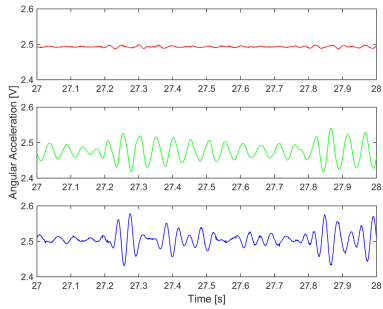
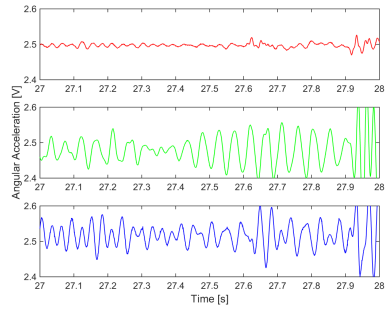


Figure B.11: PSD of sensor response:  $S_Z$  (red),  $S_Y$  (green),  $S_X$  (blue)

B



(a) Test No. 1 (V)



(b) Test No. 7 (V)

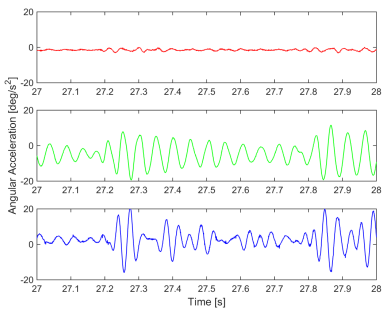
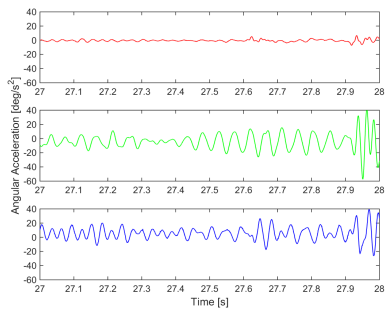
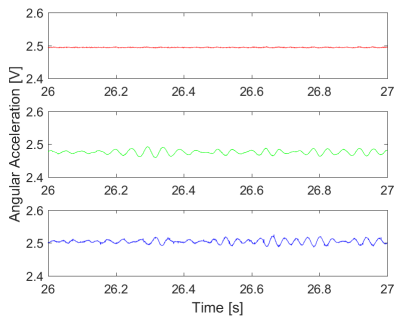
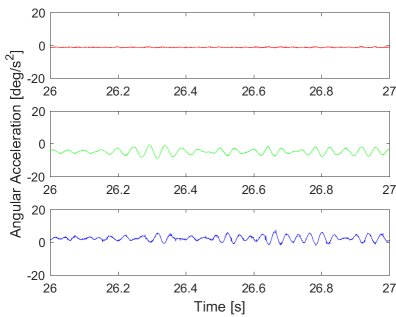
(c) Test No. 1 (°/s<sup>2</sup>)(d) Test No. 7 (°/s<sup>2</sup>)

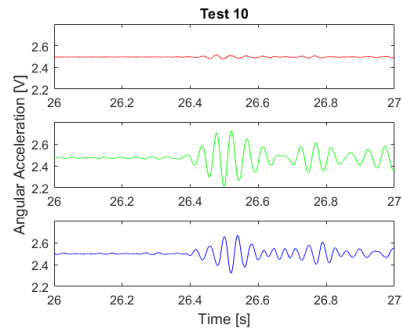
Figure B.12: Zoom of sensor response in test number 1 and 7



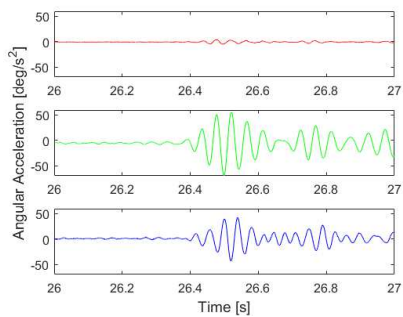
(a) Test No. 1 (V)



(c) Test No. 1 (°/s<sup>2</sup>)



(b) Test No. 10 (V)



(d) Test No. 10 (°/s<sup>2</sup>)

Figure B.13: Zoom of sensor response in test number 1 and 10



Table B.13: Mean and Standard Deviation of the sensors response from each measurement

Test No.	Mean						Standard Deviation					
	$S_Z$		$S_Y$		$S_X$		$S_Z$		$S_Y$		$S_X$	
	V	%s	V	%s	V	%s	V	%s	V	%s	V	%s
1	2.493	-1.484	2.476	-4.857	2.505	2.382	0.00100	0.248	0.00886	2.207	0.00731	1.821
2	2.501	0.410	2.481	-3.559	2.514	4.805	0.00099	0.246	0.00644	1.604	0.00580	1.445
3	2.502	0.754	2.478	-4.264	2.505	2.532	0.00098	0.244	0.00620	1.545	0.00535	1.333
4	2.501	0.400	2.476	-4.843	2.509	3.524	0.00109	0.271	0.00897	2.234	0.00723	1.801
5	2.503	0.969	2.477	-4.500	2.469	-6.535	0.00099	0.246	0.00673	1.677	0.00587	1.463
6	2.499	0.046	2.479	-4.048	2.530	8.777	0.00102	0.255	0.00809	2.015	0.00580	1.446
7	2.497	-0.497	2.478	-4.184	2.517	5.431	0.00166	0.413	0.01251	3.116	0.00973	2.424
8	2.496	-0.805	2.479	-3.924	2.513	4.468	0.00121	0.301	0.01144	2.851	0.00641	1.598
9	2.493	-1.498	2.474	-5.206	2.503	2.103	0.00113	0.281	0.00883	2.200	0.00602	1.499
10	2.493	-1.510	2.473	-5.600	2.500	1.310	0.00117	0.291	0.00851	2.119	0.00581	1.447
11	2.492	-1.835	2.472	-5.695	2.499	0.990	0.00100	0.248	0.00706	1.759	0.00635	1.581
12	2.490	-2.237	2.472	-5.617	2.498	0.774	0.00088	0.219	0.00514	1.281	0.00449	1.118
13	2.491	-2.067	2.476	-4.743	2.503	1.941	0.00097	0.242	0.00469	1.170	0.00490	1.221
14	2.493	-1.524	2.477	-4.555	2.505	2.562	0.00096	0.240	0.00600	1.493	0.00546	1.360
15	2.496	-0.824	2.478	-4.179	2.507	2.981	0.00102	0.255	0.00718	1.789	0.00651	1.622

## B

### SENSOR STATISTICS

Mean and Standard Deviation of the data in each test in V and %s are presented in [Table B.13](#) and [Table B.14](#).

Mean of the data in Volt is exhibited in [Figure B.14](#). Here, all  $S_Z$ 's response are within the range, whereas all of  $S_Y$ 's are below the range, and about half of the  $S_X$ 's are above the range. [Figure B.15](#) illustrate the mean in  $deg/s^2$ . For the standard deviation depicted in [Figure B.16](#), only  $S_Z$ 's are below the  $\leq 3mV$  line.

Several remarks after observing the mean and standard deviation plot:

- $S_Y$  and  $S_X$  have a 'similar' behaviour in contrast to  $S_Z$ . Both sensors mean values are either at the border or outside of the sensor tolerance range. Furthermore, both their standard deviation are above the noise level specification. These high standard deviation values are likely due to the influence of the external factor. Nevertheless, the likeness might also as a result of their installation in the mounting block.
- The data demonstrate that the change of temperature affects the sensors' responses as can be seen in [Figure B.14](#). Although the change happens in a small range, the trends associate higher mean value in the cool points and lower mean value at the higher temperature.
- The repeated test, depicted by the dash-dot line, confirm the result/ trend from the first test.

### B.2.3 ADDITIONAL STATIC TEMPERATURE CHECK IN AN ENVIRONMENTAL CHAMBER

The current test consist of three settings:

1. Chamber plugged-off.

In the previous measurements the chamber is turned off after 15 minutes, then one minute afterwards the data is recorded. In this test, the chamber is plugged off completely from the power source. The setup is shown in [Figure B.17](#).

Table B.14: Mean and Standard Deviation of the sensors response from each measurement, second experiment

Test No.	Mean						Standard Deviation					
	$S_Z$		$S_Y$		$S_X$		$S_Z$		$S_Y$		$S_X$	
	V	°/s	V	°/s	V	°/s	V	°/s	V	°/s	V	°/s
1	2.494	-1.204	2.476	-4.838	2.504	2.305	0.00087	0.217	0.00677	1.685	0.00598	1.489
2	2.497	-0.390	2.481	-3.381	2.512	4.163	0.00113	0.281	0.00937	2.333	0.00728	1.813
3	2.501	0.601	2.478	-4.302	2.517	5.452	0.00104	0.260	0.01052	2.620	0.00699	1.742
4	2.502	0.855	2.475	-5.003	2.521	6.592	0.00106	0.265	0.01184	2.950	0.00842	2.096
5	2.504	1.171	2.478	-4.127	2.507	3.047	0.00092	0.229	0.00868	2.163	0.00612	1.525
6	2.500	0.171	2.476	-4.722	2.524	7.151	0.00104	0.260	0.01168	2.910	0.00714	1.780
7	2.497	-0.462	2.478	-4.356	2.516	5.301	0.00102	0.254	0.00786	1.959	0.00421	1.048
8	2.496	-0.660	2.479	-3.873	2.512	4.185	0.00108	0.269	0.00955	2.379	0.00695	1.732
9	2.497	-0.458	2.474	-5.144	2.503	1.958	0.00090	0.223	0.00683	1.700	0.00553	1.379
10	2.496	-0.698	2.473	-5.488	2.499	1.003	0.00111	0.276	0.01348	3.357	0.00861	2.144
11	2.494	-1.147	2.472	-5.711	2.498	0.652	0.00093	0.233	0.00693	1.726	0.00360	0.896
12	2.491	-1.883	2.474	-5.236	2.500	1.205	0.00095	0.238	0.00500	1.244	0.00488	1.215
13	2.492	-1.730	2.475	-4.863	2.503	1.913	0.00092	0.229	0.00551	1.372	0.00441	1.098
14	2.495	-0.982	2.477	-4.516	2.505	2.481	0.00102	0.255	0.00762	1.897	0.00589	1.467
15	2.497	-0.580	2.474	-5.136	2.504	2.322	0.00090	0.225	0.00707	1.762	0.00688	1.713

B

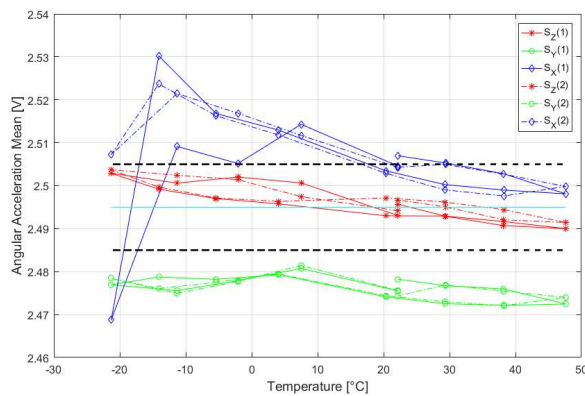


Figure B.14: Mean sensor responses

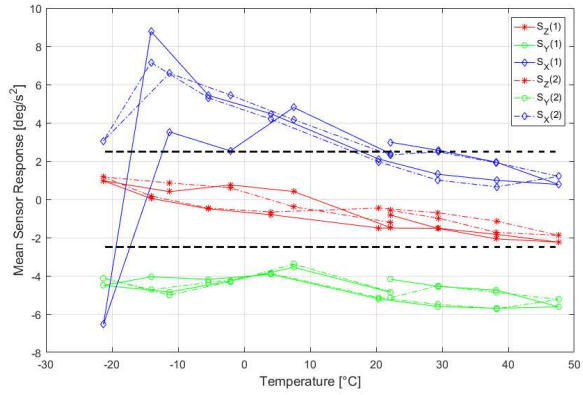


Figure B.15: Converted values of mean sensor responses

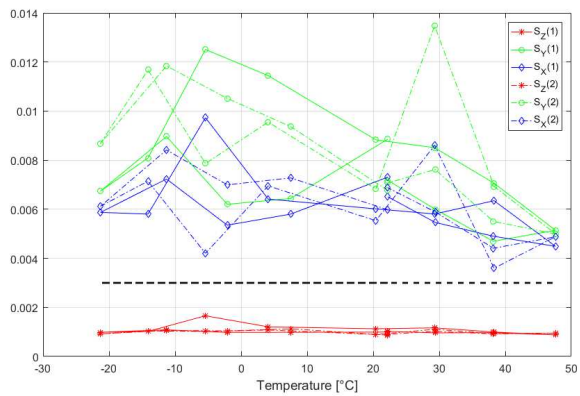


Figure B.16: Minimum sensor responses

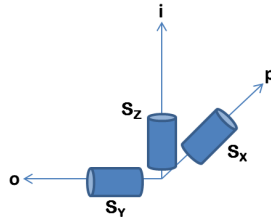


Figure B.17: Normal setup

### 2. Tilted mounting.

The sensor mounting is tilted  $90^\circ$  with the rotation axis of  $o$ . The setup is shown in [Figure B.18](#), however, due to the limitation in the chamber, the sensors are not aligned perfectly with the reference axis.

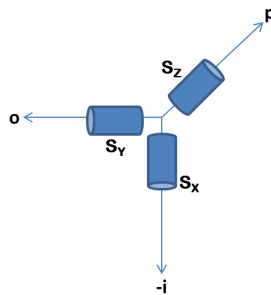


Figure B.18: Tilted mounting setup

### 3. Swapped sensors.

Only two sensors,  $S_Z$  and  $S_Y$ , are switched, but connected to their respective channels as before. Nevertheless,  $S_Z$  cannot fit into  $S_Y$  mounting hole since it's label still on. Therefore,  $S_Z$  changed its orientation, but not in the same mounting position as  $S_Y$ . The setup is shown in [Figure B.19](#).

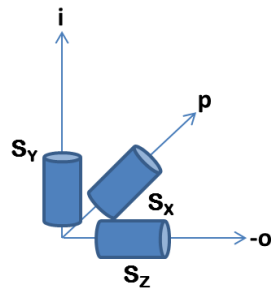


Figure B.19: Swapped sensors setup

Table B.15: Static temperature test condition, contact measurement

No	Temperature Input	Chamber Thermometer	Fluke Probe	Remarks
1	-	21	22.7	Chamber plugged-off
2	20	6	11.2	
3	30	30	31	
1	-	21	22.7	Tilted mounting
1	-	22	22.1	$S_Z$ and $S_Y$ switched
2	20	7	9	
3	30	28	28.4	

The temperature treatment in the above items are referring to the developed procedure in Progress Report 97. [Table B.15](#) contains the current measurement condition.

## B

### SENSOR RESPONSES

Time history responses from all measurement points and their respective PSDs of the plugged-off test are shown in [Figure B.20](#), the tilted mounting test in [Figure B.21](#), and the second test in [Figure B.22](#). The factory specified range are 2.489–2.509 V for  $S_Z$  (red) and 2.485–2.505 V for  $S_Y$  (green) and  $S_X$  (blue). Nevertheless, the sensor output is presented on the range of 2.4 to 2.6 in Volt, to include the oscillation range as well as to compare it with the previous temperature test in Progress Report 97.

The PSD plot of the first group is zoomed in the level  $10^{-3}$  for  $S_Z$  (red), also  $10^{-1}$  for  $S_Y$  (green) and  $S_X$  (blue), to show the oscillation frequency in the data. In the case of tilted mounting, the level are  $10^0$  for  $S_Z$  (red),  $10^{-1}$  for  $S_Y$  (green), and  $10^{-3}$  for  $S_X$  (blue). For the swapped sensors setup, the PSD is zoomed in the level  $10^{-3}$  for  $S_Y$  (green), also  $10^{-1}$  for  $S_Z$  (red) and  $S_X$  (blue). The DC component is at the level of  $10^5$ .

The following discuss observation of the test result.

- [Figure B.20](#)  
 $S_Z$  have much lower noise level than the other two sensors, similar to previous record. Plugging off the chamber seems not to have any effect on the data.
- [Figure B.21](#)  
With  $S_Z$  now parallel to the floor, it shows higher noise level than  $S_X$ .  $S_Y$  that is also parallel to the floor shows one level lower PSD than  $S_Z$ .
- [Figure B.22](#)  
 $S_Z$  and  $S_X$  demonstrate higher noise level than  $S_Y$ , their PSD confirm the similarity.  $S_Y$  sensitive axis here is perpendicular to the floor, its PSD has the same level as  $S_Z$  in [Figure B.20](#).
- No big peaks in the data.

### SENSOR STATISTICS

Mean of the data in Volt is exhibited in [Figure B.23](#) to [Figure B.25](#), standard deviation in [Figure B.26](#) to [Figure B.28](#), and root-mean-squared in [Figure B.29](#) to [Figure B.31](#). Observations from the previous record are included in the dash-dot line form.

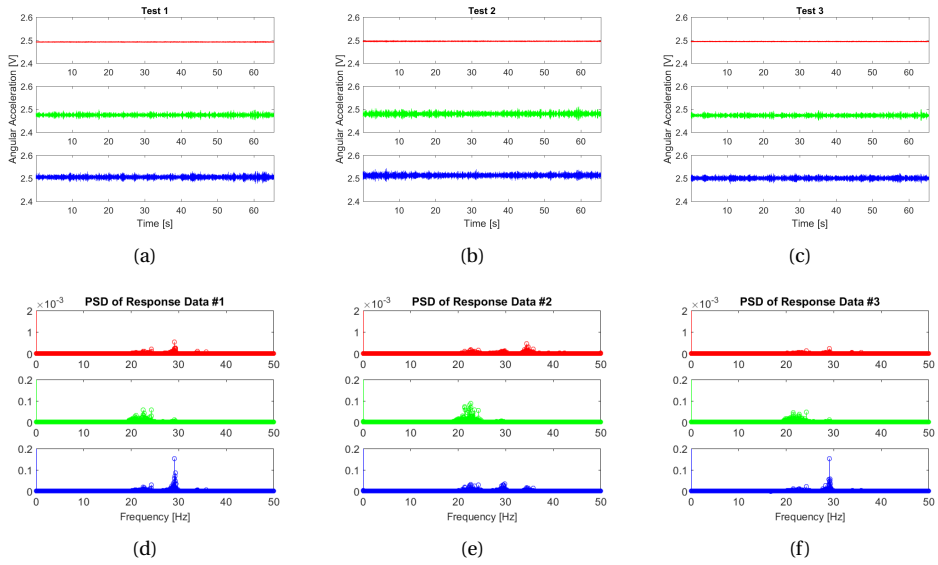


Figure B.20: Chamber plugged-off sensor response and PSD:  $S_Z$  (red),  $S_Y$  (green),  $S_X$  (blue)

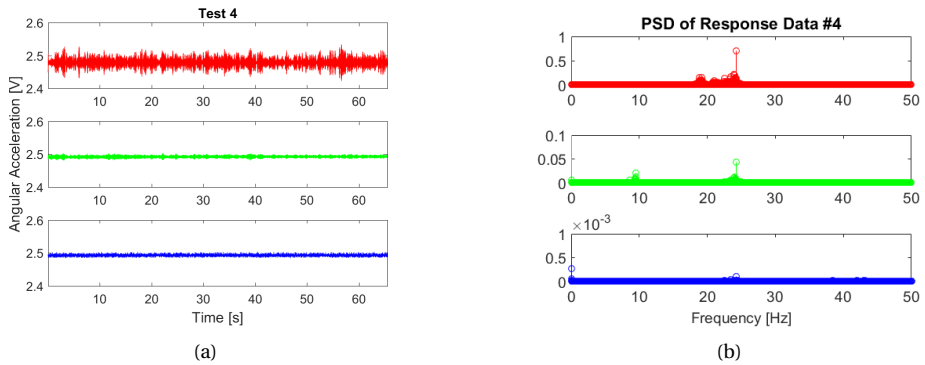


Figure B.21: Tilted mounting sensor response and PSD:  $S_Z$  (red),  $S_Y$  (green),  $S_X$  (blue)

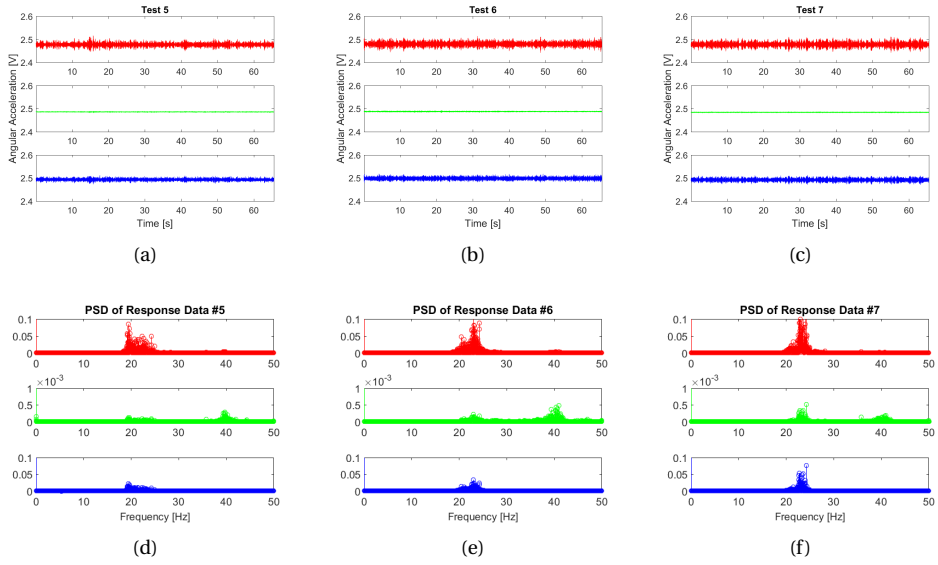


Figure B.22: Swapped setup sensor response and PSD:  $S_Z$  (red),  $S_Y$  (green),  $S_X$  (blue)

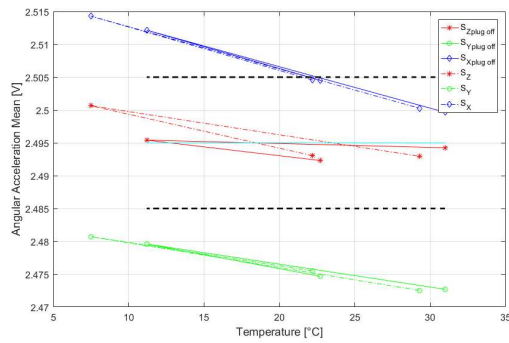


Figure B.23: Mean sensor responses - Plugged-off test

B

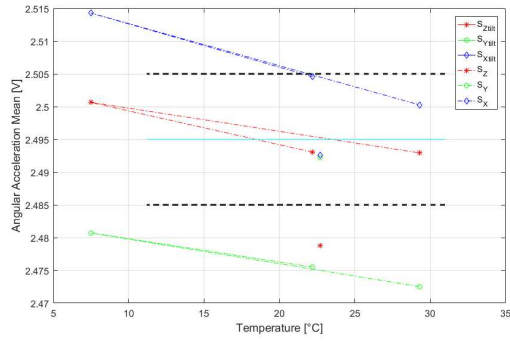


Figure B.24: Mean sensor responses - Tilted mounting test

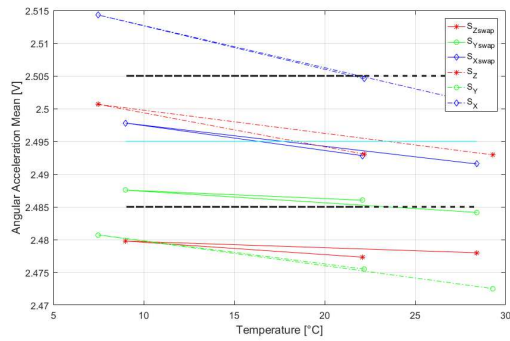


Figure B.25: Mean sensor responses - Swapped sensors test

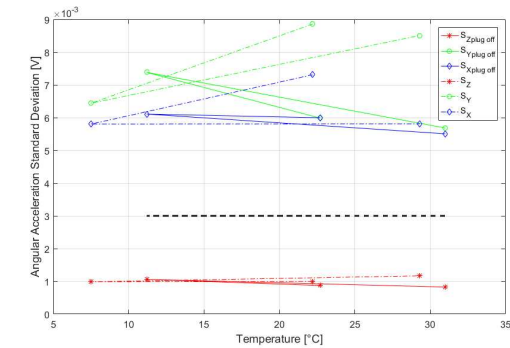


Figure B.26: STD sensor responses - Plugged-off test



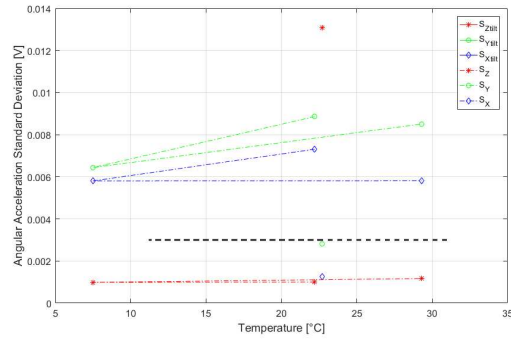


Figure B.27: STD sensor responses - Tilted mounting test

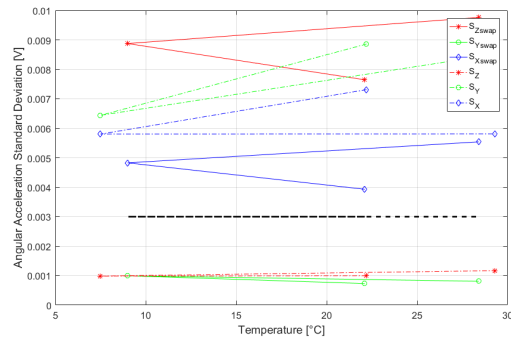


Figure B.28: STD sensor responses - Swapped sensors test

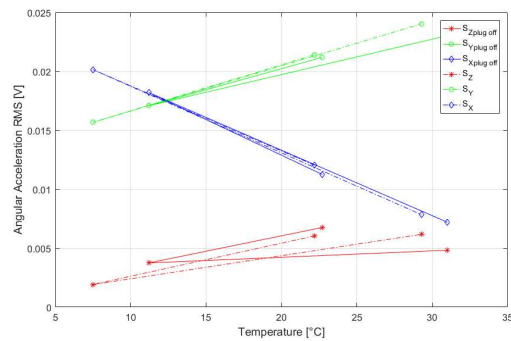


Figure B.29: STD sensor responses - Plugged-off test

B

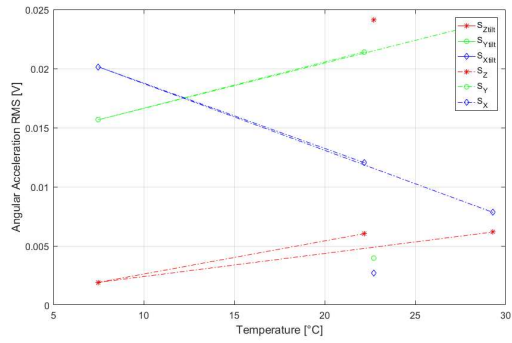


Figure B.30: STD sensor responses - Tilted mounting test

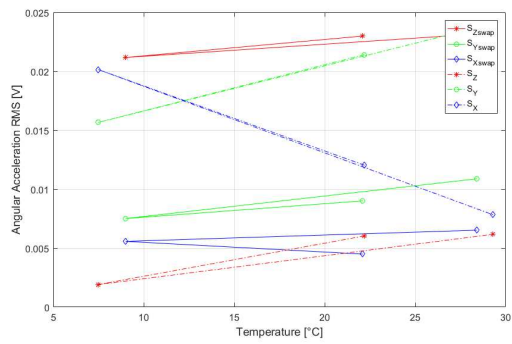


Figure B.31: STD sensor responses - Swapped sensors test



# C

## DYNAMIC TESTS

### C.1 CROSS-AXIS SENSITIVITY AND MISALIGNMENT

This part is a supplement to [Chapter 5](#), providing details on the input axis misalignment analysis of angular accelerometers in an AAMU. [Table C.1](#) lists the original position sets, while [Table C.2](#) tabulates the 180° pivoted position sets. Each sensor acquires its sensitive axis spectral response,  $P_z$ , and non-sensitive axes spectral responses,  $P_y$  and  $P_x$ , from the average of three different measurements.

As mentioned in [Section 5.3.2](#), the angular accelerometer's sensitive and non-sensitive responses are acquired from three experiments. For instance, the first column in [Table C.1](#) shows the  $S_Z$  responses in Set *A*, where the first row is the  $z$  axis response, whereas the second row encloses its  $y$ -axis response and the third row is  $x$ -axis response.

Table C.1: Average sensor's spectral responses in all experiments and original position sets.

Set	Exp	$S_Z$	$S_Y$	$S_X$
<i>A</i>	1	16.439 + 26.271i	0.069 + 0.120i	-0.036 - 0.063i
	2	-0.119 + 0.200i	-9.970 - 31.718i	0.043 + 0.092i
	3	0.050 - 0.461i	-0.189 - 0.043i	-66.503 - 9.089i
<i>C</i>	1	0.748 - 33.358i	0.013 - 0.124i	-0.00399 + 0.090i
	2	-0.166 + 0.199i	-9.922 - 37.859i	0.067 + 0.133i
	3	-0.364 + 0.093i	0.084 + 0.172i	17.107 + 40.942i
<i>E</i>	1	9.239 - 22.677i	0.0512 - 0.095i	-0.022 + 0.053i
	2	-0.166 - 0.192i	42.269 + 11.355i	-0.128 - 0.157i
	3	-0.589 - 0.127i	-0.065 + 0.363i	-24.819 + 69.360i
<i>G</i>	1	-13.241 - 88.537i	-0.040 - 0.353i	0.0304 + 0.228i
	2	0.060 - 0.526i	40.295 + 53.575i	-0.219 - 0.244i
	3	0.247 + 0.310i	0.141 - 0.176i	40.363 - 42.053i

Table C.2: Average sensor's spectral responses in all experiments and 180° pivoted position set.

Set	Exp	$S'_Z$	$S'_Y$	$S'_X$
<i>B</i>	4	2.723 + 21.421i	-0.004 - 0.0788i	-0.002 + 0.075i
	5	0.416 + 0.241i	58.704 - 24.017i	0.089 - 0.024i
	6	-0.247 + 0.179i	0.004 - 0.016i	-19.070 - 34.860i
<i>D</i>	4	-70.427 + 62.775i	0.266 - 0.204i	-0.245 + 0.191i
	5	0.495 - 0.286i	14.176 - 67.586i	-0.038 - 0.093i
	6	-0.006 + 0.228i	-0.011 + 0.014i	-48.924 + 9.851i
<i>F</i>	4	-87.117 - 31.225i	0.288 + 0.129i	-0.288 - 0.153i
	5	0.427 - 0.409i	11.074 - 83.982i	-0.029 + 0.029i
	6	0.265 - 0.092i	0.052 + 0.028i	12.346 + 24.502i
<i>H</i>	4	37.473 - 40.386i	-0.147 + 0.133i	0.157 - 0.134i
	5	-0.296 + 0.371i	2.344 + 83.675i	0.001 - 0.006i
	6	-0.029 + 0.263i	-0.068 + 0.002i	-56.712 + 19.668i

Table C.3: Non-sensitive axes total misalignment,  $\Delta P$ .

Set	$S_Z$	$S_Y$	$S_X$
A	0.09428 - 0.49481i	0.17981 + 0.09029i	0.05559 + 0.11127i
B	0.40404 + 0.13910i	0.00312 + 0.08016i	0.05842 - 0.04020i
C	0.37788 - 0.17644i	0.06319 + 0.20393i	0.05490 + 0.15574i
D	0.45663 - 0.31302i	0.26661 - 0.20462i	0.22883 - 0.18959i
E	0.59492 + 0.17912i	0.07601 - 0.37373i	0.119871 + 0.15759i
F	0.49126 - 0.40503i	0.29234 + 0.13148i	0.28689 + 0.15038i
G	0.08057 + 0.56140i	0.02947 - 0.36709i	0.19136 + 0.31537i
H	0.26887 - 0.43695i	0.15562 - 0.12594i	0.15683 - 0.13398i

# REFERENCES

- [1] J.-J. E. Slotine and W. Li, *Applied Nonlinear Control* (Prentice Hall, 1991).
- [2] H. Smaili, J. Breeman, T. Lombaerts, and D. Joosten, *A Simulation Benchmark for Integrated Fault Tolerant Flight Control Evaluation*, in *Proceedings of the AIAA Modeling and Simulation Technologies Conference and Exhibit* (AIAA, 2006).
- [3] T. J. J. Lombaerts, M. H. Smaili, O. Stroosma, Q. P. Chu, J. A. Mulder, and D. A. Joosten, *Piloted simulator evaluation results of new fault-tolerant flight control algorithm*, *Journal of Guidance, Control, and Dynamics* **32**, 1747 (2009).
- [4] H. Alwi, C. Edwards, O. Stroosma, and J. A. Mulder, *Evaluation of a sliding mode fault-tolerant controller for the el al incident*, *Journal of Guidance, Control, and Dynamics* **33**, 677 (2010).
- [5] T. Lombaerts, *Fault Tolerant Flight Control*, Ph.D. thesis, Delft University of Technology, The Netherlands (2010).
- [6] E. R. van Oort, *Adaptive Backstepping Control and Safety Analysis for Modern Fighter Aircraft*, Ph.D. thesis, Delft University of Technology, The Netherlands (2011).
- [7] Y. M. Zhang and J. Jiang, *Bibliographical Review on Reconfigurable Fault-Tolerant Control Systems*, *Annual Reviews in Control* **32**, 229 (2008).
- [8] S. Sieberling, Q. P. Chu, and J. A. Mulder, *Robust Flight Control Using Incremental Nonlinear Dynamic Inversion and Angular Acceleration Prediction*, *Journal of Guidance, Control, and Dynamics* **33**, 1732 (2010).
- [9] W. Falkena, E. R. van Oort, and Q. P. Chu, *Towards Certifiable Advanced Flight Control Systems, A Sensor-Based Backstepping Approach*, in *Proceedings of AIAA Guidance, Navigation and Control Conference* (AIAA, Reston, VA, 2011).
- [10] W. Falkena, C. Borst, E. R. van Oort, and Q. P. Chu, *Sensor-Based Backstepping*, *Journal of Guidance, Control, and Dynamics* **36**, 606 (2013).
- [11] L. G. Sun, C. C. de Visser, Q. P. Chu, and W. Falkena, *Hybrid Sensor-Based Backstepping Control Approach with Its Application to Fault-Tolerant Flight Control*, *Journal of Guidance, Control, and Dynamics* **37**, 59 (2014).
- [12] E. J. J. Smeur, Q. P. Chu, and G. C. H. E. de Croon, *Adaptive Incremental Nonlinear Dynamic Inversion for Attitude Control of Micro Air Vehicles*, *Journal of Guidance, Control, and Dynamics* **39**, 450 (2016).
- [13] C. Cakiroglu, E.-J. van Kampen, and Q. P. Chu, *Robust Incremental Nonlinear Dynamic Inversion Control Using Angular Accelerometer Feedback*, in *Proceedings of AIAA Guidance, Navigation and Control Conference* (AIAA, Reston, VA, 2018).

- [14] I. Matamoras and C. C. de Visser, *Incremental Nonlinear Control Allocation for a Tailless Aircraft with Innovative Control Effectors*, in *Proceedings of AIAA Guidance, Navigation and Control Conference* (AIAA, Reston, VA, 2018).
- [15] S. Merhav, *Aerospace Sensor Systems and Application* (Springer-Verlag, New York, 1996).
- [16] T. Meydan, *Recent Trends in Linear and Angular Accelerometers*, *Sensors and Actuators A: Physical* **59**, 43 (1997).
- [17] N. M. Barbour, J. M. Elwell, and R. H. Setterlund, *Inertial Instruments: Where to Now?* in *Proceedings of the AIAA Guidance, Navigation and Control Conference* (AIAA, Reston, VA, 1992).
- [18] M. Dumont and N. Kinsley, *Rotational Accelerometers and Their Usage in Investigating Shaker Head Rotations*, in *Sensors and Instrumentation*, Vol. 5, edited by E. W. Sit (Springer International Publishing, Cham, 2015) Chap. 10, pp. 85–92.
- [19] Gyro and Accelerometer Panel, *IEEE Standard Inertial Sensor Terminology*, Standard 528-1984 (IEEE Aerospace and Electronic Systems Society, 1984).
- [20] S. J. Ovaska and S. Väliiviita, *Angular Acceleration Measurement: A Review*, *IEEE Transactions on Instrumentation and Measurement* **47**, 1211 (1998).
- [21] A. R. Schuler, A. Grammatikos, and K. A. Fegley, *Measuring Rotational Motion with Linear Accelerometers*, *IEEE Transactions on Aerospace and Electronic Systems* **AES-3**, 465 (1967).
- [22] N. Ciblak, *Determining the Angular Motion of a Rigid Body Using Linear Accelerometers Without Integration*, in *Proceedings of the 3<sup>rd</sup> International Conference on Recent Advances in Space Technologies* (IEEE, Piscataway, NJ, 2007).
- [23] H. W. Engl, M. Hanke, and A. Neubauer, *Regularization of Inverse Problems* (Springer Netherlands, Dordrecht, 2000).
- [24] M. Bartholomew-Biggs, S. Brown, B. Christianson, and L. Dixon, *Automatic Differentiation of Algorithms*, *Journal of Computational and Applied Mathematics* **124**, 171 (2000), numerical Analysis 2000. Vol. IV: Optimization and Nonlinear Equations.
- [25] B. A. Kay, K. G. Munhall, E. V. Bateson, and J. A. S. Kelso, *A Note on Processing Kinematic Data: Sampling, Filtering, and Differentiation*, *Status Report on Speech Research* **SR-81**, 291 (1985).
- [26] F. Jauberteau and J. L. Jauberteau, *Numerical Differentiation with Noisy Signal*, *Applied Mathematics and Computation* **215**, 2283 (2009).
- [27] R. Chartrand, *Numerical Differentiation of Noisy, Nonsmooth Data*, *International Scholarly Research Network Applied Mathematics* **2011**, 11 (2011).
- [28] I. Knowles and R. J. Renka, *Methods for Numerical Differentiation of Noisy Data*, *Electronic Journal of Differential Equations Conference* **21**, 235 (2014).
- [29] S. K. Goldenstein, *A Gentle Introduction to Predictive Filters*, *Revista de Informática Teórica e Aplicada* **11**, 63 (2004).
- [30] P. R. Bélanger, *Estimation of Angular Velocity and Acceleration from Shaft Encoder Measurements*, in *Proceedings of the 1992 IEEE International Conference on Robotics and Automation* (IEEE, 1992) pp. 585–592.

- [31] X. Z. Gao, S. Valiviita, S. J. Ovaska, and J. Q. Zhang, *Neural Networks-based Approach to the Acquisition of Acceleration from Noisy Velocity Signal*, in *Proceedings of IEEE Instrumentation and Measurement Technology Conference* (IEEE, 1998) pp. 935–940.
- [32] F. Gianfelici, *A Novel Technique for Indirect Angular Acceleration Measurement*, in *Proceedings of the CIMSIA 2005 - IEEE International Conference on Computational Intelligence for Measurement Systems and Applications* (IEEE, Piscataway, NJ, 2005).
- [33] S. Väiliviita and S. J. Ovaska, *Delayless Acceleration Measurement Method for Elevator Control*, *IEEE Transactions on Industrial Electronics* **45**, 364 (1998).
- [34] J. D. Han, Y. Q. He, and W. L. Xu, *Angular Acceleration Estimation and Feedback Control: An Experimental Investigation*, *Mechatronics* **17**, 524 (2007).
- [35] E. P. Sexton, *Fluid Type Inertia Device*, Patent, United States Patent Office (1940), US2225716.
- [36] J. A. Buchanan, *Angular Classifying Accelerometer*, Patent, United States Patent Office (1943), US2310213.
- [37] X. Zhang, J. Zhang, B. Chen, K. L. Yang, and P. V. Errico, *3-axis Angular Accelerometer*, Patent, European Patent Office (2017), EP3190421A1.
- [38] L. D. Statham, *Electric Angular Accelerometer*, Patent, United States Patent Office (1949), US2481792.
- [39] G. N. Rosa, *An Angular Accelerometer for Guidance*, *Journal of Jet Propulsion* **25**, 30 (1955).
- [40] L. D. Statham, *Angular Accelerometer*, Patent, United States Patent Office (1957), US2778623.
- [41] L. D. Statham, *Angular Accelerometer*, Patent, United States Patent Office (1957), US2778624.
- [42] L. D. Statham, *Motion Sensing Device*, Patent, United States Patent Office (1957), US2778905.
- [43] L. D. Statham, *Angular Accelerometer and Switch*, Patent, United States Patent Office (1960), US2963244.
- [44] H. D. Morris and J. T. Buckingham, *Fluid Rotor Angular Accelerometer*, Patent, United States Patent Office (1970), US3520196.
- [45] S. R. Zarabadi, J. C. Christenson, and W. J. Baney, *Angular Accelerometer*, Patent, United States Patent Office (2002), US6393914.
- [46] S. R. Zarabadi, I. D. Jay, J. D. Johnson, J. C. Christenson, and T. A. Noll, *Angular Accelerometer Having Balanced Inertia Mass*, Patent, United States Patent Office (2003), US6666092.
- [47] S. R. Zarabadi, I. D. Jay, J. D. Johnson, J. C. Christenson, and T. A. Noll, *Balanced Angular Accelerometer*, Patent, United States Patent Office (2004), US6718826.
- [48] A. Taubner and H. J. von Martens, *Diffraction Grating Interferometer for the Accurate Measurement of Rotational Quantities*, *Elsevier – Measurement* **16**, 71 (1995).
- [49] A. Taubner and H. J. von Martens, *Measurement of Angular Accelerations, Angular Velocities and Rotation Angles by Grating Interferometry*, *Elsevier – Measurement* **24**, 21 (1998).

- [50] R. Marat-Mendes, C. J. Dias, and J. N. Marat-Mendes, *Measurement of the Angular Acceleration Using a PVDF and a Piezo-Composite*, *Sensors and Actuators* **76**, 310 (1999).
- [51] N. Furukawa and K. Ohnisi, *A Structure of Angular Acceleration Sensor using Silicon Cantilevered Beam with Piezoresistors*, in *Proceedings of the International Conference on Industrial Electronics, Control, Instrumentation, and Automation*, Vol. 3 (1992) pp. 1524–1529.
- [52] I. Godler, A. Akahane, K. Ohnisi, and T. Yamashita, *A Novel Rotary Acceleration Sensor*, *IEEE Control System* **15**, 56 (1995).
- [53] I. Godler, A. Akahane, T. Maruyama, and T. Yamashita, *Angular Acceleration Sensor Composed of Two Discs and Optical Pick-Up*, *Transaction of the Society of Instrument and Control Engineers* **31**, 982 (1995).
- [54] O. Kužma and V. Kalaš, *A Novel Integrated Angular Acceleration, Velocity and Position Sensor*, *Journal of Electrical Engineering* **52**, 12 (2001).
- [55] R. Lassow and T. Meydan, *An Angular Accelerometer using Amorphous Wire*, *IEEE Transactions on Magnetics* **31**, 3179 (1995).
- [56] P. J. Shirron, V. Moody, and E. Canavan, *Development of A Superconducting Angular Accelerometer*, in *Proceedings of the SPIE Cryogenic Optical Systems and Instruments VII*, Vol. 2814 (1996) pp. 188–196.
- [57] M. V. Moody, H. J. Paik, and E. R. Canavan, *Principle and Performance of A Superconducting Angular Accelerometer*, *Review of Scientific Instruments* **74**, 1310 (2003).
- [58] J. Mizuno, K. Nottmeyer, M. Amemori, Y. Kanai, and T. Kobayashi, *The Study of Silicon Bulk Micromachined Angular Acceleration Sensor*, *JSAE Review* **21**, 79 (2000).
- [59] G. J. O'Brien, D. J. Monk, and K. Najafi, *Angular Accelerometer with Dual Anchor Support*, in *Proceedings of the 12<sup>th</sup> International Conference on TRANSDUCERS, Solid-State Sensors, Actuators and Microsystems*, Vol. 2 (2003) pp. 1371–1374.
- [60] J. Li, F. Jiancheng, and S. Wei, *Pendulum Micromechanical Angular Accelerometer with Force Feedback*, in *2007 International Conference on Mechatronics and Automation* (2007) pp. 2673–2677.
- [61] J. Li, J. Fang, M. Du, and H. Dong, *Analysis and Fabrication of A Novel MEMS Pendulum Angular Accelerometer with Electrostatic Actuator Feedback*, *Microsystem Technologies* **19**, 9 (2013).
- [62] H. J. Wolfaardt and P. S. Heyns, *Dynamic Modeling of a Novel Microfluidic Channel Angular Accelerometer*, *Journal of Vibration and Control* **14**, 451 (2008).
- [63] J. Groenesteijn, H. Droogendijk, M. J. de Boer, R. G. P. Sanders, R. J. Wiegerink, and G. J. M. Krijnen, *An Angular Acceleration Sensor Inspired by the Vestibular System with A Fully Circular Fluid-Channel and Thermal Read-Out*, in *2014 IEEE 27th International Conference on Micro Electro Mechanical Systems (MEMS)* (2014) pp. 696–699.
- [64] H. Alrowais, P. Getz, M. g. Kim, J. J. Su, and O. Brand, *Bio-Inspired Fluidic Thermal Angular Accelerometer*, in *2016 IEEE 29th International Conference on Micro Electro Mechanical Systems (MEMS)* (2016) pp. 761–764.

- [65] H. Alrowais, M. G. Kim, P. Getz, and O. Brand, *Parylene-on-Oil Encapsulation Process for Bio-Inspired Angular Accelerometer*, in *2017 19<sup>th</sup> International Conference on Solid-State Sensors, Actuators and Microsystems (TRANSDUCERS)* (2017) pp. 587–590.
- [66] G. Schlöffel and F. Seiler, *Unidirectional Fiber Optic Sensor for Angular Acceleration Measurement*, *Optics Letter* **38**, 1500 (2013).
- [67] M. T. Restivo, F. G. Almeida, and D. Freitas, *Measuring Relative Acceleration: A Relative Angular Acceleration Prototype Transducer*, *Measurement Science and Technology* **24**, 025101 (2013).
- [68] H. Zhao and H. Feng, *A Novel Angular Acceleration Sensor Based on the Electromagnetic Induction Principle and Investigation of Its Calibration Tests*, *Sensors (Basel)* **13**, 10370 (2013).
- [69] H. Zhao and H. Feng, *A Novel Permanent Magnetic Angular Acceleration Sensor*, *Sensors (Basel)* **15**, 16136 (2015).
- [70] H. Liu and W. T. Pike, *A Micromachined Angular-Acceleration Sensor for Geophysical Applications*, *Applied Physics Letters* **109**, 173506 (2016).
- [71] V. Kumar, A. Ramezany, S. Mazrouei, R. Jafari, and S. Pourkamali, *A 3-Bit Digitally Operated MEMS Rotational Accelerometer*, in *2017 IEEE 30<sup>th</sup> International Conference on Micro Electro Mechanical Systems (MEMS)* (2017) pp. 1087–1090.
- [72] L. A. Potapov and V. P. Maklakov, *Electromagnetic Processes Simulation in the Angular Accelerometer with A Hollow Non-Magnetic Rotor*, in *Proceedings of the 2017 International Conference on Industrial Engineering, Applications and Manufacturing (ICIEAM)* (2017) pp. 1–5.
- [73] A. Lawrence, *Modern Inertial Technology - Navigation, Guidance, and Control* (Springer-Verlag New York, Inc., 1998).
- [74] P. F. Dunn, *Measurement and Data Analysis for Engineering and Science* (CRC Press, Boca Raton, FL, 2010).
- [75] D. H. Titterton and J. L. Weston, *Strapdown Inertial Navigation Technology - 2nd Edition* (The Institution of Electrical Engineer and The American Institute of Aeronautics and Astronautics, 2004).
- [76] Gyro and Accelerometer Panel, *IEEE Standard Specification Format Guide and Test Procedure for Non-gyroscopic Inertial Angular Sensors Jerk, Acceleration, Velocity, and Displacement*, Standard 671-1985, Reaffirmed 10 December 2008 (IEEE Aerospace and Electronic Systems Society, New York, USA, 1985).
- [77] I. McLaren, *Open and Closed Loop Accelerometers*, Flight Test Instrumentation Series (NATO AGARD, 1974).
- [78] T. D. Finley, *Technique for Calibrating Angular Measurement Devices when Calibration Standards are Unavailable*, TM-104148 (NASA, 1991).
- [79] R. D. Sill, *Measurement of Angular and Linear Acceleration Sensitivities of Endevo Model 7302 Angular Accelerometer*, in *Proceeding of the 9<sup>th</sup> Annual International Workshop on Human Subject for Biomechanics Research* (NHTSA/ Human Injury Research Division, Washington, D.C., USA, 1981) pp. 51–58.

- [80] J. D. Ramboz, *Measurement and Evaluation Methods for Angular Accelerometer*, Technical Report NBSIR 81-2337 (National Bureau of Standards, U.S. Department of Commerce, Washington, D. C., USA, 1981).
- [81] G. C. Willems, *A Detailed Evaluation of the Endevco Model 7302<sup>®</sup> Angular Accelerometer*, Technical Report NBDL-83R009 (Naval Biodynamics Laboratory, New Orleans, Louisiana, 1983).
- [82] K. G. McConnel, *Evaluation of an Angular Accelerometer*, in *Proceeding of the 2001 IMAC XIX - 19th International Modal Analysis Conference* (Society for Experimental Mechanics, 2001) p. 7.
- [83] M. Verhaegen and P. Dewilde, *Subspace Model Identification Part 1. The Output-Error State-Space Model Identification Class of Algorithms*, *International Journal of Control* **56**, 1187 (1992), <https://doi.org/10.1080/00207179208934363> .
- [84] M. Verhaegen and P. Dewilde, *Subspace Model Identification Part 2. Analysis of the Elementary Output-Error State-Space Model Identification Algorithm*, *International Journal of Control* **56**, 1211 (1992), <https://doi.org/10.1080/00207179208934364> .
- [85] M. Verhaegen, *Identification of the Deterministic Part of MIMO State Space Models Given in Innovations form from Input-Output Data*, *Automatica* **30**, 61 (1994), special issue on statistical signal processing and control.
- [86] M. Wang, X. Li, S. Cheng, M. Fu, and M. Xiao, *Experimental Model Identification of Liquid-Circular Angular Accelerometer using Subspace Method*, in *Proceedings of the 35<sup>th</sup> Chinese Control Conference* (IEEE, 2016) pp. 2218–2222.
- [87] S. Cheng, M. Fu, M. Wang, X. Li, M. Xiao, and T. Wang, *Transfer Function of Fluidic system in Liquid-Circular Angular Accelerometer*, in *Instrumentation and Measurement Technology Conference Proceedings* (IEEE International, 2016) p. 5.
- [88] S. Cheng, M. Fu, M. Wang, X. Li, M. Xiao, and T. Wang, *Modeling for Fluid Transients in Liquid-Circular Angular Accelerometer*, *IEEE Sensors Journal* **17**, 267 (2017).
- [89] S. Cheng, M. Fu, M. Wang, L. Ming, H. Fu, and T. Wang, *Dynamic Fluid in a Porous Transducer-Based Angular Accelerometer*, *Sensors (Basel)* **17**, 20 (2017).
- [90] M. Fu, S. Cheng, M. Wang, L. Ming, and T. Wang, *Permeability Modeling for Porous Transducer of Liquid-Circular Angular Accelerometer*, *Sensors and Actuators A: Physical* **257**, 145 (2017).
- [91] L. Ming, M. Wang, T. Liu, S. Cheng, M. Fu, and T. Wang, *Electrokinetic Experiments of Porous Transducer in Liquid Circular Angular Accelerometer*, in *Proceedings of the 2017 IEEE International Instrumentation and Measurement Technology Conference (I2MTC)* (IEEE, 2017) p. 6.
- [92] S. Cheng, M. Fu, and F. A. Kulacki, *Characterization of A Porous Transducer using A Capillary Bundle Model: Permeability and Streaming Potential Prediction*, *International Journal of Heat and Mass Transfer* **1**, 349 (2018).
- [93] L. A. DeMore, R. Mackin, M. Swamp, and R. Rusterholtz, *Improvements in Flight Table Dynamic Transparency for Hardware-in-the-Loop Facilities*, in *Proceedings of SPIE 4027, Technologies for Synthetic Environments: Hardware-in-the-Loop Testing V* (SPIE, 2000) pp. 101–112.

- [94] R. B. Peters, *A Dynamic Angular Calibration System for Broadband Microradian Inertial Sensors*, *AIAA*, 541 (1978).
- [95] N. Song, Q. Cai, G. Yang, and H. Yin, *Analysis and Calibration of the Mounting Errors between Inertial Measurement Unit and Turntable in Dual-Axis Rotational Inertial Navigation System*, *Measurement Science and Technology* **24**, 10 (2013).
- [96] D. Jatiningrum, C. C. de Visser, M. M. van Paassen, and M. Mulder, *A Framework for Calibrating Angular Accelerometers using a Motion Simulator*; in *Proceedings of the AIAA Modeling and Simulation Technologies Conference* (AIAA, Reston, VA, USA, 2015) p. 13.
- [97] Y. Kamer and S. Ikizoglu, *Effective Accelerometer Test Beds for Output Enhancement of An Inertial Navigation System*, *Elsevier – Measurement* **46**, 1641 (2013).
- [98] D. Dube and P. Cardou, *The Calibration of an Array of Accelerometers*, *Transactions of the Canadian Society for Mechanical Engineering* **35**, 251 (2011).
- [99] Z. Y. Zheng, Y. B. Gao, and K. P. He, *Systematic Calibration Method for FOG Inertial Measurement Units*, *Advanced Materials Research* **662**, 717 (2013).
- [100] B. Xie, Y. Qin, and Y. Wan, *A High Accuracy Calibration Method of Optical Gyro SINS*, in *3<sup>rd</sup> International Symposium on Systems and Control in Aeronautics and Astronautics (ISSCAA)* (IEEE, 2010) pp. 507–511.
- [101] W. Sun, D. Wang, L. Xu, and L. Xu, *MEMS-based Rotary Strapdown Inertial Navigation System*, *Elsevier – Measurement* **46**, 2585 (2013).
- [102] E. J. de Oliveira, W. de Castro Leite Filho, and I. M. da Fonseca, *Inertial Measurement Unit Calibration Procedure for a Redundant Tetrahedral Gyro Configuration with Wavelet Denoising*, *Journal of Aerospace Technology and Management* **4**, 163 (2012).
- [103] T. Nieminen, J. Kangas, S. Suuriniemi, and L. Kettunen, *An Enhanced Multi-Position Calibration Method for Consumer-Grade Inertial Measurement Units Applied and Tested*, *Measurement Science and Technology* **21**, 11 (2010).
- [104] I. Columbia Research Laboratories, *Force Balance Sensor Technology*, Technical Paper, Retrieved from [www.crlsensors.com](http://www.crlsensors.com) (n.d.).
- [105] M. El-Diasty, A. El-Rabbany, and S. Pagiatakis, *Temperature Variation Effects on Stochastic Characteristics for Low-Cost MEMS-Based Inertial Sensor Error*, *Measurement Science and Technology* **18**, 3321 (2007).
- [106] M. El-Diasty and S. Pagiatakis, *A Rigorous Temperature-Dependent Stochastic Modelling and Testing for MEMS-Based Inertial Sensor Errors*, *Sensors (Basel)* **9**, 8473 (2009).
- [107] X. Niu, Y. Li, H. Zhang, Q. Wang, and Y. Ban, *Fast Thermal Calibration of Low-Grade Inertial Sensors and Inertial Measurement Units*, *Sensors (Basel)* **13**, 12192 (2013).
- [108] B. Fang, W. Chou, and L. Ding, *An Optimal Calibration Method for a MEMS Inertial Measurement Unit*, *International Journal of Advanced Robotic Systems*, 1 (2014).
- [109] Y. Günhan and D. Ünsal, *Polynomial Degree Determination for Temperature Dependent Error Compensation of Inertial Sensors*, in *2014 IEEE/ION Position, Location and Navigation Symposium* (IEEE, 2014) p. 4.

- [110] S. Lambrecht, S. L. Nogueira, M. Bortole, A. A. Siqueira, M. H. Terra, E. Rocon, and J. L. Pons, *Inertial Sensor Error Reduction through Calibration and Sensor Fusion*, *Sensors (Basel)* **16**, 235 (2016).
- [111] C. Nagel, F. Ante, M. Putnik, J. Classen, and J. Mehner, *Characterization of Temperature Gradients on MEMS Acceleration Sensors*, *Procedia Engineering* **168**, 888 (2016).
- [112] D. Jatiningrum, C. C. de Visser, M. M. van Paassen, E. van Kampen, and M. Mulder, *Characterising Angular Accelerometer Calibration Setup Disturbance Using Box-Jenkins Method*, in *Advances in Aerospace Guidance, Navigation and Control: Selected Papers of the Fourth CEAS Specialist Conference on Guidance, Navigation and Control Held in Warsaw, Poland, April 2017*, edited by B. Dołęga, R. Głębocki, D. Kordos, and M. Żugaj (Springer International Publishing, Cham, Switzerland, 2018) pp. 279–294.
- [113] D. Jatiningrum, A. Muis, C. C. de Visser, M. M. van Paassen, and M. Mulder, *A High-Precision Position Turn-Table as the Reference for Angular Accelerometer Calibration Experiment*, in *Proceedings of the 5<sup>th</sup> CEAS Air and Space Conference* (CEAS, Delft, The Netherlands, 2015) p. 14.
- [114] Gyro and Accelerometer Panel, *IEEE Standard Specification Format Guide and Test Procedures for Linear Single-Axis, Nongyroscopic Accelerometers*, Std 1293-1998 (IEEE Aerospace and Electronic Systems Society, 1998).
- [115] N. S. Nise, *Control Systems Engineering, Sixth Edition* (John Wiley and Sons, Inc., Hoboken, NJ, 2011).
- [116] M. Swamp, C. Stevens, and P. Hoffstetter, *Improvements in Transient Fidelity of HWIL Flight Tables using Acceleration Feedback*, in *Proceedings of SPIE 4717, Technologies for Synthetic Environments: Hardware-in-the-Loop Testing VII* (SPIE, 2002) pp. 32–45.
- [117] S. Koekebakker, A. Scheffer, and S. K. Advani, *The Dynamic Calibration of a High Performance Motion System*, in *AIAA* (1998) pp. 541–550.
- [118] S. L. Marple, Jr., *Computing the Discrete Time Analytic Signal via FFT*, (1999) pp. 2600–2603.
- [119] M. Abramowitz and I. A. Stegun, *Handbook of Mathematical Function with Formulas, Graphs, and Mathematical Tables* (Dover, Washington, D.C., 1972).
- [120] A. H. Kadhim, T. K. M. Babu, and D. O’Kelly, *Measurement of Steady-State and Transient Load-Angle, Angular Velocity, and Acceleration Using an Optical Encoder*, *IEEE Transactions on Instrumentation and Measurement* **41**, 486 (1992).
- [121] L. Lamport, *Time, Clocks, and the Ordering of Events in a Distributed System*, *Communications of the ACM* **21**, 558 (1978).
- [122] D. Jatiningrum, C. C. de Visser, M. M. van Paassen, and M. Mulder, *Motion Simulator 2-axes Input Design for Angular Accelerometer Calibration*, in *Proceedings of the AIAA Modeling and Simulation Technologies Conference* (AIAA, Reston, VA, USA, 2016) p. 11.
- [123] D. Jatiningrum, P. Lu, C. C. de Visser, Q. P. Chu, and M. Mulder, *Development of a New Method for Calibrating an Angular Accelerometer Using a Calibration Table*, in *Proceedings of the AIAA Guidance, Navigation and Control Conference* (AIAA, Reston, VA, USA, 2015) p. 13.

- [124] J. Groenesteijn, H. Droogendijk, M. J. de Boer, R. G. P. Sanders, R. J. Wiegerink, and G. J. M. Krijnen, *An Angular Acceleration Sensor Inspired by the Vestibular System with A Fully Circular Fluid-Channel and Thermal Read-Out*, in *Proceeding of the 2014 IEEE 27th International Conference on Micro Electro Mechanical Systems (MEMS)* (IEEE, 2014) pp. 696–696.
- [125] J. Fang, S. Pan, B. Wang, and Z. Wang, *An automatic test system for Angular Accelerometer*, in *Proceeding of the Seventh International Symposium on Instrumentation and Control Technology: Measurement Theory and Systems and Aeronautical Equipment* (SPIE, 2008) p. 7.
- [126] M. Amereh, M. M. Aghdam, and M. Golkaram, *Design and Modeling of a Novel Translational and Angular Micro-Electromechanical Accelerometer*, *Journal of Aerospace Science and Technology* **50**, 15 (2016).
- [127] A. B. Chatfield, *Fundamentals of High Accuracy Inertial Navigation* (American Institute of Aeronautics and Astronautics, Inc., Reston, VA, 1997).
- [128] A. Levant, *Robust Exact Differentiation via Sliding Mode Technique*, *Automatica* **34**, 379 (1998).
- [129] M. Kirkko-Jaakkola, J. Collin, and J. Takala, *Bias Prediction for MEMS Gyroscopes*, *IEEE Sensors Journal* **12**, 2157 (2012).
- [130] K. Choi, S. Jang, and Y. Kim, *Calibration of Inertial Measurement Units Using Pendulum Motion*, *International Journal of Aeronautical and Space Sciences* **11**(3), 234 (2010).
- [131] M. A. Brodie, A. Walmsley, and W. Page, *Dynamic Accuracy of Inertial Measurement Units During Simple Pendulum Motion*, *Computer Methods in Biomechanics and Biomedical Engineering* **11**(3), 235 (2008).
- [132] P. Cappa, F. Patanè, and S. Rossi, *Two Calibration Procedures for a Gyroscope-Free Inertial Measurement System Based on a Double-Pendulum Apparatus*, *Measurement Science and Technology* **19**(5), 055204 (9pp) (2008).
- [133] V. L. Lissan and A. E. Sinélnikov, *Present State and Development Trends in the Measurement of Velocities and Accelerations*, *Measurement Techniques* **13**, 544 (1970).
- [134] V. A. Ivanov, *Angular Accelerometer on A Biaxial Test Installation*, *Measurement Techniques* **15**, 1503 (1972).
- [135] Y. G. Brunshtein and A. V. Trotsenko, *A Testbed for Calibrating Angular-Acceleration Transducers*, *Measurement Techniques* **24**, 1055 (1981).
- [136] R. Hauser, *Acutrol3000® Operator Interface User Guide*, Acutronic (2005).
- [137] *Acutrol3000® Instruction Manual*, Acutronic (2007).
- [138] J. Kiusalaas, *Numerical Methods in Engineering with MATLAB* (Cambridge University Press, Cambridge, 2005).
- [139] P. P. J. van den Bosch and A. C. van der Klauw, *Modeling, Identification, and Simulation of Dynamical Systems* (CRC Press, Inc., Boca Raton, FL, 1994).
- [140] A. Levant, *Sliding Order and Sliding Accuracy in Sliding Mode Control*, *International Journal of Control* **58**, 1247 (1993).

- [141] M. Verhaeghen and V. Verdult, *Filtering and System Identification, A Least Squares Approach* (Cambridge University Press, 2007).
- [142] C. C. de Visser, *Global Nonlinear Model Identification with Multivariate Splines*, Ph.D. thesis, Delft University of Technology, Delft (2011).
- [143] H. Akaike, *A New Look at the Statistical Model Identification*, *IEEE Transactions on Automatic Control* **19**, 716 (1974).
- [144] L. Ljung, *System Identification: Theory for the Users* (Prentice Hall, Upper Saddle River, NJ, 1999).
- [145] K. Emancipator and M. H. Kroll, *A Quantitative Measure of Nonlinearity*, *Clinical Chemistry* **39**, 766 (1993).
- [146] D. Jatiningrum, C. C. de Visser, M. M. van Paassen, and M. Mulder, *Modelling an Angular Accelerometer using the Frequency-Response Measurements*, in *Proceedings of the AIAA Guidance, Navigation and Control Conference* (AIAA, Reston, VA, USA, 2016) p. 14.
- [147] G. F. Franklin, J. D. Powell, and A. Emami-Naeini, *Feedback Control of Dynamic Systems, Sixth Edition* (Pearson Education, Inc., Upper Saddle River, NJ, 2010).
- [148] S. Pan and B. Wang, *An Automatic Test System for Angular Accelerometer*, in *Proceedings of the Seventh International Symposium on Instrumentation and Control Technology: Measurement Theory and Systems and Aeronautical Equipment* (SPIE, 2008) p. 7.
- [149] L. A. Geddes, *The First Stimulators – Reviewing the History of Electrical Stimulation and the Devices Crucial to Its Development*, *IEEE Engineering in Medicine and Biology Magazine* **13**, 532 (1994).
- [150] M. Looney, *Analyzing Frequency Response of Inertial MEMS in Stabilization Systems*, Electronic Article, [www.analog.com/analogdialogue](http://www.analog.com/analogdialogue) (2012).
- [151] Y. J. Cheon, S. W. Sung, J. Lee, C. H. Je, and I. Lee, *Improved Frequency Response Model Identification Method for Processes with Initial Cyclic Steady State*, *American Institute of Chemical Engineers* **57**, 3429 (2011).
- [152] Y. J. Cheon, H. Kim, K. S. Kim, K. H. Ryu, I.-B. Lee, J. Lee, and S. W. Sung, *A Frequency Response Identification Method for Discrete-time Processes*, *IFAC Proceedings Volumes* **45**, 331 (2012), 8<sup>th</sup> IFAC Symposium on Advanced Control of Chemical Processes.
- [153] K. Kim, Y. J. Cheon, I.-B. Lee, J. Lee, and S. W. Sung, *A Frequency Response Identification Method for Discrete-time Processes with Cyclic Steady State Conditions*, *Automatica* **50**, 3260 (2014).
- [154] A. S. French, A. V. Holden, and R. B. Stein, *The estimation of the frequency response function of a mechanoreceptor*, *Kybernetik* **11**, 15 (1972).
- [155] L. S. Shieh and M. H. Cohen, *Transfer Function Fitting from Experimental Frequency-Response Data*, *Journal of Computers and Electrical Engineering* **5**, 205 (1978).
- [156] D. T. J. Hurle, G. C. Joyce, and G. C. Wilson, *A Technique for Experimentally Determining the Transfer Function of a Czochralski Pulling Process*, *Journal of Crystal Growth* **74**, 480 (1986).

- [157] M. B. Tischler, *Frequency-Response Identification of XV-15 Tilt-Rotor Aircraft Dynamics*, Technical Memorandum NASA TM-89428 (National Aeronautics and Space Administration, 1987).
- [158] M. B. Tischler, J. W. Fletcher, V. L. Diekmann, R. A. Williams, and R. W. Cason, *Demonstration of Frequency-Sweep Testing Technique Using a Bell 214-ST Helicopter*, Technical Memorandum NASA TM-89422 (National Aeronautics and Space Administration, 1987).
- [159] M. B. Tischler and M. G. Cauffman, *Frequency-Response Method for Rotorcraft System Identification: Flight Applications to BO-105 Coupled Fuselage/ Rotor Dynamics*, *Journal of American Helicopter Society* **37**, 3 (1992).
- [160] M. B. Tischler, *System Identification Methods for Aircraft Flight Control Development and Validation*, Technical Memorandum NASA TM-110369 (National Aeronautics and Space Administration, 1995).
- [161] L. Ljung, *Some Results on Identifying Linear Systems Using Frequency Domain Data*, in *Proceedings of the 32nd Conference on Decision and Control* (IEEE, San Antonio, Texas, USA, 1993) pp. 3534–3538.
- [162] A. Brandt, *Noise and Vibration Analysis: Signal Analysis and Experimental Procedures* (John Wiley & Sons, Ltd, Hoboken, NJ, 2013).
- [163] M. B. Tischler and R. K. Remple, *Aircraft and Rotorcraft System Identification* (American Institute of Aeronautics and Astronautics, Inc., Reston, VA, 2012).
- [164] R. Pintelon and J. Schoukens, *System Identification: A Frequency Domain Approach* (IEEE Press, Piscataway, NJ, 2012).
- [165] D. Jatiningrum, C. C. de Visser, M. M. van Paassen, and M. Mulder, *Investigating Misalignment in a 3-Axis Angular Accelerometer Measurement Unit*, in *Proceedings of the AIAA Guidance, Navigation and Control Conference* (AIAA, Reston, VA, USA, 2017) p. 11.
- [166] E.-H. Shin and N. El-Sheimy, *A New Calibration Method for Strapdown Inertial Navigation Systems*, *Journal of Geodesy, Geoinformation and Land Management* **127**, 41 (2002).
- [167] Z. F. Syed, P. Aggarwal, C. Goodall, X. Niu, and N. El-Sheimy, *A New Multi-position Calibration Method for MEMS Inertial Navigation Systems*, *Measurement Science and Technology* **18**, 1897 (2007).
- [168] W. Gao, Y. Zhang, and J. Wang, *Research on Initial Alignment and Self-Calibration of Rotary Strapdown Inertial Navigation Systems*, *Sensors* **15**, 3154 (2015).
- [169] A. V. Kozlov and N. A. Parusnikov, *Off-line Determination of Relative Orientation Between the Instrument Frames of Two Strapdown Inertial Navigation Systems During Motion*, *Moscow University Mechanics Bulletin* **65**, 22 (2010).
- [170] S. Zhongguo, Z. Wenqi, X. Xiaoli, and Z. Jinsheng, *A Compensation Method of Alignment Errors during Triaxial Magnetometer Onboard Calibration on Spinning Projectile*, in *Proceedings of the Sensors Applications Symposium (SAS)* (IEEE, 2015).
- [171] J.-O. Nilsson, I. Skog, and P. Händel, *Aligning the Forces – Eliminating the Misalignments in IMU Arrays*, *IEEE Transactions on Instrumentation and Measurement* **63**, 3 (2014).

- [172] J. Chardonnes, J. Favre, and K. Aminian, *An Effortless Procedure to Align the Local Frame of an Inertial Measurement Unit to the Local Frame of Another Motion Capture System*, *Journal of Biomechanics* **45**, 2297 (2012).
- [173] R. Weinman and J. Rutkoskie, *Development, Performance Assessment, and Verification of A Calibration and Alignment Technique for A Precision IMU*, in *Guidance and Control Conference* (AIAA, Reston, VA, 1981) pp. 6–15.
- [174] M. Rhudy, Y. Gu, J. Gross, S. Gururajan, and M. R. Napolitano, *Sensitivity Analysis of Extended and Unscented Kalman Filters for Attitude Estimation*, *Journal of Aerospace Information Systems* **10**, 131 (2013).
- [175] Y. Liu, X. Xu, X. Liu, Y. Yao, L. Wu, and J. Sun, *A Self-Alignment Algorithm for SINS Based on Gravitational Apparent Motion and Sensor Data Denoising*, *Sensors* **15**, 9827 (2015).
- [176] M. Liu, Y. Gao, G. Li, X. Guang, and S. Li, *An Improved Alignment Method for the Strapdown Inertial Navigation System (SINS)*, *Sensors* **16**, 621 (2016).
- [177] Ø. Magnussen, M. Ottestad, and G. Hovland, *Calibration Procedure for an Inertial Measurement Unit Using a 6-Degree-of-Freedom Hexapod*, in *Proceedings of the International Conference on Unmanned Aircraft Systems (ICUAS)* (2012) p. 6.
- [178] J. M. D. Freitas, J. P. F. Wooler, and P. J. Nash, *Measurement of Sensor Axis Misalignment in Fibre-Optic Accelerometers*, *Measurement Science and Technology* **17**, 1819 (2006).
- [179] G. Pritschow, C. Eppler, and W.-D. Lehner, *Ferraris Sensor – The Key for Advanced Dynamic Drives*, *CIRP Annals* **52**, 289 (2003).
- [180] J. Faßnacht and P. Mutschler, *An Observer to Improve the Speed Signal Using a Ferraris Acceleration Sensor*, in *Proceeding of the 9<sup>th</sup> European Conference on Power Electronics and Applications* (2001) p. 4.
- [181] J. Faßnacht and P. Mutschler, *Benefits and Limits of Using An Acceleration Sensor in Actively Damping High Frequent Mechanical Oscillations*, in *Conference Record of the 2001 IEEE Industry Applications Conference. 36<sup>th</sup> IAS Annual Meeting (Cat. No.01CH37248)*, Vol. 4 (2001) pp. 2337–2344 vol.4.
- [182] B. Hiller, *Ferraris Acceleration Sensor – Principle and Field of Application in Servo Drives*, (2001) p. 6.

# ACKNOWLEDGEMENTS

Pursuing a PhD can be an unpredictable quest. Nevertheless, one gains immense knowledge and valuable lessons from this experience. In any case, it is an achievement for an individual but by no means achieved by themselves. It is, therefore, I would like to convey my appreciation to those who have supported me on this remarkable journey.

I would like to express my profound gratitude to my promotor, Prof. Max Mulder, for the opportunity to pursue my PhD and for having faith in my ability. I learned a lot from Max, not only academically, but also professionally and personally. His feedbacks not only significantly improve my knowledge but also the way I write academic pieces. Max' enthusiasm is contagious, and his encouragement never fails to lift my spirit and to keep pushing on my progress, especially at times when I am not so confident in myself. Thank you, Max, the continuation of my study is in large part due to your support.

My utmost gratitude goes to Dr Coen de Visser, my co-promotor, who is there from the very beginning, and my number one critics. He guided me to navigate among all of the uncertainty in my research topic throughout the years. His continuous encouragement and positivity aid me to find my way, although I can also count on his advice when facing intersections. I walked away from our many meetings with fresh insights and renewed motivation out of the challenging yet eye-opening discussions. Coen, thank you for being patient and helping me improve!

I would also like to extend my highest appreciation to Dr René van Paassen, who joined my supervisory team in the early third year. His extensive knowledge and constructive advice have been valuable in resolving the challenges of my topic. By his perceptive comments, not only my writings become more comprehensive, but it also drives me to revisit the concept. He also provides huge favour in translating my Summary into Dutch. Thanks, René, for introducing another perspective to my research, and for providing answers to my questions, even the most trivial ones.

A word of acknowledgement to Dr Qiping Chu for laying the foundation for my research topic and advice on the research formulation in the early stage. He keeps his office open for me to discuss aspects of my work in every now and then.

To Peng Lu, thank you for lending me your expertise in the sliding mode differentiation method, which is a significant contribution in one part of my research.

For the people behind the scene yet invaluable, my sincerest recognition to you. Andries Muis is like my fairy godfather; he helped to make my somewhat peculiar measurement set-up comes true. In addition to being my go-to person related to the calibration lab, Andries often keep me in check during the long measurement hours (although, that could be because he is worried that I might blow up the lab). Ferdinand Postema plays a crucial role in establishing the synchronisation mechanism in my experiment. Menno Klaassen supports me on more than an occasion, especially during the temperature effect experiment. Harold Thung, who is also a fellow runner in the yearly Delft Golden

Tenloop, provides terrific assistance related to computers. Our lovely Bertine Markus, her unwavering support for administration and practical matters in our ever-growing research group, is very admirable, and of course, heartily thanked.

I gratefully acknowledge Dr Thanh Lan Vu from the Defence Science and Technology Organisation (DSTO), Australia, one of the few people who understand and work with multi-axis motion simulators. Our encounter at the AIAA SciTech 2015 was followed by valuable discussions across continents for several months. Although our collaboration did not go as planned, this deliberation provides crucial insight into my topic and help propels the project forward.

Special thanks to Prof. Hari Muhammad, my former supervisor at the Institute of Technology Bandung, who connects me with Prof. Bob Mulder, and eventually Prof. Max Mulder, to host my study.

My indispensable recognition to the Islamic Development Bank (IDB) for the funding under the Merit Scholarship Programme for High Technology, which makes my PhD project possible.

The people in the Control and Simulation research group are fantastic colleagues, be it in the daily life, the coffee breaks, the weekly PhD lunches, the incidental birthday treats, the yearly barbecues and heidag, and many other seasonal parties and random outings. I thank you all for this occasions and delightful moments. My fellow SIM 0.04, it is a great pleasure to share the room-with-unobstructed-view with you. João and Honza, are the first two before me, and awesome friends since. Past and current roomies, Peng, Hann Woei, Tommaso, Ye Zhou, Annemarie, Shuo, Tom, Shushuai, Ying, Bo, and Yingfu, also those who temporarily occupy the space: Paul, Fauzi, Emmanuel, Kirk, and Sihao. Through all the small talks and silent moment, I enjoy your presence! To other fellow PhDs during my time at the C&S: Rita, Wouter, Joost, Jan, Jia, Laurens, Mariam, Herman, Ligu, Deniz, Maarten, Rolf, Yazdi, Gustavo, Sjoerd, Jaime, Sophie, Tao, Ewoud, Henry, Lodewijk, Tim, Ye Zhang, Yingzhi, Kasper, Ivan, Kimberly, Junzi, Wei, Sherry, Isabel, Jerom, Julia, Dirk, Sarah, Mario, Neno, Yke, Diana, Jelmer, Daniel, Paolo, Ezgi, Malik, Anne, and our post-doc, Matej, you all are great comrades! The staffs: Daan, Erik-Jan, Marilena, Olaf, Joost, Bob, Jacco, Xander, Herman, Clark, Hans, Guido, Bart, Christophe, Alwin, Fred, everyone is genuinely open and helpful.

Outside of the C&S setting, I spent my time in the last couple of years, again, in the company of the people from the group, and some related others. Thanks to my conference buddies: Sophie, Yazdi, Jaime, Tommaso, Ye Zhang, Yingzhi, Hann Woei, Tao, Ewoud, and Henry, for all the shared commotions and many adventures that follow. Julia and Michiel, what a coincidence that the three of us meet here in the Faculty and among others, got to chat over our similar experience. To my badminton pals: Wei and Amanda, Sophie, Tommaso, Tao, Emmanuel, Sherry, Hann Woei, and Indra, even though it was only last less than a year, I truly enjoyed our games. Special thanks to Daan for exceptionally organise the yearly N-Team, which allow me to relive one of my passion, basketball, in a fun way.

My life with my family in the Netherlands, in Delft especially, are convenient because of these people who contribute to a home-away-from-home. To Yazdi and Elly, Ocha and Reza, Mbak Pungky and Mas Senot, Mbak Cisca and Mas Stevie, Vera and David, Sandra and Julius, Budi and Nida, Mas Marwan and Mbak Ririn, thank you not only for sharing

both general and family-related info, as well as enjoyable chat, but also your delicious cooking. A special shout to Karina, who allocates some of her busy student life when we occasionally need someone to watch over our daughter. Thanks to the many Indonesian students at Persatuan Pelajar Indonesia (PPI) Delft, especially the board members during the 2013-2014 and 2014-2015 periods, with whom I have the honour to serve in, the In-Delftnesia 2014 committee, and the badminton squad. Interacting with these bright and enthusiastic bunch of people leaves me optimistic for the future. I am lucky to have such friendly and helpful neighbours in our small apartment-complex and also a cool landlord, my appreciation to all of you. The parents and teachers whom I met at my daughter's school and extracurricular activities, thank you for all the advice and small talks that undoubtedly improve my Dutch.

Warm thanks to our extended family in the Netherlands: Tante Swanny and Om Peng, Tante Nanan and Om Harry, Tante Tini and Om Frans, Widya and Arief, who helped us settle in and many other favours. Tribute to my family in Indonesia, for their incredible support despite the distance, my father Gito, my sister Rukmi, my parents-in-law Lilyana and Djoko, my brother-in-law Wisnu, and in the memory of my late mother, Siti. Your encouragement and positivity work for my benefit in finishing my study.

Huge thanks to my husband Indra, the only one who never asks about the progress of my PhD but always be there and supportive, nevertheless. Last but not least, a big hug for my lively daughter Airie, with her sometimes (un)necessary distractions that brought colours to my days. I am grateful to have the two of you there throughout the journey.

Looking at all the above, I consider myself very fortunate to be surrounded by these many extraordinary people, in one of the most memorable time of my life.

*Hartstikke bedankt!*

Delft, October 2018



# CURRICULUM VITÆ

## Dyah JATININGRUM

03-09-1979      Born in Madiun, Indonesia

### EDUCATION

2012–2018      Doctoral, Aerospace Engineering  
Technische Universiteit Delft, Delft, The Netherlands

2006–2008      Master, Aeronautics and Astronautics  
Institut Teknologi Bandung, Bandung, Indonesia

1998–2004      Bachelor, Aeronautics and Astronautics  
Institut Teknologi Bandung, Bandung, Indonesia

### ACADEMIC ACTIVITIES

Reviewer for Sensors & Actuators: A. Physical

Reviewer for International Journal of Aerospace Engineering

Reviewer for AIAA Guidance, Navigation, and Control Conference

## PROFESSIONAL EXPERIENCE

- 2011 Industrial Intern – Aircraft Design and Production Process  
PT Dirgantara Indonesia (*Indonesian Aerospace (IAe)*)  
Bandung, Indonesia
- 2010 Flight Recorder Specialist Trainee  
Australian Transport Safety Bureau (ATSB)  
Canberra, Australia
- 2009–2012 Flight Recorder Specialist  
Komite Nasional Keselamatan Transportasi (KNKT)  
(*National Transportation Safety Committee (NTSC)*)  
Jakarta, Indonesia
- 2005–2012 Researcher – Aerospace Engineering  
Badan Pengkajian dan Penerapan Teknologi (BPPT)  
(*Agency for the Assessment and Application of Technology*)  
Jakarta, Indonesia  
*Projects:*
- 2012 Analysis and Evaluation of Wind Tunnel Test Result in  
Aircraft Design Optimization
- 2011 Development and Utilization of UAV PUNA as a  
Surveillance Technology of Indonesian Navy Ships
- 2007–2009, Test to Support Design of N219 Aircraft  
2011
- 2007–2008 Development of Automatic Dependent Surveillance-  
Broadcast (ADS-B)-Based Flight Monitoring System
- 2006 Fire Suppression Operation utilizing Be-200 aircraft
- 2005–2012 Development of Unmanned Aerial Vehicle
- 2005–2011 Development of Wing-in-Surface Effect Craft
- 2002 Undergraduate Intern – Life Determination of Geosynchronous  
Satellite with Fuel Estimation Program  
PT Telkom Indonesia (Persero) Tbk.  
Bogor, Indonesia

# LIST OF PUBLICATIONS

11. **D. Jatiningrum**, C. C. de Visser, M. M. van Paassen, E. van Kampen, and M. Mulder, *Characterising Angular Accelerometer Calibration Setup Disturbance Using Box–Jenkins Method*, *Advances in Aerospace Guidance, Navigation and Control: Selected Papers of the Fourth CEAS Specialist Conference on Guidance, Navigation and Control Held in Warsaw, Poland, April 2017*, edited by Bogusław Dołęga, Robert Głębocki, Damian Kordos, and Marcin Żugaj, 279–294 (Springer International Publishing, Cham, Switzerland, 2018).
10. **D. Jatiningrum**, C. C. de Visser, M. M. van Paassen, and M. Mulder, *Investigating Misalignment in a 3-Axis Angular Accelerometer Measurement Unit*, *AIAA Guidance, Navigation and Control Conference* (Grapevine, Texas, 2017).
9. **D. Jatiningrum**, C. C. de Visser, M. M. van Paassen, and M. Mulder, *Modelling an Angular Accelerometer using the Frequency-Response Measurements*, *AIAA Guidance, Navigation and Control Conference* (San Diego, California, 2016).
8. **D. Jatiningrum**, C. C. de Visser, M. M. van Paassen, and M. Mulder, *Motion Simulator 2-axes Input Design for Angular Accelerometer Calibration*, *AIAA Modeling and Simulation Technologies Conference* (San Diego, California, 2016).
7. **D. Jatiningrum**, A. Muis, C. C. de Visser, M. M. van Paassen, and M. Mulder, *ZA High-Precision Position Turn-Table as the Reference for Angular Accelerometer Calibration Experiment*, 5<sup>th</sup> CEAS Air and Space Conference (Delft, The Netherlands, 2015).
6. **D. Jatiningrum**, P. Lu, C. C. de Visser, Q. P. Chu, and M. Mulder, *Development of a New Method for Calibrating an Angular Accelerometer Using a Calibration Table*, *AIAA Guidance, Navigation and Control Conference* (Kissimmee, Florida, 2015).
5. **D. Jatiningrum**, C. C. de Visser, M. M. van Paassen, and M. Mulder, *A Framework for Calibrating Angular Accelerometers using a Motion Simulator*, *AIAA Modeling and Simulation Technologies Conference* (Kissimmee, Florida, 2015).
4. **D. Jatiningrum**, H. Muhammad, *Development of Manual for Sail-Flight Test Program of Wing-in-Surface Effect Craft*, Taiwan-Indonesia Workshop in Aeronautical Science, T'ai-nan, Taiwan, December 2008.
3. **D. Jatiningrum**, Y. I. Jenie, S. D. Jenie, *Test Flying Unmanned WiSE as a Means for Proof of Concept*, 28<sup>th</sup> International Council of Aeronautical Science Conference, Anchorage, AK, USA, September 2008.
2. **D. Jatiningrum**, T. Indriyanto, *Flight Dynamics and Performance of WiSE B2 on X-Plane*, Regional Conference on Aeronautical Science, Technology and Industry, Bandung, Indonesia, 2007.
1. **D. Jatiningrum**, S. D. Jenie, *Remote Control Model Test of Wing-in-Surface Effect Craft*, Taiwan-Indonesia Workshop in Aeronautical Science, T'ai-nan, Taiwan, November 2006.